ANISOTROPY OF THE ELECTRON-PHONON INTERACTION IN ALUMINIUM

EFFECTS OF ANISOTROPIES OF THE ELECTRON-PHONON INTERACTION AND THE FERMI SURFACE ON ELECTRONIC PROPERTIES OF ALUMINIUM

By

HON KIT LEUNG, B.Sc.

A Thesis

Submitted to the School of Graduate Studies

in Partial Fulfilment of the Requirements

for the Degree

Doctor of Philosophy

McMaster University

May 1974

DOCTOR OF PHILOSOPHY (1974) McMASTER UNIVERSITY
(Physics) Hamilton, Ontario

TITLE: Effects of Anisotropies of the Electron-Phonon Interaction and the Fermi Surface on Electronic Properties of Aluminium

AUTHOR: Hon Kit Leung, B.Sc. (McMaster University)

SUPERVISORS: Dr. D. W. Taylor, Dr. J. P. Carbotte

NUMBER OF PAGES: v, 178

SCOPE AND CONTENTS:

We have made a theoretical investigation of some of the transport properties of Aluminium. Our calculations include fully (a) the real Fermi Surface in the 4-OPW model of Ashcroft, (b) the electron-phonon matrix element with 15-OPW mixing for the electronic states and (c) the details of the variations of the Fermi velocities on the Fermi Surface (FS).

This is the first calculation to go beyond a spherical surface and single plane wave description of the electron-phonon interaction in Aluminium. We obtain results for the mass-enhancement parameter for electrons on the Fermi Surface, the superconducting energy gaps, the transport lifetimes as they enter in the electrical resistivity and thermal resistivity. Results for the Hall coefficient and effect of phonon-drag on the electrical resistivity and thermopower are also obtained. We have investigated the effect of a small amount of non-magnetic impurities on the Hall coefficient and Deviations from Mathieson's Rule. For all these effects a great deal of agreement is obtained with experimental data.

ACKNOWLEDGEMENTS

I wish to thank my research supervisors, Dr. D. W. Taylor and Dr. J. P. Carbotte for their patience and guidance throughout this project.

I also wish to extend my thanks to Dr. C. R. Leavens, Dr. B. Hayman, Dr. P. Tomlinson and Mr. B. White for their helpful discussions.

I wish to acknowledge the financial assistance of the National Research Council of Canada and McMaster University.

Finally, my appreciation and thanks to Cheryl Hayman for the typing of this thesis.

TABLE OF CONTENTS

CHAPTER I

INTRODUCTION

The picture that we have today of a metal is an assembly of nearly free conduction electrons plus a system of ion cores condensed in a regular crystal lattice. The most important property of the conduction electrons is their ability to propagate from one end of a crystal to the other with relative ease. When an electric field is applied to a crystal it is these electrons that carry the current. They further contribute to the electronic thermal conductivity and the Hall coefficient. Beside the conduction electrons there is the system of ions. Each ion is situated in a deep potential well and can be displaced only slightly from equilibrium. This motion can be described in terms of simple harmonic oscillators. In fact, the dynamics of the crystal lattice can be described in terms of a set of coupled oscillators. The normal modes of vibrations of the system of harmonic oscillators are called phonons.

The coupling between the conduction electrons and the crystal lattice is fundamental to this thesis. The conduction electrons are coupled directly to the ion core through the Hartree potential. When a conduction electron comes close to an ion core it will not only experience this attractive Hartree field but will also be subject to an opposing (repulsive) tendency due to the fact that its wavefunction must be orthogonal to the core electron wavefunctions. Thus we should add to any function which we have in mind as the description of a

conduction wavefunction, an admixture of core states chosen to make it orthogonal to all core states. A plane wave that is made orthogonal to the core states in this way is called an orthogonalized plane wave (OPW). An OPW is a better description of the conduction electron than a plane wave since it has the appropriate rapid wriggles inside the core region of the ion. A mixture of such orthogonalized plane waves is sufficient for describing the conduction electron. A physically equivalent description is to take a few plane waves to describe the conduction electrons and a weak pseudopotential for the Hartree field. This pseudopotential formulation has the great advantage in that perturbation theory can be applied.

The crystal lattice has two important effects on the dynamics of the electrons. When the crystal lattice is in static equilibrium, it provides the crystal potential which changes the wavefunction of a conduction electron from a simple plane wave to a combination of plane waves. As a consequence, distortions are introduced in the spherical Fermi surface near the Bragg planes. Further, when the atoms are displaced from equilibrium an additional force is felt by the conduction electrons which is called the electron-phonon interaction.

In a pure crystal it is the electron-phonon interaction which leads to the electrical resistivity. Also, an electron propagating in the system will have its mass renormalized because it carries with it a cloud of phonons. The same interaction also leads to superconductivity at low temperatures in which case a gap develops in the quasi-particle description of the conduction electrons. To calculate such effects one needs a knowledge of the electrons, the phonons and the electron-phonon interaction. The information that is needed is completely

contained in what we will call the directional weighted phonon frequency distributions. They differ from the ordinary frequency distributions in that each mode is weighted by an appropriate electron-phonon coupling strength. In this thesis, four such frequency distributions will be needed, denoted by $\alpha^2F(\underline{k},\omega)$, $\alpha^2_{tr}F(\underline{k},\omega)$, $\alpha^2_{LL}F(\underline{k},\omega)$ and $\alpha^2_{LL'}F(\underline{k},\omega)$. The first is relevant to the calculation of mass enhancement and superconductivity. The second is used in the calculation of electrical transport properties and the last two are needed in the discussion of the phonon-drag effects.

We shall now describe in more detail the contents of the following chapters.

In Chapter II, we lay down the foundations of our realistic calculations. Section 2.1 starts with a discussion of the pseudopotential in metals originally due to Herring (1940), Phillips and Kleinman (1959), and Cohen and Heine (1961) which proves to be very successful in the calculation of the electronic properties of metals. In Section 2.2, we compute the Fermi Surface of Aluminium in the model suggested by Ashcroft (1963a). He parametrized the FS using 4-OPW's to fit accurately the de Haas-van Alphen data of Gunnersen (1957). After obtaining the accurate FS, we proceed to calculate the wavefunctions of the electronic states by using the Heine-Abarenkov potential (Harrison, 1966) and mixing 15-OPW's in order to preserve the crystal symmetries in the wavefunctions. Then we calculate the Fermi Surface area elements $dS_{\underline{k}}$ and the Fermi velocities $V_{\underline{k}}$ over the FS in the $(\frac{1}{48})$ symmetry zone. Lastly, in Section 2.3, we work out the electron-phonon interaction in the 15-OPW formulation in a manner similar to the work done by Sham (1961) and Sham and Ziman (1963).

Chapter III is mainly concerned with the calculations of the directional phonon distributions $\alpha^2F(\underline{k},\omega)$, $\alpha^2_{tr}F(\underline{k},\omega)$, $\alpha^2_{IL}F(\underline{k},\omega)$, and $\alpha^2_{LL}F(\underline{k},\omega)$ analogous to those defined in Leavens and Carbotte (1972), Hayman and Carbotte (1972, 1973). These distributions, which are frequency distributions weighted by appropriate electron-phonon strengths, containing all of the information on the phonons, the electrons and the electron-phonon interaction needed to calculate the transport properties. For example, $\alpha^2_{tr}F(\underline{k},\omega)$ gives the transport scattering times as they enter the electrical resistivity. Section 3.2 deals with the method of calculation, and in Section 3.3, we discuss the results of the calculations in comparison with the (one-OPW) S-OPW results. In detail, we discuss the singularities that arise in the low frequency region when a S-OPW is used in the distribution functions. We also discuss the prescription suggested by Allen and Cohen (1970) to correct this problem so as to obtain qualitatively correct behaviour at low frequencies. This is compared with our proper 15-OPW treatment.

In Chapter IV, we calculate the directional electron mass enhancement $\lambda_{\underline{k}}$, the directional gap function $\Delta_{\underline{k}}$ and the superconducting transition temperature of single-crystal Aluminium. Similar calculations have been done by Swihart et al (1965a, 1965b) for Pb, Hg and Al and Ashcroft and Wilkins (1965) for Pb, Al and Na. Their agreement with experiment is, in general, within 15%. Allen and Cohen (1970) using a spherical FS, isotropic phonon frequencies and a S-OPW calculated the $\lambda_{\underline{k}}$ for a number of metals. They also included a survey of other calculations. Rice and Sham (1970), Pecheur and Toussaint (1973) calculated $\lambda_{\underline{k}}$ in K and in Zn and Cd respectively. Whereas Leavens and Carbotte (1972), and Truant (1972) use realistic force constant models

for the phonons. Balsley (1969) uses 2-OPW matrix elements for the Umklapp process. Nowak (1972) uses a force constant model for the phonons, APW's for the electron wavefunctions and matrix elements and a realistic FS in his calculation for Cu. He obtained quantitative agreement with the large anisotropies over the FS in the electron lifetimes due to the phonons. Tomlinson (1972, 1973) used a similar approach in calculations for Zinc. Our calculation is, then, very close to that of Nowak and Tomlinson except we and Tomlinson use OPW's instead of APW's. In Section 4.1, we calculate $\lambda_{\underline{k}}$ and discuss the anisotropies comparing them to the S-OPW calculations. We also compare our results with those obtained in previous calculations. Section 4.2 contains calculations of the directional energy gaps and a discussion on their anisotropies. Finally, in Section 4.3, the critical superconducting temperature for pure Al is computed and compared with experiment.

In Chapter V, we discuss transport properties in Aluminium. The pioneering work was done by Bloch (1928) and improved by Bardeen (1937) using a Debye theory and free electrons. Bailyn (1960) included the details of the phonon spectrum in his calculations in the alkali metals. A Born-von Kármán model and a spherical FS were used. The next significant calculation was due to Ziman and Collins (1961) employing a modified Debye spectrum and a "twelve-cone" model for the electrons. They obtained some quantitative agreement with experiment. Greene and Kohn (1965) used a force constant model for the phonons and a phase-shift analysis to describe the electron-ion scattering. They obtained good high temperature results but their low temperature results were in serious disagreement with experiment. The importance of anisotropy, which is ignored in the usual variational solutions to the Boltzmann equation used

by the previous authors, was pointed out by Bailyn (1960), Collins and Ziman (1961) and emphasized by Deutsch et al (1961). Robinson and Dow (1968) employed the relaxation (scattering) time approach to the solution of the Boltzmann equation, hence incorporating in a natural way the anisotropies that might arise from differences in scattering times over the FS. Using this approach, Hayman and Carbotte (1972, 1973) achieved a lot of success in calculating the transport properties of the alkali metals. In Section 5.1, we discuss the Boltzmann equation, and in 5.2, the relaxation time approach to the solution of the Boltzmann equation. In Section 5.3, we calculate the ideal phonon-limited electrical resistivity. We discuss the anisotropy in the scattering times and find the same order of magnitude of variation in $\tau_{\underline{k}}$ as found by Nowak (1972) in Copper. We then show the results of calculations of the electrical resistivity $\rho^{e}(T)$ in S-OPW, variational and scattering time approximations. In Section 5.4, we calculate the thermal resistivity $\rho^{th}(T)$ and compare the variational and scattering time solutions. Section 5.5 deals with the Hall coefficient of Aluminium in the low field limit. In particular, we investigate its variation with temperature especially in the low temperature range where experiments show a change of sign. The formulation is based on that of Ziman (1961a) and Polovov and Sumin (1964). In the alkali metals, experiments have been done by Alderson and Farrell (1969). They attempted to interpret their data on the residual impurity and phonon-drag contributions as due to the variation of n^{*}/n but their arguments were inconclusive. Later work by Hayman and Carbotte showed that the variation is a reflection of the anisotropies in the scattering times but the effect of impurity scattering was neglected. Tsuji (1958) showed that the expression for R_H can be reduced

to an integral over the average radii of curvature on the FS. This served as the starting point of the study on the Hall coefficient of the dilute alloys of Cu and Ag by Dugdale and Firth (1969a, 1969b). They interpreted their data using a two band model to obtain rough estimates of the ratio of scattering times at the necks and bellies on the FS. Recently Douglas and Datars (1973a, 1973b) used Chambers (1956) path integral method to study the magneto-conductivity in Aluminium. They found that the FS curvatures are the main effect in explaining the variation of R_H as a function of field. They also investigated the effects of a two band model similar to Dugdale and Firth to R_H. We discuss the method of calculation of R_H and the geometry in Section 5.1. In Section 5.2, we calculate R_H as a function of temperature in an ideal pure sample and in the presence of isotropic impurity scattering. We also investigate the effect of the FS by keeping $V_{\underline{k}}$ and $dS_{\underline{k}}$ appropriate to the real FS but putting all the radii of curvature equal to k_F^o. In Section 5.3, we study the variation as a function of $p = \frac{\tau_h}{\tau_e}$ by assigning an average impurity scattering time for each of the hole and electron surfaces. In Section 5.4 and Section 5.5, we study $R_H(T)$ as a function of $q = \frac{\tau_B''}{\tau_{NB}}$ and $S = \frac{\tau_B'}{\tau_{NB}}$. Here, q is the ratio of the impurity scattering times for all states at the Bragg planes and for those not at the Bragg planes. For the ratio S we restrict τ_B' to only those states on the hole surface near the Bragg planes.

Another interesting topic is, of course, the Deviations from Matthiessen's Rule for the resistivity of dilute alloys (DMR), for it yields information about the anisotropies in scattering times due to both the impurity and phonon scattering. There have been many papers written on the different contributions to the (DMR), such as inelastic

scattering by vibrating impurity ions (Koshimo 1960, Taylor 1964), interference between scattering by vibrating impurities and host ions (Kagan and Zhernov 1966, 1971, Bhatia and Gupta 1969) anisotropies due to phonon scattering (Kus 1973) and combined with impurity scattering (Dugdale and Basinski 1967, Kohler 1949). These effects are intricate and hard to separate, so we restrict ourselves to low temperatures to avoid most of these effects and concentrate mainly on the effects due to the anisotropies in the scattering times. Section 5.6 then, studies the behaviour of (DMR) for Al-Mg and Al-Ag alloys as a function of temperature in the following cases (i) isotropic scattering by impurities, (ii) as a function of p, (iii) as a function of q, (iv) as a function of S. Here the meanings of p, q and S are the same as in Section 5.5.

In Chapter VI, we study the effect of phonon-drag on the thermopower of Aluminium. Although the theory was laid down by Ziman (1960) and later extended by Bailyn (1967) by including the phonon scattering, there has not been any attempt to calculate this effect quantitatively. With the frequency distributions $\alpha^2_{LL}F(\underline{k},\omega)$ and $\alpha^2_{LL}F(\underline{k},\omega)$, Hayman and Carbotte (1973) found they could correlate qualitatively with experiment the behaviour of phonon-drag effects on the thermopower in the alkali metals. With all the information on the FS of Aluminium on hand, we calculate the thermopower in Aluminium in this Chapter and compare with experiment (Gripshover 1967).

Chapter VII is devoted to a conclusion.

CHAPTER II

ELECTRONS IN METALS

2.1 The Pseudopotential

The usual starting point for a formal theory of the electron-phonon interaction is to write down the total Hamiltonian for the system of ions and electrons. With the aid of the well-known Born-Oppenheimer theorem (1927) we can treat the lattice coordinates as parameters and solve the Schrödinger equation for the electrons,

$$T\psi_{\underline{k}} + V(\underline{r})\psi_{\underline{k}} = E_{\underline{k}}\psi_{\underline{k}} \qquad 2.1.1$$

Here, $T = -\frac{\hbar^2\nabla^2}{2m}$ is the kinetic energy operator for the electron with energy $E_{\underline{k}}$ and in a state $\underline{k}$. $V(\underline{r}) \equiv V(\underline{r},\underline{R}_l)$ is the self-consistent crystal potential as seen by the electron at $\underline{r}$ with the ion at position $\{\underline{R}_l\}$. The electron ground state will be obtained by solving Equation 2.1.1 by requiring $\{\underline{R}_l\} = \{\underline{R}_l^o\}$ where $\underline{R}_l^o$ denotes the equilibrium position of the l^{th} ion. It is well-known that in a metal the electrons behave like plane waves in the interstitial regions between ions while near the ions their wavefunctions oscillate due to the Pauli-exclusion principle. Hence, Herring (1940) suggested that perhaps a more sensible set of eigenfunctions than the plane waves for the electrons in a metal are the so-called orthogonalized plane waves $|OPW\rangle_{\underline{k}}$ (OPW), where

$$|OPW\rangle_{\underline{k}} = |\underline{k}\rangle - \sum_{\alpha} \langle\alpha|\underline{k}\rangle\,|\alpha\rangle \qquad 2.1.2$$

$|\underline{k}\rangle$ is the wavefunction of the plane wave in state $\underline{k}$, and $|\alpha\rangle$ is the wavefunction for the core electron in state α. Phillips and Kleinman (1959) noted that one can substitute Equation 2.1.2 into 2.1.1 and rearrange terms to obtain an equation similar to the Schrödinger equation,

$$T\phi_{\underline{k}} + W(\underline{r})\phi_{\underline{k}} = E_{\underline{k}}\phi_{\underline{k}} \qquad 2.1.3$$

where $\phi_{\underline{k}}$ is related to the true wavefunction $\psi_{\underline{k}}$ by,

$$\psi_{\underline{k}} = 1 - \sum_{\alpha} \langle\alpha|\phi_{\underline{k}}\rangle\,|\alpha\rangle \qquad 2.1.4$$

and $W(\underline{r})$ is related to $V(\underline{r})$ through,

$$W(\underline{r}) = V(\underline{r}) + \sum_{\alpha}(E_{\underline{k}} - E_{\alpha})\,|\alpha\rangle\langle\alpha| \qquad 2.1.5$$

These "mirrored" functions $\phi_{\underline{k}}$ and potential $W(\underline{r})$ are called the pseudowavefunction and pseudopotential. A comparison between Equation 2.1.3 and 2.1.1 shows that the eigenenergies $E_{\underline{k}}$ are identical. Whereas the potential $V(\underline{r})$ is usually a strong attractive potential, Equation 2.1.5 tells us that the strength of $V(\underline{r})$ is greatly weakened by the repulsive part as expressed in the second term. This enables one to use a pertubative approach in solving Equation 2.1.3 and hence Equation 2.1.1. The pseudopotential thus defined is actually an operator and non-local in nature. Although the solutions for $\psi_{\underline{k}}$ and $E_{\underline{k}}$ are unique, the $\phi_{\underline{k}}$ and $W(\underline{r})$ are not (Bassani and Celli (1961), Cohen and Heine (1961)). There are various ways of optimizing and treating the non-local features of the pseudopotential. Excellent reviews can be found in Harrison's book (1966) and an article by Cohen and Heine (1970). Suffice it to say at this point that the pseudopotential has proved to be very useful both as a concept and in computations of various electronic and lattice properties in metals.

If we take $V(\underline{r})$ to be the potential due to a static lattice in equilibrium, then solutions of Equation 2.1.3 give us the dispersion curves $E_{\underline{k}}$ versus $\underline{k}$. Electrons occupy states in $\underline{k}$ space to form a filled region known as the Fermi sea, and its surface, which will determine the most important electron properties, is known as the Fermi Surface (FS). A considerable contribution to our knowledge has in fact come from the fitting of pseudopotentials to experimental data on the F.S. For example, Ashcroft and Gurild (1965) took the pseudopotential of Aluminium fitted to de Haas-van Alphen data (Ashcroft 1963a) and calculated the electrical resistivity of (molten) Aluminium. Ashcroft and Wilkins (1965) calculated the phonon mass enhancement parameter for electrons at low temperatures. Animalu et al (1966) used the Heine-Abarenkov (HA) potentials to give a good interpretation of the phonon spectrum of Al. Carbotte and Dynes (1967a, 1967b) have combined the knowledge of the phonon spectrum and the pseudopotential in calculating the superconducting transition temperature as well as the high temperature (solid) ideal resistivity. Datars and Douglas (1973a, 1973b) used the F.S. fitted by Ashcroft (1963a) to compute path integrals over the F.S. in their magnetoconductivity studies. In view of the success of the previous calculations, we shall describe the F.S. following Ashcroft's (1963a) fitting procedure and employ the (HA) potential to describe the electron-phonon interaction.

2.2 Calculation of the F.S. and the electronic wavefunctions of Aluminium

Aluminium has a f.c.c. crystal structure with valence three. The First Brillouin Zone (FBZ) in $\underline{k}$ space is shown in Figure 2.2.1(a). The FBZ contains the same crystal symmetries as the Wigner-Seitz cell of the direct lattice space. We note, for example, that the [100], [010] and [001] are equivalent directions by crystal symmetry and each is a four-fold symmetry axis, whereas ΓL has three-fold symmetry. Other symmetry points are designated by the letters U, W, K. A qualitative picture of the occupied states in Aluminium can be obtained by using the S-OPW approximation. In such an approximation the F.S. is a sphere centred at Γ with radius k_F°. For Aluminium, $k_F^\circ = 1.127(\frac{2\pi}{a})$, so the F.S. extends beyond the FBZ and intersects with the neighbouring second and third zones. In the reduced zone scheme we can follow the method of Harrison (1960) by drawing spheres with radius k_F° centred at other points and let them intersect inside the FBZ. Those regions contained inside two spheres form the F.S. in 2nd zone etc. For more details, we refer to Harrison (1966). For Aluminium, the FBZ is completely filled while Figure 2.2.1(b) and Figure 2.2.1(c) show the second and third zone surfaces. The 2nd zone is a closed surface with the states inside unoccupied and hence will be referred to as a hole surface while the 3rd zone consists of electron surfaces (occupied states inside) with arms along the edges of the FBZ. In a more proper treatment of the electron wavefunction in which plane waves of the same energies are mixed by the

Fig. 2.2.1 The Fermi Surface of Al

(a) The Brillouin Zone of face centered cubic Aluminium

(b) The S-OPW second band hole surface of Aluminium

(c) The S-OPW third band electron Fermi Surface of Aluminium

(d) The 4-OPW third band electron Fermi Surface of Aluminium, after Ashcroft (1963)[a]

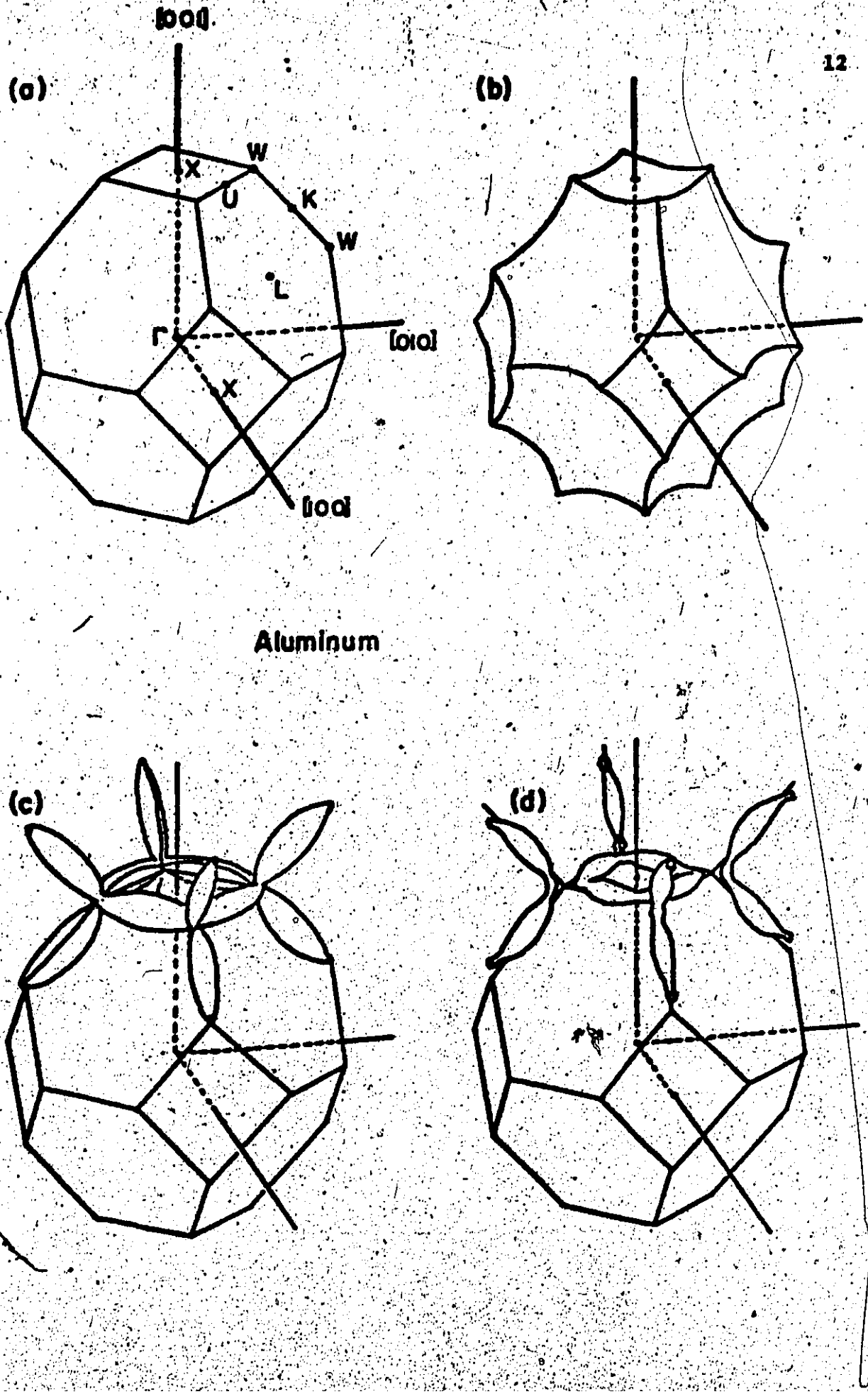
[001]
(a)
X
W
U
K
W
L
Γ
[010]
X
[100]
(b)
Aluminum
(c)
(d)

pseudopotential, the essential modifications introduced in the description of the F.S. are mainly at the intersections with the Bragg planes. Figure 2.2.1(a) shows that the electron arms in a 4-OPW approximation (Ashcroft 1963a) are modified most drastically near the point W where three Bragg planes meet. Similarly for the hole surfaces, all the sharp edges are rounded off.[1]

To obtain a more quantitative picture of the Fermi Surface, we follow the procedure of Ashcroft (1963a). We restrict our attention to $(\frac{1}{48})$ of the symmetry zone. In Figure 2.2.2 we draw the six equivalent $(\frac{1}{48})$ symmetry zones in the positive octant in wave-number space. We choose the $(\frac{1}{48})$ zone (labelled I) which is defined by the following inequalities — $k_z \geq 0$, $k_x \geq k_y$, and $k_y \geq k_z$. Once the F.S. is determined in this sector, it is a simple matter to map out the other directions using the symmetry operations. In the $(\frac{1}{48})$ zone the electronic wavefunctions will, in general, be described by the mixture of four plane waves $|\underline{k} + \underline{G}_n\rangle = \frac{1}{\sqrt{V}} \exp i(\underline{k} + \underline{G}_n)\cdot\underline{r}$ where $\underline{G}_1 = (0,0,0)$, $\underline{G}_2 = (2,0,0)$, $\underline{G}_3 = (1,1,1)$ and $\underline{G}_4 = (1\bar{1}\bar{1})$. We are assuming that the other farther away components produce little effect. This is then the 4-OPW approximation. We can write down the eigenvalue equation corresponding to Equation 2.1.3,

$$\sum_{j=1}^{4} \langle \underline{k}+\underline{G}_i | T + W(r) | \underline{k}+\underline{G}_j \rangle C_{\underline{k}j} = E_{\underline{k}} C_{\underline{k}i} \quad , \; i = 1,2,3,4 \qquad 2.2.1$$

assuming

$$\phi_{\underline{k}} = \sum_{n=1}^{4} C_{\underline{k}n} |\underline{k}+\underline{G}_n\rangle \qquad 2.2.2$$

[1] In the approximation of a local pseudopotential $W(\underline{r})$, it turns out that Equation 2.2.1 only depends on the parameters $W(\underline{G}_3)$ and $W(\underline{G}_2)$. Ashcroft found that the values of $W(111) = .0179$ ryd, $W(200) = .0562$ ryd and $E_F = .85605$ ryd fit the de Haas-van Alphen experimental

Fig. 2.2.2 The six equivalent ($\frac{1}{48}$) zones in the positive octant in the FCC crystal of Aluminium

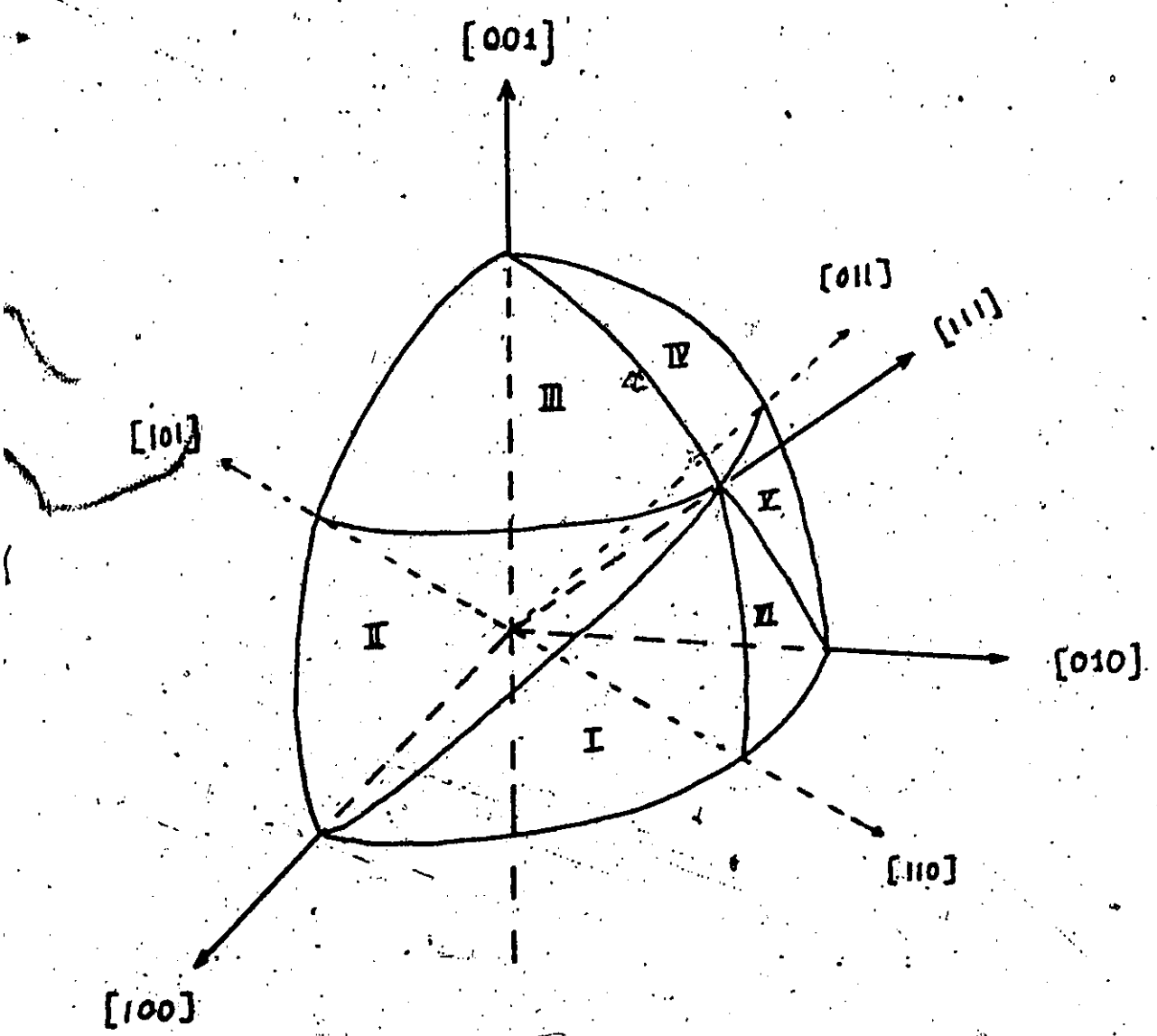
[001]
[011]
[111]
[101]
[010]
[110]
[100]
I
II
III
IV
V
VI

data very well. Later optical experiments by Hughes et al (1969) gave W(200) = .053, and soft x-ray analysis by Rooke (1968) yielded W(111) = .017 ± .013 and W(200) = .053 ± .013. Both are consistent with Ashcroft's values. With Ashcroft's parameters we divide up the $(\frac{1}{48})$ zone (labelled I) into a fine mesh of approximately 4,000 (θ,ϕ) directions at $\frac{1}{2}°$ intervals. The k_z[001] axis is taken to be the polar axis and ϕ is measured from the [100] axis. At each of these directions we let the length $k = |\underline{k}|$ be the varying parameter. With $k_F^o = 1.12725$ as the initial value for $k_1(\theta,\phi)$ we diagonalize Equation 2.2.1 and thus obtain the eigenvalues for $E_{\underline{k}n}^{(1)}$, n = 1 to 4. Depending on the length and direction the zone index n is found and $E_{\underline{k}n}^{(1)}$ is compared to E_F(= .85605 Ryd). By using steps of 0.01 $(\frac{2\pi}{a})$ another value $k_2(\theta,\phi)$ is obtained so that the energy eigenvalues $E_{\underline{k}n}^{(2)}$ and $E_{\underline{k}n}^{(1)}$ form upper or lower bounds for E_F, e.g. $E_{\underline{k}n}^{(2)} < E_F < E_{\underline{k}n}^{(1)}$. Once this information is obtained, we can easily use a bisection method to obtain $k_F(\theta,\phi)$ within an accuracy of ±0.00005$(\frac{2\pi}{a})$. If E_F is found to lie between bands, then the Fermi sea is bounded by a Bragg plane in that particular direction. We plot the $\theta = 90°$ plane cross-section of the F.S. in Figure 2.2.3 and this is identical to what Ashcroft obtained (1963).

Next we calculate the velocity vector $\underline{V}_{\underline{k}}$ on the F.S. in the $(\frac{1}{48})$ symmetry zone. This can be easily accomplished by varying $\underline{k}_F$ at the F.S. in the three cartesian directions by .01 $(\frac{2\pi}{a})$ and computing the change in $E_{\underline{k}}$. Remembering that $\underline{V}_{\underline{k}} = \frac{1}{\hbar}\left(\frac{\partial\varepsilon_{\underline{k}}}{\partial k_x}, \frac{\partial\varepsilon_{\underline{k}}}{\partial k_y}, \frac{\partial\varepsilon_{\underline{k}}}{\partial k_z}\right)$, we obtain the vectors $\underline{V}_{\underline{k}}$ at each of the 4,000 points in the $(\frac{1}{48})$ zone. In order to have an idea of how $|\underline{V}_{\underline{k}}|$ changes over the F.S. we compute $V_{\underline{k}}^2/V_F^{o2}$

Fig. 2.2.3 The cross-section of the Fermi Surface of Aluminium on the (001) plane through Γ.

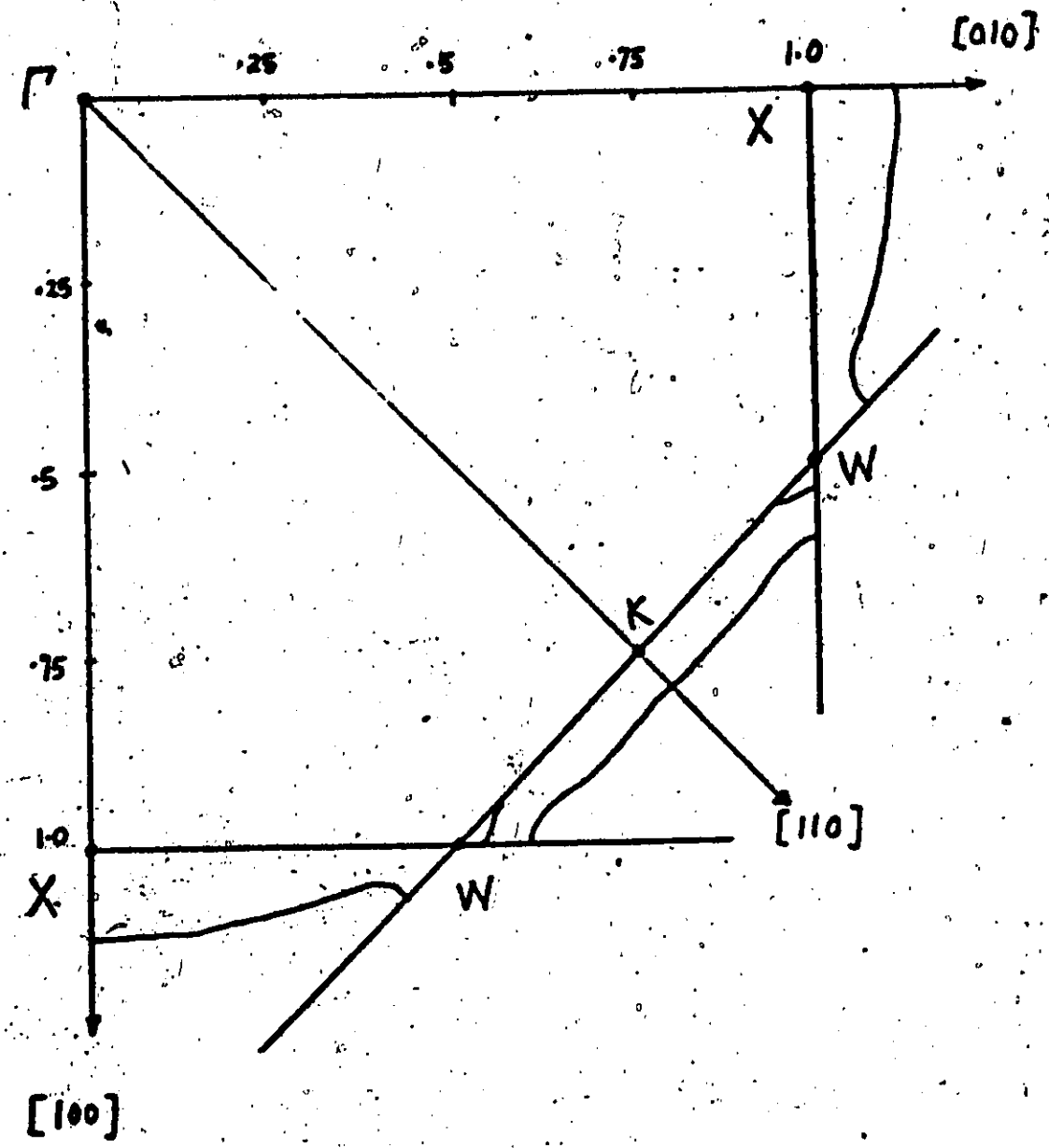
Γ
·25
·5
·75
1·0
[010]
X
·25
·5
·75
1·0
W
K
[110]
X
W
[100]

and plot the sections $\theta = 90°$ and $\phi = 45°$ on Figure 2.2.4. From Figure 2.2.4(a) when we start from the [100] axis which is on the middle of the hole surface, the velocity is close to the free electron value. As we move closer to the Bragg plane the velocity decreases to a value of about $0.8V_F^\circ$. After passing through a region with no F.S., we reach the electron arm surface. The velocity at the Brillouin Zone Boundary (BZB) is very small (about $0.5V_F^\circ$) and increases very rapidly as we move further away from the boundary (to a value of $0.9V_F^\circ$). In the $\phi = 45°$ plane we again see similar behaviour, i.e., on the hole surface the velocity is almost constant and of value $1.0V_F^\circ$ until it reaches the BZB where it has decreased to about $0.8V_F^\circ$. The electron surface shows more variation: $0.5V_F^\circ$ at the BZB and $0.9V_F^\circ$ at the top centre of the arm. This is easily understood in terms of influences due to the Bragg planes. The hole surface is more extensive and most of its surface is farther away from the Bragg plane defined by $\underline{G} = (111)$, whereas the electron arm surface is closer to the two Bragg planes defined by $\underline{G} = (100)$ and $\underline{G} = (111)$. The variation in the velocities is important in taking averages over the F.S. because they are directly related to the density of states. Moreover, as will be seen in later sections, they are related to quantities such as the Hall coefficient and the impurity scattering.

We can calculate the total density of states at the F.S. by noting that (Kittel 1967)

$$N(0) = \frac{2}{(2\pi)^3} \int \frac{dS_k}{\nabla E_k} \qquad 2.2.3$$

Fig. 2.2.4 The variation of the ratio V_k^2/V_F^{*2} over the FS of Aluminium

(a) in the plane defined by $\theta = 90°$

(b) in the plane defined by $\phi = 45°$

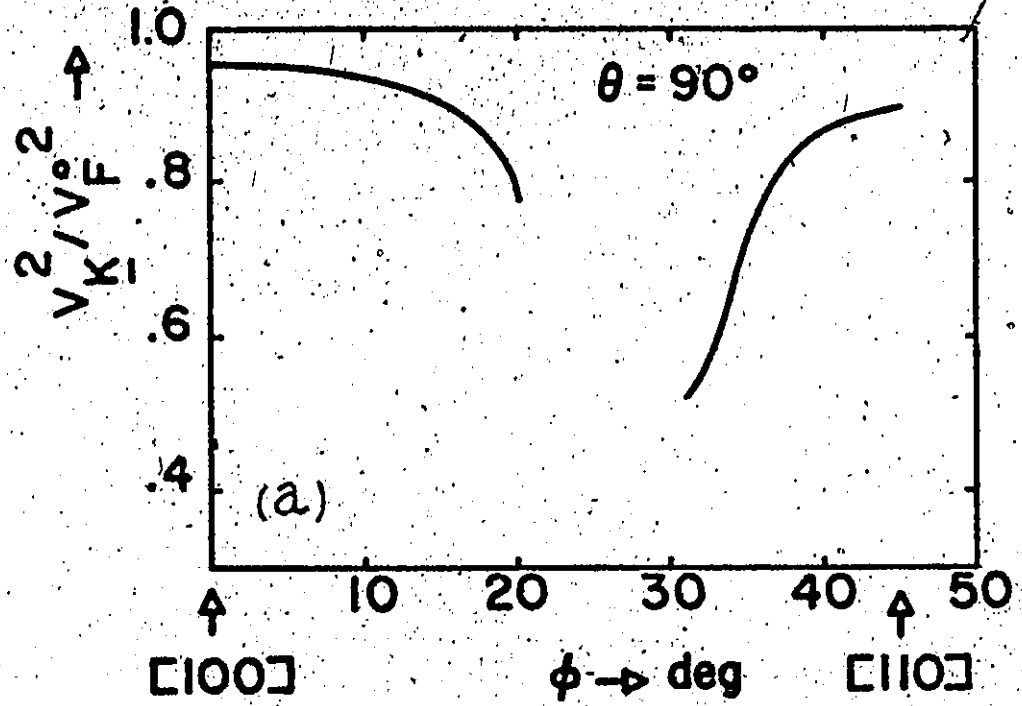

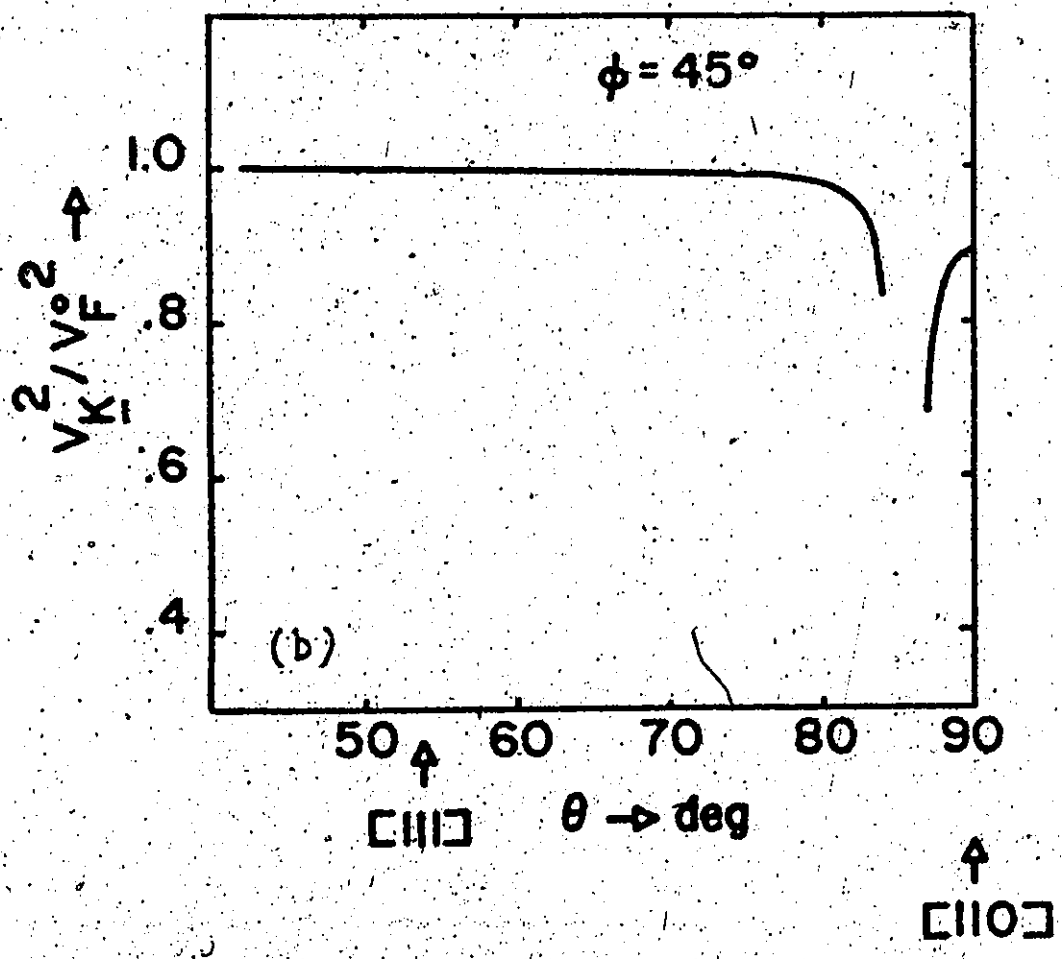

where $dS_{\underline{k}}$ is the element of area at the point $\underline{k}$ on the F.S. Although the total area of the F.S. in this model is smaller than that of the free electron F.S. (about 80%) due to the intersections with Bragg planes, the fact remains that $V_{\underline{k}}$ is smaller at various regions near the Bragg planes. In the end we obtain a value for N(o) which is 91% of the free electron F.S.

Later computations of the electron-phonon matrix elements will involve scattering of electrons across the entire F.S. Although the wavefunctions for the electron states were obtained in the previous calculation of the Fermi Surface as a result of the diagonalization procedure, we feel that for the electron-phonon interaction it is necessary to extend the description of the electrons to combinations of 15 plane waves in order to keep the full symmetry of the crystal lattice. This is referred to as the 15-OPW approximation. The pseudopotential that we use is the Heine-Abarenkov (HA) model pseudopotential tabulated in Harrison (1966). Essentially it is a local, on-sphere approximation which implies W(q) = W(q). A plot of the (HA) pseudopotential is shown in Figure 2.2.5.

If we rewrite the Equations 2.2.1 and 2.2.2 by extending the summations to 15 terms then we find that all we need are six Fourier components. These are listed below in Table 2.2.1.

Table 2.2.1

The Fourier Components at the Six Reciprocal Lattice Vectors

No.	1	2	3	4	5	6
$\underline{G}$ $(\frac{2\pi}{a})$	(111)	(200)	(220)	(311)	(040)	(222)
W(G) ryd	-.0174	.0560	.0569	.0216	.0142	.0099

The relative positions of these six components on the pseudopotential are marked on Figure 2.2.5. The 15-OPW components correspond to the following $\underline{G}$ vectors:

$\underline{G}_1 = (0,0,0)$, $\underline{G}_2 = (200)$, $\underline{G}_3 = (\bar{2}00)$, $\underline{G}_4 = (020)$, $\underline{G}_5 = (0\bar{2}0)$,

$\underline{G}_6 = (002)$, $\underline{G}_7 = (00\bar{2})$, $\underline{G}_8 = (111)$, $\underline{G}_9 = (\bar{1}11)$, $\underline{G}_{10} = (1\bar{1}1)$

$\underline{G}_{11} = (11\bar{1})$, $\underline{G}_{12} = (1\bar{1}\bar{1})$, $\underline{G}_{13} = (\bar{1}\bar{1}1)$, $\underline{G}_{14} = (\bar{1}1\bar{1})$, $\underline{G}_{15} = (\bar{1}\bar{1}\bar{1})$.

The value of k_p at each of the 4,000 directions of (θ,ϕ) is fed into the set of eigenvalue equations and diagonalized. The coefficients for the mixing of the 15-OPW are stored together with the data on $k_p(\theta,\phi)$ $dS_{\underline{k}}$ and $\underline{V}_{\underline{k}}(\theta,\phi)$ on a tape. By using the symmetry operations, the details of the F.S. and the above electronic properties on it are thus obtained through an interpolation scheme.

For computational convenience, we use computational units (C.U.) in which $\underline{k}$ is measured in units of $(\frac{2\pi}{a})$ and energy in units of $\frac{\hbar^2}{2m}(\frac{2\pi}{a})^2$. Choosing the free electron mass m, one C.U. is equal to .454 ryd.

Fig. 2.2.5 The Heine-Abarenkov model pseudopotential $\omega(q)$ as a function of q. The 'x' corresponds to the position of the Fourier components used in the 15-OPW calculation of the coefficients of the electron wavefunctions

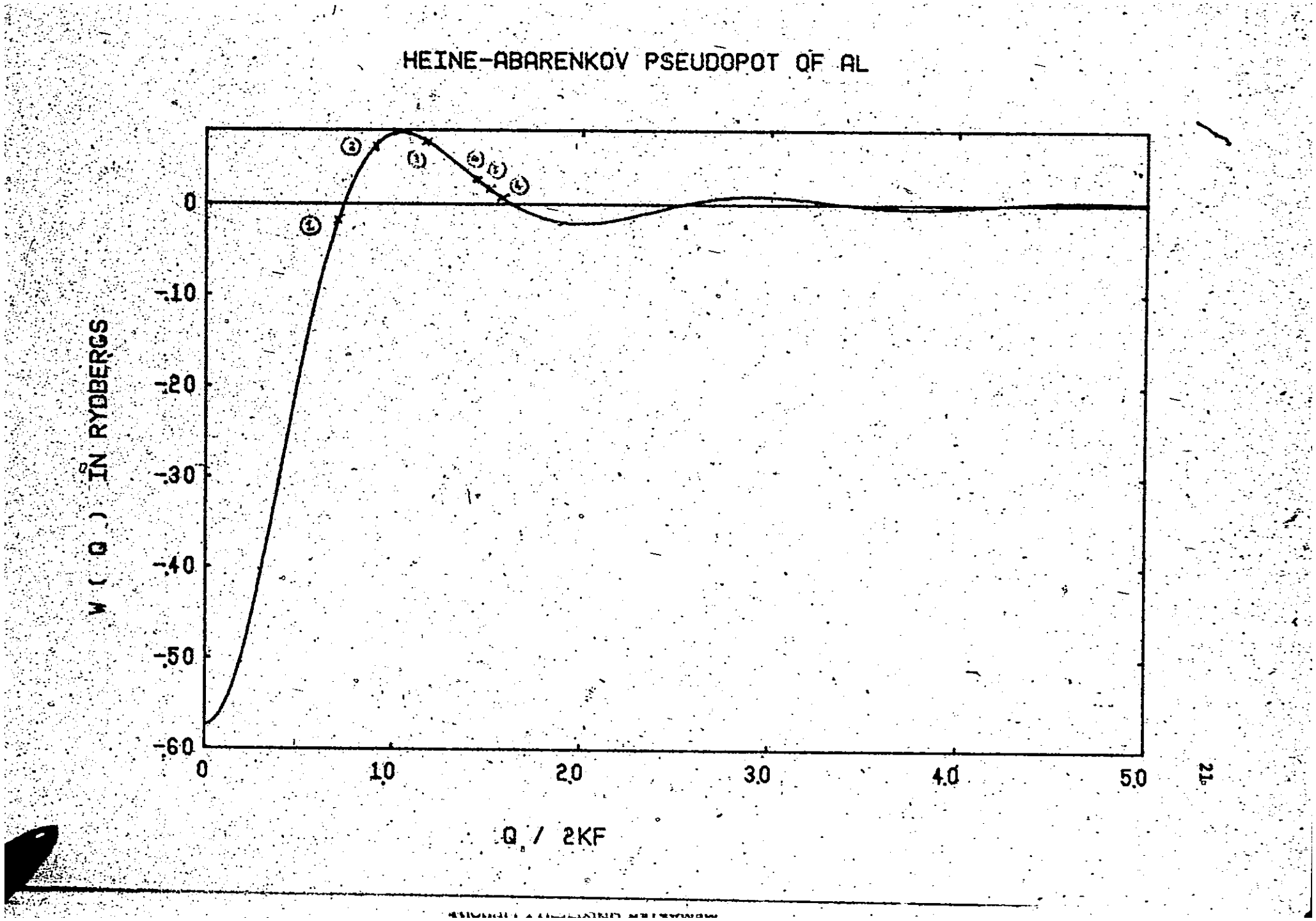
HEINE-ABARENKOV PSEUDOPOT OF AL
W (Q) IN RYDBERGS
0
-.10
-.20
-.30
-.40
-.50
-.60
0
1.0
2.0
3.0
4.0
5.0
Q / 2KF
21

2.3 The Electron-Phonon Interaction

In this section, we shall describe the interactions between the electrons and ions in the metal in the S-OPW and multi-OPW approximations. In the pseudopotential formalism the interaction can be handled very conveniently. A full derivation can be found in Sham and Ziman (1965) and Carbotte and Dynes (1968). Very simply we state that an electron at $\underline{r}$ in state $|\underline{k}\rangle$ sees the ionic potential at $\underline{R}_l$ as $w(\underline{r} - \underline{R}_l)$, where $w(\underline{r})$ is the pseudopotential of the host ion. Hence the total scattering amplitude of the electron from state $|\underline{k}\rangle$ into $|\underline{k}'\rangle$ is given by

$$\langle \underline{k}' | W(\underline{r}) | \underline{k} \rangle = \frac{1}{V} \sum_l \int d^3\underline{r}\, e^{i(\underline{k}-\underline{k}')\cdot\underline{r}}\, w(\underline{r}-\underline{R}_l) \qquad 2.3.1$$

in the S-OPW approximation. Here, V is the total volume of the crystal and $W(\underline{r}) = \sum_l w(\underline{r}-\underline{R}_l)$ is the crystal potential. By using the transformation $\underline{y} = \underline{r} - \underline{R}_l$, Equation 2.3.1 splits into two factors: a structural term $S(\underline{k}'-\underline{k})$ and a potential term,

$$\langle \underline{k}' | W(\underline{r}) | \underline{k} \rangle = S(\underline{q}) \langle \underline{k}' | w | \underline{k} \rangle \equiv \left(\frac{1}{N} \sum_l e^{i\underline{q}\cdot\underline{R}_l} \right) \left(\frac{1}{\Omega_0} \int d^3\underline{y}\, e^{-i\underline{k}'\cdot\underline{y}}\, w(\underline{y})\, e^{i\underline{k}\cdot\underline{y}} \right) \qquad \ldots\ldots 2.3.2$$

where N = number of ions, Ω_0 = vol/ion = $\frac{V}{N}$ and $\underline{q} = \underline{k}'-\underline{k}$. Expanding $\underline{R}_l = \underline{R}_l^\circ + \underline{\eta}_l$ about the equilibrium position $\underline{R}_l^\circ$, the term $S(\underline{q})$ leads to a Bragg term involving the static lattice and a second term involving the lattice vibrations. The contribution to $\langle \underline{k}' | W(\underline{r}) | \underline{k} \rangle$ from this latter term is,

$$-\frac{i}{N} \sum_l e^{i(\underline{k}-\underline{k}')\cdot\underline{R}_l^\circ}\, (\underline{k}-\underline{k}')\cdot\underline{\eta}_l\, \langle \underline{k}' | w | \underline{k} \rangle \equiv W_{ep}(\underline{k}\underline{k}') \qquad \ldots\ldots 2.3.3$$

and the contribution to the Hamiltonian H' is

$$H' = \sum_{kk'} W_{ep}(kk')\, C_{\underline{k}}^{+} C_{\underline{k}} \qquad 2.3.4$$

where $C_{\underline{k}}^{+}$, $C_{\underline{k}}$ are the usual creation and annihilation operators for electrons. We further invoke the harmonic approximation and write $\underline{\eta}_l$ in terms of the phonon representation

$$\underline{\eta}_l = \frac{1}{\sqrt{MN}} \sum_{\underline{k}\lambda} \frac{\underline{e}(\underline{k},\lambda)\, e^{i\underline{k}\cdot\underline{R}_l^0}}{(2\,\omega(\underline{k},\lambda))^{\frac{1}{2}}} (a_{-\underline{k}\lambda}^{+} + a_{\underline{k}\lambda}) \qquad 2.3.5$$

where M is the ionic mass, $\omega(\underline{k},\lambda)$ is the frequency of the phonon with polarization index λ, $\underline{e}$ the polarization vector in the λ branch, $a_{-\underline{k}\lambda}^{+}$, $a_{\underline{k}\lambda}$ phonon creation and annihilation operators. Substituting Equation 2.3.5 into expression 2.3.3 and performing the summations, keeping in mind that the phonons are restricted to the FBZ, we obtain in place of Equation 2.3.4 the simple result in the S-OPW approximation,

$$H' = \sum_{\underline{k}\underline{k}'\lambda} g_{\underline{k}'\underline{k}\lambda}\, C_{\underline{k}'}^{+} C_{\underline{k}} (a_{-(\underline{k}'-\underline{k})\lambda}^{+} + a_{\underline{k}'-\underline{k}\lambda}) \qquad 2.3.6(a)$$

where

$$g_{\underline{k}'\underline{k}\lambda} = \frac{i(\underline{k}-\underline{k}')\cdot\underline{e}(\underline{k}'-\underline{k},\lambda)\,\langle \underline{k}'|w|\underline{k}\rangle}{(2MN\,\omega(\underline{k}'-\underline{k},\lambda))^{\frac{1}{2}}} \qquad 2.3.6(b)$$

and is called the electron-phonon coupling constant.

In polyvalent metals such as Aluminium, the electron wave-functions can be adequately described only by a mixture of plane waves (OPW's), that is, we write the (pseudo) wavefunction of the electron as

$$\phi_{\underline{k}} = \sum_{n} C_{\underline{k}n}\, |\underline{k}+\underline{G}_n\rangle \qquad 2.3.7$$

We now express $w(\underline{r}-\underline{R}_l)$ in terms of Fourier components $w(\underline{q})$ and again expand $\underline{R}_l$ as $\underline{R}_l^0 + \underline{\eta}_l$, and obtain

$$w(\underline{r}-\underline{R}_l) \simeq \frac{1}{V} \sum_{\underline{q}} e^{i\underline{q}\cdot(\underline{r}-\underline{R}_l^0)} (1 - i\underline{q}\cdot\underline{\eta}_l)\, w(\underline{q}) \qquad 2.3.8$$

The first term is again due to the static lattice and can be neglected. Making the same substitutions as before we obtain (after simplification), the equivalent coupling constant

$$g_{\underline{k}'\underline{k}\lambda} = \frac{1}{V}\sum_{\underline{q}}\sqrt{\frac{N}{M}}\;\frac{-i\underline{q}\cdot\underline{e}(\underline{k}'-\underline{k},\lambda)}{(2\omega(\underline{k}'-\underline{k},\lambda))^{\frac{1}{2}}}\int d^3\underline{y}\;\phi^*_{\underline{k}'}(\underline{y})\,\phi_{\underline{k}}(\underline{y})\,\omega(\underline{q})\,e^{i\underline{q}\cdot\underline{y}} \qquad \text{.....2.3.9}$$

Substituting Equation 2.3.7, the expansion for $\phi_{\underline{k}}$, into Equation 2.3.9 and performing the integral over $\underline{y}$ yields the result

$$g_{\underline{k}'\underline{k}\lambda} = \frac{-i\underline{e}(\underline{k}'-\underline{k},\lambda)}{(2MN\omega(\underline{k}'-\underline{k}\lambda))^{\frac{1}{2}}}\left\{\sum_{nn'}(\underline{k}'+\underline{G}_{n'}-\underline{k}-\underline{G}_n)\langle\underline{k}'+\underline{G}_{n'}|w|\underline{k}+\underline{G}_n\rangle\, C^*_{\underline{k}'n'}\, C_{\underline{k}n}\right\} \qquad \text{2.3.10}$$

A comparison with Equation 2.3.6 immediately reveals that the 15-OPW result (Equation 2.3.10) has the same form as the S-OPW result except that $\langle\underline{k}'|w|\underline{k}\rangle$ in the S-OPW formalism has to be replaced by the complicated expression in the curly brackets of Equation 2.3.10.

As we will see in subsequent sections, the inclusion of many OPW's in the description of the electron states will lead to some qualitatively as well as quantitatively different results from the S-OPW case.

CHAPTER III

CALCULATIONS OF THE WEIGHTED DISTRIBUTION FUNCTIONS

3.1 Definitions

The essential information on the electron-phonon interaction is contained in the four weighted distributions $\alpha^2F(\underline{k},\omega)$, $\alpha^2_{tr}F(\underline{k},\omega)$, $\alpha_{IL}F(\underline{k},\omega)$ and $\alpha_{LL}F(\underline{k},\omega)$. In this Chapter we will define them and show the method of calculation. The application of these directional distribution functions for the calculation of the various properties will be dealt with in full detail in later sections. The simpler forms of these distributions (in the S-OPW approximation) can be found in Leavens and Carbotte (1972) and Hayman and Carbotte (1973). In terms of integrals over the F.S. they are defined as

$$\alpha^2F(\underline{k},\nu) = (8\pi^3\hbar^2)^{-1}\int \frac{dS_{k'}}{v_{\underline{k}'}} \sum_{\lambda} |g_{\underline{k}\underline{k}'\lambda}|^2 \delta(\nu-\omega_{\underline{k}\underline{k}'\lambda}) \qquad 3.1.1$$

$$\alpha^2_{tr}F(\underline{k},\nu) = (8\pi^3\hbar^2)^{-1}\int \frac{dS_{k'}}{v_{\underline{k}'}} \sum_{\lambda} |g_{\underline{k}\underline{k}'\lambda}|^2 \left(1-\frac{\underline{v}_{\underline{k}}\cdot\underline{v}_{\underline{k}'}}{v^2_{\underline{k}}}\right) \delta(\nu-\omega_{\underline{k}\underline{k}'\lambda}) \qquad .....3.1.2$$

$$\alpha^2_{IL}F(\underline{k},\nu) = (8\pi^3\hbar^2)^{-1}\int \frac{dS_{k'}}{2k_F^2 v_{\underline{k}'}} \sum_{\lambda} |g_{\underline{k}\underline{k}'\lambda}|^2 \underline{q}\cdot(\underline{k}-\underline{k}') \delta(\nu-\omega_{\underline{k}\underline{k}'\lambda}) \qquad .....3.1.3$$

$$\alpha^2_{LL}F(\underline{k},\nu) = (8\pi^3\hbar^2)^{-1}\int \frac{dS_{k'}}{2k_F^2 v_{\underline{k}'}} \sum_{\lambda} |g_{\underline{k}\underline{k}'\lambda}|^2 \underline{q}\cdot\underline{q} \delta(\nu-\omega_{\underline{k}\underline{k}'\lambda}) \qquad 3.1.4$$

where $g_{\underline{k}\underline{k}'\lambda}$ is the electron-phonon coupling parameter defined in Equation 2.3.10. In the case of S-OPW, the surface integrals become angular integrals and $g_{\underline{k}\underline{k}'\lambda}$ is replaced by Equation 2.3.6(b). $\omega_{\underline{k}-\underline{k}'\lambda}$ is the

phonon frequency with momentum vector $\underline{k}-\underline{k}'$ reduced to the FBZ, i.e. $\underline{k}-\underline{k}' = \underline{q} + \underline{G}$ for some suitable value of $\underline{G}$. These directional functions describe weighted scattering processes of an electron in state $|\underline{k}\rangle$ into all possible final states due to the interaction with the phonons. The delta functions express the energy conservation during these scattering processes.

3.2 Method of Calculation

We shall follow the method suggested by Leavens and Carbotte (1972). Realistic phonons are incorporated in the computation of the integrals. Phonon dispersion curves along the symmetry directions have been measured by the technique of inelastic neutron scattering by Gilat and Nicklow (1966), and the data fitted by means of a least-square fit to the Born-von Kármán model. The model assumes that the ions are held in their equilibrium positions by means of springs described by force constants. The force springs for each particular atom are assumed to extend to neighbouring atoms up to a certain distance and beyond that are assumed negligible. With these force constants $\phi_{\alpha\beta m}$ ($\phi_{\alpha\beta m}$ is the force on the ion at the origin in the direction due to a unit displacement of the m^{th} ion in the β direction. α and β represent the x, y and z directions), then, a dynamical matrix can be set up at any $\underline{q}$ vector

$$\omega^2_{\underline{q}\lambda}\,\underline{e}_{\underline{q}\lambda} = \sum_{\beta} D_{\alpha\beta}(\underline{q})\,\underline{e}_{\underline{q}\lambda} \qquad 3.2.1$$

where α,β are the cartesian components, $\underline{e}_{\underline{q}\lambda}$ the polarization vector in the λ^{th} branch and wave vector $\underline{q}$. $D_{\alpha\beta}(\underline{q})$ is related to the force constants $\phi_{\alpha\beta m}$ by

$$D_{\alpha\beta}(\underline{q}) = \frac{1}{M}\sum_{m} e^{-i\underline{q}\cdot\underline{R}^0_m}\,\Phi_{\alpha\beta m} \qquad 3.2.2$$

where now M is the ionic mass, $\underline{R}^0_m$ the equilibrium positions of the m^{th} ion. Diagonalization of Equation 3.2.1 yields simultaneously the frequencies $\omega_{\underline{q}\lambda}$ ($\lambda = 1,2,3$) and the corresponding eigenvectors $\underline{e}_{\underline{q}\lambda}$.

The electron-ion pseudopotential form factor $w(q)$ is taken to be

that of Heine and Abarenkov (1964) tabulated in Harrison (1966) for q between zero and $10k_F^\circ$, where k_F° is the free electron Fermi radius. In order to obtain a smoother function through these data points, the range $10k_F^\circ$ is divided into five equal sections and each is fitted with a 10^{th} degree polynomial. With this information the numerical integral of the directional distributions can be evaluated in a straightforward way. The range of frequencies $0 < \nu < \omega_c$ is divided into 100 channels each of width $\omega_c/100$, ω_c being the maximum phonon frequency in Al ($= 10^{13}$ cps.). The surface of the Fermi sphere is divided into $90 \times 180 = 16{,}200$ small areas whose contributions to the density of states are calculated in Section 2.2. These areas are obtained by dividing up the Fermi sphere by ninety lines of latitude, 180 lines of longitude all at 2° apart. An initial point (k,θ,ϕ) is selected inside one of these small areas, then a systematic way is set up to scan through each of these 16,200 points labelled by (k',θ',ϕ'), k' being the length of the wave vector $\underline{k}'$ in direction defined by (θ',ϕ'). The length $\underline{k}'-\underline{k} = \underline{Q}$ is calculated, $\underline{Q}$ being the momentum wave vector of the phonon involved. $\underline{Q}$ is fed into Equation 3.2.1 and a diagonalization yields the proper values of $\omega_{\underline{q}\lambda}$, $e_{\underline{q}\lambda}$ where $\underline{q}$ is the wave vector $\underline{Q}$ reduced to the FBZ.

Then the mixing coefficients $C_{\underline{k}m}$ for $\phi_{\underline{k}}$ and $C_{\underline{k}'n'}$ for $\phi_{\underline{k}'}$ are read in and for each of the $15 \times 15 = 225$ terms which make up $g_{\underline{k}\underline{k}'\lambda}$, $\underline{G}=\underline{k}'-\underline{G}_n, -\underline{k}+\underline{G}_n$ in Equation 2.3.10 is calculated. From the first value of $\underline{G}$, $w(\underline{G})$ is determined and then added to the next term in the curly bracket in Equation 2.3.10. After $g_{\underline{k}\underline{k}'\lambda}$ is calculated, we can turn to calculate the other geometrical weight factors in the various

distributions, namely $1 - \frac{\underline{v}_k \cdot \underline{v}_{k'}}{v_k^2}$, $\underline{q} \cdot (\underline{k}-\underline{k}')$ and $\underline{q}\,\underline{q}$ which cause no trouble at all except that one keeps in mind that $\underline{q}$ is a phonon variable. Thus, we must be careful to reduce it back in FBZ before it is used in evaluating Equation 3.1.3 and 3.1.4.

The results come out as a histogram function of ν. For normalisation purposes we define the function

$$N(\nu,\theta,\phi) = (8\pi^3\hbar)^{-1} \int \frac{dS_{k'}}{v_{k'}} \sum_{\lambda} \delta(\nu - \omega_{\underline{q}\lambda}) \qquad 3.2.3$$

and we calculate $N(\nu,\theta,\phi)$ together with the above functions. Using the property of the delta function we obtain

$$\int d\nu\, N(\nu,\theta,\phi) = 3\,N(0) \qquad 3.2.4$$

Thus, we sum all the contributions to $N(\nu,\theta,\phi)$ in the computer programme and compare it to 3 to find the proper normalization constant.

The electron in state (k,θ,ϕ) has a renormalized mass m^* due to the interaction with the phonon system, and is given by (Allen and Cohen 1970)

$$m^*(\theta,\phi) = m_b(1+\lambda(\theta,\phi)) \qquad 3.2.5$$

where m_b is the free mass and

$$\lambda(\theta,\phi) = 2\int_0^{\infty} \frac{d\nu}{\nu}\, \alpha^2F(\underline{k},\nu) \qquad 3.2.6$$

Evaluation of $\lambda(\theta,\phi)$ can be simply done by incorporating it with the calculation of $\alpha^2F(\underline{k},\nu)$ in an obvious way.

The computations of these weighted distributions were performed on the CDC 6400 computer at McMaster University, and it was found that for each particular direction (θ,ϕ) it would take about 1200 seconds for the calculation of the four distributions. Hence it is apparent that we have to restrict ourselves to a coarser mesh of directions in

Fig. 3.2.1 A schematic diagram showing the relative positions of the 62 directions in the $(\frac{1}{48})$ zone of the FS

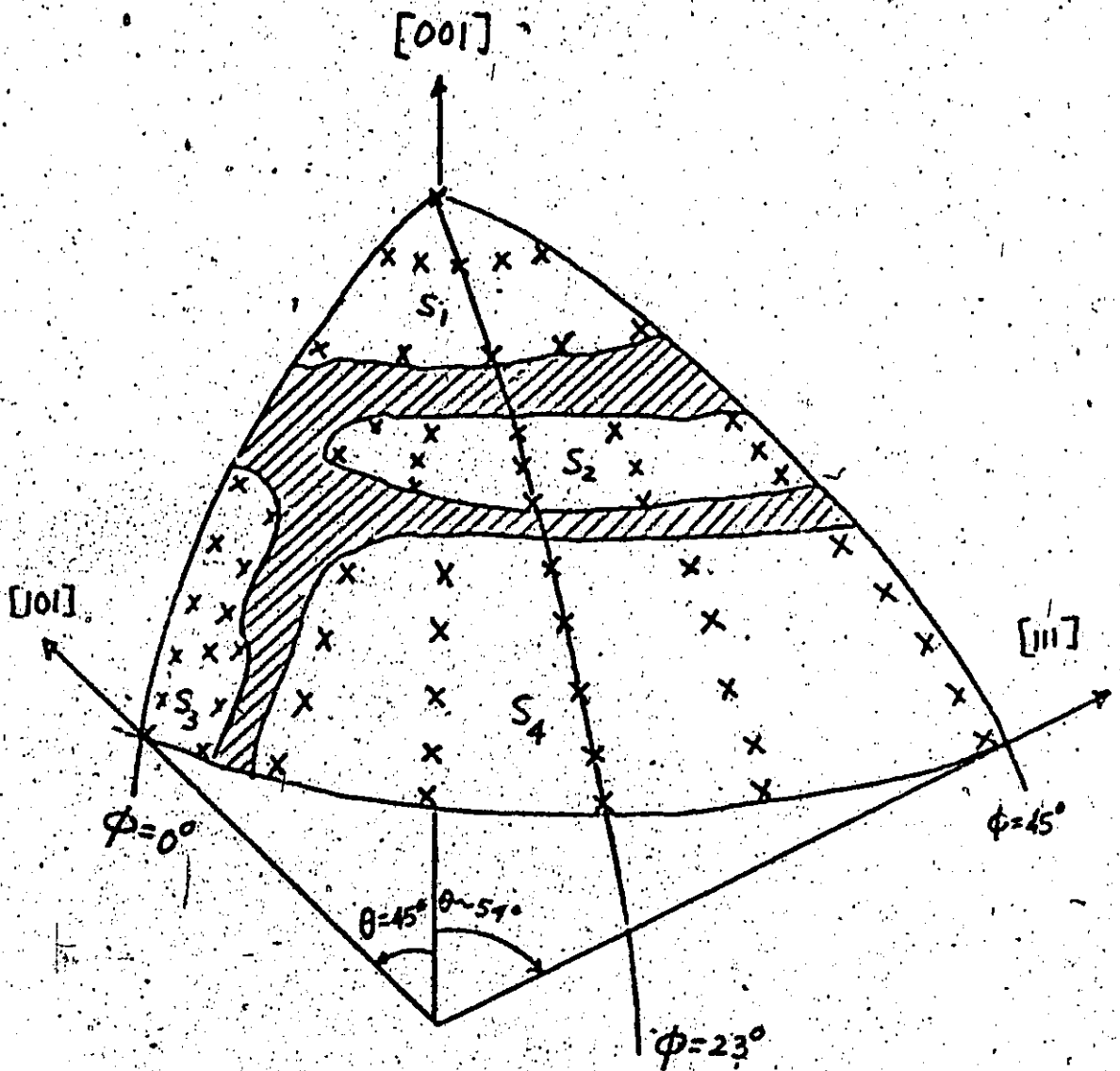

the $(\frac{1}{48})$ zone, one which is at the same time sufficiently fine to be able to use a simple interpolation scheme. For these purposes we decided on 62 directions more or less evenly distributed over the $(\frac{1}{48})$ zone. They are schematically shown in Figure 3.2.1. S_1 and S_4 are hole surfaces while S_2 and S_3 are the electron arms. The numerical order and the angular measures of these directions are listed in the first and second columns in Table 3.2.1. The third column shows the lengths of the Fermi vectors $k(\theta,\phi)$ and the fourth column the magnitude of the square of the velocity $V_{\underline{k}}^2$.

Integrals over the F.S. involving these directional distributions are to be performed in the later sections. They can be written in the general form,

$$\int_{F.S.} \frac{dS_k}{v_k} g(\underline{k},\underline{V}_k) \qquad 3.2.7$$

where $g(\underline{k},\underline{V}_{\underline{k}})$ represents some function defined over the F.S. The calculation of $g(\underline{k},\underline{V}_{\underline{k}})$ usually poses no great difficulties, except in the case when $g(\underline{k},\underline{V}_{\underline{k}})$ is related to the weighed frequency functions which are only defined at the 62 directions in the $(\frac{1}{48})$ symmetry zone.

The problem is then to find suitable weight factors $l_{\underline{k}}$ at the 62 points such that Equation 3.2.7 can be replaced by a numerical sum,

$$\sim 48 \sum_{j=1}^{62} l_{\underline{k}j} \frac{dS_{kj}}{v_{kj}} g(k_j, V_{kj}) \qquad 3.2.8$$

where the Σ is performed over the 62 directions. The factor 48 is the symmetry factor for converting to the whole F.S.

Instead of a high order interpolation of the various functions $g(\underline{k},\underline{V}_{\underline{k}})$ over the 16,200 points on the Fermi Surface, we note that since the 62 directions are quite evenly distributed, we may be able to obtain quite good results by employing just a linear interpolation scheme.

One advantage of such a scheme becomes apparent when we note from Equation 3.2.8 that the set of numbers $1_{\underline{k}} \frac{dS_{\underline{k}}}{V_{\underline{k}}}$ is then independent of the function $g(\underline{k}, V_{\underline{k}})$.

To calculate $1_{\underline{k}} \frac{dS_{\underline{k}}}{V_{\underline{k}}}$, we simply note the distance of each surface element $dS_{\underline{k}}$ from the neighbouring 62 directions on the F.S. and we assign the appropriate weight to $\frac{dS_{\underline{k}}}{V_{\underline{k}}}$ according to the linear interpolation scheme. The fifth column in Table 3.2.1 shows the results of such calculations.

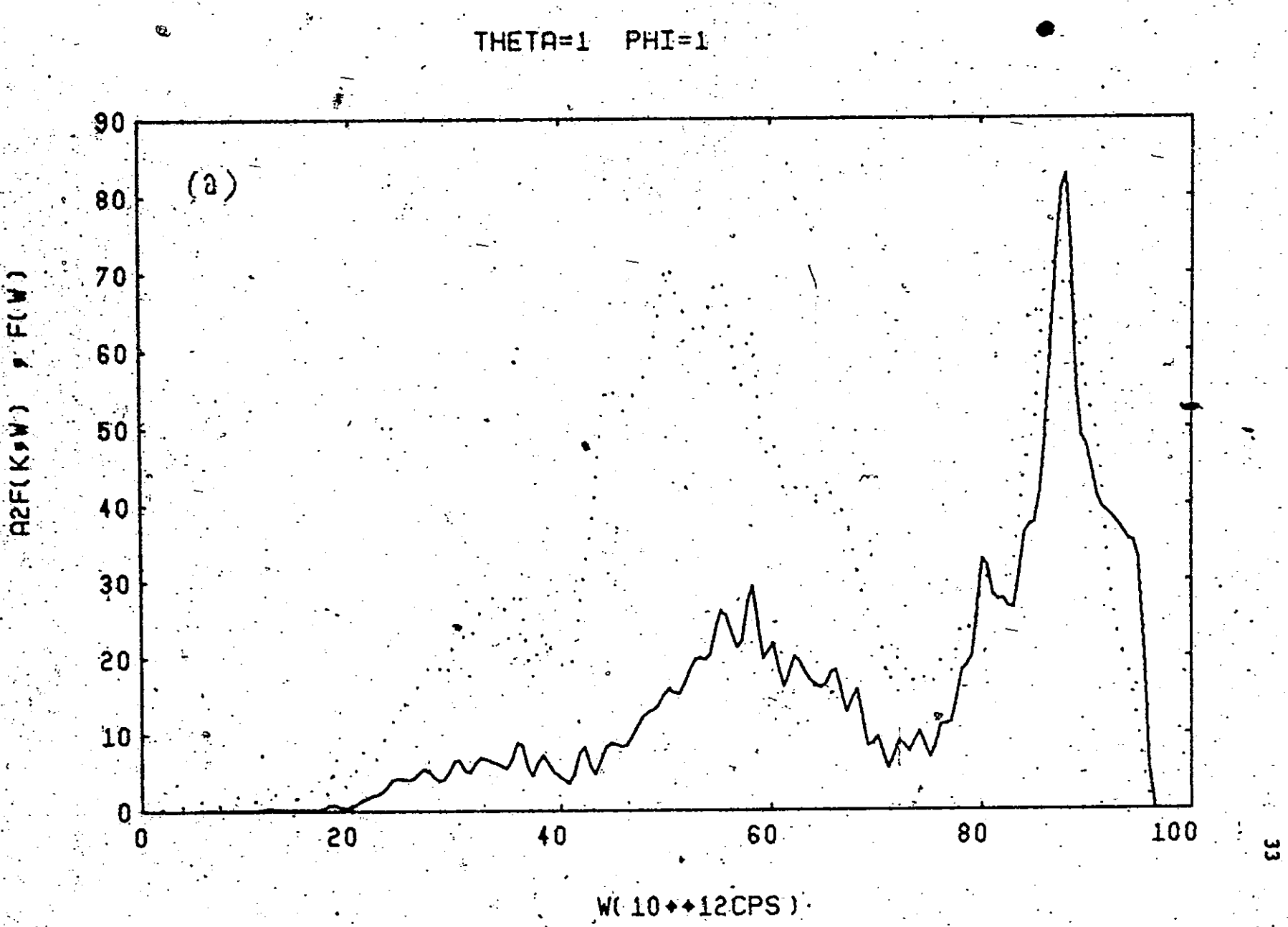

Fig. 3.2.2 The calculated $\alpha^2F(\underline{k},\omega)$ and $F(\underline{k},\omega)$ frequency weighted distributions in the 15-OPW approximation.

——— $\alpha^2F(\underline{k},\omega)$

..... $F(\underline{k},\omega)$

(a) - (d) ϕ = 1° θ = 1°,21°,29°,45°

(e) - (i) ϕ = 23° θ = 15°,19°,21°,31°,49°

(j) - (m) ϕ = 45° θ = 13°,17°,23°,31°,53°

The y-scale is magnified by a factor of 100

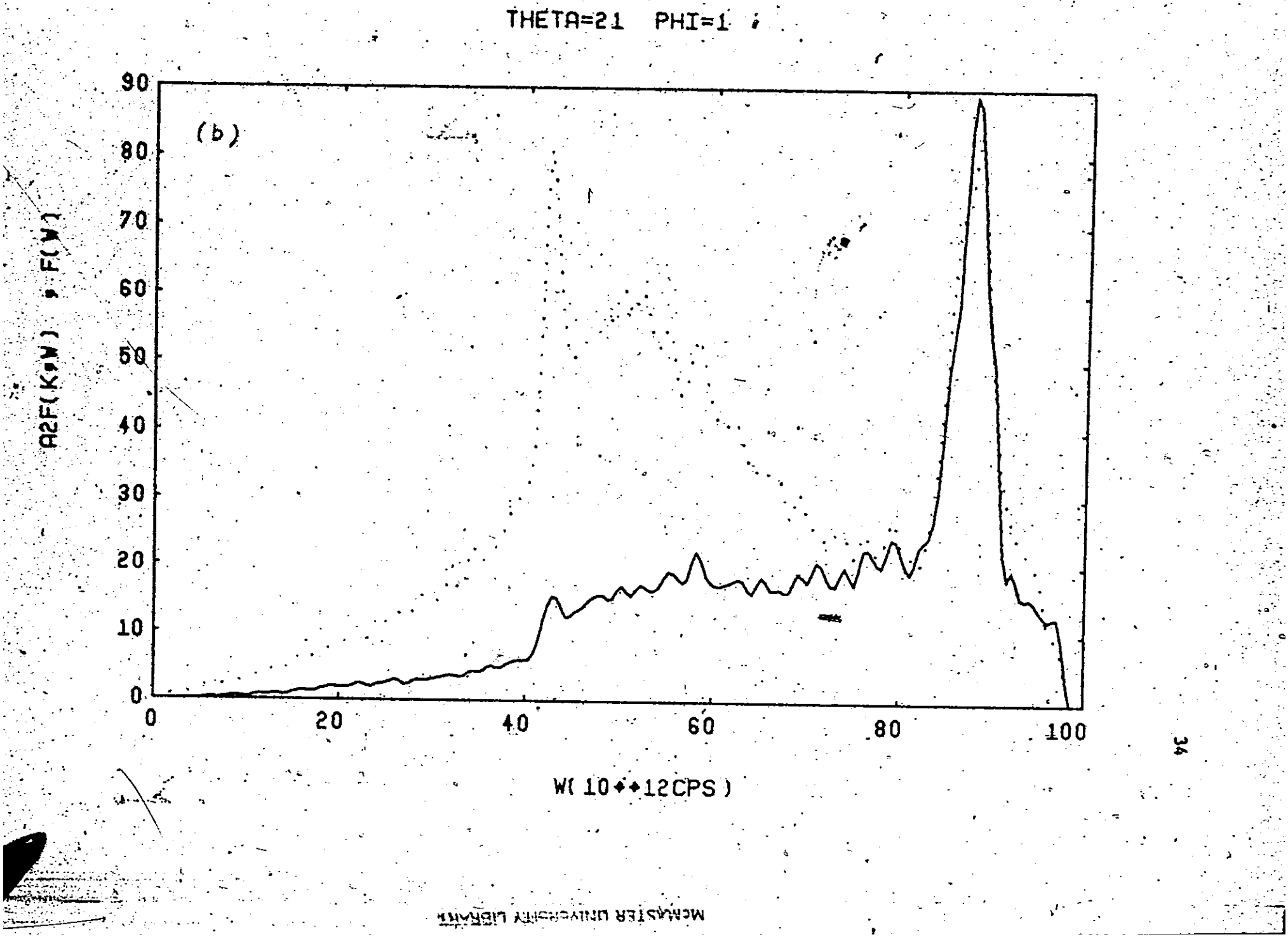

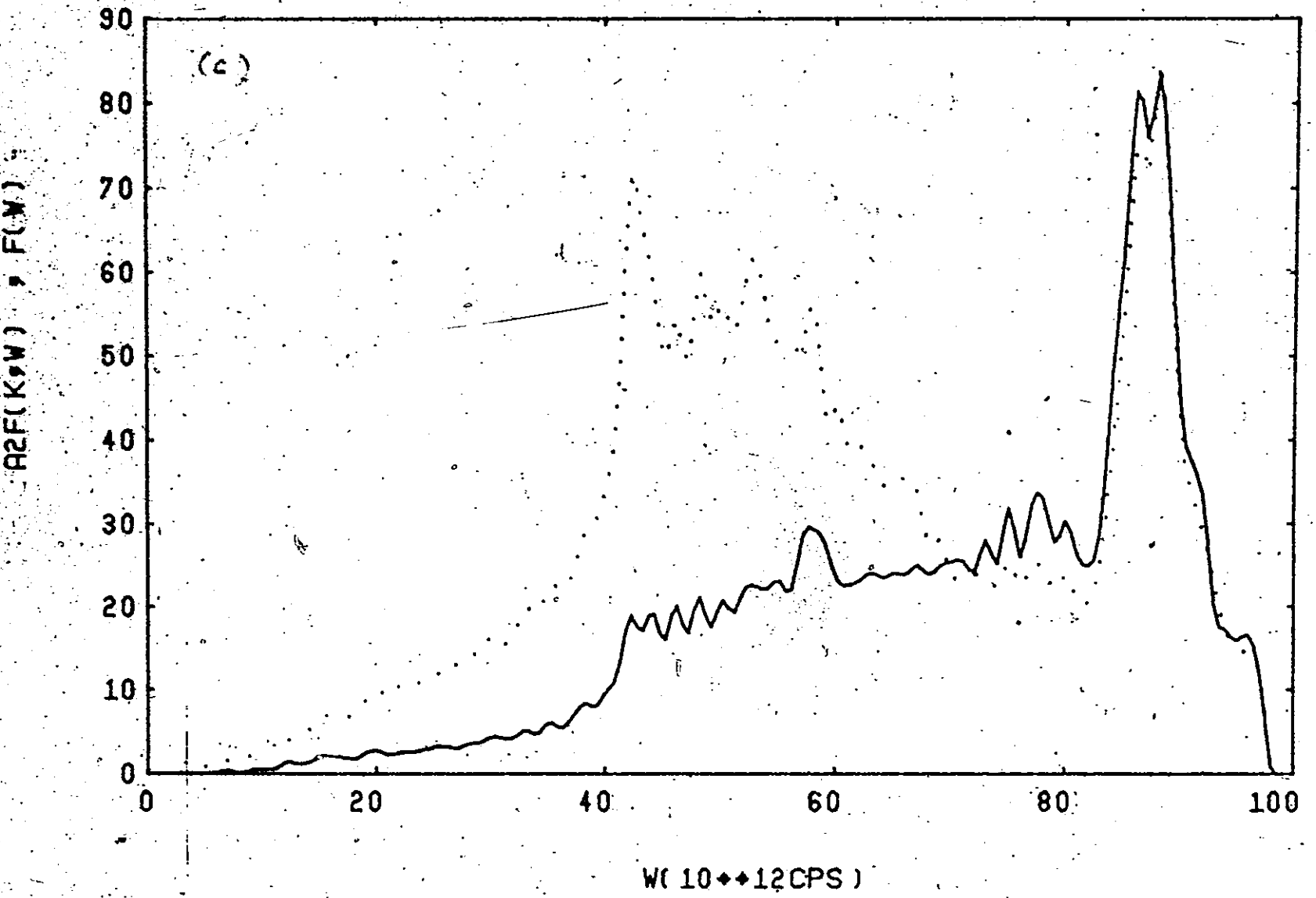

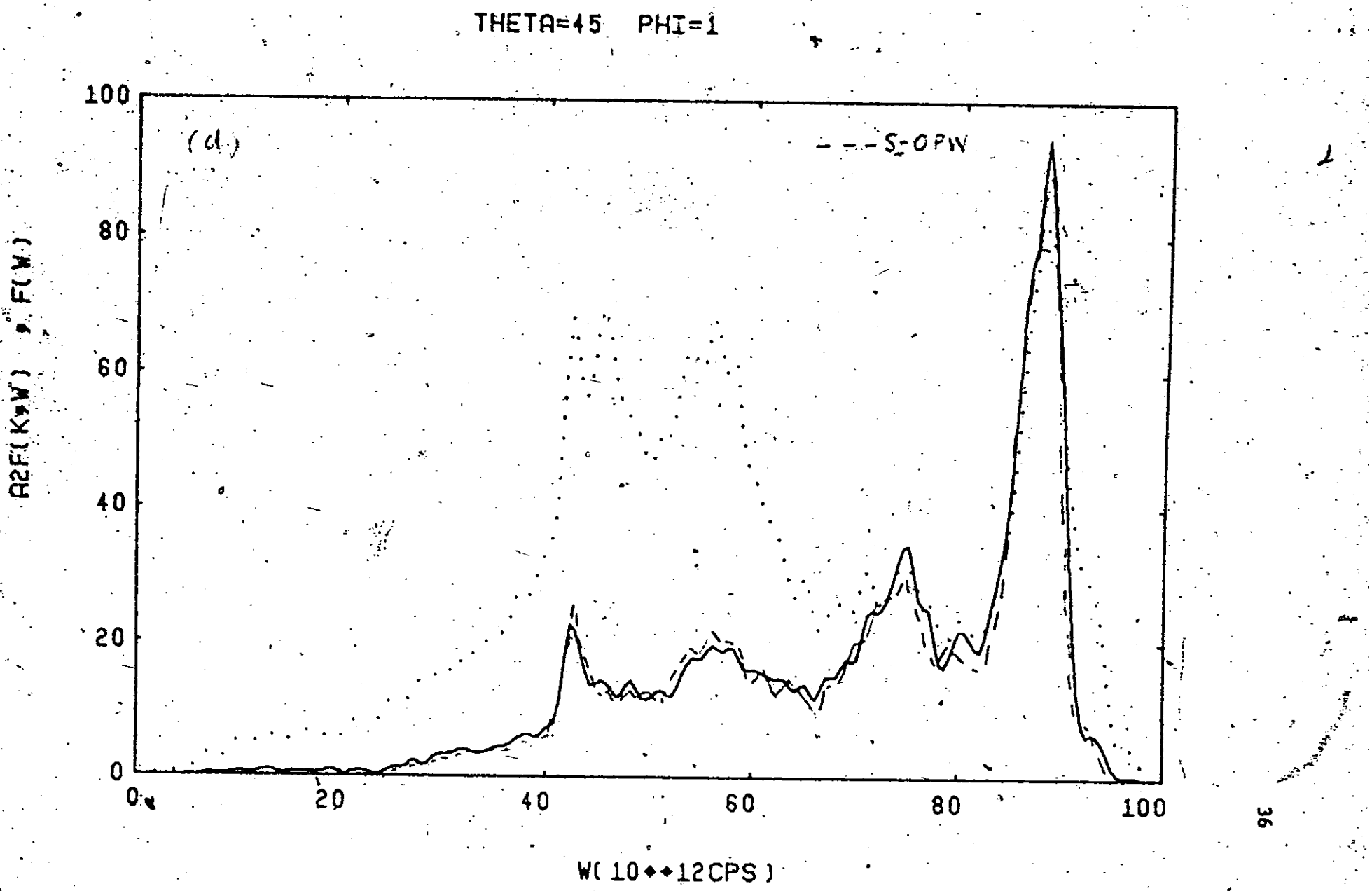

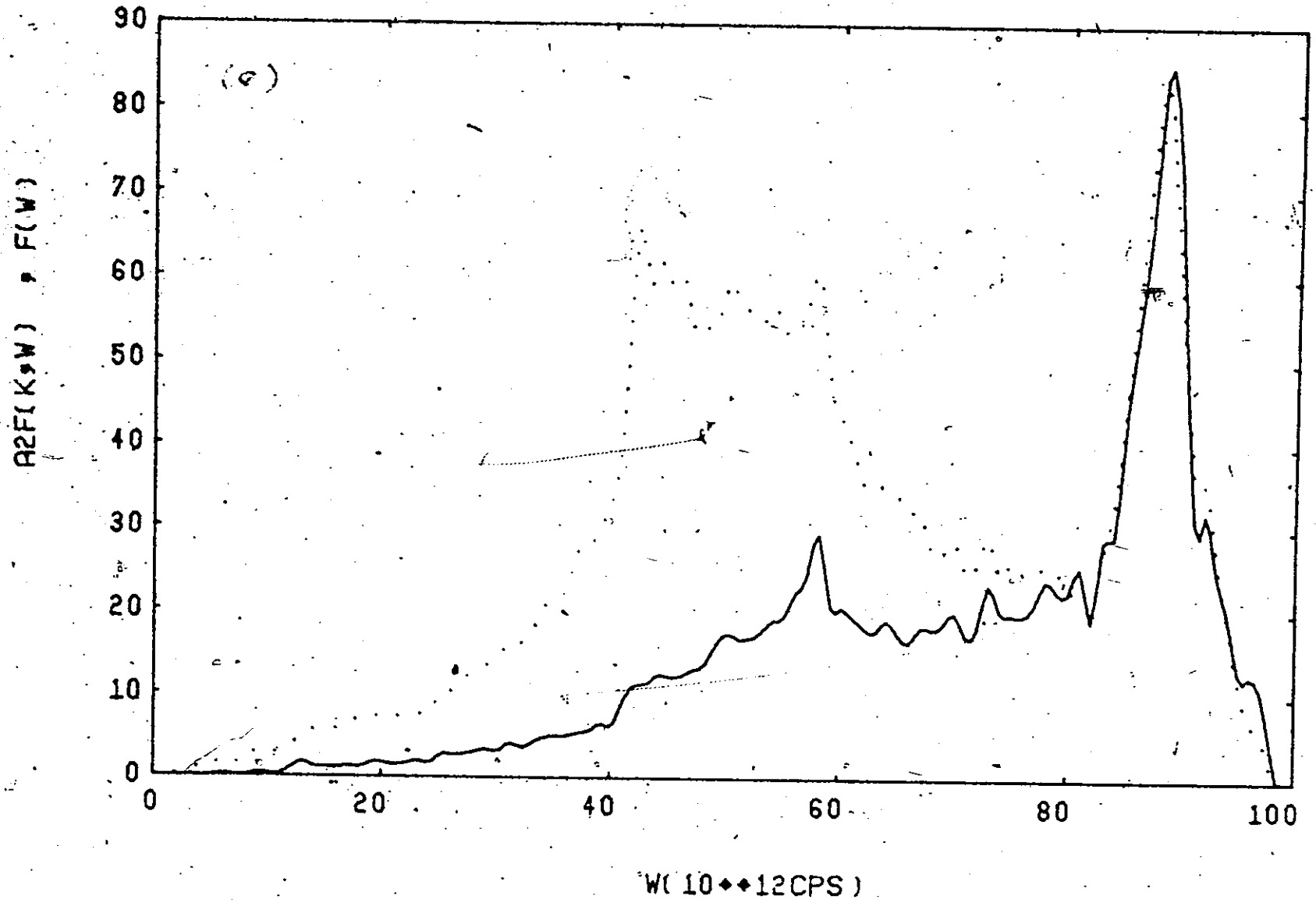

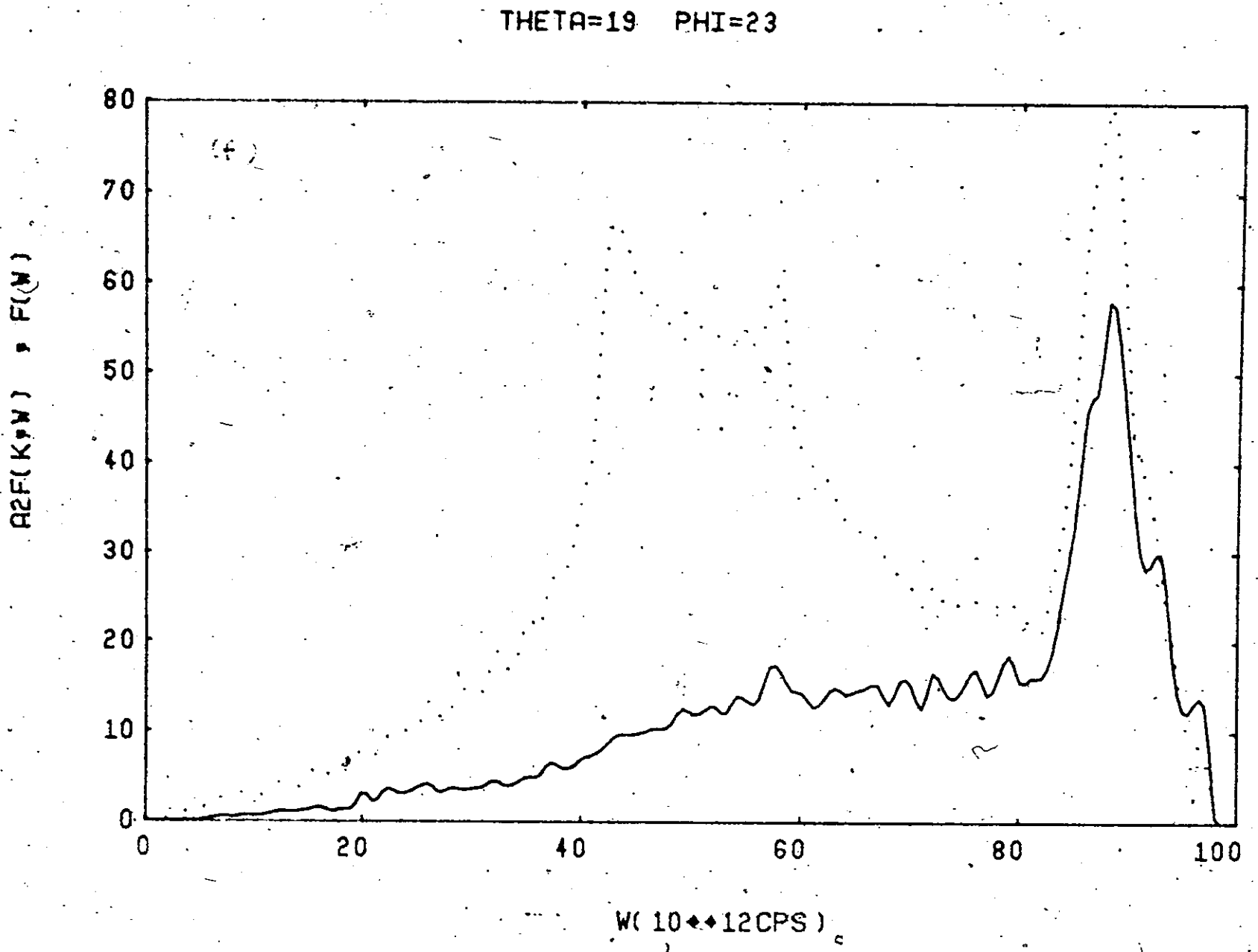

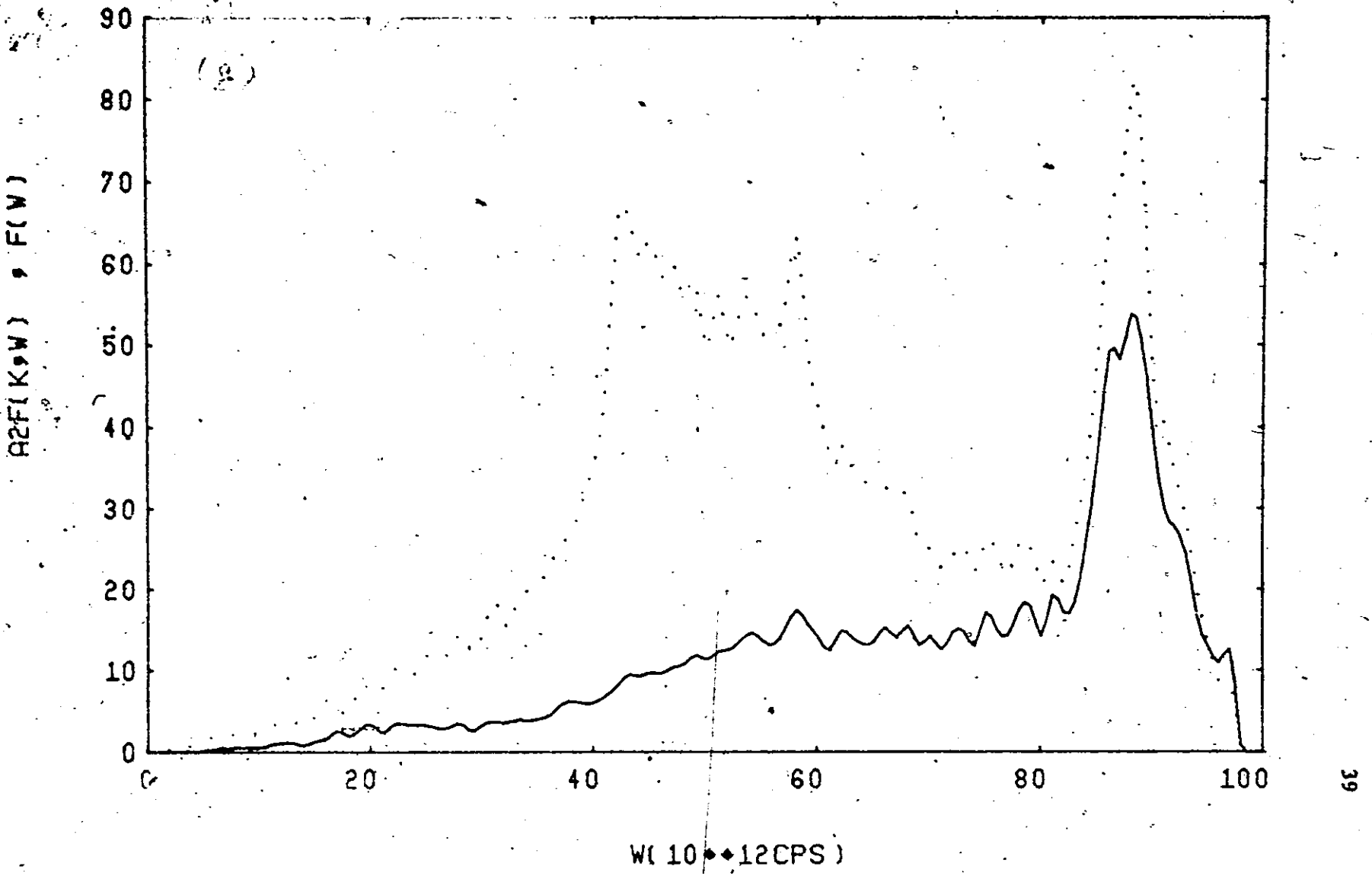

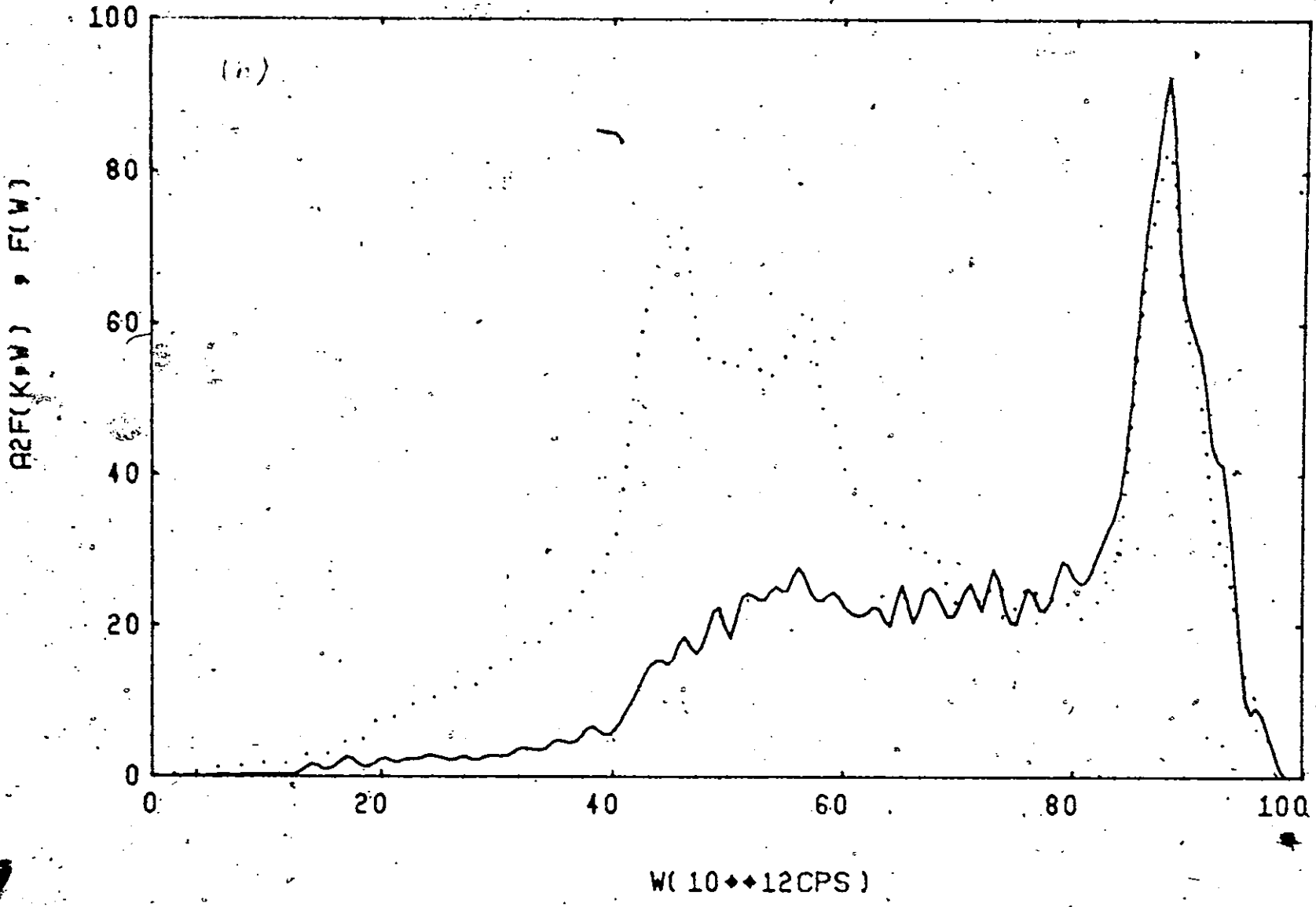

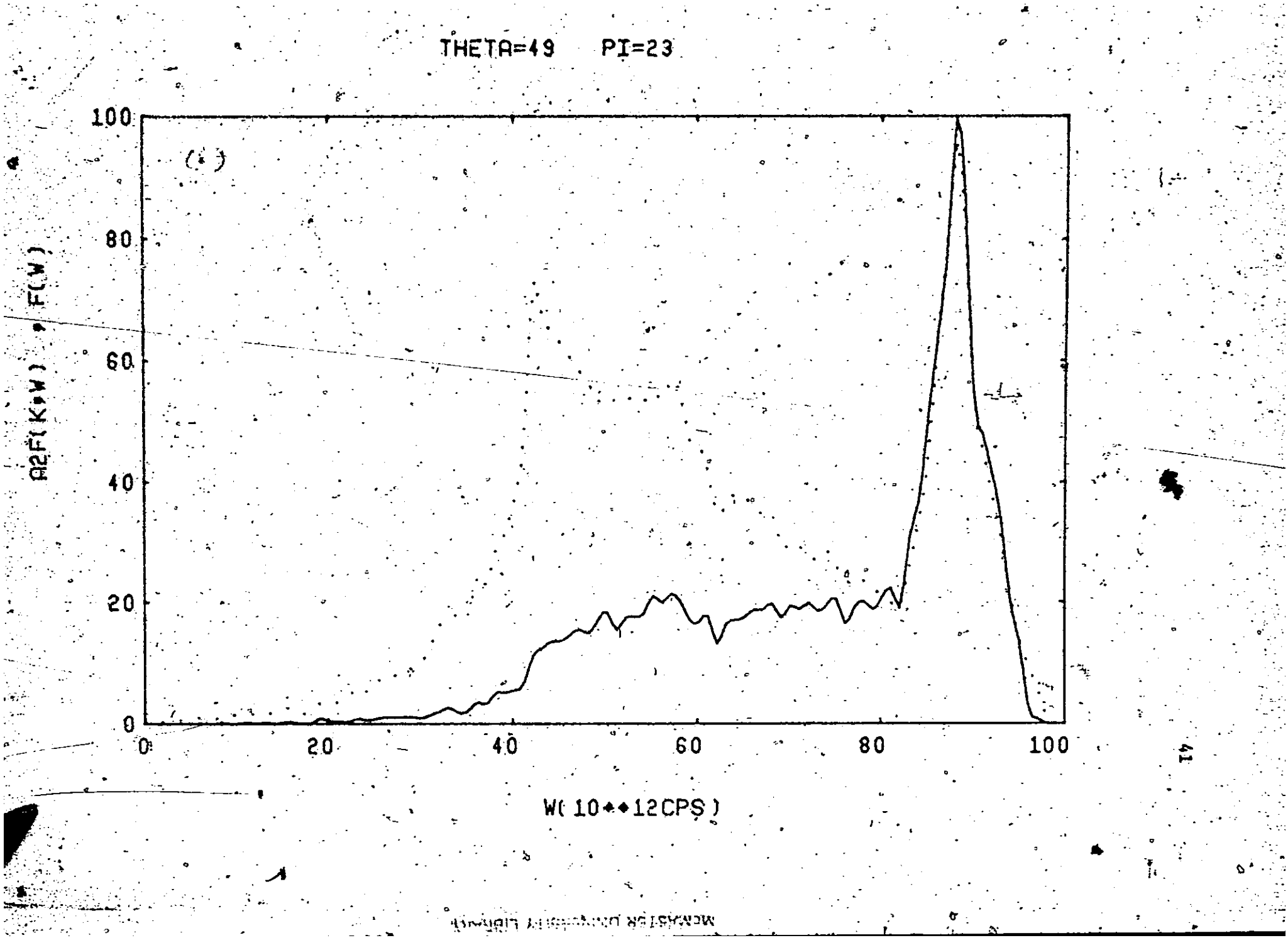
THETA=49 PI=23
(a)
100
80
60
40
20
0
0
20
40
60
80
100
A2F(K,W) * F(W)
W(10**12CPS)

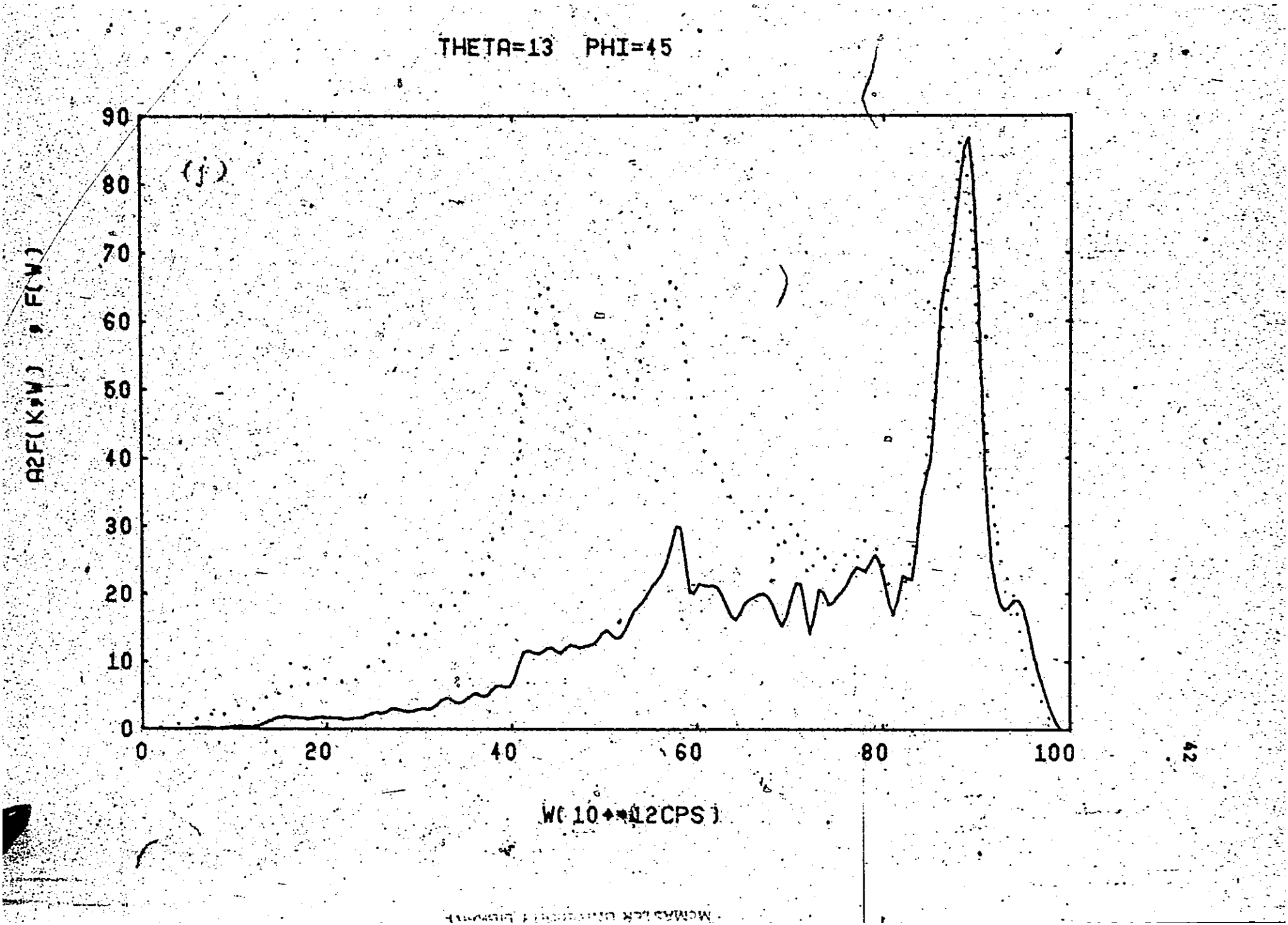
THETA=13 PHI=45
(j)
A2F(K,W) , F(W)
90
80
70
60
50
40
30
20
10
0
0
20
40
60
80
100
W(10**12CPS)

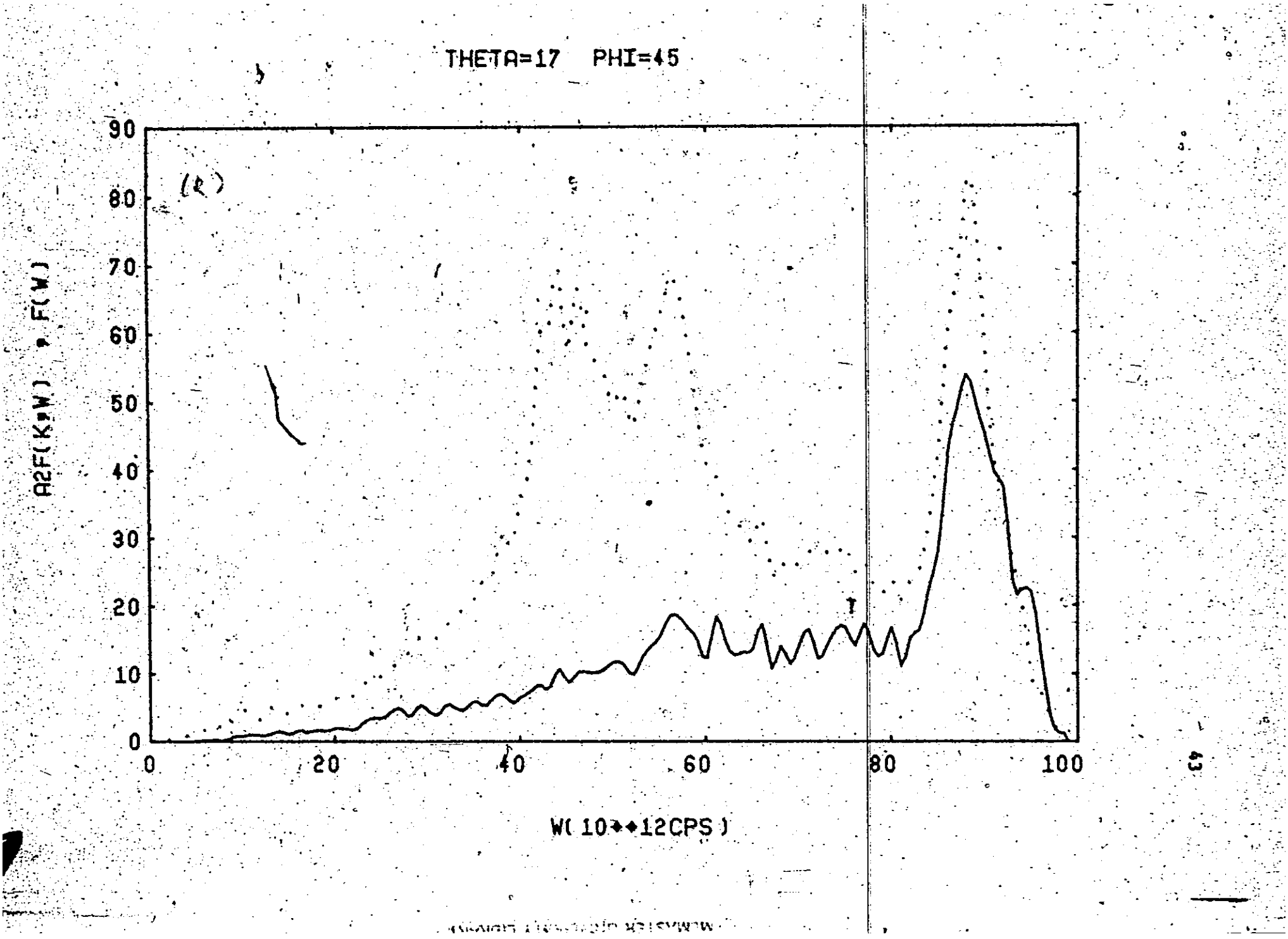
THETA=17 PHI=45
(a)
A2F(K,W) * F(W)
0
10
20
30
40
50
60
70
80
90
0
20
40
60
80
100
W(10**12CPS)

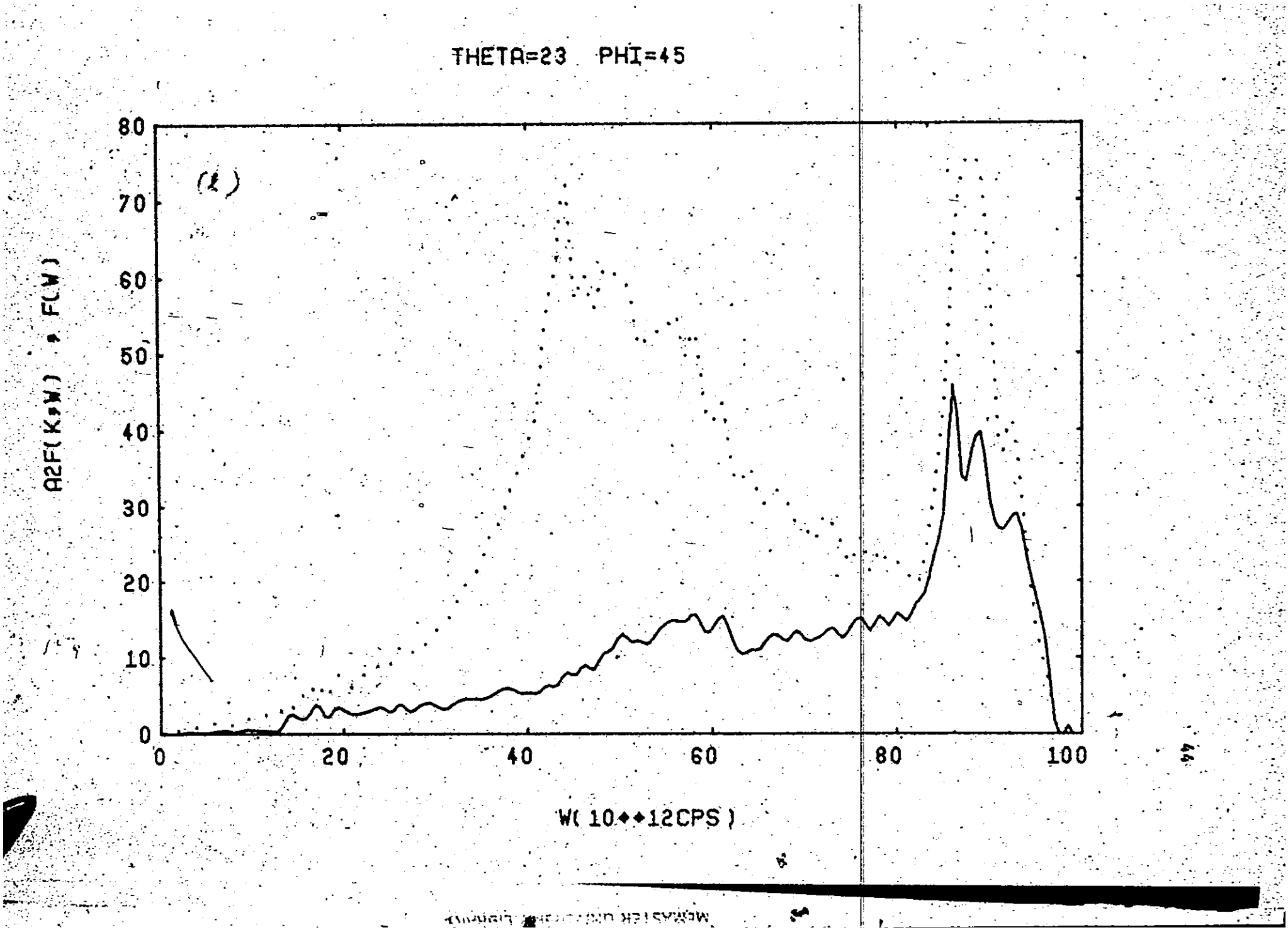
THETA=23 PHI=45
(t)
A2F(K,W) * F(W)
0
10
20
30
40
50
60
70
80
0
20
40
60
80
100
W(10**12CPS)

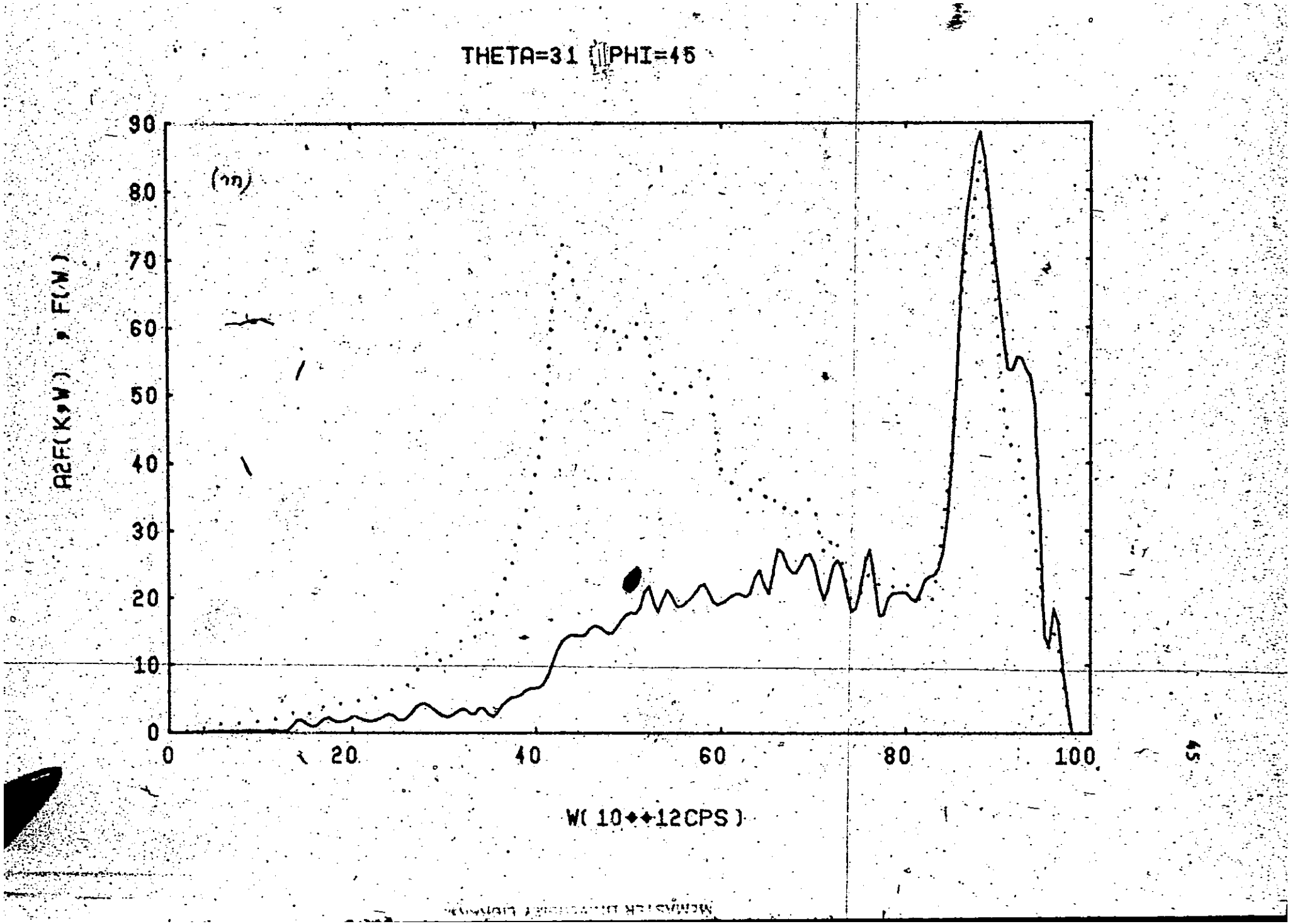
THETA=31 PHI=45
(nn)
A2F(K,W) * F(W)
0
10
20
30
40
50
60
70
80
90
0
20
40
60
80
100
W(10**12CPS)

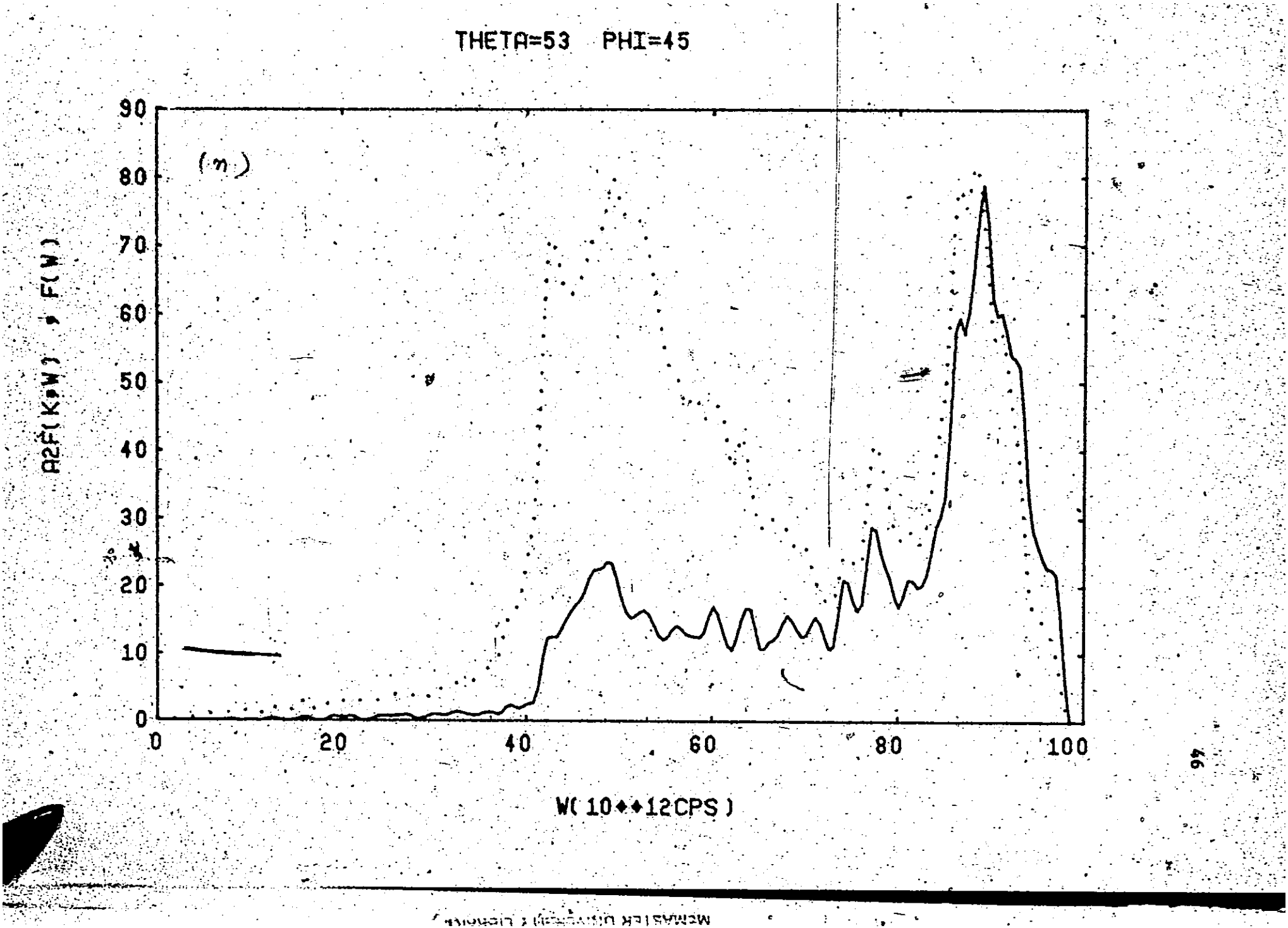
THETA=53 PHI=45
(n)
A2F(K,W) & F(W)
90
80
70
60
50
40
30
20
10
0
0
20
40
60
80
100
W(10**12CPS)

3.3 Results and Discussions

We performed the calculations of the distribution functions $\alpha^2F(\underline{k},\omega)$ and obtained highly peaked functions similar to the phonon frequency distribution functions $F(\underline{k},\omega)$. In Figure 3.3.1(a) to Figure 3.3.1(a) we plot the histograms of $\alpha^2F(\underline{k},\omega)$ at the directions along the main planes defined by $\phi = 1°, \phi = 23°$ and $\phi = 45°$. The dotted functions are the $F(\underline{k},\omega)$. Van Hove singularities are manifested in these functions. The low frequency peaks are associated with the maximum frequencies of the transverse branches and the upper one with a saddle point in the longitudinal branch of the phonon spectrum. The low frequency peak of $\alpha^2F(\underline{k},\omega)$ is usually lower than the corresponding peak of $F(\underline{k},\omega)$ and it is believed to be caused by the condition that $(\underline{k}'-\underline{k})\cdot\underline{e}_{q\lambda}$ is zero for transverse branches (see Equation 2.3.6(b)) (when the process is a normal one)

TABLE 3.2.1

Sixty-Two Points on F.S. of Al

No. Surface 1	(θ,ϕ) (S_1)	$k(\theta,\phi)$ $(\frac{2\pi}{a})$	$V_{\underline{k}}^2$(C.U.)	$1_{\underline{k}}\cdot\frac{S_{\underline{k}}}{V_{\underline{k}}/V_F}\times 10^3$(C.U.)
1	(1,1)	1.122	4.6411	3.376
2	(9,1)	1.122	4.5539	3.505
3	(21,1)	1.203	4.6389	6.285
4	(9,9)	1.122	4.5470	5.935
5	(17,9)	1.123	4.5486	6.465
6	(9,23)	1.122	4.5406	4.200
7	(15,23)	1.126	2.5593	8.290
8	(9,35)	1.122	4.5227	2.400
9	(13,35)	1.125	4.3343	2.720
10	(9,45)	1.122	4.5195	2.093
11	(13,45)	1.125	4.1922	2.760

No.	(θ,ϕ)	$k(\theta,\phi)$ $(\frac{2\pi}{a})$	V_k (C.U.)	$1_k \cdot \frac{S_k}{V_k/V_p^\circ} \times 10^3$ (C.U.)
Surface 2	(S_2)			
12	(23,9)	1.103	1.9163	1.028
13	(21,11)	1.107	2.5301	1.938
14	(19,17)	1.110	2.6058	1.180
15	(21,15)	1.108	2.7797	2.480
16	(23,15)	1.103	2.1468	2.113
17	(19,23)	1.111	2.9299	3.940
18	(21,23)	1.108	2.0373	3.980
19	(23,23)	1.102	2.3419	2.800
20	(17,35)	1.112	3.9984	4.180
21	(21,35)	1.108	3.1041	5.530
22	(23,35)	1.101	2.3250	2.780
23	(17,45)	1.112	2.5067	2.295
24	(21,45)	1.108	1.5924	2.745
25	(23,45)	1.101	4.9656	1.450
Surface 3	(S_3)			
26	(29,1)	1.123	4.6389	1.590
27	(31,1)	1.133	4.6389	3.090
28	(33,1)	1.138	4.6386	2.260
29	(37,1)	1.129	3.9126	2.440
30	(41,1)	1.127	4.6765	2.180
31	(45,1)	1.126	3.3357	1.590
32	(31,3)	1.137	4.6318	2.010
33	(35,3)	1.129	2.6405	1.910
34	(37,3)	1.127	3.9476	2.036
35	(41,3)	1.125	4.7026	1.736
36	(41,5)	1.121	4.7237	1.736
37	(43,5)	1.122	4.8226	1.775
38	(45,3)	1.124	4.4330	1.775
Surface 4	(S_4)			
39	(31,7)	1.152	4.5779	1.900
40	(33,7)	1.145	4.5767	2.910
41	(35,9)	1.140	2.7622	6.832
42	(45,9)	1.135	4.9108	8.987
43	(31,15)	1.151	1.1723	3.050
44	(33,15)	1.143	4.2062	4.66
45	(35,15)	1.138	2.6647	8.23
46	(43,15)	1.132	4.8818	1.268
47	(47,15)	1.132	4.9891	6.175
48	(31,23)	1.151	2.1853	3.900
49	(35,23)	1.138	1.4120	1.022
50	(43,23)	1.132	4.8910	1.706

No. Surface A_k	(θ,ϕ) (S_k)	$k(\theta,\phi)$ $(\frac{2\pi}{a})$	$V_{\underline{k}}$ (C.U.)	$1_{\underline{k}} \cdot \frac{S_k}{V_{\underline{k}}/V_F} \times 10^3$ (C.U.)
51	(49,23)	1.131	5.0465	9.710
52	(31,35)	1.152	3.0421	3.970
53	(33,35)	1.142	1.8459	5.800
54	(35,35)	1.137	3.4835	1.022
55	(43,35)	1.132	3.2811	1.996
56	(51,35)	1.130	5.0860	1.189
57	(31,45)	1.152	4.9710	2.000
58	(33,45)	1.142	1.7176	2.910
59	(35,45)	1.138	3.3888	5.116
60	(43,45)	1.131	3.3190	1.312
61	(53,45)	1.129	5.1062	8.077
62	(33,23)	1.143	2.1713	5.820

For $\underline{k}$ situated far away from the Bragg plane the S-OPW approximation is believed to be valid. We expect our results to resemble those from a S-OPW calculation. We choose such a direction at (45°,1°) and plot the S-OPW results as a dashed line and one can see from Figure 3.2.2(d) that they are virtually the same as the 15-OPW results.

This conclusion should also apply to other directions such as the [001] and [111] directions which are not shown here.

It is more interesting to compare the results along a bad direction such as (29°,1°). In such a direction $\underline{k}$ is very close to a Bragg plane and the mixing of other plane waves with similar energies becomes dominant. In the high frequency regions the $\alpha^2F(\underline{k},\omega)$'s are qualitatively the same. In the low frequency regions, the S-OPW calculations for the $\alpha^2F(\underline{k},\omega)$ functions show anomalous behaviour. As found by Allen and Cohen (1970), Leavens and Carbotte (1972) and Hayman (1974), the $\alpha^2F(\underline{k},\omega)$ does not go to zero rapidly enough, as $\omega \to 0$. This is a well-known failure of the S-OPW approximation. In order to compare

the results, we find that it is convenient to define a function $\alpha^2(\underline{k},\omega)$ by

$$\alpha^2(\underline{k},\omega) = \alpha^2 F(\underline{k},\omega) \,/\, F(\underline{k},\omega) \qquad 3.3.1$$

where $F(\underline{k},\omega)$ is the directional phonon frequency spectrum. Thus $\alpha^2(\underline{k},\omega)$ in a certain sense corresponds approximately to $g_{\underline{k}\underline{k}',\lambda}$. Figure 3.3.1 shows the results for $\alpha^2(\underline{k},\omega)$ in the S-OPW approximation at (27°,0°) and (30°,0°). It is seen immediately that the behaviour of $\alpha^2(\underline{k},\omega)$ at (30°,0°) increases, as $\omega \to 0$, to a large magnitude and then drops suddenly to zero. In the (27°,0°) direction, the magnitude of $\alpha^2(\underline{k},\omega)$ increases sharply to very large values and is divergent at $\omega = 0$.

Figure 3.3.2(a) to Figure 3.3.2(e) show the $\alpha^2(\underline{k},\omega)$ functions in the 15-OPW approximation. Figure 3.3.2(a), 3.3.2(d) and 3.3.2(e) show the directions where $\underline{k}$ is far away from the Bragg planes. $\alpha^2(\underline{k},\omega)$ goes gradually to zero as $\omega \to 0$, as expected. Figure 3.3.2(b) and 3.3.2(c) show $\alpha^2(\underline{k},\omega)$ for (21,1) and (29,1), and we see that even in these directions, where $\underline{k}$ is very close to the Bragg planes, the behaviour of $\alpha^2(\underline{k},\omega)$ is still regular and decreases to zero as $\omega \to 0$. The unphysical behaviour of the $\alpha^2(\underline{k},\omega)$ in a S-OPW calculation led Allen and Cohen to try an approximate treatment (1970), avoiding this singularity by multiplying the S-OPW results by some appropriate damping factor below a certain critical frequency $\frac{1}{2}\omega_c$. We see from our multi OPW calculations that their treatment is qualitatively correct.

What leads to the breakdown of the S-OPW treatment of the electron-phonon matrix element at low ω? The answer lies in the inadequacy of the description of the electron wavefunction in an over-

Fig. 3.3.1 The function $\alpha^2_{\underline{k}}(\omega) = \frac{\alpha^2 F(\underline{k},\omega)}{F(\underline{k},\omega)}$ as a function of ω in Al in S-OPW.

(a) $\theta = 27°$, $\phi = 0°$

(b) $\theta = 30°$, $\phi = 0°$

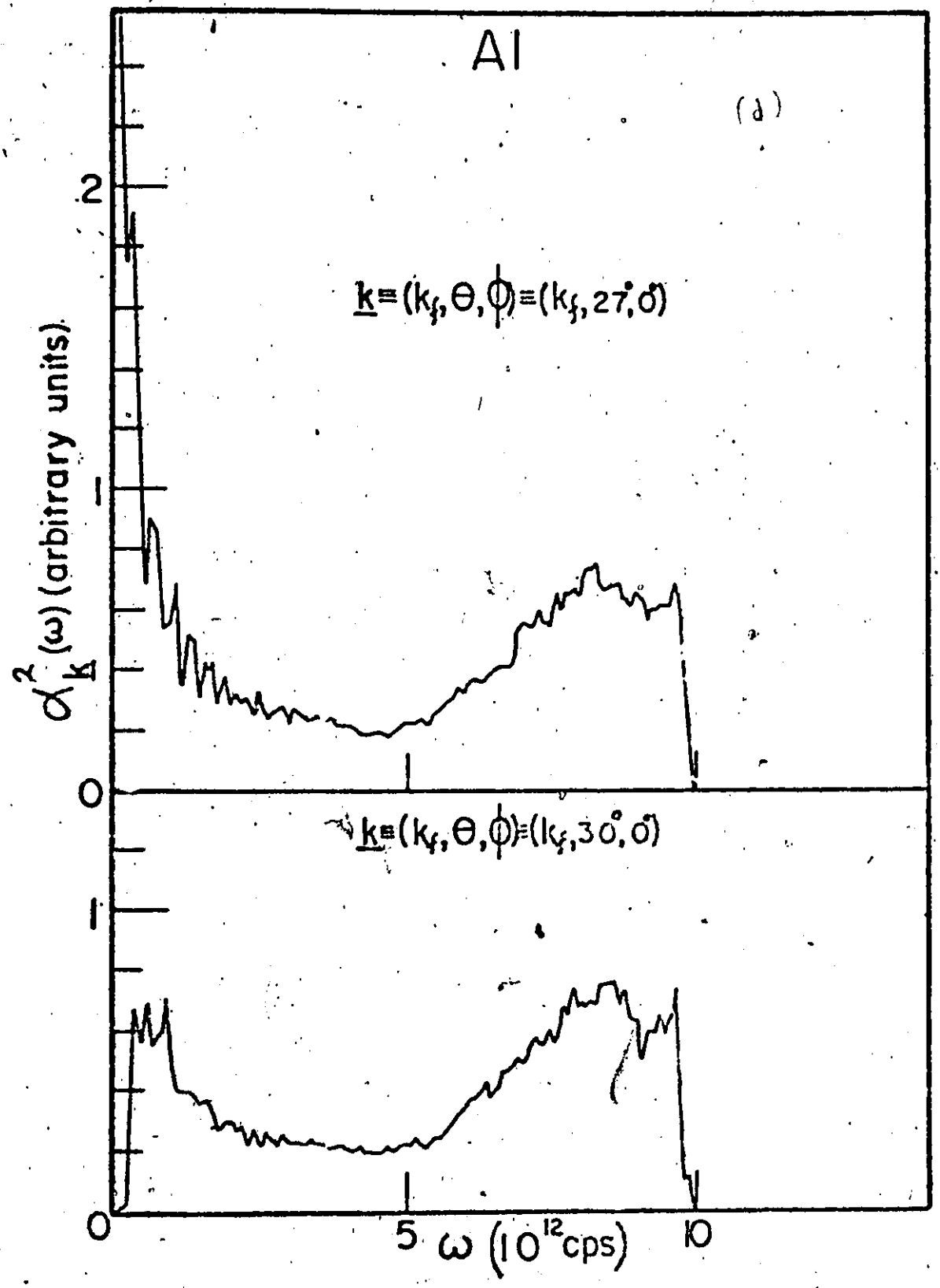
Al
(a)
$\underline{k}=(k_f,\theta,\phi)=(k_f,27^\circ,0^\circ)$
$\underline{k}=(k_f,\theta,\phi)=(k_f,30^\circ,0^\circ)$
$\alpha_k^2(\omega)$ (arbitrary units)
2
1
0
1
0
5
ω (10^{12}cps)
10

Fig. 3.3.2 The $\alpha^2(\underline{k},\omega) \equiv \frac{\alpha^2 F(\underline{k},\omega)}{P(\underline{k},\omega)}$ functions as functions of ω in the 15-OPW approximation.

(a) (1°,1°)
(b) (21°,1°)
(c) (29°,1°)
(d) (45°,1°)
(e) (53°,45°)

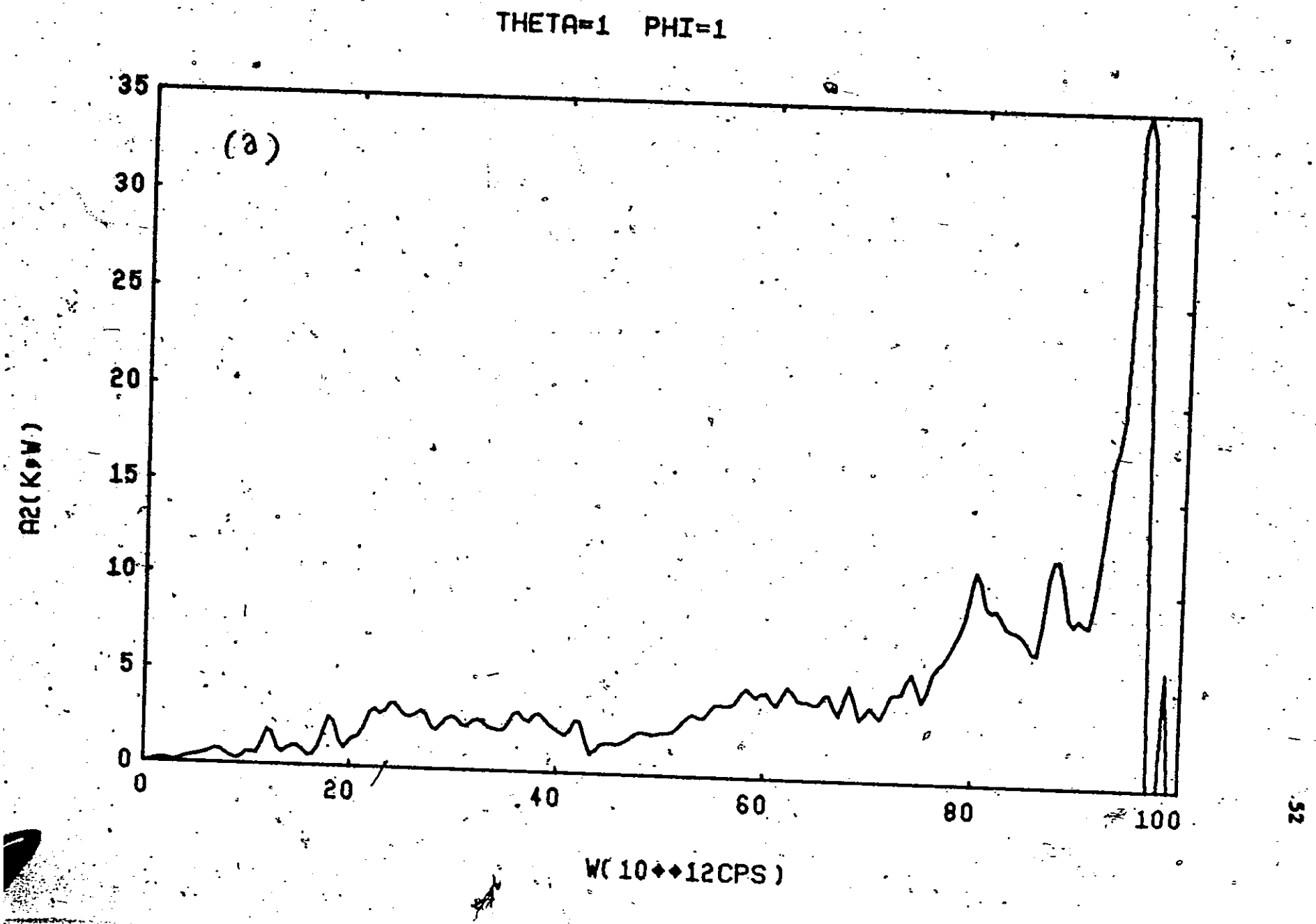
THETA=1 PHI=1
(a)
35
30
25
20
15
10
5
0
0
20
40
60
80
100
A2(K,W)
W(10**12CPS)

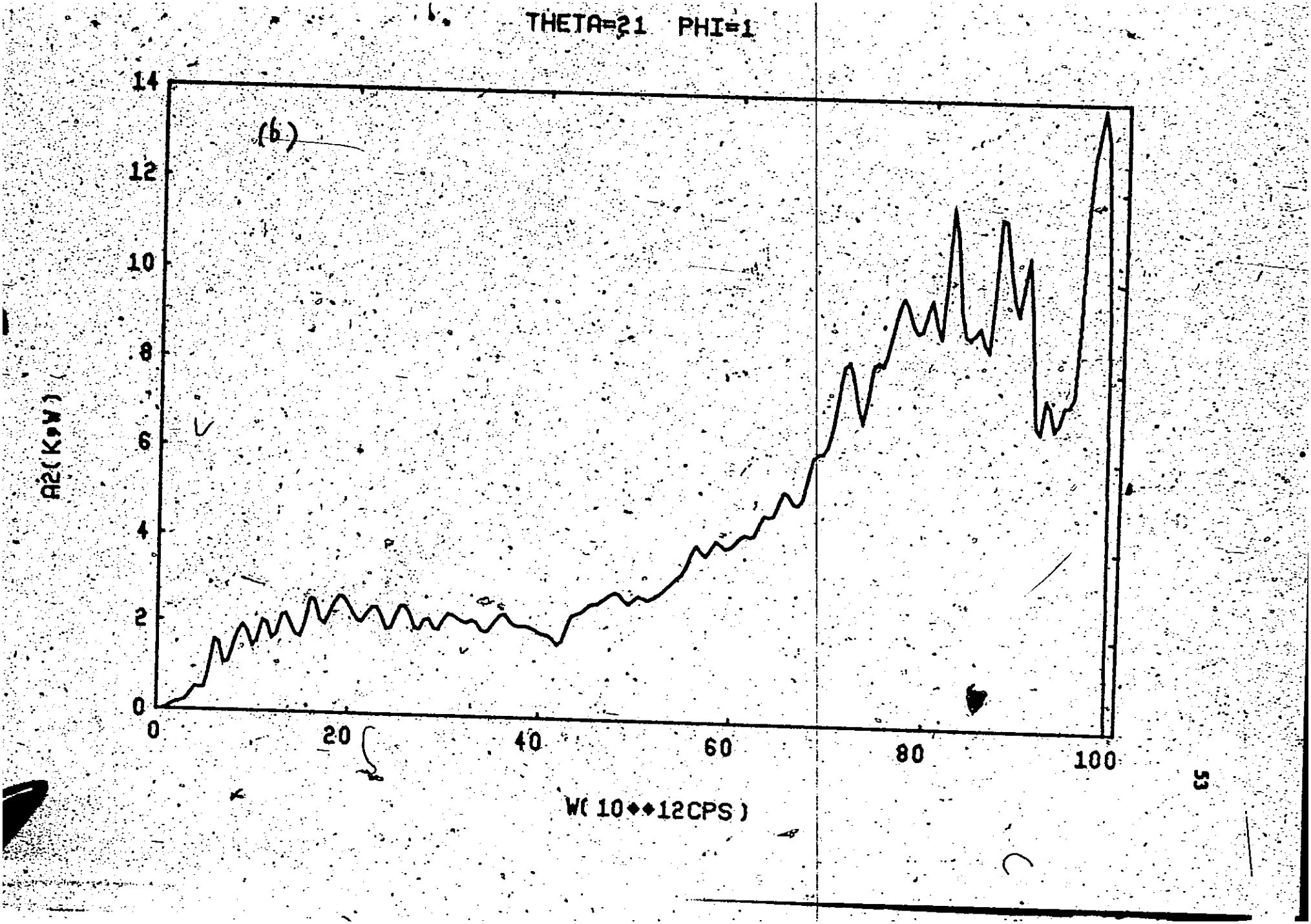
THETA=21 PHI=1
(b)
14
12
10
8
6
4
2
0
A2(K,W)
0
20
40
60
80
100
W(10**12CPS)

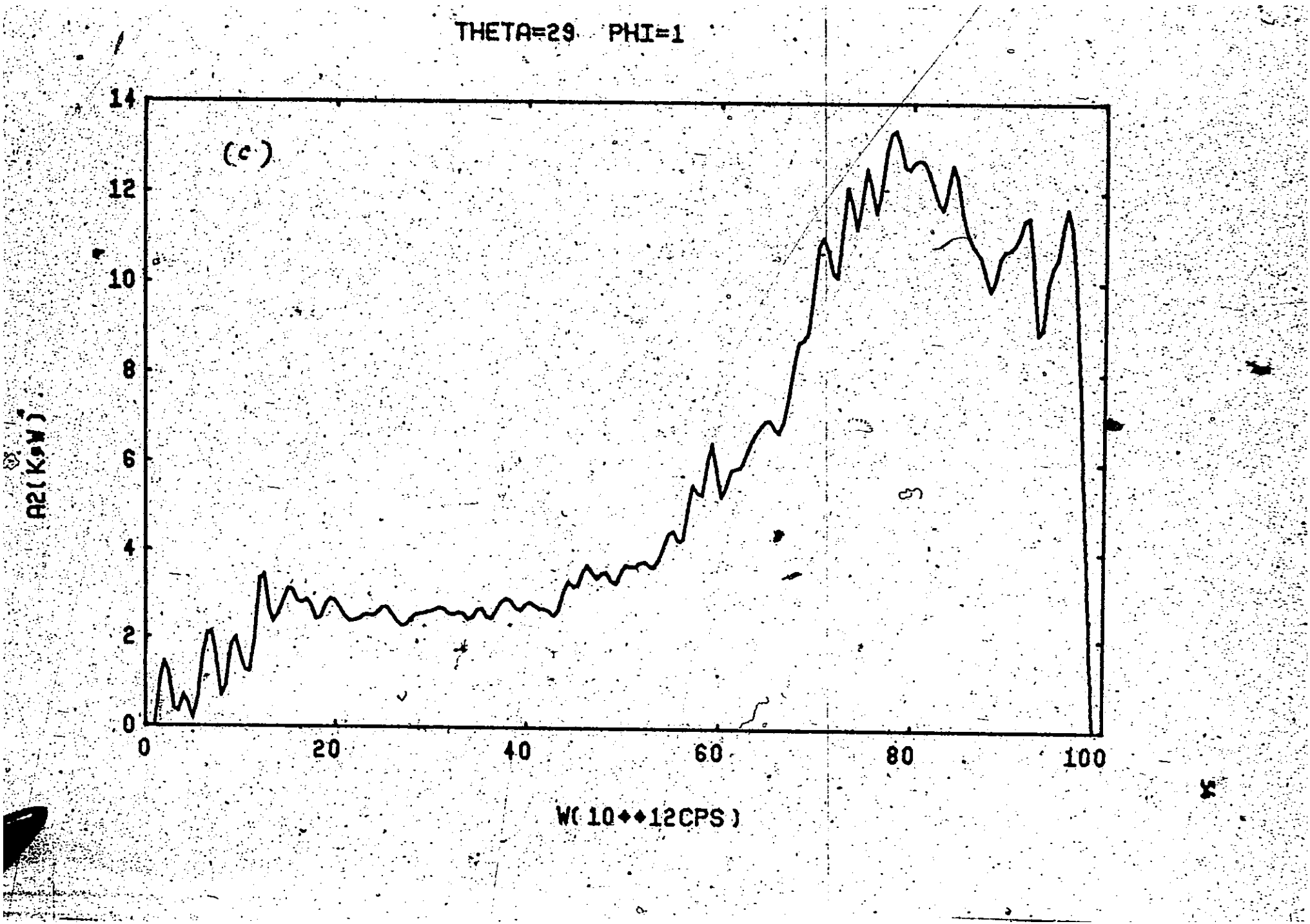
THETA=29 PHI=1
(c)
14
12
10
8
6
4
2
0
0
20
40
60
80
100
A2(K,W)
W(10**12CPS)

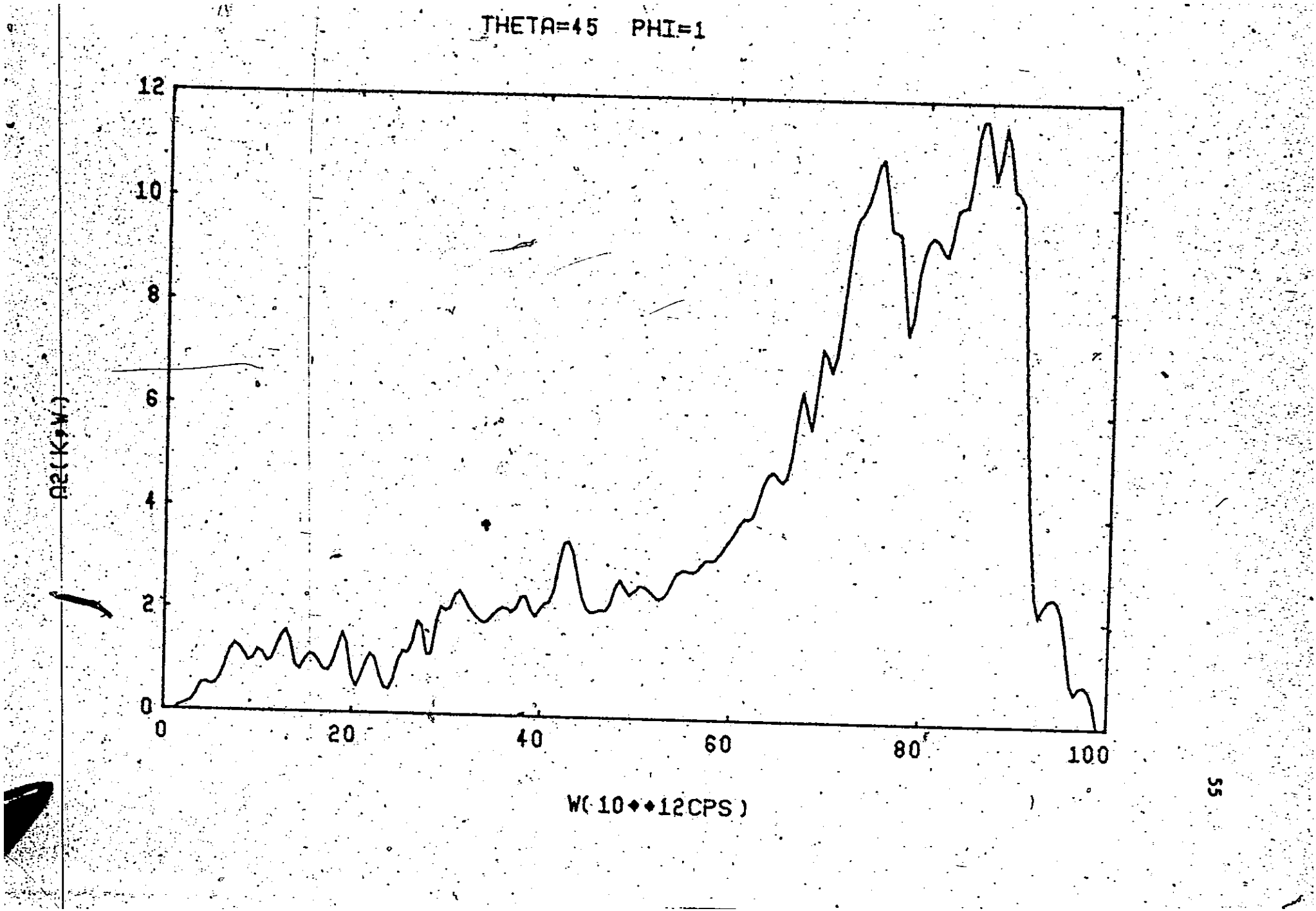
THETA=45 PHI=1
12
10
8
6
4
2
0
0
20
40
60
80
100
Q2(K,W)
W(10**12CPS)

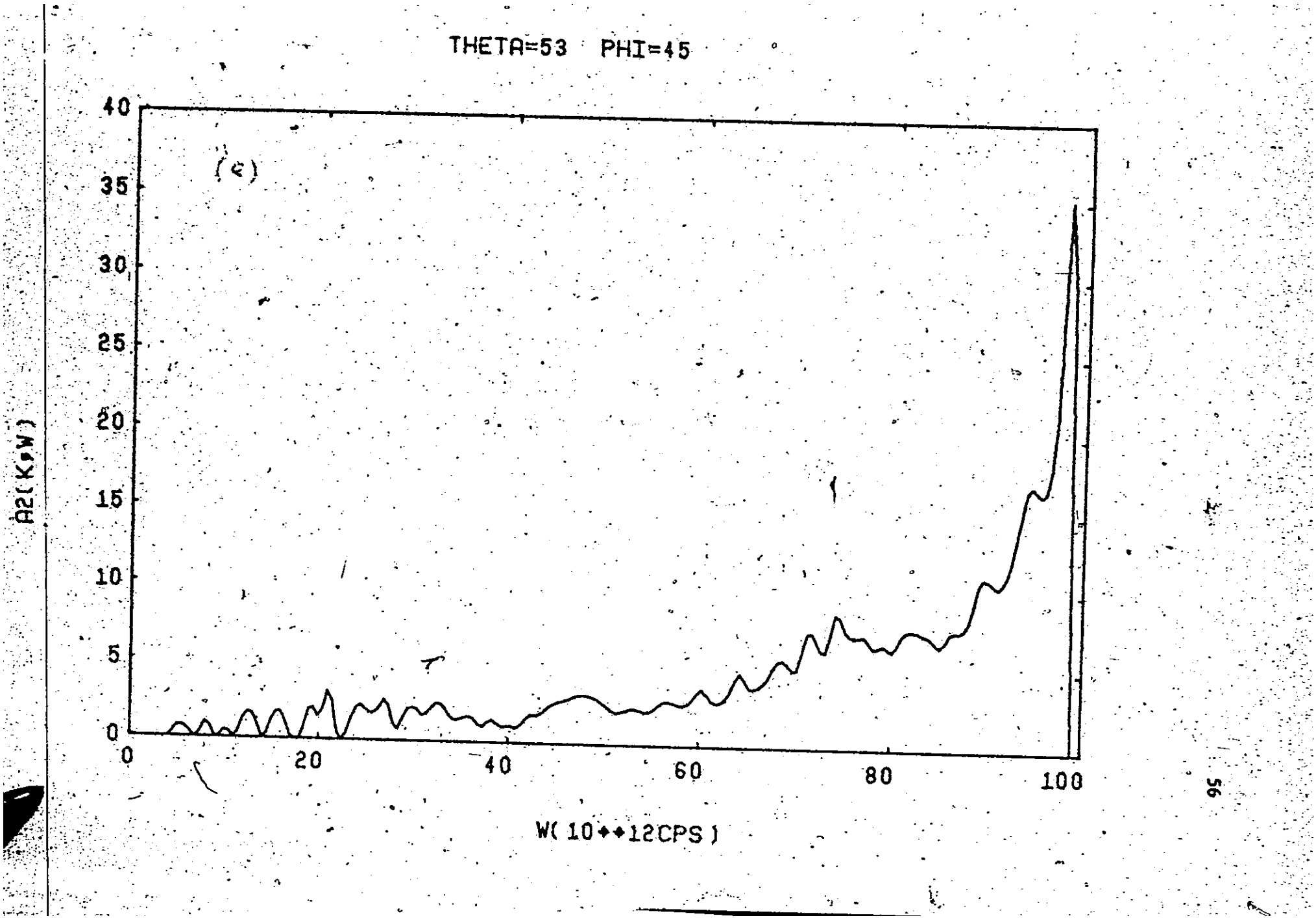
THETA=53 PHI=45
(c)
40
35
30
25
20
15
10
5
0
0
20
40
60
80
100
A2(K,W)
W(10**12CPS)

Fig. 3.3.3 The geometry of Normal and Umklapp electron-phonon scattering processes (schematic)

(a) Normal process $\underline{G} = 0$

(b) Umklapp process $|\underline{G}| \neq 0$

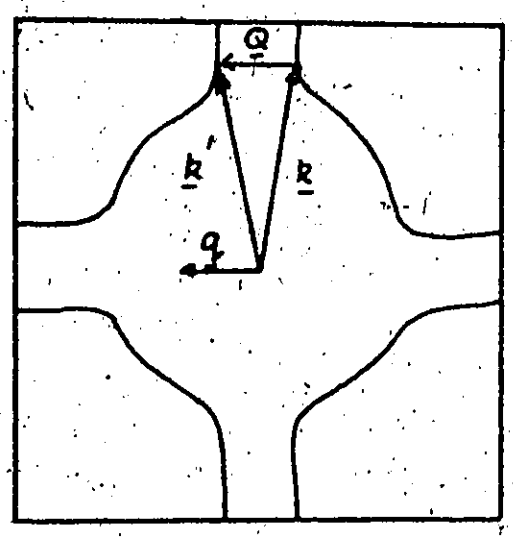

(a)

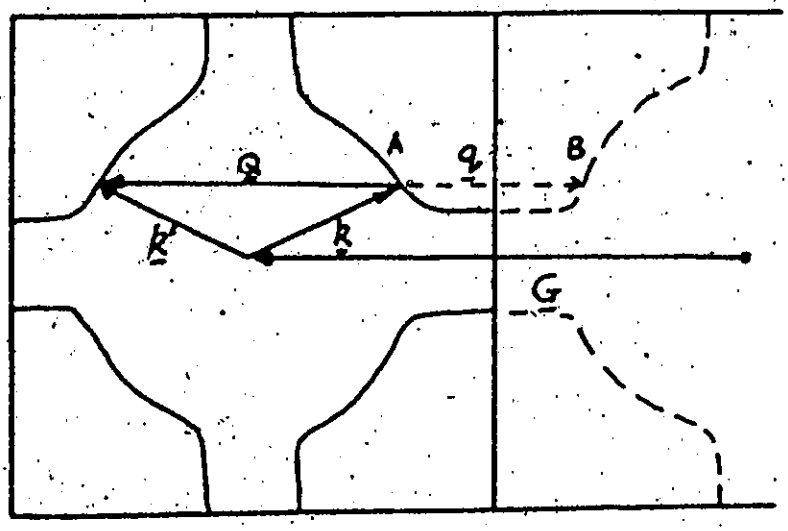

(b)

simplified picture. A good description of this breakdown is found in Shaw and Zimen (1963). They use a 2-OPW description to approach this problem. Their results can be easily extended to the multi-OPW case. Essentially, the argument goes as follows.

The matrix element that governs the scattering of an electron from $|\underline{k}\rangle$ to $|\underline{k}'\rangle$ in the S-OPW approximation is given by

$$|g_{\underline{k}'\underline{k}\lambda}|^2 \propto \left|\frac{(\underline{k}'-\underline{k})\cdot\underline{e}_{\underline{k}'-\underline{k},\lambda}}{\sqrt{\omega_{\underline{k}'-\underline{k},\lambda}}}\right|^2 \qquad 3.3.2$$

This comes from Equation 2.3.6(b). Here $\underline{k}'-\underline{k} = \underline{q} + \underline{G}$, $\underline{q}$ being the phonon momentum vector reduced to the FBZ by some $\underline{G}$. If $\underline{G} = 0$ the process is Normal, if $\underline{G} \neq 0$ then the process is called Umklapp. This distinction is essential for the phonons are only defined in the FBZ and repeated periodically into the neighbouring zones. These processes are illustrated in Figure 3.3.3(a) and Figure 3.3.3(b), and are self-explanatory. In (b) U-process $\underline{q}$ is found by adding $\underline{Q} + \underline{G}$, which is the same as $\underline{q}$ marked by A B as in the picture in the repeated zone scheme. In the N-process as $q \to 0$, since $q \propto \omega$ for long-wavelength phonons $|g_{\underline{k}'\underline{k}\lambda}|^2 \to C\frac{q^2}{\omega^2}$ = constant. In the U-process as $\underline{Q}$ increases further in diagram 3.3.3(b), i.e., $\underline{k}'$ and $\underline{k}$ approach the BZ boundary $|\underline{q}|$ decreases, i.e., A → B. So that when $\underline{k}'-\underline{k} \to \underline{G}$

$$|g_{\underline{k}'\underline{k}\lambda}|^2 \to C\frac{q^2}{\omega_{\underline{q}\lambda}} \qquad 3.3.3$$

where C is some constant, but $\omega_{\underline{G}} = \omega_{\underline{q}=0} = 0$. Hence $|g_{\underline{k}\underline{k}'\lambda}|^2 \to \infty$ as shown in diagram 3.3.1. However, if A → B, $\underline{q} = 0$, state $|\underline{k}\rangle$ is identical to $|\underline{k}'\rangle$ and the result is unphysical.

The above expression for $|g_{\underline{k}\underline{k}'\lambda}|^2$, when using a 2-OPW approximation (i.e. using Equation 2.3.10 and letting the n, n' indices run

over 1,2) becomes

$$g_{\underline{k}\underline{k}'\lambda} \propto \omega(\underline{k}'-\underline{k})^{-\frac{1}{2}} \Big\{ C_1'C_1(\underline{k}'-\underline{k})\, w(\underline{k}'-\underline{k}) + C_2'C_2(\underline{k}'+\underline{G}-\underline{k}+\underline{G}) \cdot w(\underline{k}'+\underline{G}-\underline{k}+\underline{G}) + C_1'C_2(\underline{k}'-\underline{k}+\underline{G})\, w(\underline{k}'-\underline{k}+\underline{G}) + C_2'C_1(\underline{k}'+\underline{G}-\underline{k})\, w(\underline{k}'+\underline{G}-\underline{k}) \Big\}$$

.....3.3.4

and $w(\underline{q})$ is the pseudopotential matrix element. Here the states $|\underline{k}\rangle$ and $|\underline{k}'\rangle$ have been expressed in terms of the mixtures of plane waves:

$$|\underline{k}\rangle = C_1 \exp i\underline{k}\cdot\underline{r} + C_2 \exp i(\underline{k}-\underline{G})\cdot\underline{r}$$

$$|\underline{k}'\rangle = C_1' \exp i\underline{k}'\cdot\underline{r} + C_2' \exp i(\underline{k}'-\underline{G})\cdot\underline{r} \qquad 3.3.5$$

where we have suppressed the $\underline{k}$ label on the coefficients C_1, C_2 in an obvious manner. The coefficients C_1 and C_2 and C_1', C_2' can be easily shown to satisfy the following relations as $|\underline{k}\rangle$ and $|\underline{k}'\rangle$ approach the BZ boundary, i.e. $\underline{q} = 0$ (or $\underline{k}'-\underline{k} = \underline{G}$),

$$C_1 = -C_2 = 1/\sqrt{2}$$

$$C_1' = C_2' = 1/\sqrt{2} \qquad 3.3.6$$

Equation 3.3.6 expresses the fact that the symmetry of the wavefunctions are basically quite different for the state $|\underline{k}\rangle$ and $|\underline{k}'\rangle$. So when $\underline{k}'-\underline{k} \to \underline{G}$ corresponds to the situation of Figure 3.3.3(b), Equation 3.3.4 simplifies to

$$|g_{\underline{k}\underline{k}'\lambda}|^2 \longrightarrow \text{CONSTANT} \qquad 3.3.7$$

A natural extension to the multi OPW approximation is obvious, and the result in Equation 3.3.7 is obtained if the crystal symmetries of the wavefunctions in expanding electronic states similar to those in Equation 3.3.5 are preserved. This is the prime reason for using 15-OPW rather than just 4-OPW, for the cancellation in 3.3.4 depends on the symmetries of the wavefunctions

and is not just a coincidence. Calculations of $\alpha^2_{\underline{k}}(\omega)$ indeed show that the above reasoning is valid.

Lastly, we plot the $\alpha^2_{tr}F(\underline{k},\omega)$, $\alpha^2_{LL}F(\underline{k},\omega)$ and $\alpha^2_{LL}F(\underline{k},\omega)$ in Figure 3.3.6 (a to n). These functions are similar in form to $\alpha^2F(\underline{k},\omega)$ and have important applications in transport properties. It is sufficient to mention here that while the S-OPW calculation shows that $\alpha^2_{tr}F(\underline{k},\omega)$ is positive definite for all $\underline{k}$ and ω because the weight factor is $(1 - \cos\theta)$, it is not necessarily true in the full calculation that employs the details of the FS. This is because $1 - \frac{V_{\underline{k}'}}{V_{\underline{k}}}$ may be negative if $|V_{\underline{k}'}| > |V_{\underline{k}}|$ which may happen when we pick $\underline{k}$ close to the Bragg plane. By referring to Figure 2.2.4, we can see that the magnitude of $V_{\underline{k}}$ near the Bragg planes are invariably less than V_F°. The effects of these anisotropies will be discussed in more detail in subsequent sections.

Fig. 3.3.4 The calculated $\alpha_{tr}^2 F(\underline{k},\omega)$, $\alpha_{IL}^2 F(\underline{k},\omega)$ and $\alpha_{LL}^2 F(\underline{k},\omega)$ weighted distribution functionn as functions of ω.

——— $\alpha_{tr}^2 F(\underline{k},\omega)$

..... $\alpha_{IL}^2 F(\underline{k},\omega)$

- - - $\alpha_{LL}^2 F(\underline{k},\omega)$

(a) - (d) $\phi = 1°$ $\theta = 1°, 21°, 29°, 45°$

(e) - (i) $\phi = 23°$ $\theta = 15°, 19°, 21°, 31°, 49°$

(j) - (n) $\phi = 45°$ $\theta = 13°, 17°, 23°, 31°, 53°$

The y-scale is magnified by a factor of 100

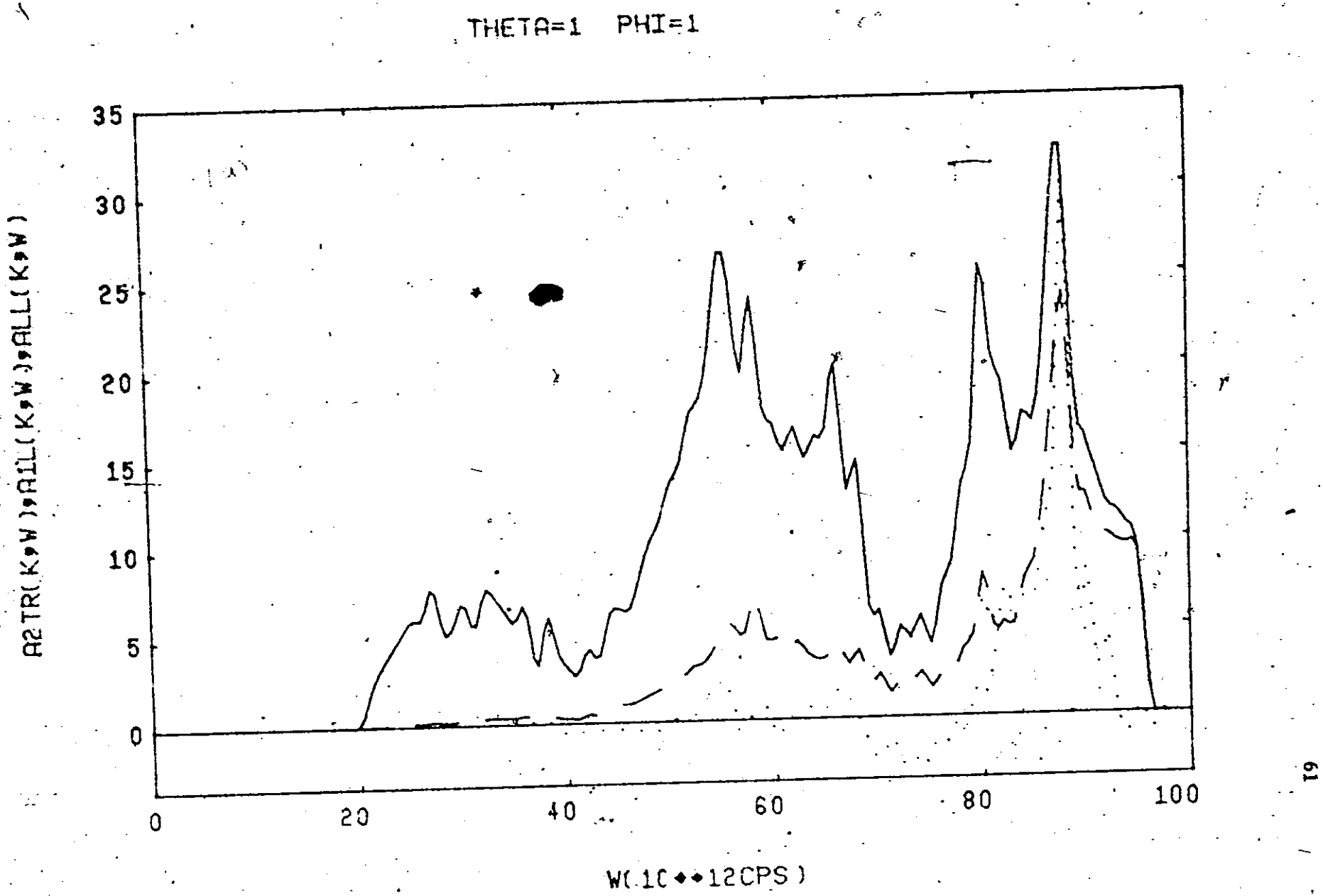
THETA=1 PHI=1
A2TR(K,W)*A1L(K,W)*ALL(K,W)
35
30
25
20
15
10
5
0
0
20
40
60
80
100
W(10**12CPS)

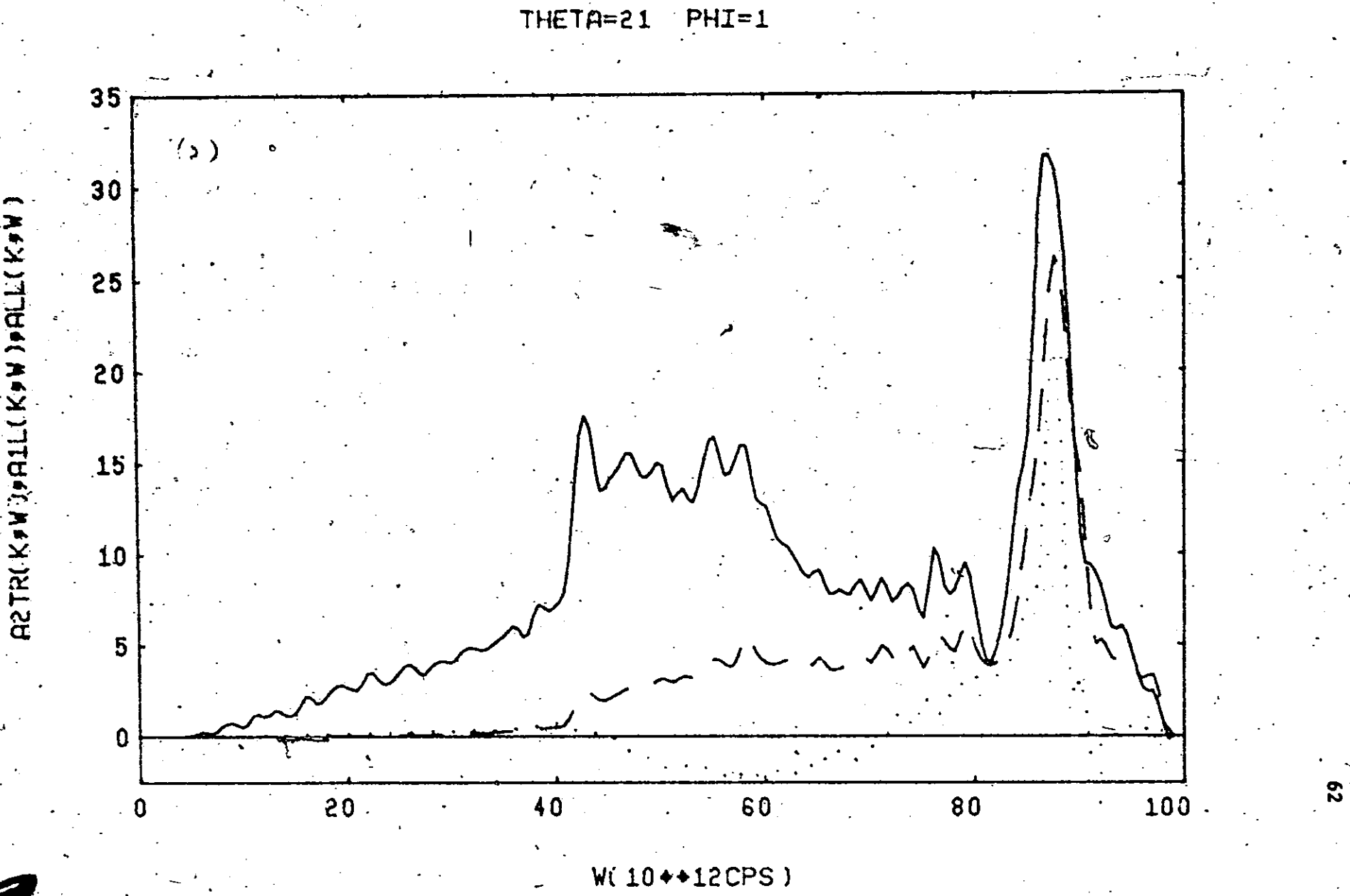
THETA=21 PHI=1
(a)
A2TR(K,W),A1L(K,W),ALL(K,W)
35
30
25
20
15
10
5
0
0
20
40
60
80
100
W(10**12CPS)

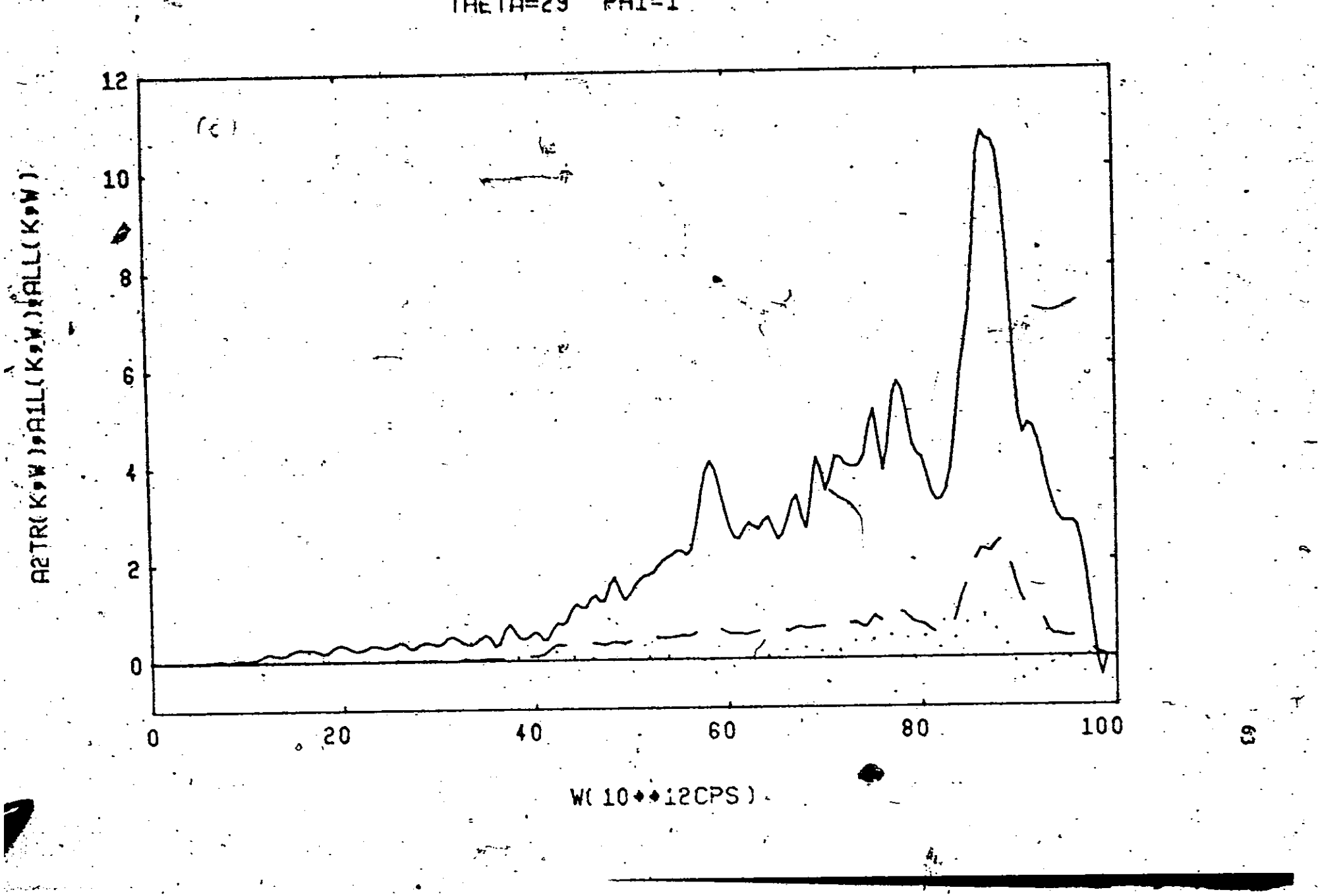
THETA=29 PHI=1
A2TR(K,W)/A1L(K,W)/ALL(K,W)
12
10
8
6
4
2
0
0
20
40
60
80
100
W(10**12CPS)

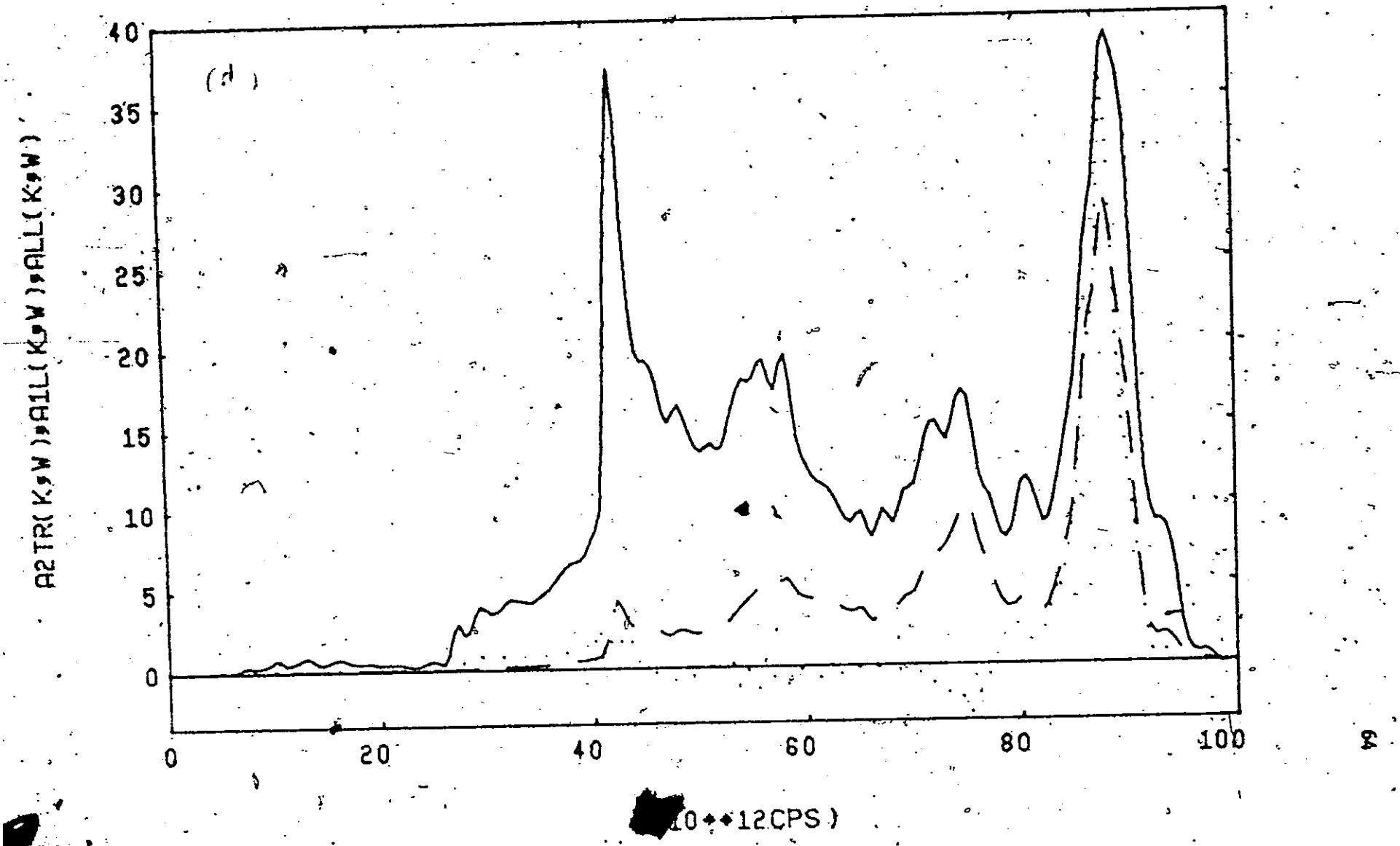
THETA=45 PHI=1
(d)
A2TR(K,W),A1L(K,W),ALL(K,W)
40
35
30
25
20
15
10
5
0
0
20
40
60
80
100
(10**12CPS)

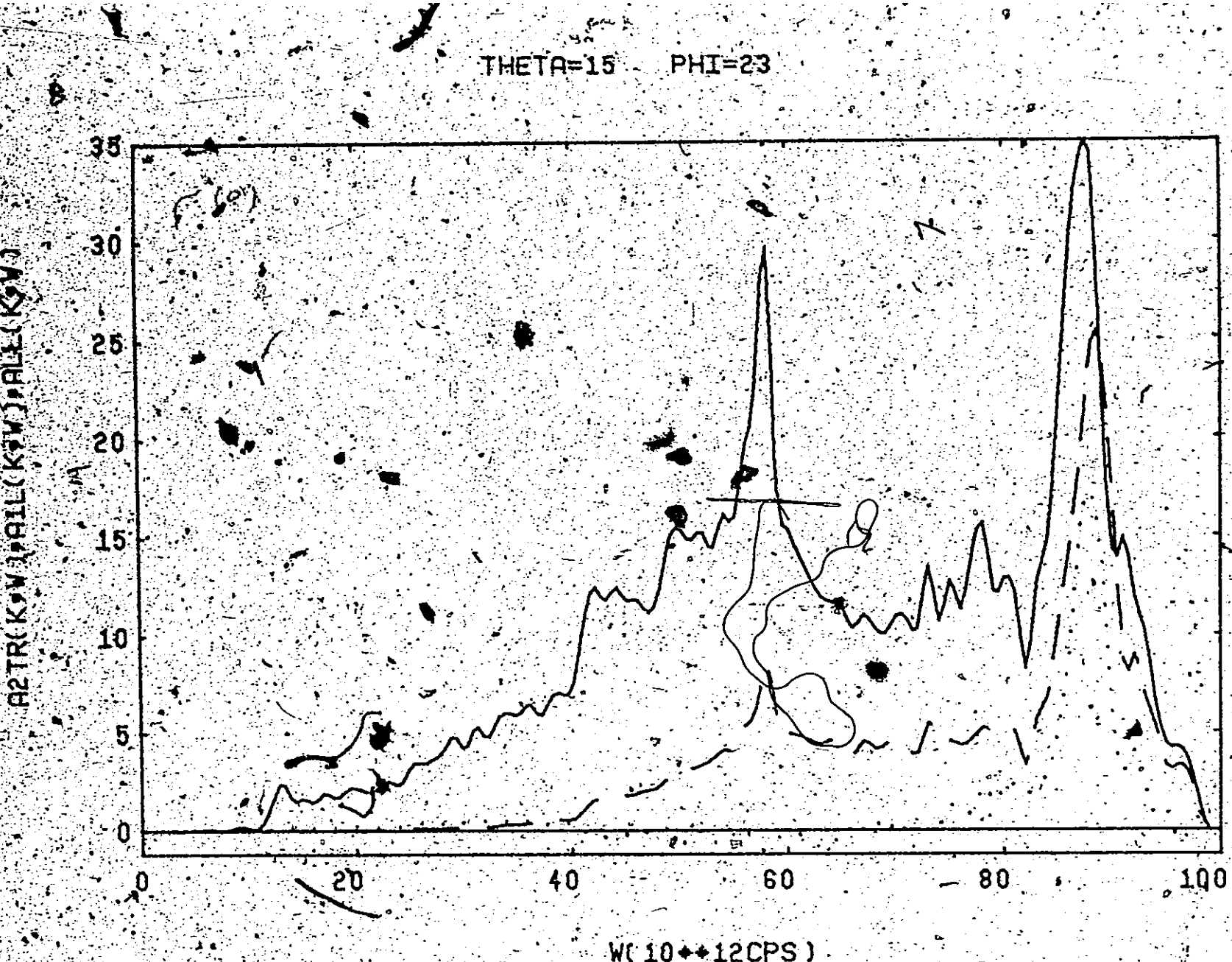

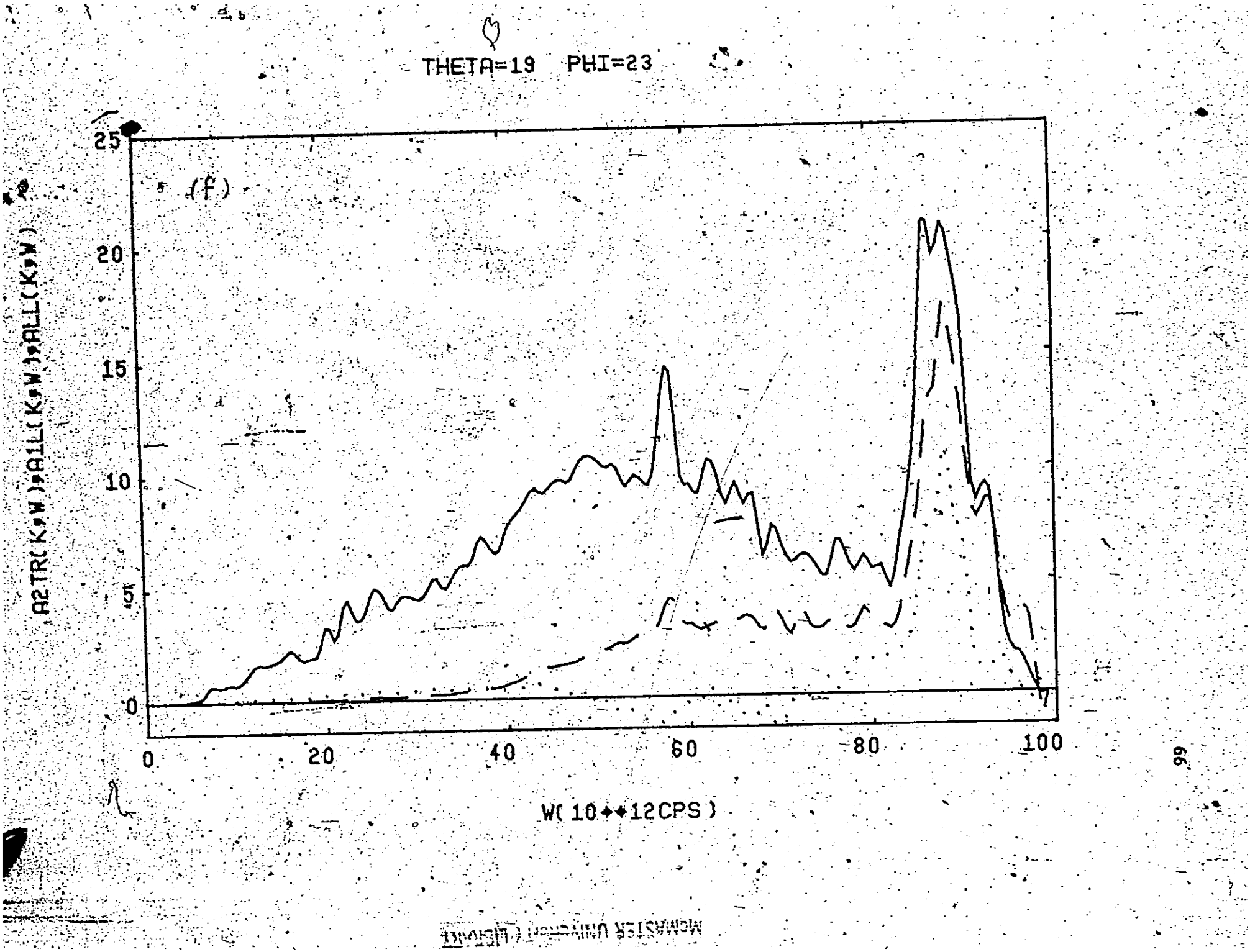

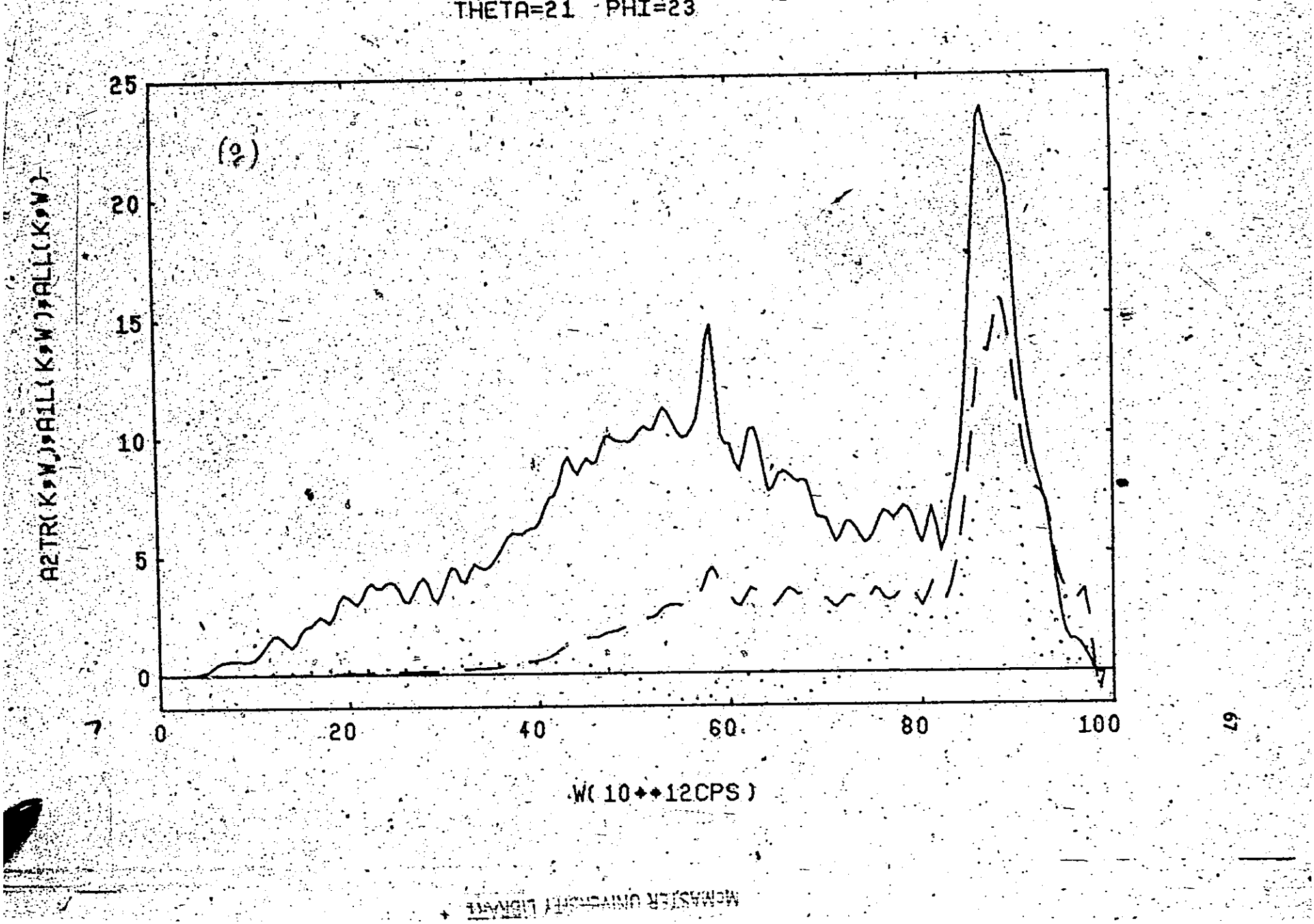

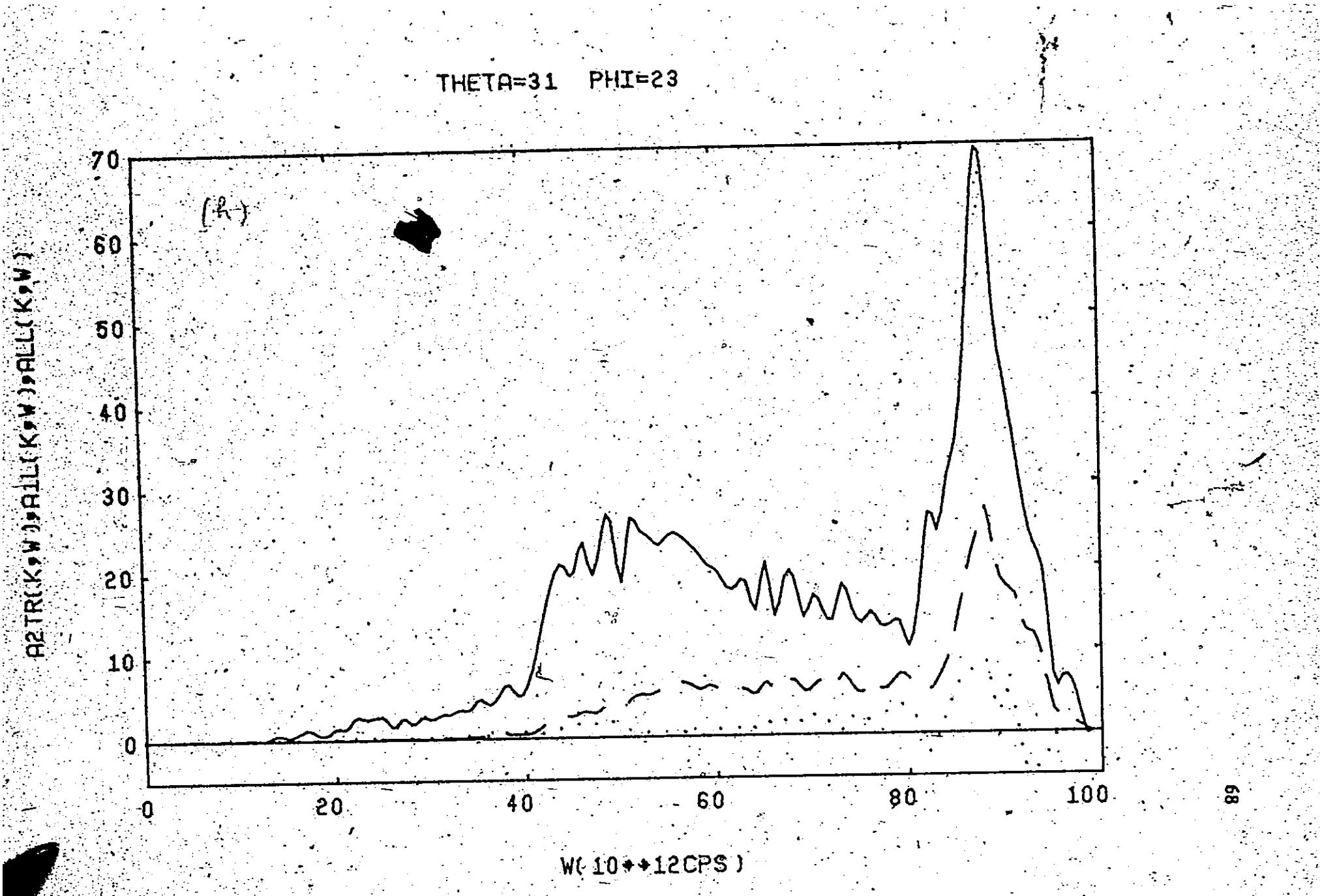

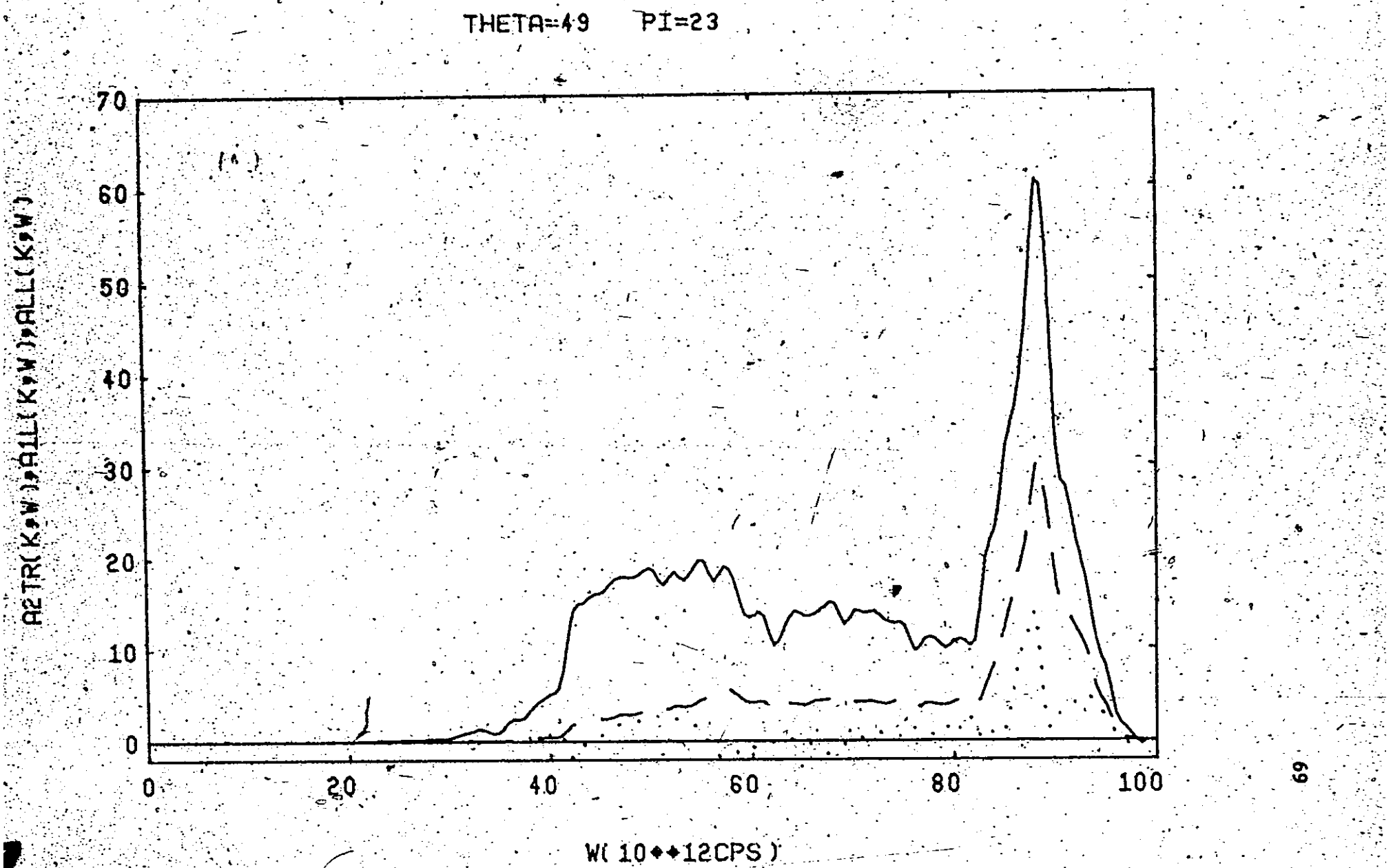

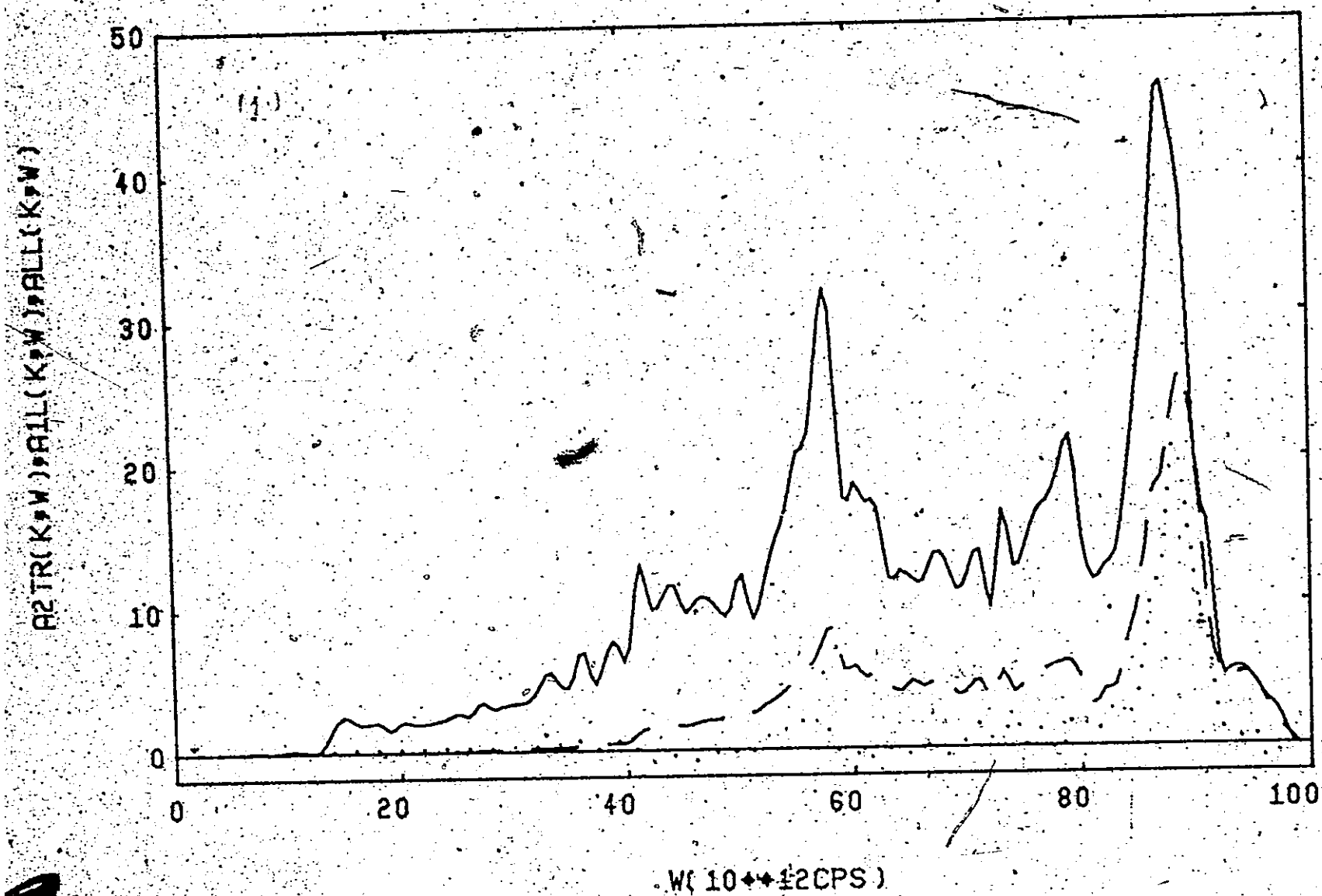
THETA=13 PHI=45
50
40
30
20
10
0
0
20
40
60
80
100
A2TR(K,W),ALL(K,W),ALL(K,W)
W(10**12CPS)

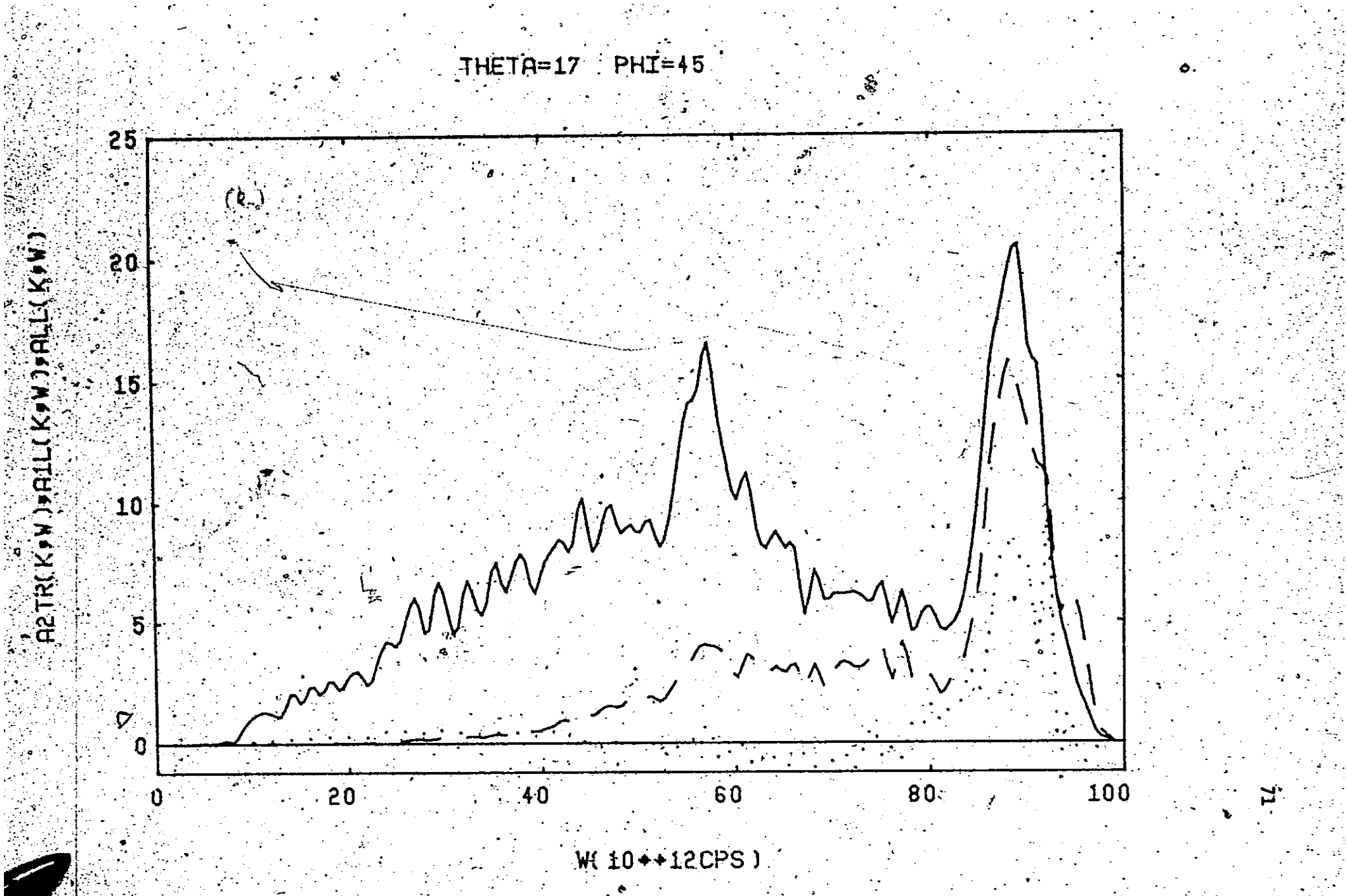

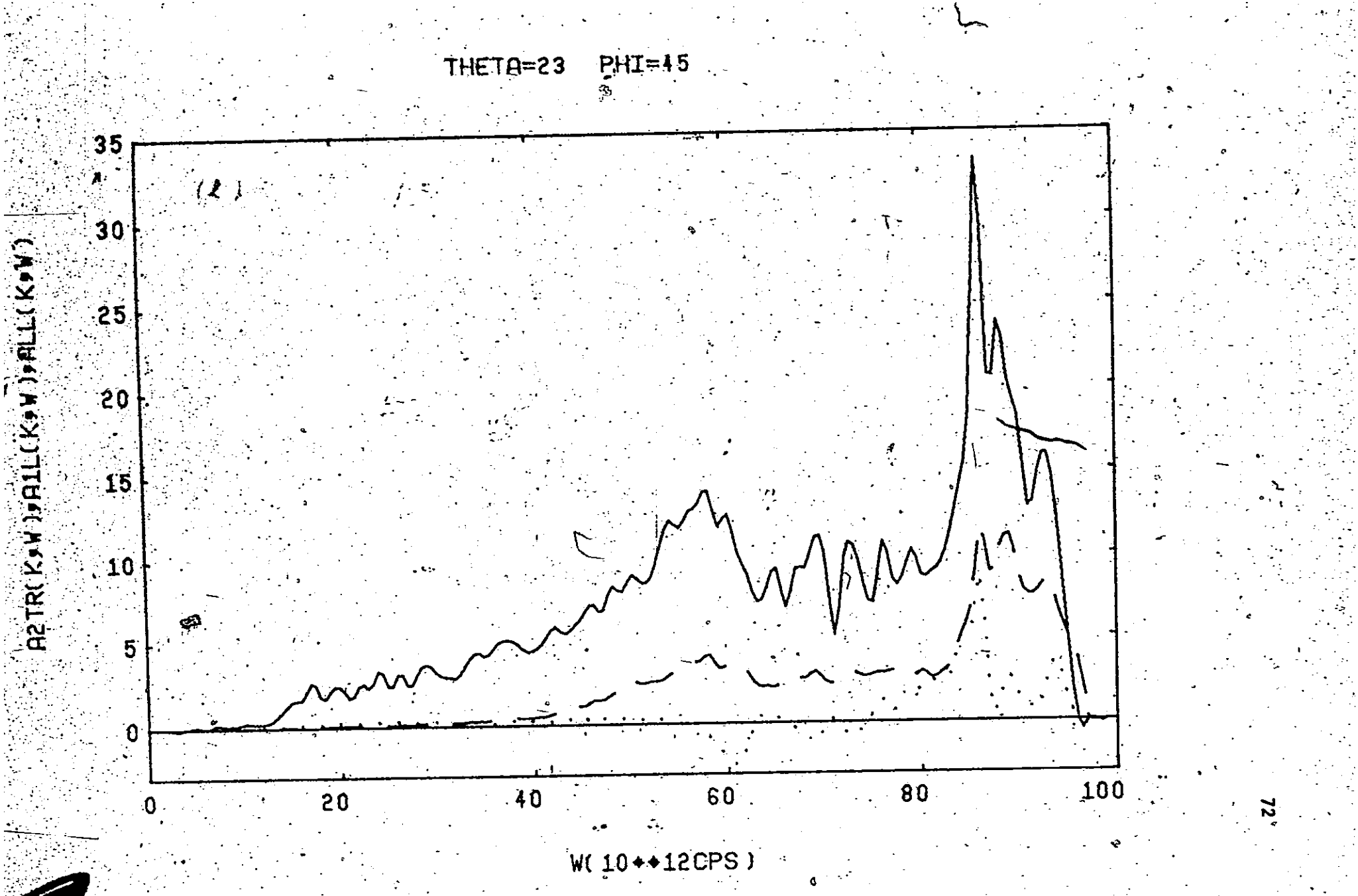
THETA=23 PHI=45
A2TR(K,W)/A1L(K,W)/ALL(K,W)
35
30
25
20
15
10
5
0
0
20
40
60
80
100
W(10**12CPS)

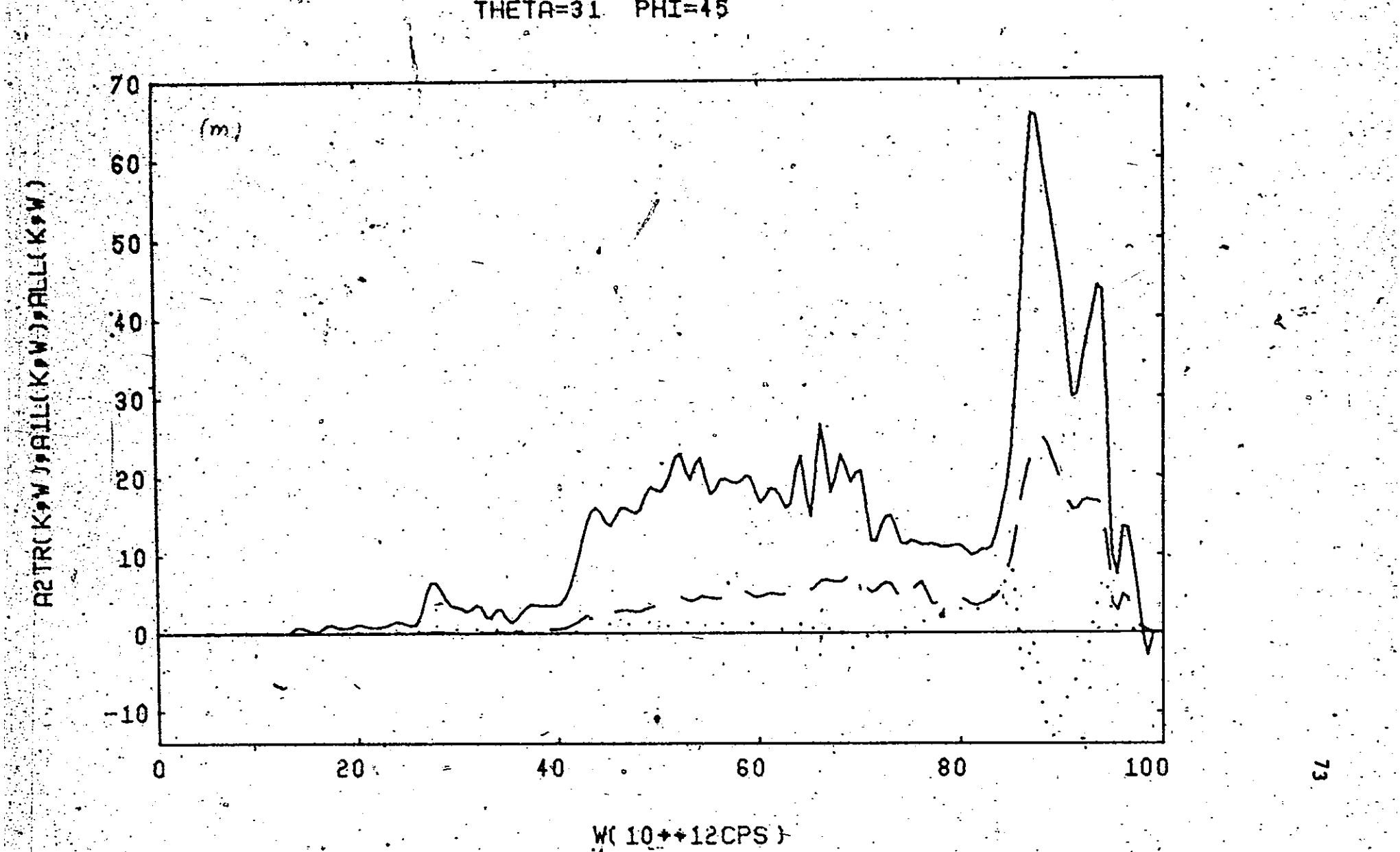
THETA=31 PHI=45
(m)
70
60
50
40
30
20
10
0
-10
0
20
40
60
80
100
A2TR(K,W),ALL(K,W),ALL(K,W)
W(10++12CPS)

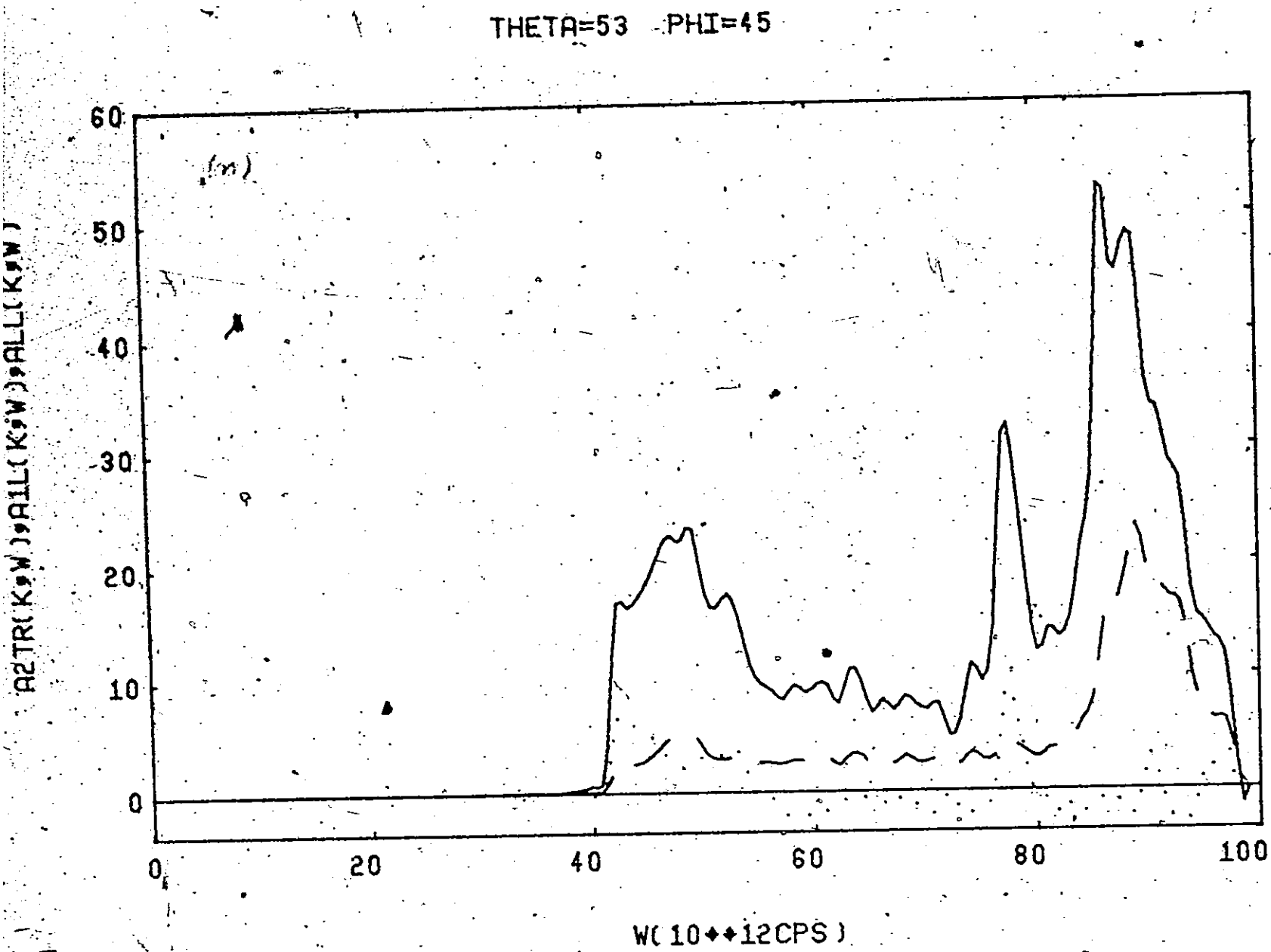
THETA=53 PHI=45
(n)
60
50
40
30
20
10
0
0
20
40
60
80
100
W(10**12CPS)
A2TR(K,W),A1L(K,W),ALL(K,W)

CHAPTER IV

THE ANISOTROPIES IN THE DIRECTIONAL MASS ENHANCEMENT PARAMETER AND THE DIRECTIONAL SUPERCONDUCTING ENERGY GAPS IN ALUMINIUM

4.1 The Anisotropies of the Mass Enhancement Parameter

The phonon renormalized directional effective mass for an electron in the state (k,θ,ϕ) on the F.S., $m^*(\theta,\phi)$, is given by (Allen and Cohen 1970) as

$$m^*(\theta,\phi) = m_b\,(1+\lambda(\theta,\phi)) \qquad 4.1.1$$

with

$$\lambda(\theta,\phi) = 2\int_0^{\omega_m} \frac{d\nu}{\nu}\,\alpha^2F(\hat{k},\nu) \qquad 4.1.2$$

where m_b is the band mass and $\lambda(\theta,\phi)$ is the directional mass enhancement parameter. Previous calculations on Aluminium were done in a S-OPW formulation by Ashcroft and Wilkins (1965), Janak (1968), Trofimenkoff et al (1968) and Pytte (1967). A proper calculation of $\lambda(\theta,\phi)$ should include in the computation, information on:

(i) Distortion of Fermi Surface from sphericity at the Brillouin Zone Boundaries.

(ii) The proper treatment of the electron-ion matrix elements. In the framework of a pseudopotential theory this implies the proper mixing of OPW's.

(iii) Anisotropies in the realistic frequencies and also the proper polarisation vectors of the phonons.

The calculations done by previous authors have not treated properly all of the above features. Wilkins used a perturbation expansion for evaluating the two-OPW matrix elements in (ii) and attempted the integrations over the distorted FS. Pytte obtained a similar result by ignoring the anisotropies in the phonon spectrum and by using a 2-OPW treatment in (i) and (ii). Trofimenkoff ignored (i) and (ii) and used realistic phonons. Janak ignored all effects.

Our calculations for $\lambda(\theta,\phi)$ differ from all the above attempts in that we use (i) Ashcroft's fit of the FS, (ii) a 15 OPW treatment of the electron-ion interaction, (iii) realistic phonons calculated from a Born-von Kármán fit to neutron inelastic scattering data.

The results for $\lambda(\theta,\phi)$ using Equation 4.1.2 are presented in Table 4.3.1 for 62 directions in the $(\frac{1}{48})$ of the Brillouin Zone (see Table 3.2.1 for key to directions). Leavens and Carbotte (1971) also calculated the $\lambda(\theta,\phi)$ by treating (i) and (ii) in the S-OPW approximation but treated (iii) in the same way as we do. Their results are reproduced in Figure 4.1.1 along the two principle planes, namely $\phi = 0°$, $\phi = 45°$. They exhibit a sharp peak at about $\theta=29°$ in both principle planes. This originates from the matrix element's singular behaviour at low ω discussed in some detail in Section 3.3. Allen and Cohen (1970) suggested an approximate (and somewhat arbitrary) way of treating the divergence in $\alpha^2F(\underline{k},\omega)$ at low frequency ($\omega < \omega_{c/5}$) by multiplying by a damping factor to get a new $\alpha^2_c F(\underline{k},\omega)$ as shown in Figure 4.1.2. With these functions $\lambda(\theta,\phi)$ can be recalculated and results are shown in Figure 4.1.3. The sharp peak is now moderated into a broad maximum around 29° whereas the values of λ at other directions (θ,ϕ) are not

Fig. 4.1.1 The directional electron-phonon mass-enhancement parameter, $\lambda(\theta,\phi)$, for Al as calculated within the S-OPW approximation.
The results for the two arcs $\phi=0°$ and $45°$ on the irreducible $(\frac{1}{48})^{th}$ are to be distinguished as follows:

$\phi = 0°$

$\odot$ $\phi = 45°$

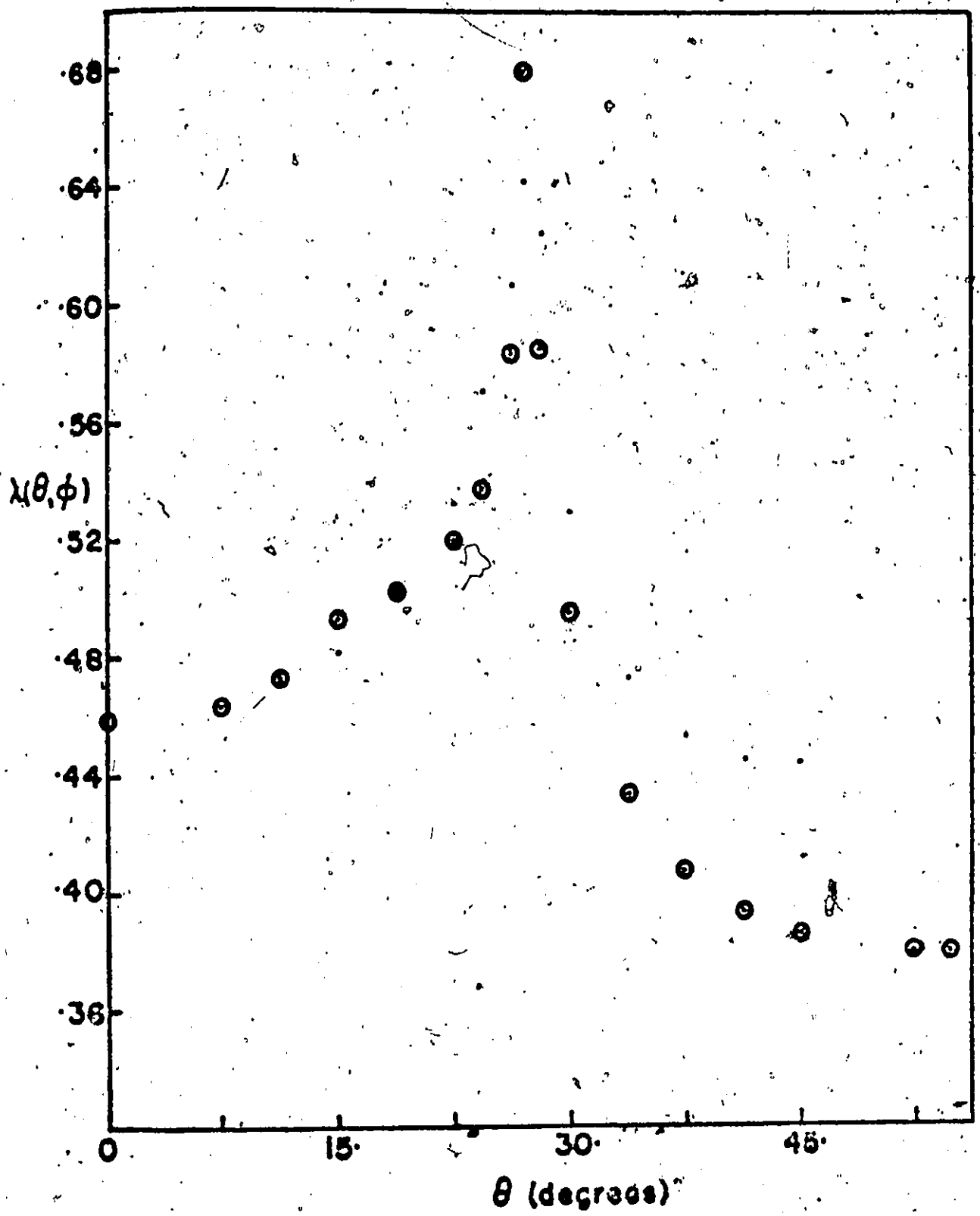
.68
.64
.60
.56
λ(θ,φ)
.52
.48
.44
.40
.36
0
15°
30°
45°
θ (degrees)

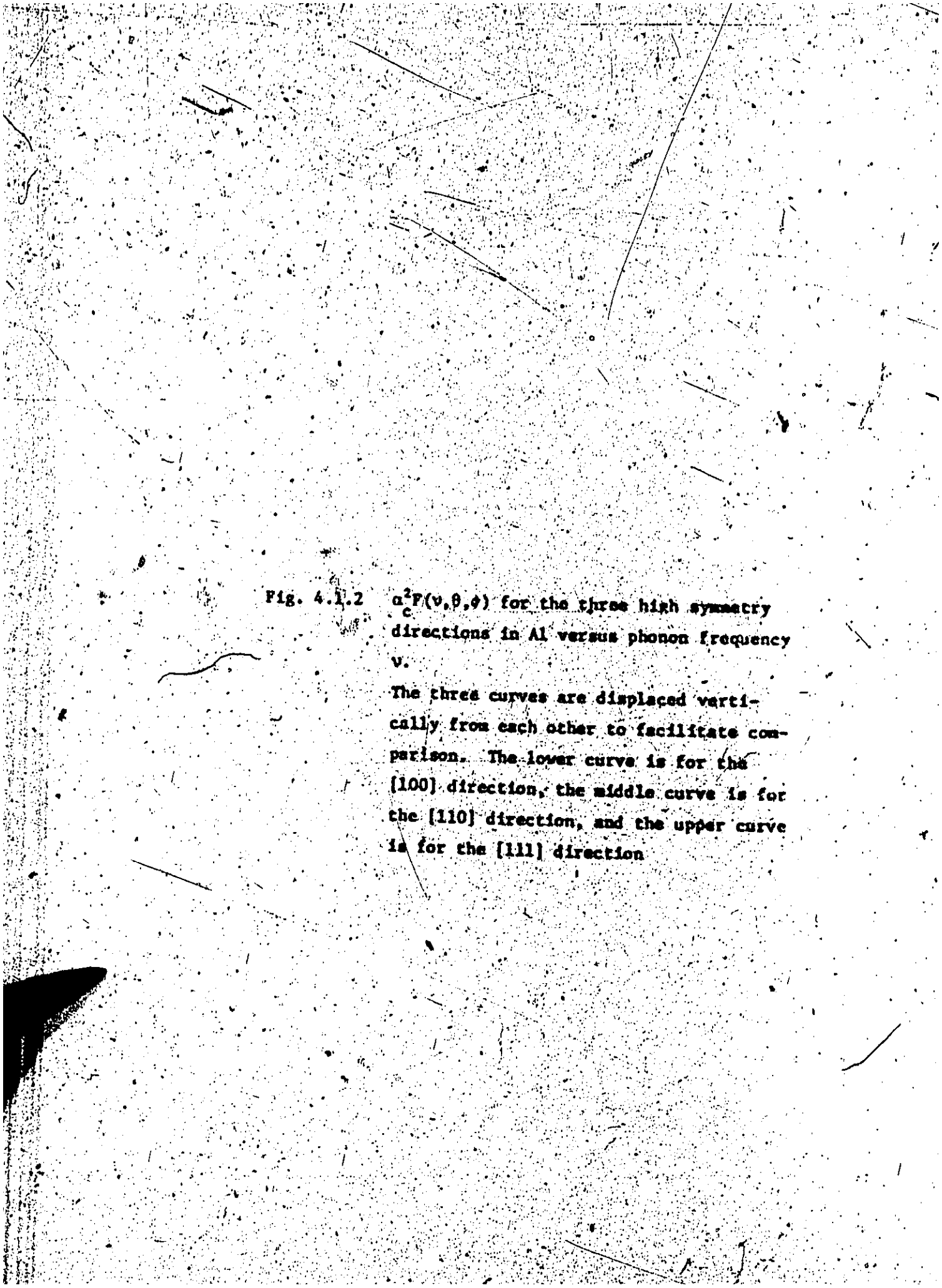

Fig. 4.1.2 $\alpha_c^2 F(\nu,\beta,\phi)$ for the three high symmetry directions in Al versus phonon frequency ν.

The three curves are displaced vertically from each other to facilitate comparison. The lower curve is for the [100] direction, the middle curve is for the [110] direction, and the upper curve is for the [111] direction

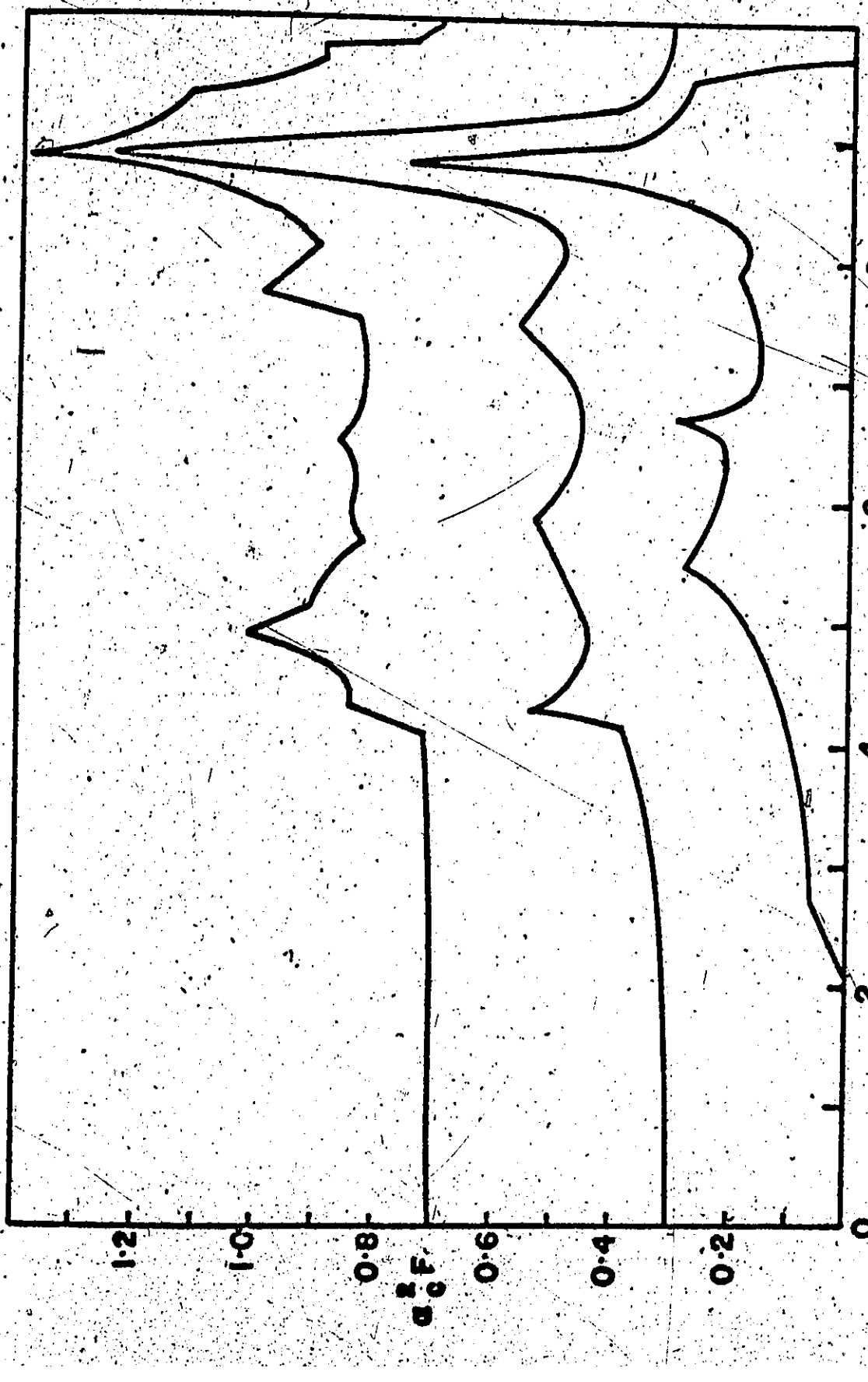
1·2
1·0
0·8
0·6
0·4
0·2
0
$\alpha^2 F$
2
4
6
8
$\nu(10^{12}$ c.p.s.)

Fig. 4.1.3 The directional electron-phonon mass-enhancement parameter, $\lambda(\theta,\phi)$, for Al calculated with the corrected function $\alpha_c^2 F(\nu,\theta,\phi)$.
The results for the three arcs ϕ=0°, 22 1/2° and 45° on the irreducible $(\frac{1}{48})^{th}$ are to be distinguished as follows:

· ϕ = 0°

x ϕ = 22 1/2°

⊙ ϕ = 45°

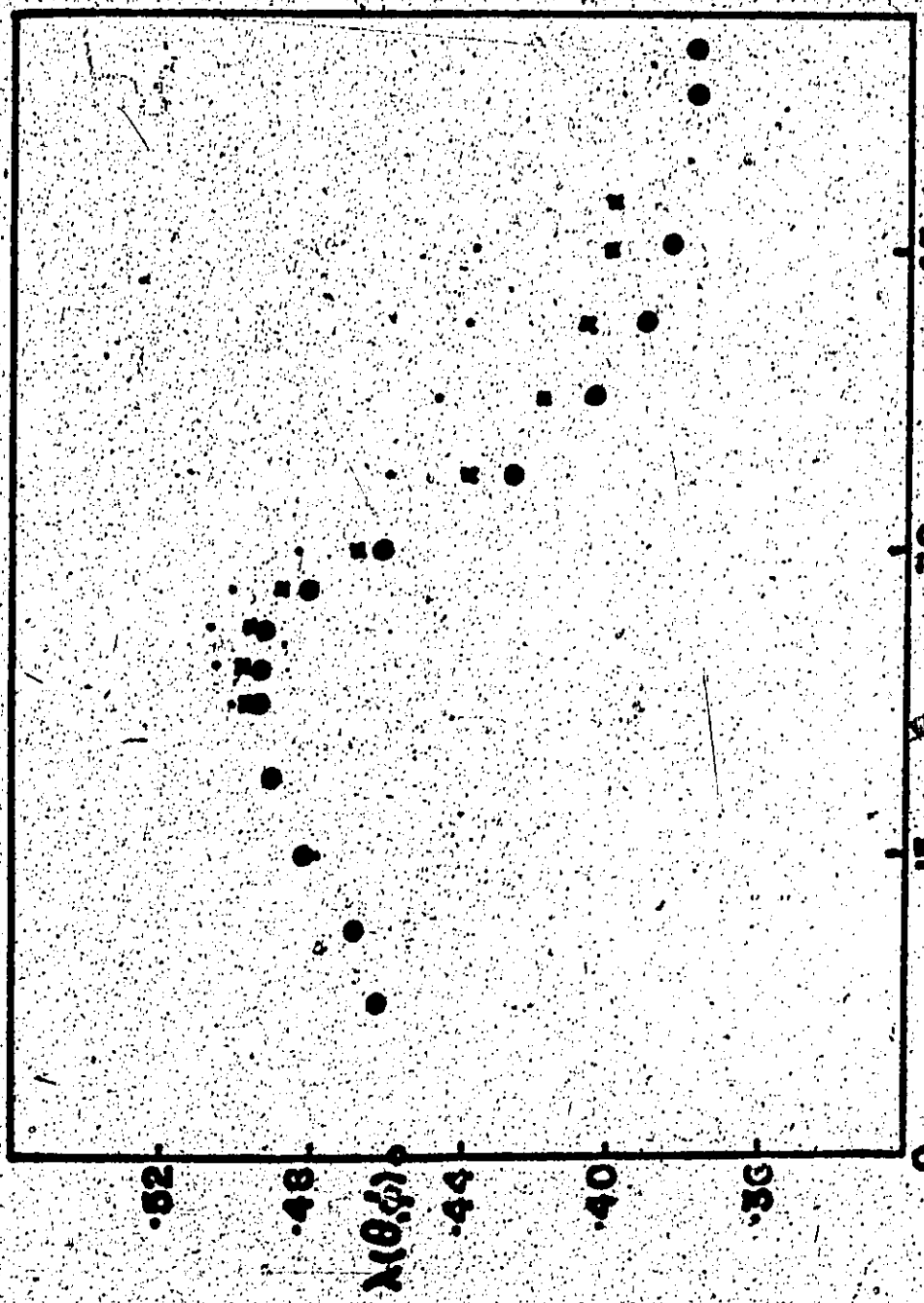
.52
.48
.44
.40
.36
λ(θ,φ)
0
15
30
45
θ (degrees)

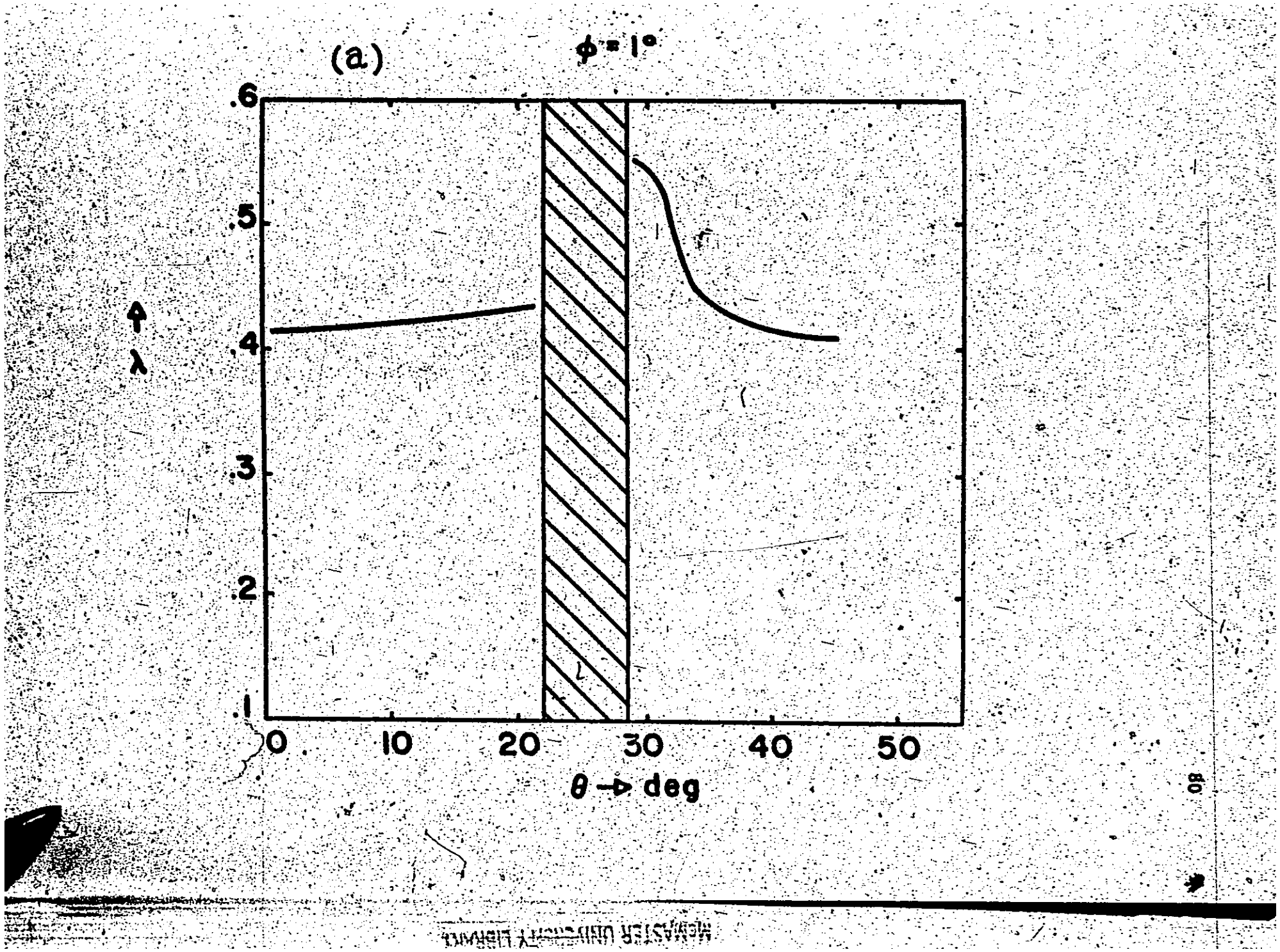

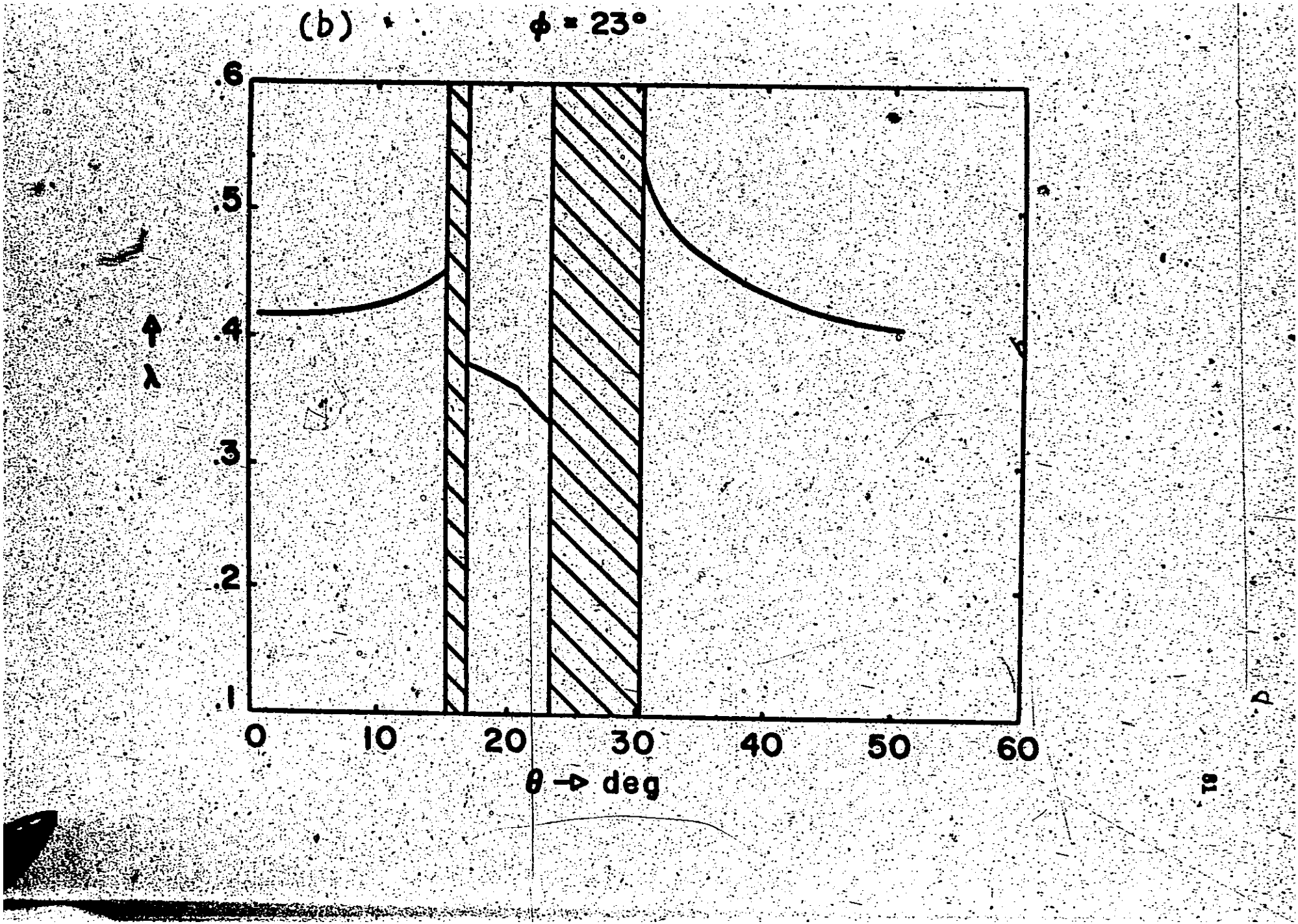
(b)
$\phi = 23°$
.6
.5
.4
.3
.2
.1
λ
0
10
20
30
40
50
60
$\theta \rightarrow$ deg

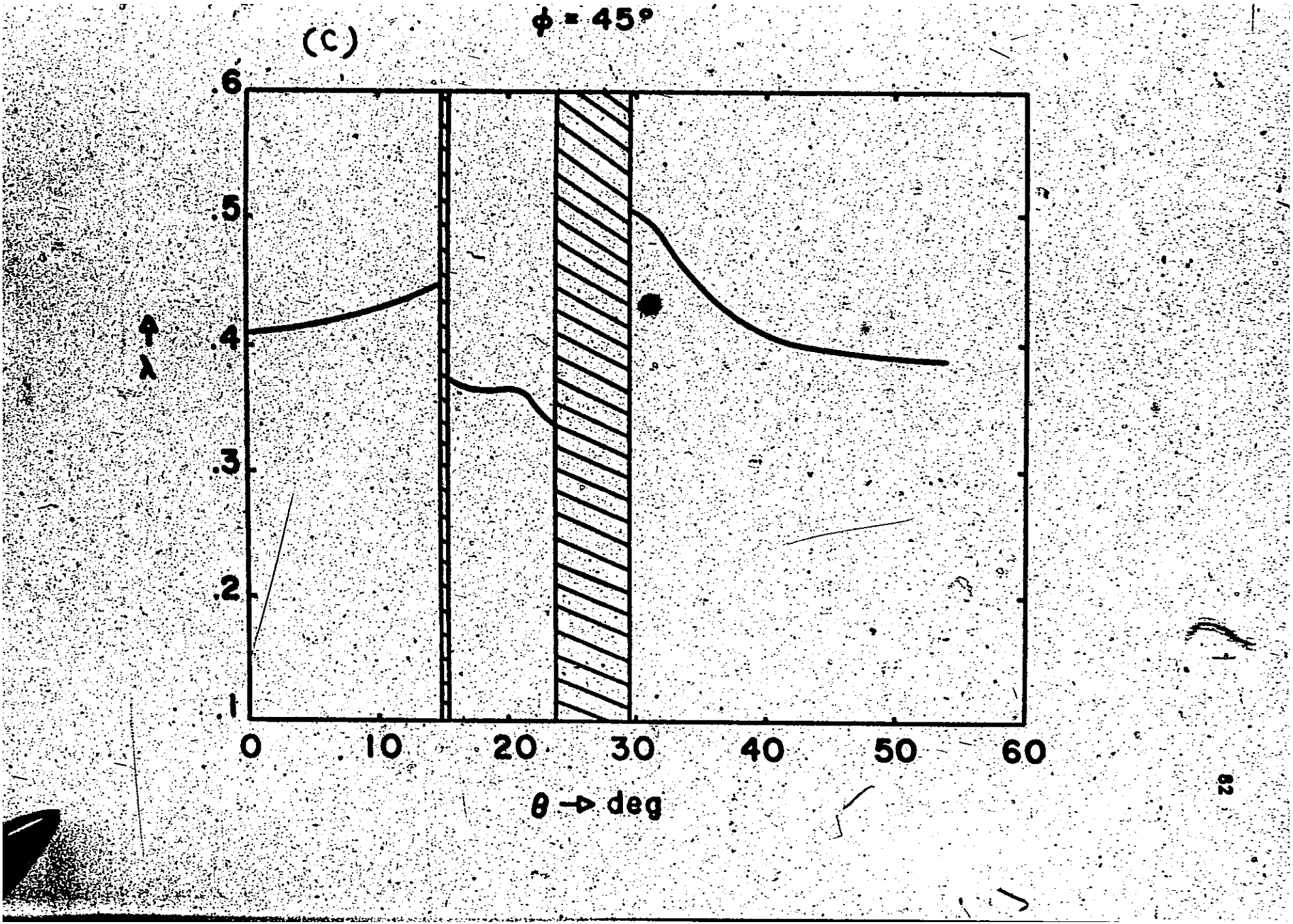
(c)
$\phi = 45°$
.6
.5
.4
.3
.2
.1
$\frac{\phi}{\lambda}$
0
10
20
30
40
50
60
$\theta \rightarrow$ deg

appreciably changed.

Figures 4.1.4 show our calculations in the full treatment. The graphs of $\lambda(\theta,\phi)$ show considerable anisotropies similar to those found in the simpler models. These are caused by the anisotropies in the phonon spectrum and the electron-phonon interaction which enter into the computations in a complicated fashion. The details have been discussed at length in the literature and so we do not repeat them here. Comparing our results with those of Leavens using a S-OPW and $\alpha^2_c F(\underline{k},\omega)$ we can see that the value of $\lambda(\theta,\phi)$ starts at the pole at some intermediate value and gradually rises towards $\theta = 30°$ and then decreases to some minimum value at $\theta = 45°$. In the full treatment, the behaviour of $\lambda(\theta,\phi)$ at the polar regions ($\theta = 0°$) is similar, but now there are regions corresponding to Bragg planes in which no $\lambda(\theta,\phi)$ values are defined. The second different feature lies in the fact that the function exhibits discontinuities in its magnitude. For example, if we take the plane defined by $\phi = 45°$, the value of λ rises slowly between the pole and $\theta \approx 15°$. Between $\theta = 15\frac{1}{2}°$ and $24°$, λ lies on the electron arm and the magnitude of λ attains the much lower value of about 0.375 compared to 0.45 at the band edge. After $29\frac{1}{2}°$, λ lies on the hole surface again and exhibits a large discontinuity jumping to a value of 0.501 from a value of 0.34. From then on the behaviour is similar to the S-OPW result, gradually decreasing to a minimum of 0.38. These anisotropies stem from the fact that the wavefunctions are quite different from a S-OPW near the Bragg planes. Our calculations show that their effects on $\lambda(\theta,\phi)$ can be quite drastic, not only qualitatively but also quantitatively. The discrepancies cannot be explained merely in terms of the

low frequency behaviour of $\alpha^2F(\underline{k},\omega)$ functions, as Allen and Cohen (1969) had assumed.

In fact, a survey of the calculated values of λ obtained by previous calculations shows that they are consistently high. λ = .49 Ashcroft and Wilkins, λ = 0.50 and 0.53 by Janak and λ = 0.46 by Pytte and Trofimenkoff. An average of $\lambda(\theta,\phi)$ in different directions over the FS gives us λ = 0.43.

From specific heat data, the experimental result for m^*_{exp} = 1.45 . If one takes the calculations of Rice (1968) for λ_{e-e} (-0.01) and m_b = 1.06 (Ashcroft and Wilkins 1965), then we get

$$m^* = m_b(1+\lambda) = 1.50 \qquad 4.1.3$$

It can be seen that a lower value of λ leads to somewhat better agreement with experiment. For example, Ashcroft and Wilkins give m^* = 1.57 which is larger than our value of 1.50.

4.2 The Calculations of the Anisotropies in Energy Gaps in Superconducting Aluminium

The anisotropic Eliashberg gap equations relate the energy gaps and the renormalization function Z to certain normal-state parameters. Derivations of the equations in the isotropic (dirty) limit can be found in "Theory of Superconductivity" by Schrieffer (1964). Generalizations to the anisotropic case are discussed by Bennett. Leavens (1971) has derived a set of much simplified equations from the anisotropic Eliashberg equations valid in the weak-coupling limit. His central results, which enable one to calculate the directional energy gaps are,

$$\Delta_0^{(1)}(\theta,\phi) = \frac{1}{1+\lambda(\theta,\phi)}\left[-\bar{\lambda}(\theta,\phi) + \left[\lambda(\theta,\phi) - \mu^*\right] \log\left(\frac{2\omega_c}{\Delta_0}\right)\right]\Delta_0 \qquad \ldots\ldots 4.2.1$$

where $\lambda(\theta,\phi)$ is the phonon mass enhancement parameter, ω_c is the maximum phonon frequency and μ^* is the coulomb parameter. It is given by,

$$\mu^* = \frac{N(0)\,V_c}{1 + N(0)\,V_c \log\left(E_F/\omega_c\right)} \qquad 4.2.2$$

where N(o) is the single spin electron density of states at the FS, V_c is the average screened coulomb interaction for scattering at the FS and E_F is the Fermi energy.

Δ_0 is the result of an isotropic calculation and $\Delta_0^{(1)}$ is the next iteration for the directional gap.

$\bar{\lambda}(\theta,\phi)$ is another weighted integral of $\alpha^2F(\underline{k},\omega)$,

$$\bar{\lambda}(\theta,\phi) = 2\int_0^{\omega_c} \frac{d\nu}{\nu}\,\alpha^2F(\underline{k},\nu)\log\left(1+\frac{\omega_c}{\nu}\right) \qquad 4.2.3$$

Following the suggestion of Leavens (private communications) we choose $\mu^* = 0.13$ and $\Delta_0 = 0.18$ meV and calculate $\bar{\lambda}(\theta,\phi)$ at the 62 directions. After calculating $\bar{\lambda}(\theta,\phi)$ we then compute the gaps as a function of direction (θ,ϕ). The results for $\lambda(\theta,\phi)$, $\bar{\lambda}(\theta,\phi)$ and $\Delta(\theta,\phi) \equiv \Delta_0^{(1)}(\theta,\phi)$ are presented in Table 4.3.1. The variations of $\Delta(\theta,\phi)$ in the three principal planes are shown in Figure 4.2.2 whereas the similar results for the S-OPW model are shown in Figure 4.2.1. Comparison between $\lambda(\theta,\phi)$ and $\Delta(\theta,\phi)$ shows close similarities in anisotropy. The same observations made between the S-OPW calculations of $\lambda(\theta,\phi)$ and $\Delta(\theta,\phi)$ show the same trend. However, the anisotropies are seen to be larger in our calculations of λ and Δ than in the S-OPW calculations.

An average over the Fermi Surface for the quantity $\langle\bar{\lambda}(\theta,\phi)\rangle$ and the gap $\langle\Delta_0^{(1)}(\theta,\phi)\rangle$ give the values of 0.419 and 0.177 meV.

Fig. 4.2.1 The directional energy gap $\Delta_0^{(1)}(\Omega)$ for Al calculated in S-OPW approximation using corrected $\alpha_c^2 F(\nu,\Omega)$

. $\phi = 0°$

x $\phi = 22\ 1/2°$

⊙ $\phi = 45°$

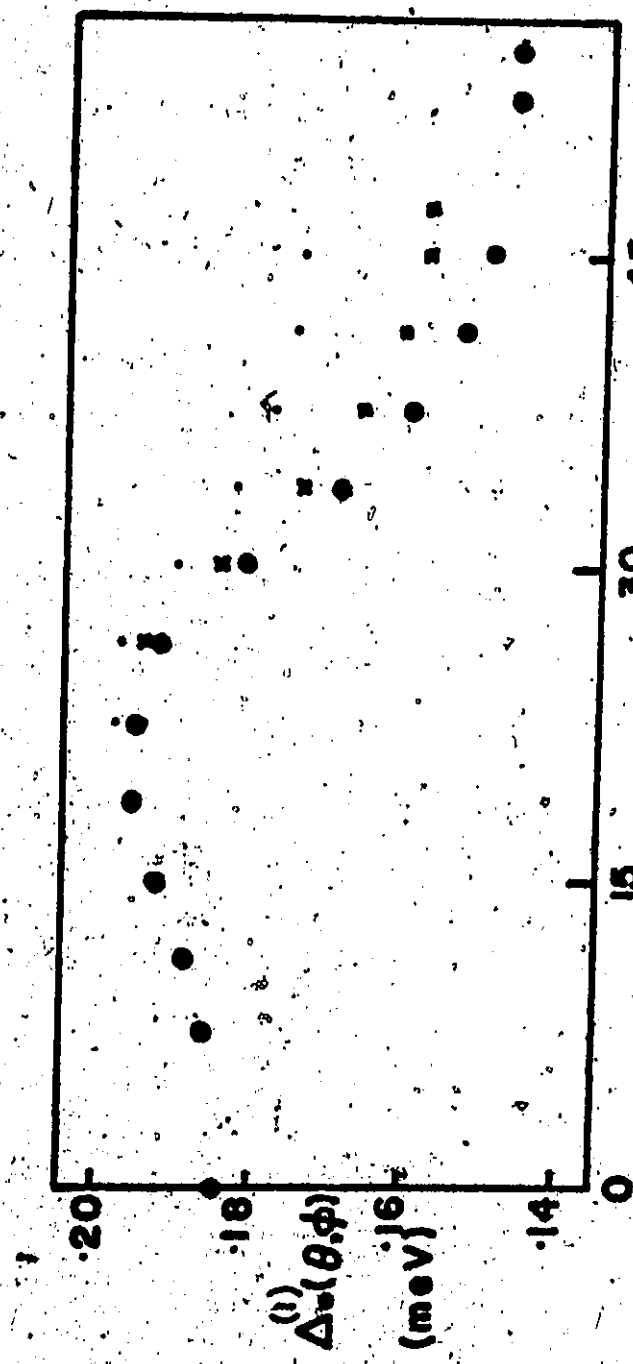
.20
.18
.16
.14
0
15
30
45
θ (degrees)
$\Delta_{\alpha}^{(1)}(\theta,\phi)$
(meV)

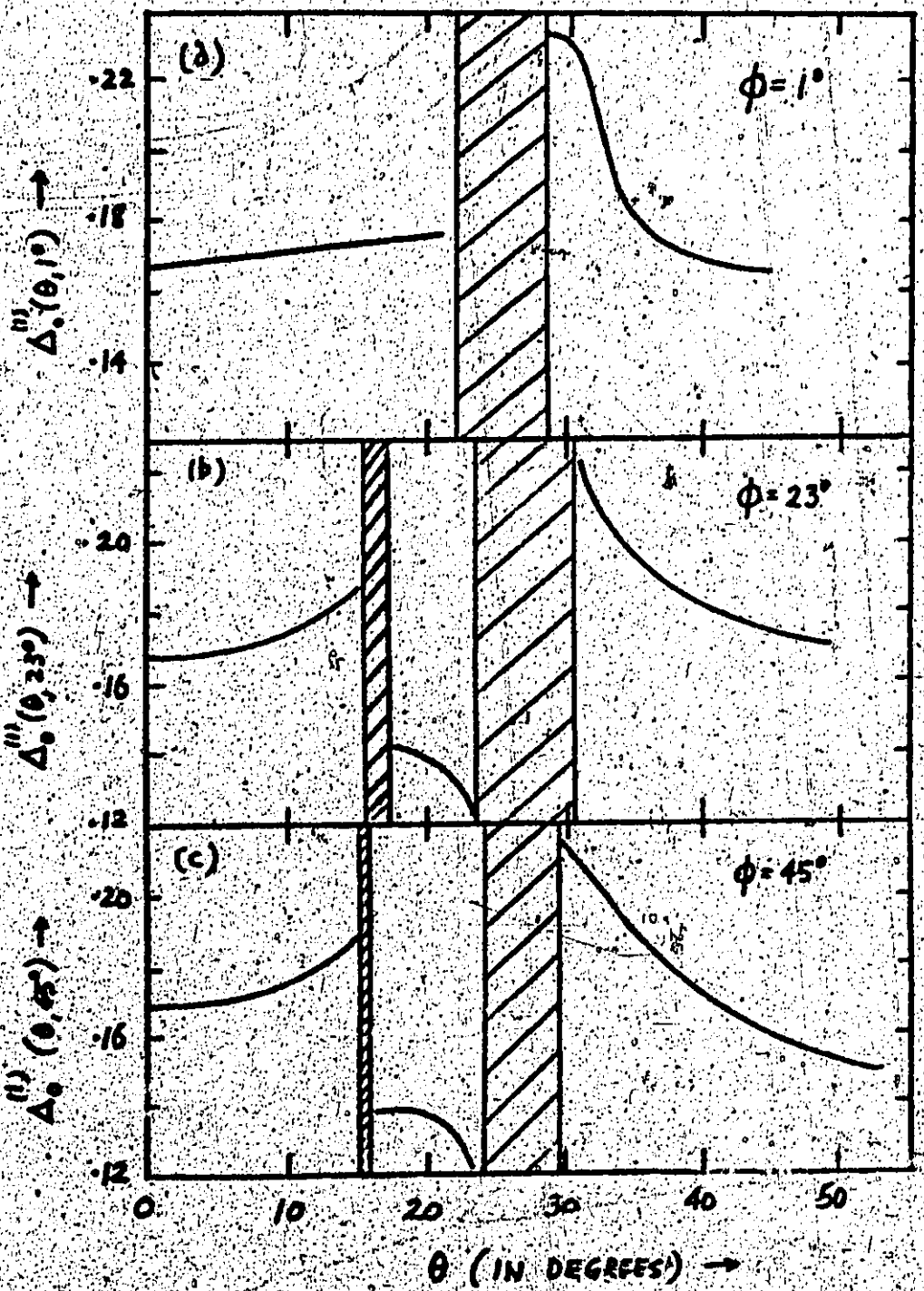
(a)
$\phi = 1°$
(b)
$\phi = 23°$
(c)
$\phi = 45°$
$\Delta_0^{(1)}(\theta, 1°)$ →
$\Delta_0^{(1)}(\theta, 23°)$ →
$\Delta_0^{(1)}(\theta, 45°)$ →
-.22
-.18
-.14
-.20
-.16
-.12
-.20
-.16
-.12
0
10
20
30
40
50
θ (IN DEGREES) →

4.3 Calculation of the Critical Temperature

Leavens and Carbotte (1972) have derived from the isotropic Eliashberg equations a simpler set of equations for a weak coupling superconductor. The (isotropic) superconducting energy gap Δ_0 in the "dirty" limit is given by,

$$\Delta_0 = 2\omega_c \exp\left(-(1+\lambda+\bar{\lambda})/(\lambda-\mu^*)\right) \qquad 4.3.1$$

where ω_c is the maximum phonon frequency, λ, $\bar{\lambda}$ are the average over the FS of $\lambda(\theta,\phi)$, $\bar{\lambda}(\theta,\phi)$ as defined in Equations 4.1.2 and 4.2.3, μ^* is given by Equation 4.2.2 and set equal to 0.13.

The superconducting gap for the pure single-crystal superconductor is higher than the isotropic gap in the "dirty" superconductor as found by experiments (Lynton et al 1957, Gayley et al 1962). We shall now calculate the pure single-crystal gap. The directional energy gaps $\Delta_0^{(1)}(\theta,\phi)$ have already been given. We first define anisotropy parameters $a_{\underline{k}}$, $b_{\underline{k}}$ and $\bar{b}_{\underline{k}}$ by the expressions

$$\Delta_0(\underline{k}) = \langle \Delta_0(\underline{k}) \rangle (1+a_{\underline{k}}) \qquad 4.3.2$$

$$\lambda(\underline{k}) = \langle \lambda(\underline{k}) \rangle (1+b_{\underline{k}}) \qquad 4.3.3(a)$$

$$\bar{\lambda}(\underline{k}) = \langle \bar{\lambda}(\underline{k}) \rangle (1+\bar{b}_{\underline{k}}) \qquad 4.3.3(b)$$

We assume following Leavens and Carbotte that the anisotropy in the first iteration results $\Delta_0^{(1)}(\theta,\phi)$ will be very nearly the same as in the complete gap $\Delta_0(\theta,\phi)$ where

$$\langle f(\underline{k}) \rangle = \int \frac{dS_{\underline{k}}}{v_{\underline{k}}} f(\underline{k}) \Big/ \int \frac{dS_{\underline{k}}}{v_{\underline{k}}} \qquad 4.3.4$$

If we now define further $\langle ab \rangle$, $\langle a\bar{b} \rangle$ and $\langle a^2 \rangle$ by

$$\langle \Delta_0(\underline{k})\lambda(\underline{k}) \rangle = \langle \Delta_0(\underline{k}) \rangle \left[1 + \langle \lambda \rangle (1 + \langle ab \rangle) \right]$$

$$\langle \bar{\lambda}(\underline{k}) \Delta_0(\underline{k}) \rangle = \langle \bar{\lambda} \rangle \langle \Delta_0 \rangle (1 + \langle a\bar{b} \rangle) \qquad 4.3.5$$

$$\langle \Delta_0^2(\underline{k}) \rangle = \langle \Delta_0(\underline{k}) \rangle (1 + \langle a^2 \rangle)$$

we can write down an expression for $\langle \Delta_0(\underline{k}) \rangle$ which was derived by Leavens and Carbotte. It is

$$\langle \Delta_0(\underline{k}) \rangle = 2\omega_c \exp\left[- \frac{1 + (1 + \frac{1}{2}\langle a^2 \rangle + 2\langle ab \rangle)\lambda + (1 + \langle ab \rangle)\bar{\lambda} - \frac{\langle a^2 \rangle \mu^*}{2}}{(1 + \langle ab \rangle)\lambda - \mu^*} \right] \qquad \ldots\ldots 4.3.6$$

We have computed the above parameters and obtain the following values: $\langle a^2 \rangle = 0.0187$, $\langle ab \rangle = 0.0145$, $\langle a\bar{b} \rangle = 0.0131$. In the S-OPW calculation, Leavens obtained $\langle a^2 \rangle = 0.0084$ and for $\langle ab \rangle$ and $\langle a\bar{b} \rangle$ 0.0081 and 0.0142 respectively. Our results give

$$\langle \Delta_0(\underline{k}) \rangle / \Delta_0 = 1.059 \qquad 4.3.7$$

whereas those of Leavens give 1.022 for the same ratio.

Leavens and Carbotte also derived a formula for the computation of the critical temperature T_c. For the pure single-crystal,

$$k_B T_c^{sfc} = 1.14\, \omega_c \exp\left[- \frac{1 + (1 + \langle ab \rangle)\lambda(T_c) + (1 + \langle a\bar{b} \rangle)\bar{\lambda}}{1 + \langle ab \rangle \lambda - \mu^*} \right]$$

and for the "dirty" sample, $\ldots\ldots 4.3.8$

$$k_B T_c = 1.14\,\omega_c \exp\left[-(1+\lambda(\tau_c)+\bar{\lambda})/(\lambda-\mu^*)\right] \qquad 4.3$$

Noting that for a weak superconductor like aluminium we can set $\lambda(T_c) = \lambda(T=0)=\lambda$ to a good approximation, we computed the above quantities and obtained,

$$T_c^{psc}/T_c = 1.091 \qquad 4.3.10$$

The S-OPW calculation yields a smaller ratio, namely 1.039 while the experimental value of Cheeke and Ducla-Soares (1968) are 1.19°K and 1.132°K for the "pure" and "dirty" samples, respectively, so that,

$$T_c^{psc}/T_c^{exp} = 1.051 \qquad 4.3.11$$

The agreement with experiment is far from exact but still satisfactory particularly since the experimental results are not so directly interpretable.

Table 4.3.1

λ, $\bar{\lambda}$ and Directional Energy Gap in Al

No. Surface 1	$\lambda(\theta,\phi)$	$\bar{\lambda}(\theta,\phi)$	$\Delta_0^{(1)}(\theta,\phi)$
1	.413	.406	.169
2	.420	.416	.172
3	.430	.435	.176
4	.421	.416	.172
5	.442	.445	.183
6	.422	.417	.173
7	.448	.449	.186
8	.423	.418	.174
9	.445	.444	.185
10	.423	.418	.174
11	.439	.439	.182

No.	$\lambda(\theta,\phi)$	$\bar{\lambda}(\theta,\phi)$	$\Delta_\theta^{(1)}(\theta,\phi)$
Surface 2			
12	.350	.370	.130
13	.366	.387	.139
14	.361	.381	.137
15	.362	.385	.137
16	.353	.378	.131
17	.369	.390	.141
18	.365	.389	.138
19	.341	.369	.124
20	.363	.381	.138
21	.371	.397	.141
22	.343	.373	.125
23	.365	.383	.139
24	.367	.395	.139
25	.340	.373	.123
Surface 3			
26	.549	.556	.233
27	.540	.543	.230
28	.467	.466	.196
29	.425	.422	.175
30	.416	.411	.170
31	.408	.404	.166
32	.539	.542	.229
33	.413	.415	.168
34	.407	.406	.165
35	.407	.403	.165
36	.356	.368	.135
37	.364	.371	.140
38	.375	.376	.147
Surface 4			
39	.540	.544	.230
40	.519	.515	.221
41	.493	.481	.210
42	.467	.448	.198
43	.524	.527	.223
44	.494	.485	.210
45	.473	.456	.201
46	.439	.416	.185
47	.436	.412	.183
48	.521	.522	.222
49	.463	.443	.196
50	.421	.393	.176

No. Surface 4 (contd.)	$\lambda(\theta,\phi)$	$\bar{\lambda}(\theta,\phi)$	$\Delta_\theta^{(1)}(\theta,\phi)$
51	.413	.384	.172
52	.501	.498	.213
53	.468	.454	.198
54	.447	.425	.189
55	.403	.372	.167
56	.392	.360	.161
57	.495	.493	.210
58	.471	.454	.200
59	.444	.421	.187
60	.399	.368	.165
61	.387	.354	.158
62	.482	.468	.205

CHAPTER V

TRANSPORT PROPERTIES IN ALUMINIUM

5.1 The Boltzmann Equation

The usual treatment of the transport properties of electrons starts from the statistical point of view in which one assumes that there exists a distribution function $f_{\underline{k}}(\underline{r})$ which measures the probability of finding an electron in a state of momentum $\underline{k}$ at position $\underline{r}$. On the application of an external field $\underline{E}$ one can look at the changes made in this function. This approach was first used by Boltzmann, and a detailed treatment can be found in Ziman (1960). The Boltzmann equation simply says that in a steady state situation, as would be the case in making physical measurements,

$$\frac{df_{\underline{k}}(\underline{r})}{dt} = 0 . \qquad 5.1.1$$

This can be written as

$$\left.\frac{\partial f_{\underline{k}}(\underline{r})}{\partial t}\right|_{drift} + \left.\frac{\partial f_{\underline{k}}(\underline{r})}{\partial t}\right|_{scatt} = 0 \qquad 5.1.2$$

where the first term refers to the drifting of electrons in phase space $(\underline{k},\underline{r})$ due to any fields present, and the second term takes into account the changes due to all the scattering mechanisms present in the system. In considering the electrons in a metal, the scattering term becomes

$$\left.\frac{\partial f_{\underline{k}}(\underline{r})}{\partial t}\right|_{scatt} = \left.\frac{\partial f_{\underline{k}}(\underline{r})}{\partial t}\right|_{phonon\ scat.} + \left.\frac{\partial f_{\underline{k}}(\underline{r})}{\partial t}\right|_{impurity} \qquad .....5.1.3$$

We shall consider the phonon scattering mechanism first and later include the effects of impurities.

For small fields we introduce the function $\Phi_{\underline{k}}$ which measures the deviation from $f^0_{\underline{k}}(\underline{r})$ (the equilibrium function),

$$f_{\underline{k}}(\underline{r}) = f^0_{\underline{k}}(\underline{r}) - \underline{\Phi}_{\underline{k}} \frac{\partial f^0_{\underline{k}}}{\partial \varepsilon_{\underline{k}}} \qquad 5.1.4$$

Using this expression and writing out the drift term, we obtain from Equation 5.1.2 the linearized Boltzmann equation,

$$-e\,\underline{v}_{\underline{k}} \cdot \underline{E}\, \frac{\partial f^0_{\underline{k}}}{\partial \varepsilon_{\underline{k}}} = -\left.\frac{\partial f_{\underline{k}}(\underline{r})}{\partial t}\right|_{scat.} \qquad 5.1.5$$

Restricting ourselves to scattering by phonons for the moment, then

$$\left.\frac{\partial f_{\underline{k}}(\underline{r})}{\partial t}\right|_{scat} = \sum_{\underline{k}'} \frac{1}{\beta}\left(\underline{\Phi}_{\underline{k}'} - \underline{\Phi}_{\underline{k}}\right) f^0_{\underline{k}}\left(1 - f^0_{\underline{k}'}\right) W^{\underline{k}'}_{\underline{k}} \qquad 5.1.6$$

where $\beta = \frac{1}{k_B T}$, k_B the Boltzmann constant, T the temperature. $W^{\underline{k}'}_{\underline{k}}$ is the probability for electron scattering from $\underline{k}$ to $\underline{k}'$ due to phonons, and it can be written as

$$W^{\underline{k}'}_{\underline{k}} = \frac{2\pi}{\hbar} \sum_{\lambda} |g_{\underline{k}\underline{k}'\lambda}|^2 \eta^0(\omega_{\underline{q}\lambda}) \left\{ \delta(\varepsilon_{\underline{k}'} - \varepsilon_{\underline{k}} - \hbar\omega_{\underline{q}\lambda}) + e^{\beta\hbar\omega_{\underline{q}\lambda}}\, \delta(\varepsilon_{\underline{k}'} - \varepsilon_{\underline{k}} + \hbar\omega_{\underline{q}\lambda}) \right\} \qquad 5.1.7$$

where $\hbar$ is the Planck's constant, $\eta^0(\omega_{\underline{q}\lambda})$ the equilibrium occupation number of phonons with frequency $\omega_{\underline{q}\lambda}$, momentum $\underline{q} = \underline{k}' - \underline{k} + \underline{G}$, and polarization λ. The δ functions express the fact that energy is conserved in the collision processes.

In the variational approach to the solution of the Boltzmann equation, the R.H.S. of Equation 5.1.6 is interpreted as an operator

acting on functions $\phi_{\underline{k}}$. The properties of this operator and the definition of a suitable inner product enables one to formulate a variational principle (Ziman 1960). The resulting formula for the electrical resistivity in which cubic symmetry, but not necessarily a spherical FS is assumed, is

$$\rho_v(T) = \frac{V \sum_{\underline{k}\underline{k}'} \frac{1}{2\beta} \left(\Phi_{\underline{k}} - \Phi_{\underline{k}'}\right)^2 f_{\underline{k}}^{\circ}\left(1 - f_{\underline{k}'}^{\circ}\right) W_{\underline{k}}^{\underline{k}'}}{\left| \sum_{\underline{k}} e \underline{v}_{\underline{k}} \Phi_{\underline{k}} \frac{\partial f_{\underline{k}}^{\circ}}{\partial \varepsilon_{\underline{k}}} \right|^2} \qquad 5.1.8$$

where V is the volume of the crystal. A usual choice for $\phi_{\underline{k}}$ that is found in most of the literature is

$$\Phi_{\underline{k}} \propto \underline{q}_{\underline{k}} \cdot \underline{u} \qquad 5.1.9$$

where $\underline{u}$ is the direction of the electric field. After some elaborate simplifications of Equation 5.1.8, we arrive at the final formulae for the resistivity

$$\rho_v(T) = \frac{\pi 2\pi^5 \hbar^2}{e^2 k_B T} \frac{\int_0^{\infty} d\omega \, R(\omega) \, \beta_{tr}^2 F(\omega)}{\left(\int_{FS} \frac{d\underline{S}_{\underline{k}}}{v_{\underline{k}}} |v_{\underline{k}}|^2 \right)^2} \qquad 5.1.10$$

Here $R(\omega)$ is a thermal factor $\hbar\omega \left(e^{k\omega\beta} - 1\right)^{-1} \left(1 - e^{-\beta\hbar\omega}\right)^{-1}$ and $\alpha_{tr}^2 F(\underline{k},\omega)$, the distribution function defined in Equation 5.1.10, is related to $\beta_{tr}^2 F(\omega)$ by,

$$\beta_{tr}^2 F(\omega) = \left(4\pi\hbar\right)^{-1} \int_{FS} \frac{d\underline{S}_{\underline{k}}}{v_{\underline{k}}} |v_{\underline{k}}|^2 \alpha_{tr}^2 F(\underline{k},\omega) \qquad 5.1.11$$

5.2 Relaxation Time Solution to the Boltzmann Equation

The formula for the resistivity given in 5.1.11 results from a variational principle which demands that all trial functions $\phi_{\underline{k}}$ give values higher than the true $\rho(T)$. Robinson and Dow (1968) (RD) pointed out, however, that strong anisotropies are observed in the electron-phonon interaction. Even in the case of the alkalis, Deutsch et al (1961) suggest that the angular variations in conduction electron relaxation times can be as large as a factor of 3. RD suggest another approximate solution to the Boltzmann equation working within the framework of a relaxation time formulation. This approach to the problem is more physical and natural. Imagine that, if the electric field is turned off, then due to the scattering with phonons, the electron system will relax back to equilibrium, i.e.

$$-\left.\frac{\partial f_{\underline{k}}}{\partial t}\right|_{scatt} = \frac{f_{\underline{k}} - f_{\underline{k}}^{\circ}}{\tau_{\underline{k}}} \qquad 5.2.1$$

where $\tau_{\underline{k}}$ is some characteristic (relaxation) time for $f_{\underline{k}}$ to reduce to the equilibrium state described by $f_{\underline{k}}^{\circ}$. Equation 5.1.6 can now be written as,

$$f_{\underline{k}} - f_{\underline{k}}^{\circ} = -\frac{\partial f_{\underline{k}}^{\circ}}{\partial \varepsilon_{\underline{k}}} e\tau_{\underline{k}} \underline{v}_{\underline{k}} \cdot \underline{E} \qquad 5.2.2$$

or

$$\Phi_{\underline{k}} = e\tau_{\underline{k}} \underline{v}_{\underline{k}} \cdot \underline{E} \qquad 5.2.3$$

In general, $\tau_{\underline{k}}$ is highly anisotropic. Substitution of 5.2.3 into Equation 5.1.7 combined with Equation 5.1.6 gives

$$\underline{v}_{\underline{k}} \cdot \underline{u} \frac{\partial f_{\underline{k}}^{\circ}}{\partial \varepsilon_{\underline{k}}} = \beta \sum_{\underline{k}'} (\tau_{\underline{k}} \cdot \underline{v}_{\underline{k}'} - \tau_{\underline{k}'} \underline{v}_{\underline{k}}) \cdot \underline{u} \, f_{\underline{k}}^{\circ} (1 - f_{\underline{k}}^{\circ}) W_{\underline{k}}^{\underline{k}'} \qquad \ldots\ldots 5.2.4$$

Using Equation 5.1.8 we integrate over $E_{\underline{k}}$, making use of the delta functions. Then, on taking the dot product of $V_{\underline{k}}$ on both sides, we obtain,

$$|V_{\underline{k}}|^2 = \frac{4\pi\beta}{\hbar}\frac{V}{8\pi^3\hbar}\sum_{\lambda}\int_0^{\infty} d\omega R(\omega)\delta(\omega-\omega_{\underline{q}\lambda})\int_{F.S.}\frac{dS_{\underline{k}'}}{v_{\underline{k}'}}|g_{\underline{k}\underline{k}'}|^2 \cdot$$

$$\left\{\tau_{\underline{k}}(v_{\underline{k}}^2 - v_{\underline{k}}\cdot v_{\underline{k}'}) + (\tau_{\underline{k}}-\tau_{\underline{k}'})\, v_{\underline{k}}\cdot v_{\underline{k}'}\right\} \qquad 5.2.5$$

Ignoring the $\tau_{\underline{k}} - \tau_{\underline{k}}$, term since it is alternatively positive and negative 48 times, we solve for $\frac{1}{\tau_{\underline{k}}}$ and obtain, using Equation 3.1.2,

$$\frac{1}{\tau_{\underline{k}}(T)} = 4\pi\beta\int_0^{\infty} d\omega\, R(\omega)\,\alpha^2_{tr}F(\underline{k},\omega) \qquad 5.2.6$$

Now using the fact that the current density is given by

$$\underline{J} = \frac{2}{V}\sum_{\underline{k}} e\, v_{\underline{k}}\cdot f_{\underline{k}} \qquad 5.2.7$$

we obtain the final result for the conductivity,

$$\sigma_{ST}(T) = \frac{1}{\rho_{ST}(T)} = \frac{e^2}{12\pi^3\hbar}\int_{F.S.}\frac{dS_{\underline{k}}}{v_{\underline{k}}}|v_{\underline{k}}|^2\,\tau_{\underline{k}}(T) \qquad 5.2.8$$

This is the relaxation time solution. One can compare Equation 5.2.8 with the formula in the variational treatment Equation 5.1.11, and remember that $\frac{1}{\tau_{\underline{k}}(T)}$ is given by 5.2.6, then if we say that the variational solution assumes the addition of partial resistivities ($\propto\frac{1}{\tau}$), the relaxation time solution adds up partial conductivities, a concept which seems to be more appealing on physical grounds.

5.3 Calculation of Phonon-Limited Resistivity of Aluminium

In Chapter III, we have evaluated the weighted distribution function

$$\alpha^2_{tr} F(\underline{k},\omega) = (8\pi^3\hbar^2)^{-1} \int_{FS} \frac{dS_{k'}}{v_{k'}} |g_{\underline{k}\underline{k}'\lambda}|^2 \left(1 - \frac{\underline{v}_k \cdot \underline{v}_{k'}}{v_k^2}\right) \delta(\omega - \omega_{\underline{k}\underline{k}'\lambda}) \quad \ldots\ldots 5.3.1$$

in 62 directions in the $(\frac{1}{48})^{th}$ zone. With the aid of these results we can now use Equation 5.2.6 to compute $\tau_{\underline{k}}(T)$ as a function of temperature between 10°K and 300°K. The results are tabulated in Table 5.3.1 for T = 20°K, 50°K and 100°K. Plots of $\tau_{\underline{k}}(T)$ to show the anisotropies are given in Figure 5.3.1 for the ϕ = 1°, 23° and 45° planes. At low temperatures, such as 20°K, the phonons are few in number and the scattering weak, hence the $\tau_{\underline{k}}(T)$ are long. On looking at Figure 5.3.1 (a) we can see the typical value of $\tau_{\underline{k}}(T)$ is of the order 10^{-10} to 10^{-12} seconds. There can be large anisotropies over a given region depending on the character of the wavefunctions. For instance, the variation over the hole surface can be as much as a factor of twenty. Nowak (1972) found in his study of the lifetimes of electrons in copper that they can vary by a factor of thirty. This shows that the character of the wavefunction can induce large anisotropies in quantities such as $\tau_{\underline{k}}(T)$. The anisotropy in the S-OPW calculations of Truant (1972) who used $\alpha^2_{tr} F(\underline{k},\omega)$, is shown in Figure 5.3.2. Large fluctuations in $\tau_{\underline{k}}(T)$ are seen at low temperatures but only over a factor of 2. This is again due to the fact that the low frequency part of $\alpha^2_{tr} F(\underline{k},\omega)$ is not treated properly. At low temperatures, the function R(ω) samples the low frequency regions

Table 5.3.1

Relaxation Times $\tau^{\oplus}(\underline{k},T)$
$\tau^{\oplus}(\underline{k},T)$ in secs

No.			
$\phi = 1°$	T = 20°K	T = 50°K	T = 100°K
1	1.65×10^{-11}	4.13×10^{-13}	7.35×10^{-14}
2	1.18×10^{-11}	3.81×10^{-13}	7.00×10^{-14}
3	4.23×10^{-12}	3.10×10^{-13}	6.77×10^{-14}
26	4.27×10^{-12}	2.79×10^{-13}	4.18×10^{-14}
27	7.99×10^{-12}	2.92×10^{-13}	4.98×10^{-14}
28	7.43×10^{-12}	3.15×10^{-13}	5.72×10^{-14}
29	8.31×10^{-12}	3.65×10^{-13}	6.49×10^{-14}
30	9.04×10^{-12}	3.87×10^{-13}	6.71×10^{-14}
31	9.17×10^{-12}	3.96×10^{-13}	6.86×10^{-14}
$\phi = 23°$	T = 20°K	T = 50°K	T = 100°K
1	1.65×10^{-11}	4.13×10^{-13}	7.35×10^{-14}
6	1.13×10^{-11}	3.78×10^{-13}	7.00×10^{-14}
7	6.03×10^{-12}	3.77×10^{-13}	6.59×10^{-14}
17	3.71×10^{-12}	3.14×10^{-13}	7.54×10^{-14}
18	3.57×10^{-12}	3.28×10^{-13}	7.85×10^{-14}
19	4.89×10^{-12}	4.17×10^{-13}	9.19×10^{-14}
48	1.30×10^{-11}	3.72×10^{-13}	5.63×10^{-14}
62	1.27×10^{-11}	4.15×10^{-13}	6.38×10^{-14}
49	2.12×10^{-11}	4.62×10^{-13}	6.71×10^{-14}
50	1.02×10^{-10}	6.26×10^{-13}	7.90×10^{-14}
51	1.43×10^{-10}	6.74×10^{-13}	8.22×10^{-14}
$\phi = 45°$	T = 20°K	T = 50°K	T = 100°K
1	1.65×10^{-11}	4.13×10^{-13}	7.35×10^{-14}
10	1.08×10^{-11}	3.88×10^{-13}	6.98×10^{-14}
11	7.61×10^{-12}	3.75×10^{-13}	6.76×10^{-14}
23	4.20×10^{-12}	3.15×10^{-13}	7.50×10^{-14}
24	3.59×10^{-12}	3.20×10^{-13}	7.69×10^{-14}
25	7.01×10^{-12}	4.50×10^{-13}	9.13×10^{-14}
57	1.31×10^{-11}	4.36×10^{-13}	6.46×10^{-14}
58	1.39×10^{-11}	4.60×10^{-13}	6.83×10^{-14}
59	2.42×10^{-11}	5.37×10^{-13}	7.45×10^{-14}
60	2.19×10^{-10}	7.72×10^{-13}	8.98×10^{-14}
61	3.34×10^{-10}	8.45×10^{-13}	9.50×10^{-14}

Fig. 5.3.1 The variation of the electrical scattering times $\tau^{e}(\underline{k},T)$ over the $(\frac{1}{48})$ zone on the FS

(a) T = 20°K

(b) T = 50°K

(c) T = 100°K

——— ϕ = 1°

-x-x- ϕ = 23°

o-o-o- ϕ = 45°

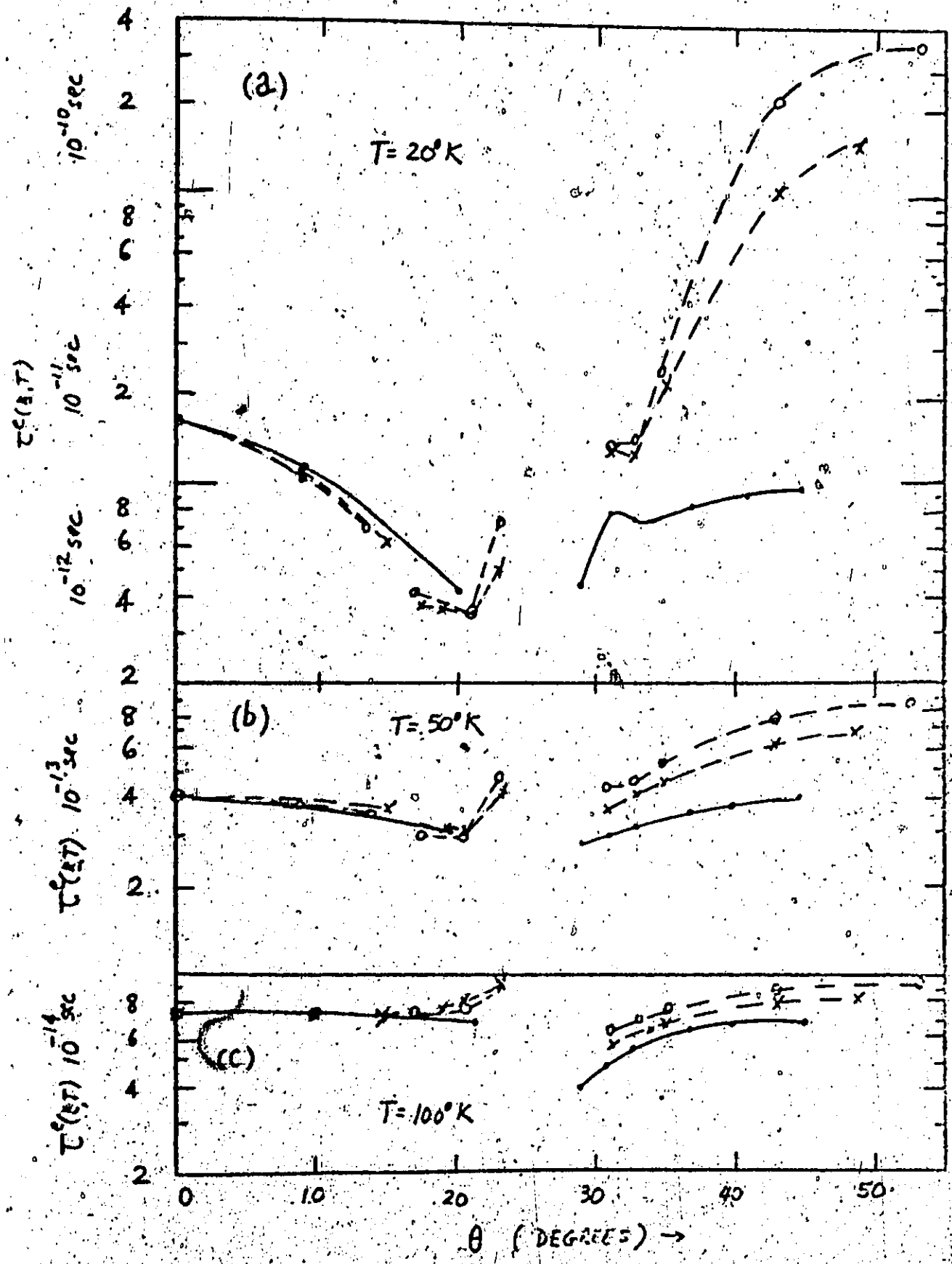
(a)
T = 20° K
(b)
T = 50° K
(c)
T = 100° K
$\tau^c(\vec{k},T)$
10^{-10} sec
10^{-11} sec
10^{-12} sec
10^{-13} sec
10^{-14} sec
0
10
20
30
40
50
θ (DEGREES) →

Fig. 5.3.2 The variation of the ratio $\tau^{e}(\theta,\phi,T)/\tau^{e}(\theta,\phi,T)$ in the S-OPW calculation (Truant 1972) over the FS in the $(\frac{1}{48})$ zone

(a) T = 30°K

(b) T = 60°K

(c) T = 120°K

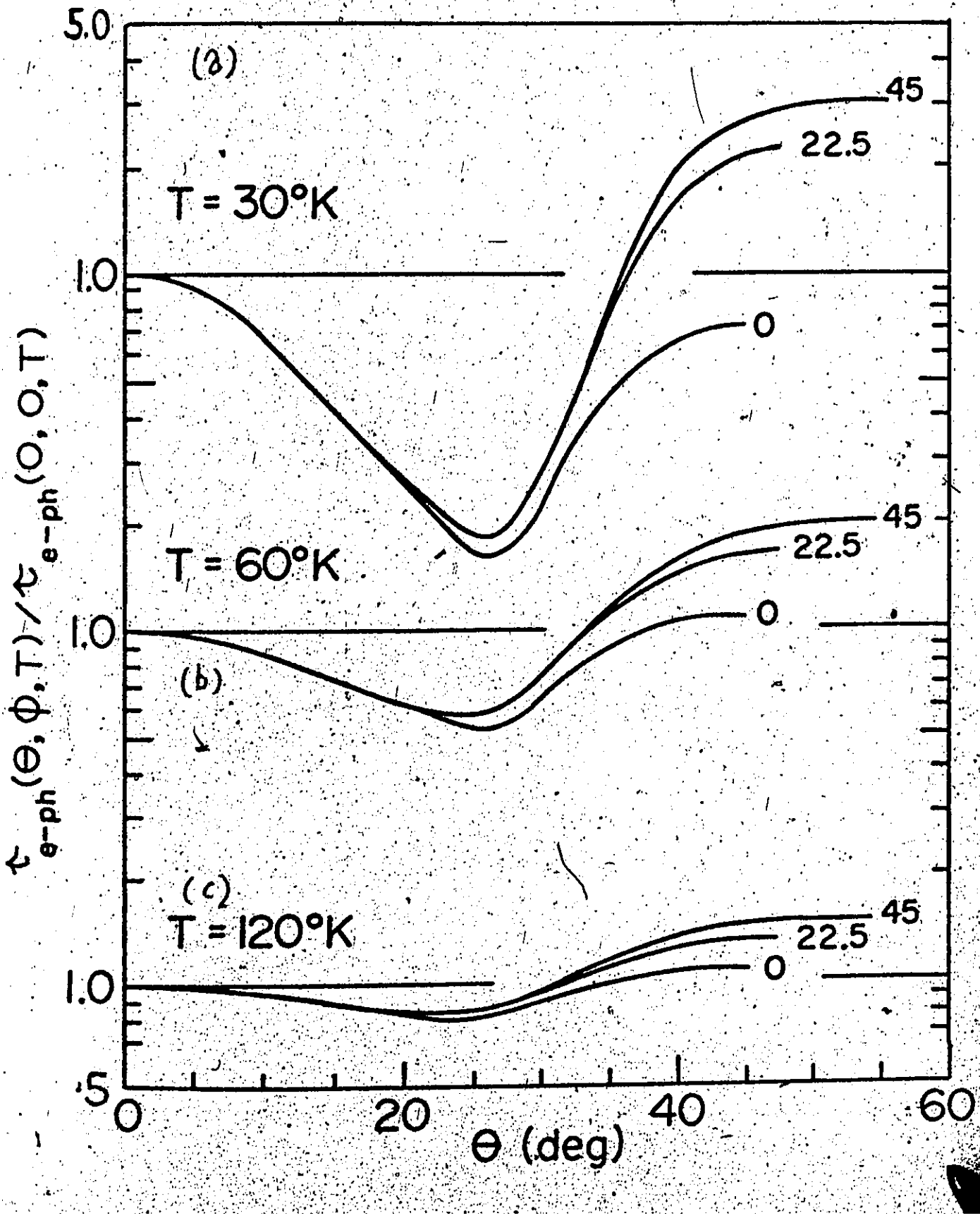
5.0
(a)
T = 30°K
45
22.5
0
1.0
T = 60°K
45
22.5
0
1.0
(b)
(c)
T = 120°K
45
22.5
0
1.0
.5
0
20
40
60
θ (deg)
$\tau_{e-ph}(\theta, \phi, T)/\tau_{e-ph}(0, 0, T)$

and the details at small ω are important. At high temperatures, both the 8-OPW and 15-OPW calculations show similar behaviour

Table 5.3.2

The Electrical Resistivity of Aluminium as a Function of Temperature

T (°K)	ρ_V(Ω-cm)	ρ_{ST}(Ω-cm)
10	1.919×10^{-6}	1.392×10^{-6}
13	5.172×10^{-6}	8.565×10^{-6}
15	8.741×10^{-6}	3.032×10^{-5}
20	2.468×10^{-3}	4.052×10^{-4}
25	5.550×10^{-3}	2.088×10^{-3}
30	1.090×10^{-2}	6.226×10^{-3}
40	3.109×10^{-2}	2.491×10^{-2}
50	6.614×10^{-2}	5.928×10^{-2}
60	1.157×10^{-1}	1.084×10^{-1}
80	2.495×10^{-1}	2.411×10^{-1}
100	4.123×10^{-1}	4.018×10^{-1}
150	8.616×10^{-1}	8.431×10^{-1}
200	1.313×10^{0}	1.285×10^{0}
300	2.185×10^{0}	2.137×10^{0}

except, of course, that there are complications due to non-sphericities of the FS in the 15-OPW calculations. This, in general, gives rise to forbidden regions and discontinuities in $\tau_{\underline{k}}(T)$. Thus, we can say that on the whole, the anisotropies calculated in a 8-OPW approximation are dominant in the high temperature region. Thus, we expect that the two approximations will give similar results in calculating $\rho(T)$ in these

regions but will diverge at low temperatures. A glance at the S-OPW result in Figure 5.3.3 compared to experiment shows that this is indeed the case. In the calculation for alkali metals, Hayman (1974) found a S-OPW is sufficient to give satisfactory agreement with experiment.

We have calculated the electrical resistivities using both the variational and relaxation time equations 5.1.11 and 5.2.8, denoted by $\rho_v(T)$ and $\rho_s(T)$ respectively. The results are presented in Table 5.3.2. Experimental data on the Aluminium resistivity are taken from Seth and Woods (1970) and Cook et al (1973) and they are plotted on Figure 5.3.3. The S-OPW variational calculations are also shown (as open circles).

The calculated resistivity in the relaxation time approximation shows a remarkable agreement with the experiment data. At $T > 80°K$, it lies slightly lower than experiment, agrees well at T less than 80°K until about 20°K and then lies below the experiment. The high temperature disagreement is typical for all the other calculations. One possible reason is that anharmonic effects come into play at higher temperatures. Secondly, it seems to be characteristic of the (HA) potential used. At low temperature less than 20°K, we note that the resistivities are extremely small in magnitude, $\rho \sim 10^{-5}$ μΩcm. Our calculations, based on a mesh of 2° x 2° for the calculation of $\alpha^2_{tr}F(\underline{k},\omega)$, might not be that reliable at very low frequencies. Secondly, the experimental sample always contains very small traces of impurities and it seems that we are in a region where it is hard to subtract out all the residual resistivities.

Fig. 5.3.3 The electrical resistivity of pure Aluminium as a function of temperature

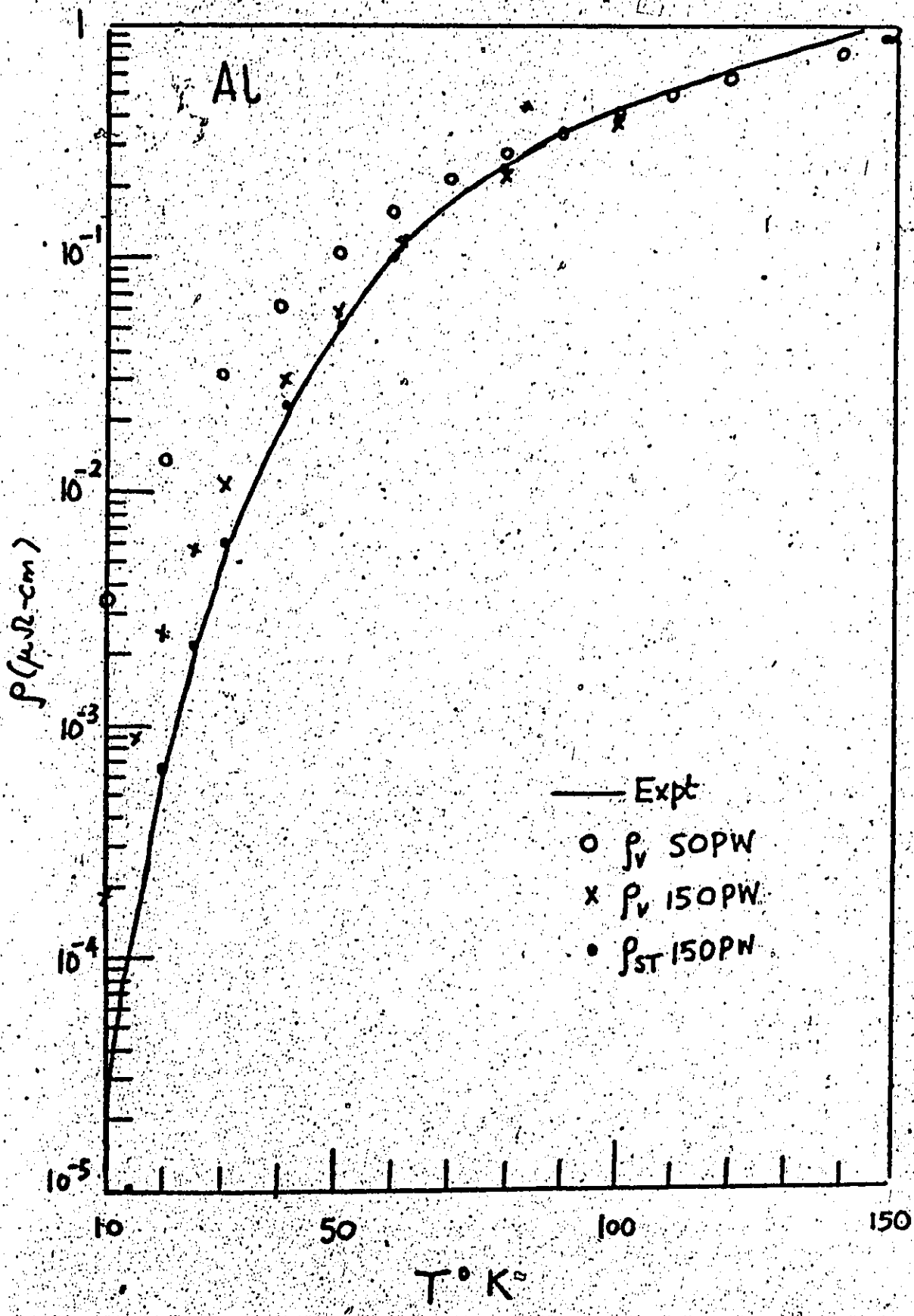
Al
1
10^{-1}
10^{-2}
10^{-3}
10^{-4}
10^{-5}
ρ(μΩ-cm)
10
50
100
150
T° K
Expt
o ρ_V 50PW
x ρ_V 150PW
• ρ_{ST} 150PW

The variational solution whose computations are based on the same set of $\alpha^2_{tr}F(\underline{k},\omega)$ functions is not in such good agreement with the experimental data. There is a tendency for the variational solution to give higher electrical resistivities than the relaxation time approach. Hayman and Carbotte (1972) have made an intensive study of the transport properties and conclude that the variational solution is always higher than the scattering time solution, if one restricts oneself to the conventional trial function (5.1.9).

5.4 The Thermoresistivity in Aluminium

In this Section, we will follow Ziman (1960) and derive the equations that are needed to calculate the thermoresistivity in Aluminium. Again, the question of impurities is neglected, and we assume the phonons are in thermodynamic equilibrium. Cubic symmetry is applied at the appropriate stages to simplify algebra. However, a non-spherical Fermi Surface and as many of the band structure effects as possible are included.

We start with the Boltzmann equation, this time a thermal gradient $\nabla T(\underline{x})$ being applied, and as the electrons are displaced, an electric field $\underline{E}$ is also set up. The equation is,

$$\underline{v}_{\underline{k}} \cdot \nabla T \cdot \left(\frac{\varepsilon_{\underline{k}} - \mu}{T} \right) \frac{\partial f_{\underline{k}}^{o}}{\partial \varepsilon_{\underline{k}}} - e \underline{v}_{\underline{k}} \cdot \underline{E} \frac{\partial f_{\underline{k}}^{o}}{\partial \varepsilon_{\underline{k}}} = - \left. \frac{\partial f_{\underline{k}}}{\partial t} \right|_{scatt} \qquad 5.4.1$$

where μ is the Fermi energy parameter. The trial solution is still assumed to be $\phi_{\underline{k}}$, where

$$f_{\underline{k}} = f_{\underline{k}}^{o} - \underline{\phi}_{\underline{k}} \frac{\partial f_{\underline{k}}^{o}}{\partial \varepsilon_{\underline{k}}} . \qquad 5.4.2$$

Ziman assumes as a first order approximation,

$$- \left. \frac{\partial f_{\underline{k}}}{\partial t} \right|_{scatt} = \frac{f_{\underline{k}} - f_{\underline{k}}^{o}}{\tau_{\underline{k}}} \qquad 5.4.3$$

and letting $\underline{E} = 0$ in 5.4.1., obtains

$$\underline{\phi}_{\underline{k}} = - \tau_{\underline{k}} \underline{v}_{\underline{k}} \cdot \nabla T \cdot \left(\frac{\varepsilon_{\underline{k}} - \mu}{T} \right) \qquad 5.4.4$$

The solution obtained is in the lowest order approximation and the derivation of the variational solution is then essentially the same as in the previous Section. The result for the thermal resistivity $W_L(T)$ is given by

$$W_L(T) = TV \sum_{\underline{k}\underline{k}'} \frac{1}{2\beta} \left(\varepsilon_{\underline{k}} - \varepsilon_{\underline{k}'}\right)^2 f^0_{\underline{k}} \left(1 - f^0_{\underline{k}'}\right) W^{\underline{k}'}_{\underline{k}} \Big/ \left| \sum_{\underline{k}} |v_{\underline{k}}| \left(\varepsilon_{\underline{k}} - \mu\right) \underline{\alpha}_{\underline{k}} \frac{\partial f^0_{\underline{k}}}{\partial \varepsilon_{\underline{k}}} \right|^2 \qquad 5.4.5$$

where the notation is the same as before.

Using Equation 5.4.4 to simplify the denominator, and the definition of $W^{\underline{k}'}_{\underline{k}}$ [Equation 5.1.7], we can rewrite Equation 5.4.5 after some straightforward but lengthy algebraic simplifications as

$$W_L(T) = \left(\mathcal{L}_0 T\right)^{-1} \left(\frac{4\pi}{\beta}\right)\left(\frac{48\pi^4 k^2}{e^2}\right) \cdot \frac{\int_0^\infty d\omega\, R(\omega)\, \bar{Z}(\omega)}{\int_{F.S.} \frac{d\underline{S}_{\underline{k}}}{v_{\underline{k}}} |v_{\underline{k}}|^2} \qquad 5.4.6$$

where $\mathcal{L}_0 = \frac{\pi^2 k_B^2}{3e^2}$ is the Lorentz ratio,

$$\bar{Z}(\omega) = \left[1 - \frac{1}{2\pi^2}\left(\frac{\hbar\omega}{\beta}\right)^2\right] \beta^2_{tr} F(\omega) + \frac{3}{2\pi^2}\left(\frac{\hbar\omega}{\beta}\right)^2 \beta^2 F(\omega) \qquad 5.4.7$$

and

$$\beta^2_{tr} F(\omega) = \left(4\pi k\right)^{-1} \int_{F.S.} \frac{d\underline{S}_{\underline{k}}}{v_{\underline{k}}} |v_{\underline{k}}|^2 \alpha^2_{tr} F(\underline{k}, \omega) \qquad 5.4.8$$

$$\beta^2 F(\omega) = \left(4\pi k\right)^{-1} \int_{F.S.} \frac{d\underline{S}_{\underline{k}}}{v_{\underline{k}}} |v_{\underline{k}}|^2 \alpha^2 F(\underline{k}, \omega) \qquad 5.4.9$$

The denominator has been obtained using cubic symmetry,

$$\int_{F.S.} \frac{d\underline{S}_{\underline{k}}}{v_{\underline{k}}} \int_{F.S.} \frac{d\underline{S}_{\underline{k}'}}{v_{\underline{k}'}} |v_{\underline{k}}|^2 |v_{\underline{k}'}|^2 \cos^2\left(\underline{v}_{\underline{k}} \cdot \underline{v}_{\underline{k}'}\right) = \frac{1}{3}\left(\int_{F.S.} \frac{d\underline{S}_{\underline{k}}}{v_{\underline{k}}} |v_{\underline{k}}|^2\right)^2 \qquad 5.4.10$$

To obtain the analogous solution in the relaxation time formulation, we start with Equation 5.4.3 to characterize $\phi_{\underline{k}}$ by $\tau_{\underline{k}}$. Equation 5.4.1 is solved by putting $\underline{E} \neq 0$, this being the experimental setup. Following the procedure of the previous section, we perform similar algebraic manipulations which lead to a final result for $W_L(T)$.

$$\frac{1}{W_L(T)} = \alpha_0^2 T \frac{\theta^2}{12\pi^3\hbar} \int_{F.S.} \frac{dS_k}{v_k} |v_k|^2 \tau_{\underline{k}}^{th}(T) \qquad 5.4.11$$

where $W_L(T)$ is the thermal resistivity, τ^{th} is the thermal scattering time given by

$$\left[\tau_{\underline{k}}^{th}(T)\right]^{-1} = \frac{4\pi}{\beta} \int_0^{2\omega} d\omega\, R(\omega)\, Z(\omega) \qquad 5.4.12$$

As seen from Equation 5.4.12, the thermal scattering time involves not just the $\alpha_{tr}^2 F(\underline{k},\omega)$ function but also the $\alpha^2 F(\underline{k},\omega)$. The $\alpha^2 F(\underline{k},\omega)$ functions are positively definite while $\alpha_{tr}^2 F(\underline{k},\omega)$ may have negative regions, (refer to Figure 3.3.6). We have computed the thermal scattering times as a function of temperature between 10°K and 300°K. These are tabulated in Table 5.4.1. In Figure 5.4.1 we plot them along the principal planes defined by ϕ = 1°, 23° and 45° at the temperatures 20°K, 50°K and 100°K. The anisotropies are similar to those in the electrical scattering times $\tau(\underline{k},T)$. The anisotropies at low temperatures, say 20°K, are not as large as that in $\tau(\underline{k},T)$, varying by a factor of 4. At high temperatures the anisotropies are again washed out. It is worth noting that the order of magnitude of $\tau^{th}(\underline{k},T)$ at high temperatures is of the same order of magnitude (10^{-14}sec) as $\tau(\underline{k},T)$ but at low temperature they are smaller (10^{-12}sec), compared to $\tau(\underline{k},T)$ (10^{-10}sec – 10^{-12}sec). This is mainly due to the extra factors in 5.4.12 which are related to the slightly more complicated trial wavefunctions defined in Equation 5.4.4. It states that $\phi_{\underline{k}}$ depends not only on $\tau_{\underline{k}} v_{\underline{k}}$ but also on the ratio of available

energy of the electron to the temperature, namely the factor $(\epsilon_k - \epsilon_F)/T$. Once the thermal scattering times $\tau^{th}(\underline{k},T)$ are computed, then it is a straightforward matter to compute the thermal resistivities in accordance with the variational solution for $w_L(T)(=\rho_V{}^{th})$, Equation 5.4.6, and the relaxation (scattering) time solution for $w_L(T)(=\rho_{SC}{}^{th})$, Equation 5.4.11. The results are listed in Table 5.4.2. Experimental results obtained from Cook et al (unpublished) are tabulated in the third column. In Figure 5.4.2 we present these results on semi-log graphs. The variational solution again is found to lie above the scattering time solution at low temperatures while above 50°K they are almost identical. Compared to experiment, they lie above the experimental data at low temperatures and then below, crossing at T ~ 120°K. The discrepancies are quite large and only qualitative agreement is obtained. From their study on the alkali metals, Hayman and Carbotte (1972) found similar discrepancies. It is believed that the discrepancies arise because of the crudeness of the trial wavefunction $\phi_{\underline{k}}$ which is used in the solution of the Boltzmann equation. More complicated trial wavefunctions have been suggested by several authors, particularly by Ekin (1973). Calculations using more complicated forms of the trial wavefunctions were not done here. Discussions on contributions to the thermal resistivities at high temperatures (> 300°K) in terms of normal and Umklapp processes can be found in Trofimenkoff and Ekin (1971) on Potassium and Laubitz and Cook (1972) on Al and Pb. The interested reader is asked to refer to their work.

Table 5.4.1

Relaxation Times $\tau^{th}(\underline{k},T)$ in secs

No. $\phi = 1°$	T = 20°K	T = 50°K	T = 100°K
1	3.31×10^{-12}	1.34×10^{-13}	3.37×10^{-14}
2	2.89×10^{-12}	1.29×10^{-13}	3.28×10^{-14}
3	2.03×10^{-12}	1.18×10^{-13}	3.13×10^{-14}
26	1.61×10^{-12}	1.02×10^{-13}	2.47×10^{-14}
27	2.07×10^{-12}	1.03×10^{-13}	2.49×10^{-14}
28	2.51×10^{-12}	1.16×10^{-13}	2.83×10^{-14}
29	2.84×10^{-12}	1.30×10^{-13}	3.15×10^{-14}
30	3.12×10^{-12}	1.35×10^{-13}	3.23×10^{-14}
31	3.12×10^{-12}	1.37×10^{-13}	3.29×10^{-14}
$\phi = 23°$	T = 20°K	T = 50°K	T = 100°K
1	3.31×10^{-12}	1.34×10^{-13}	3.37×10^{-14}
6	2.85×10^{-12}	1.29×10^{-13}	3.27×10^{-14}
7	2.26×10^{-12}	1.20×10^{-13}	3.06×10^{-14}
17	1.69×10^{-12}	1.30×10^{-13}	3.65×10^{-14}
18	1.57×10^{-12}	1.33×10^{-13}	3.76×10^{-14}
19	1.58×10^{-12}	1.50×10^{-13}	4.25×10^{-14}
48	2.25×10^{-12}	1.14×10^{-13}	2.70×10^{-14}
62	3.09×10^{-12}	1.16×10^{-13}	2.66×10^{-14}
49	3.96×10^{-12}	1.32×10^{-13}	3.02×10^{-14}
50	6.39×10^{-12}	1.55×10^{-13}	3.38×10^{-14}
51	6.87×10^{-12}	1.60×10^{-13}	3.47×10^{-14}
$\phi = 45°$	T = 20°K	T = 50°K	T = 100°K
1	3.31×10^{-12}	1.34×10^{-13}	3.37×10^{-14}
10	2.80×10^{-12}	1.28×10^{-13}	3.26×10^{-14}
11	2.52×10^{-12}	1.27×10^{-13}	3.15×10^{-14}
23	1.84×10^{-12}	1.31×10^{-13}	3.66×10^{-14}
24	1.55×10^{-12}	1.31×10^{-13}	3.72×10^{-14}
25	1.66×10^{-12}	1.53×10^{-13}	4.35×10^{-14}
57	2.26×10^{-12}	1.25×10^{-13}	2.93×10^{-14}
58	3.10×10^{-12}	1.31×10^{-13}	3.04×10^{-14}
59	4.28×10^{-12}	1.43×10^{-13}	3.23×10^{-14}
60	7.57×10^{-12}	1.71×10^{-13}	3.66×10^{-14}
61	8.22×10^{-12}	1.79×10^{-13}	3.82×10^{-14}

Fig. 5.4.1 The variation of the thermal scattering time τ^{th} of electronic states on the FS as a function of θ in the $(\frac{1}{48})$ zone

(a) T = 20°K

(b) T = 50°K

(c) T = 100°K

—— ϕ = 1°

-x-x- ϕ = 23°

-o-o- ϕ = 45°

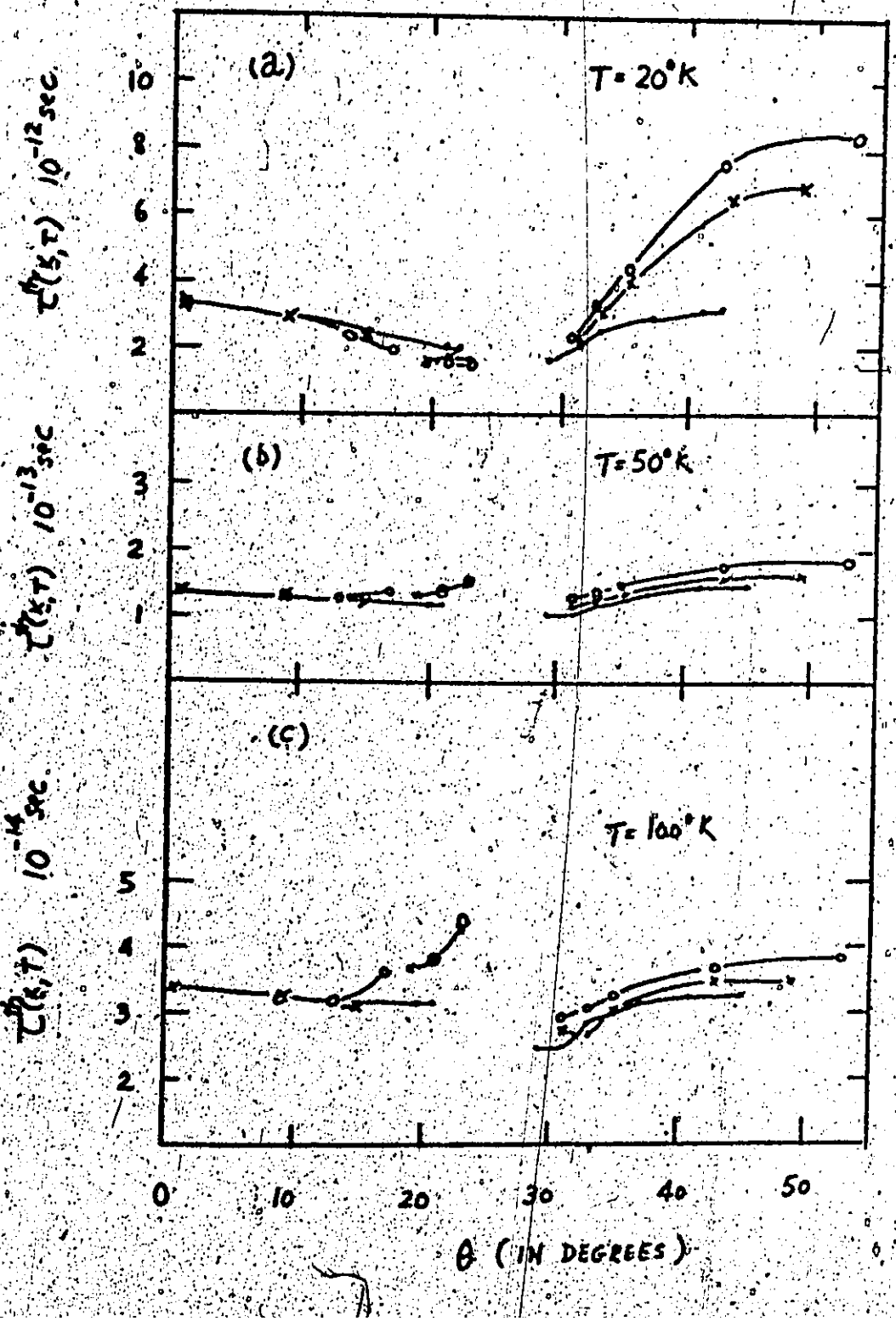
(a)
T = 20°K
(b)
T = 50°K
(c)
T = 100°K
$\tau^{(0)}(k,T)$ 10^{-12} sec
$\tau^{(0)}(k,T)$ 10^{-13} sec
$\tau^{(0)}(k,T)$ 10^{-14} sec
θ (IN DEGREES)

Table 5.4.2

Thermal Resistivity of Al

T(°K)	ρ_V^{th} m deg/watt	ρ_{ST}^{th} m deg/watt	ρ_{exp}^{th} (Cook et al) m deg/watt
10	3.85×10^{-4}	2.47×10^{-4}	-
15	9.37×10^{-5}	6.36×10^{-5}	-
20	1.84×10^{-4}	1.39×10^{-4}	6.94×10^{-5}
30	5.30×10^{-4}	4.83×10^{-4}	1.88×10^{-4}
40	1.09×10^{-3}	1.05×10^{-3}	4.71×10^{-4}
50	1.75×10^{-3}	1.72×10^{-3}	0.92×10^{-3}
80	3.27×10^{-3}	3.23×10^{-3}	2.51×10^{-3}
100	3.71×10^{-3}	3.66×10^{-3}	3.36×10^{-3}
120	3.87×10^{-3}	3.82×10^{-3}	3.83×10^{-3}
150	3.88×10^{-3}	3.82×10^{-3}	4.11×10^{-3}
200	3.75×10^{-3}	3.68×10^{-3}	4.23×10^{-3}
250	3.62×10^{-3}	3.55×10^{-3}	4.23×10^{-3}
300	3.53×10^{-3}	3.46×10^{-3}	4.23×10^{-3}
350	3.46×10^{-3}	3.39×10^{-3}	-

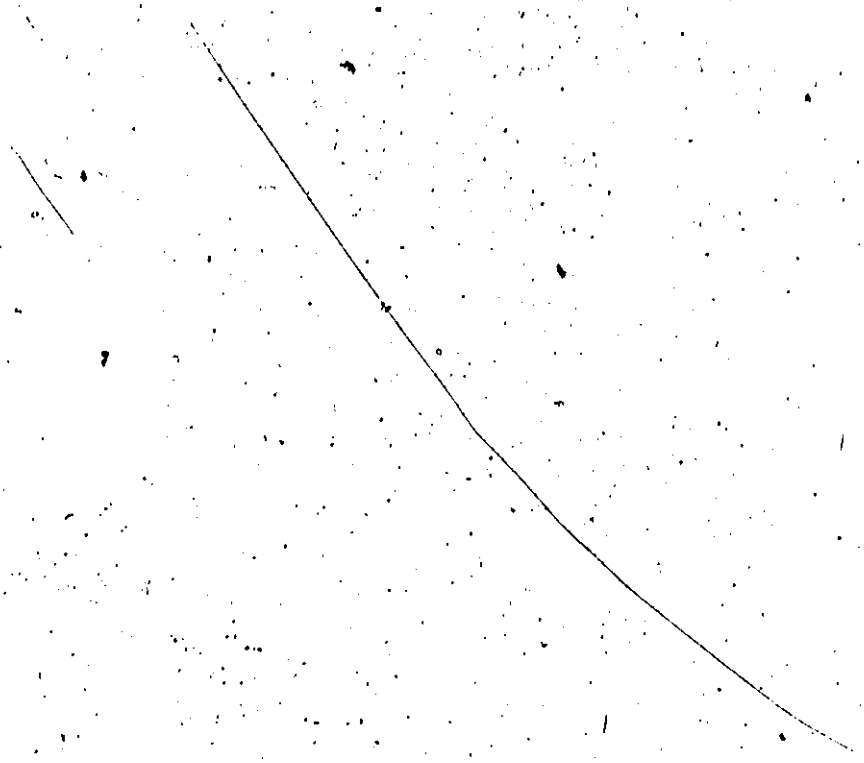

Fig. 5.4.2 The Thermal Resistivity of pure Aluminium as a function of temperature

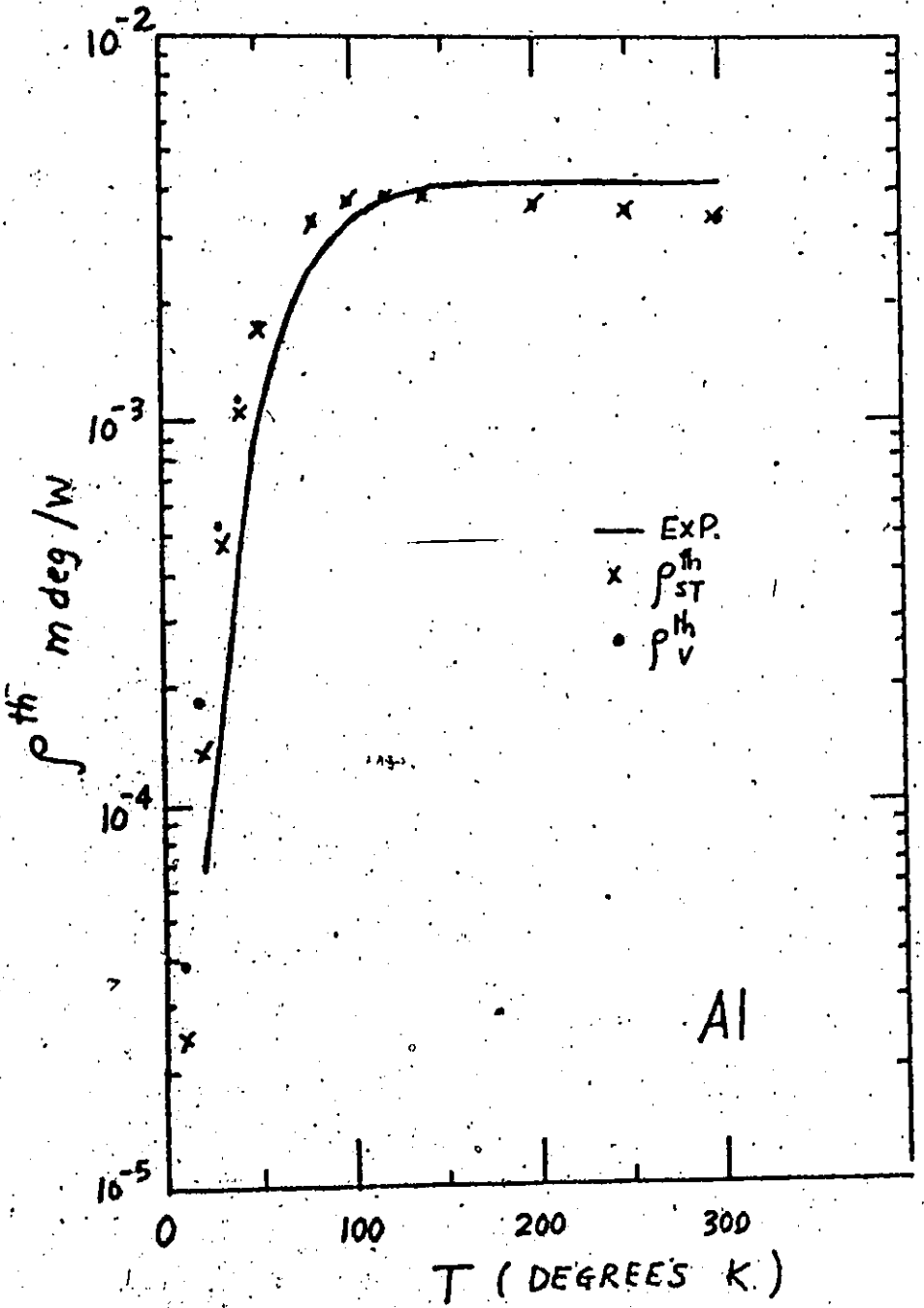
10^{-2}
10^{-3}
10^{-4}
10^{-5}
ρ^{th} m deg /W
EXP.
ρ_{ST}^{th}
ρ_{V}^{th}
Al
0
100
200
300
T (DEGREES K.)

5.5 The Hall Coefficient

(a) The phenomenon

While investigating the nature of the force acting on a conductor carrying a current in a magnetic field, Hall (1879) observed that when a magnetic field is applied at right angles to the direction of flow an electric field is set up in a direction perpendicular to both the direction of the current and magnetic field (see Figure 5.5.1 below).

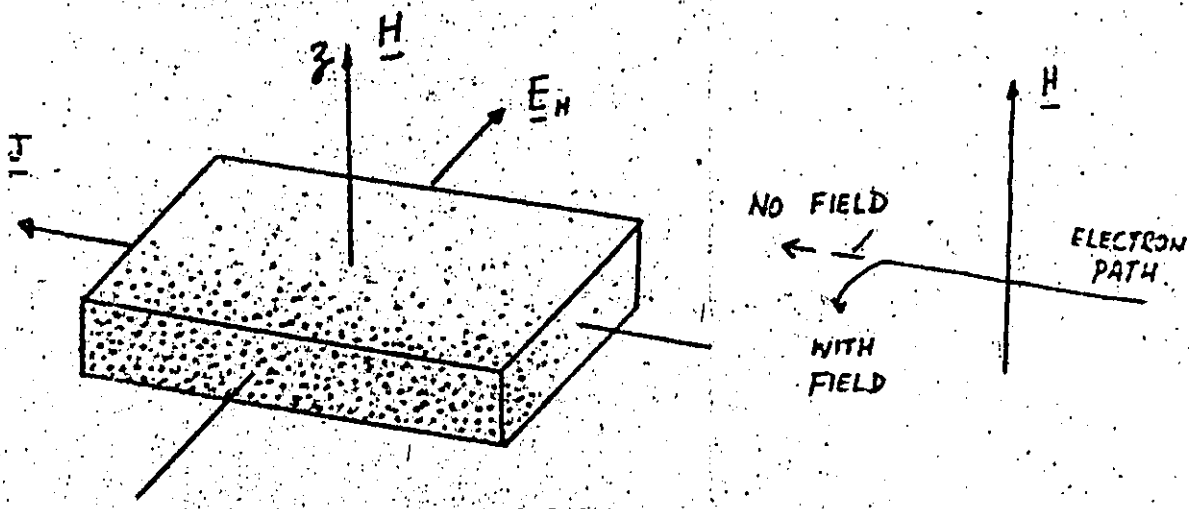

Fig. 5.5.1

This field gives rise to the induced Hall voltage. A simple view of the Hall field can be found in Kittel (1967). A semi-classical treatment of the electron dynamics states that an electron of energy $\varepsilon_{\underline{k}}$ on the FS, moving with velocity $\underline{v}_{\underline{k}}$ in a magnetic field, experiences a Lorentz force $\underline{F}$, where

$$\underline{F} = \underline{v}_{\underline{k}} \times \underline{H} \qquad 5.5.1$$

We can then write down the equation of motion which is

$$\underline{F} = \frac{d\underline{P}_k}{dt} \qquad 5.5.2$$

where $\underline{P}_k$ is the momentum of the electron. Combining these two equations we easily see that the motion of the electron in $\underline{P}$ space is perpendicular to $\underline{H}$ and the instantaneous change $d\underline{P}$ is also perpendicular to $V_{\underline{k}}$. Since the energy of the electron $E_{\underline{k}}$ is not changed, the electron moves on the FS, and the orbit which it traces out is known as a cyclotron orbit. In the absence of collisions, the electron makes a complete circuit in period,

$$T_c = \frac{2\pi}{\omega_c} = \frac{c\hbar}{eH}\oint_{orbit}\frac{dk}{v_\perp} \qquad 5.5.3$$

where ω_c is known as the cyclotron frequency. $V_\perp$ is the component of $V_{\underline{k}}$ in the plane normal to $\underline{H}$ at the point $\underline{k}$. It can easily be shown that for closed orbits in p space enclosing area A,

$$\omega_c = \frac{2\pi}{T_c} = \frac{eH}{m^*_c c} \qquad 5.5.4$$

where $m^*_c = \frac{\hbar^2}{2\pi}\frac{\delta A}{\delta E}$ is the cyclotron mass. 5.5.5

A study of cyclotron resonance then gives information about the dimensions of the FS of a metal.

In the free electron model, one can show (derived in the next section) that the ratio of the Hall field to the product of the current and the magnitude of the field, R_H, is a constant,

$$R_H = \frac{E_H}{JH} = \frac{1}{nec} \qquad 5.5.6$$

where R_H is known as the Hall coefficient, E_H the Hall field, J the electron current and n is the number density of free charge carriers

(see Kittel, 1967, for a simple derivation).

The interesting fact that R_H depends on e explicitly means that this coefficient gives information on the nature of the charge carriers, positive for hole carriers and negative for electron carriers.

With the definition of the cyclotron frequency ω_c in Equation 5.5.4, Chambers (1960) found it convenient to classify the various conditions of magnetic influence into five main categories. We are mainly interested in those conditions where the influence of the anisotropies of both the FS and the scattering times $\tau(\underline{k},T)$ manifest themselves. This is the so-called low (magnetic) field region in which the condition $\omega_c\tau << 1$ is satisfied. Under these circumstances, the scattering lifetime of the electron is short enough that it only sees the local topologies of the FS. This is in contrast to the high field condition $\omega_c\tau > 1$, in which case the electron moves fast enough to complete a cyclotron orbit on the FS. This gives information about the connectedness of the FS. The low field limit can also be achieved experimentally by making measurements at high temperatures or doping with impurities so that τ, accordingly, becomes shorter.

(b) Hall coefficient in the low field limit

In this section, we shall describe the Hall coefficient under the low field condition. Our study of the Hall coefficient will bring out useful information on the effects of anisotropies in the scattering times and the relative importance of impurity scattering. We shall follow the approach given in Hurd (1972) very closely to derive the expression for the Hall coefficient. The theory is simply the following.

The Boltzmann equation for isothermal conditions with applied electric and magnetic fields $\underline{E}$ and $\underline{H}$ can be written

$$\frac{e}{\hbar}\left[\underline{E} + \underline{v} \times \underline{H}\right] \cdot \nabla_{\underline{k}} f_{\underline{k}} = -\frac{f_{\underline{k}} - f_{\underline{k}}^{\circ}}{\tau_{\underline{k}}} \qquad 5.5.7$$

where $\tau(\underline{k})$ is the relaxation time. Letting $f_{\underline{k}} - f_{\underline{k}}^{\circ} = g_{\underline{k}}(\underline{v})$ be the deviation function in Equation 5.5.7, and simplifying by neglecting terms containing both $\underline{E}$ and $g(\underline{v})$, gives

$$\left(1 + \tilde{Q}\right) g_{\underline{k}}(\underline{v}) = \frac{-\tau_{\underline{k}} e \underline{E} \cdot \nabla_{\underline{k}} \varepsilon_{\underline{k}}}{\hbar} \frac{\partial f_{\underline{k}}^{\circ}}{\partial \varepsilon_{\underline{k}}} \qquad 5.5.8$$

where

$$\tilde{Q} = \frac{e \tau_{\underline{k}}}{c \hbar^2}\left(\nabla_{\underline{k}} \varepsilon_{\underline{k}} \times \underline{H} \cdot \nabla_{\underline{k}}\right) \qquad 5.5.9$$

In the case of small $\underline{H}$, Equation 5.5.8 can be solved in an iterative manner for $g_{\underline{k}}(\underline{v})$, where the zeroth term is

$$g_{\underline{k}}^{\circ}(\underline{v}) = -\frac{\tau_{\underline{k}} e \underline{E} \cdot \nabla_{\underline{k}} \varepsilon_{\underline{k}}}{\hbar} \frac{\partial f_{\underline{k}}^{\circ}}{\partial \varepsilon_{\underline{k}}} \qquad 5.5.10$$

and n^{th} term $\quad g_{\underline{k}}^{n}(v) = \tilde{Q}^{n} g_{\underline{k}}^{\circ}(\underline{v}) \qquad 5.5.11$

If we substitute Equations 5.5.10 and 5.5.11 into the current density

$$\underline{J} = \frac{e}{4\pi^3} \int_{Ef.} \underline{v}_{\underline{k}} f_{\underline{k}} \, d^3\underline{k} \qquad 5.5.12$$

and only retain the terms linear in $\underline{E}$ and quadratic in $\underline{H}$, we can identify the coefficients with the usual galvano-magnetic properties. For cubic symmetry using the same geometry as in Figure 5.5.1, that is, $\underline{J} = (J_x, 0, 0)$, $\underline{H} = (0, 0, H_z)$, $\underline{E} = (E_x, E_y 0)$, we arrive at the set of equations,

$$\sigma_0 = -\frac{e^2}{4\pi^3\hbar^2}\int_{F.S.} \tau^e_{\underline{k}}\left(\frac{\partial\varepsilon_\kappa}{\partial k_x}\right)^2\left(\frac{\partial f^\circ_\kappa}{\partial\varepsilon_\kappa}\right)d^3\underline{k} \qquad 5.5.13$$

$$R_H = \frac{\sigma_H}{\sigma_0^2} \qquad 5.5.14$$

where

$$\sigma_H = -\frac{e^3}{4\pi^3 c\hbar^4}\int_{F.S.}\left\{[\tau^e_{\underline{k}}]^2\left[\left(\frac{\partial\varepsilon_\kappa}{\partial k_x}\right)^2\frac{\partial^2\varepsilon_\kappa}{\partial k_y^2} - \frac{\partial\varepsilon_\kappa}{\partial k_x}\frac{\partial\varepsilon_\kappa}{\partial k_y}\frac{\partial^2\varepsilon_\kappa}{\partial k_y\partial k_x}\right]\right.$$

$$\left. + \tau^e_{\underline{k}}\left[\left(\frac{\partial\varepsilon_\kappa}{\partial k_x}\right)^2\frac{\partial\varepsilon_\kappa}{\partial k_y}\frac{\partial\tau^e_\kappa}{\partial k_y} - \frac{\partial\varepsilon_\kappa}{\partial k_x}\left(\frac{\partial\varepsilon_\kappa}{\partial k_y}\right)^2\frac{\partial\tau^e_\kappa}{\partial k_x}\right]\right\}\left(\frac{\partial f^\circ_{\underline{k}}}{\partial\varepsilon_{\underline{k}}}\right)d^3k \qquad .....5.5.15$$

and σ_0 is just the expression given in Equation 5.2.8 for the conductivity.

From Equation 5.5.15, it is evident that the anisotropy in $\tau(\underline{k})$ plays a dominant role in the behaviour of the Hall coeffient. If $\tau(\underline{k}) \equiv \tau$ is isotropic, then the value of R_H is independent of the magnitude of τ. In this case, R_H is a function only of the topology of the FS,

$$R_H = -\frac{4\pi^3}{ec}\,\frac{\int_{FS}\left\{\left(\frac{\partial\varepsilon_\kappa}{\partial k_x}\right)^2\frac{\partial^2\varepsilon_\kappa}{\partial k_y^2} - \frac{\partial\varepsilon_\kappa}{\partial k_x}\frac{\partial\varepsilon_\kappa}{\partial k_y}\frac{\partial^2\varepsilon_\kappa}{\partial k_x\partial k_y}\right\}\frac{\partial f^\circ_\kappa}{\partial\varepsilon_\kappa}d^3\underline{k}}{\left[\int_{F.S.}\left(\frac{\partial\varepsilon_\kappa}{\partial k_x}\right)^2\frac{\partial f^\circ_\kappa}{\partial\varepsilon_\kappa}d^3k\right]^2} \qquad .....5.5.16$$

This is the form used by Cooper and Raimes (1959).

In the more general case, in accord to Ziman (1961a), for a crystal with cubic symmetry, the second term in Equation 5.5.15, when integrated will vanish and R_H is given by

$$R_H = \frac{36\pi^3}{\pi ec}\,\frac{\int_{F.S.}[\tau^e_{\underline{k}}]^2\left[\left(\frac{\partial\varepsilon_\kappa}{\partial k_x}\right)^2\frac{\partial^2\varepsilon_\kappa}{\partial k_y^2} - \frac{\partial\varepsilon_\kappa}{\partial k_x}\frac{\partial\varepsilon_\kappa}{\partial k_y}\frac{\partial^2\varepsilon_\kappa}{\partial k_x\partial k_y}\right]\frac{dS_\kappa}{v_\kappa}}{\left(\int_{F.S.}\tau^e_{\underline{k}}\,v_\kappa\,dS_\kappa\right)^2} \qquad .....5.5.17$$

This expression can be related to $(\overline{\frac{1}{\rho}})$ the mean value of the curvature of the FS at point $\underline{k}$ through the relationship found by Tsuji (1958), and R_H then becomes

$$R_H = \frac{12\pi^3}{ec} \frac{\int_{F.S.} \tau_{\underline{k}}^2 v_{\underline{k}}^3 \left(\overline{\frac{1}{\rho}}\right) \frac{dS_{\underline{k}}}{v_{\underline{k}}}}{\left(\int_{F.S.} \tau_{\underline{k}}^e v_{\underline{k}}^2 \frac{dS_{\underline{k}}}{v_{\underline{k}}}\right)^2} \qquad 5.5.18$$

Dugdale and Firth (1969a, 1969b) used Equation 5.5.18 as the starting point in their study of the Hall coefficient in dilute alloys of Copper and Silver. They recognized the fact that $\tau(\underline{k})$ of the electrons has strong anisotropies over the Fermi Surface and attempted to study the variation of R_H in terms of a two band model. In their model they assign average times τ_B, τ_N as parameters for the belly and neck regions as well as approximate values of $(\overline{\frac{1}{\rho}})$ for each region to study R_H.

For the free electron model R_H can easily be calculated. We use Equation 5.5.18 and assume $\tau(\underline{k})$ is isotropic over the FS. Letting

$$\frac{1}{\rho} = k_F^{-1}, \quad v_{\underline{k}} = \frac{\hbar k}{m}$$

$$R_{f.e.} = \frac{12\pi^3}{ce} \frac{\int_{F.S.} \frac{\hbar^2 k}{2m} dS_{\underline{k}}}{\left(\int_{F.S.} \frac{\hbar k}{m} dS_{\underline{k}}\right)^2} = \frac{3\pi^2}{e k_F^3} \qquad 5.5.19$$

which, for Aluminium, where $k_F = 1.127(\frac{2\pi}{a})$ and $a = 4.04$ Å gives $R_{fl.} = -3.43 \times 10^{-11}$ m³/A-sec

(c) Calculations and results

The electron-phonon scattering times $\tau(\underline{k})$ over the $(\frac{1}{48})$ zone of the FS have been calculated for the temperature range 10°K to

300°K previously in Section 5.3. Rather than using the approximate Equation 5.5.18 involving the average of the curvatures $(\frac{1}{\rho})$ (Dugdale and Firth, 1969a,b), we realized that it is more convenient and fundamental to use Equation 5.5.16 in which the integrand contains the second derivatives of energy vs. $\underline{k}$ on the FS. However, in order to do the integral in Equation 5.5.16 over the $(\frac{1}{48})$ zone, we need to symmetrize its integrand according to the 48 symmetry operations. The result is then

$$R_H = \frac{36\pi^3}{\hbar e c} \times \beta \int_{(\frac{1}{48})^{th}} [\tau_k]^2 Q'(\epsilon_{\underline{k}}, \underline{k}) \frac{dS_{\underline{k}}}{v_{\underline{k}}} \Big/ \left(\int_{(\frac{1}{48})^{th}} \tau_{\underline{k}} v_{\underline{k}} dS_{\underline{k}} \right)^2 \qquad 5.5.20$$

where

$$Q'(\epsilon_{\underline{k}}, \underline{k}) = \left[\left(\frac{\partial^2 \epsilon}{\partial k_x^2} + \frac{\partial^2 \epsilon}{\partial k_y^2} + \frac{\partial^2 \epsilon}{\partial k_z^2} \right) \left\{ \left(\frac{\partial \epsilon}{\partial k_x} \right)^2 + \left(\frac{\partial \epsilon}{\partial k_y} \right)^2 + \left(\frac{\partial \epsilon}{\partial k_z} \right)^2 \right\} \right.$$

$$\left. - \sum_{\substack{xyz \\ \text{cyclic}}} \frac{\partial \epsilon}{\partial k_x} \left(\frac{\partial \epsilon}{\partial k_x} \frac{\partial^2 \epsilon}{\partial k_x^2} + \frac{\partial \epsilon}{\partial k_y} \frac{\partial^2 \epsilon}{\partial k_x \partial k_y} + \frac{\partial \epsilon}{\partial k_z} \frac{\partial \epsilon}{\partial k_x} \right) \right] \qquad 5.5.21$$

$Q^1(\epsilon_{\underline{k}}, \underline{k})$ is quite a sensitive function over the FS, since it depends on the second derivative of $\epsilon_{\underline{k}}$ with respect to $\underline{k}$. We first used a value of $\Delta\underline{k} = 0.1 \frac{2\pi}{a}$ to evaluate 5.5.21 and then decreased Δk until $Q^1(\epsilon_{\underline{k}}, \underline{k})$ converged. The final value of $\Delta k = .001 \frac{2\pi}{a}$ is used in the following. A fine mesh consisting of 53 latitudes and 45 longitudes each 1° apart is then used to calculate the values of $Q^1(\epsilon_{\underline{k}}, \underline{k})$ over the $(\frac{1}{48})$ zone.

Table 5.5.1

Computed Values of Q_k at 62 Points in $\frac{1}{48}$ Zone

S_1 No.	Q_k (10^{-3} C.U.)	S_2	Q_k (10^{-3} C.U.)
1	9.737	24	9.499
2	9.093	25	7.923
3	-54.085		
4	12.033	S_3	
5	-55.976	26	2.619
6	11.770	27	-15.470
7	-41.62	28	3.046
8	6.636	29	8.741
9	- 3.281	30	9.099
10	5.776	31	6.740
11	- 9.342	32	3.985
S_2		33	14.015
12	.9701	34	17.845
13	5.606	35	19.313
14	7.326	36	19.313
15	8.034	37	18.392
16	8.526	38	18.392
17	17.473		
18	13.397	S_4	
19	14.327	39	-13.736
20	24.801	40	- 8.756
21	19.063	41	- 7.493
22	14.971	42	- 1.724
23	11.828	43	-13.371
S_4			
44	- 9.231	53	-13.854
45	11.548	54	14.813
46	43.572	55	67.488
47	6.476	56	34.538
48	-39.244	57	-19.853
49	14.652	58	- 6.956
50	56.686	59	7.421
51	15.592	60	47.876
52	-39.832	61	25.835
		62	-13.939

They are finally weighted with appropriate weight factors $l_{\underline{k}} \frac{dS_{\underline{k}}}{V_{\underline{k}}}$. The final results for $Q_{\underline{k}} = l_{\underline{k}} Q^1(\epsilon_{\underline{k}},\underline{k}) \frac{dS_{\underline{k}}}{V_{\underline{k}}/V_0}$ (in C.U.) are presented in tabular form over the FS in the $(\frac{1}{48})^{th}$ zone in Table 5.5.1. On examining Table 5.5.1 and referring to the Fermi Surface (Table 3.2.1 and Figure 3.2.1) it is evident that $Q_{\underline{k}}$ is negative along the regions where the hole surface meets the Bragg planes defined by (002) and (111). On first sight, since $Q_{\underline{k}}$ is related to the curvature on the FS, then from Figure 2.2.2, one might conclude that all the regions on the Fermi Surface touching the zone boundaries should contribute a negative value to $Q_{\underline{k}}$. However, this is not so, due to the following two considerations.

(i) From Equations 5.5.16 and 5.5.1, it can be seen that $Q_{\underline{k}}$ involves the average curvature. The arms of the electron surface have negative curvature in one cross-section but positive curvature in the perpendicular plane. Hence the total average curvature might turn out to be non-negative.

(ii) $Q_{\underline{k}}$ is the contribution of the average curvatures from all the equivalent points with respect to $\underline{k}$ on the FS. Since the second derivatives are quite directionally dependent, $Q_{\underline{k}}$ gives an overall curvature effect.

We calculated the Hall coefficient for a pure sample of Aluminium by using the scattering times $\tau(\underline{k},T)$ from Section 5.3 in Equation 5.5.20. The results are tabulated in Table 5.5.2(a). Figure 5.5.2 shows the variation of R_H as a function of temperature. The values of R_H are negative at all temperatures. It is very negative at low temperature and possesses a local minimum of -22.75 at 15°K. It rises rapidly with temperature and saturates at about 80°K, and at very high temperatures (300°K), it has a value of -3.76. The experimental value at

room temperature is - 3.51 (Schenz and Koch et al, 1967, Powell and Evans, 1943). Comparing this value to what we obtained, we see that within our numerical accuracy this value is quite consistent. Of course, the result from a free electron model gives - 3.43 (see Equation 5.5.19) which is a coincidence.

To see the effects of the curvatures of the FS on R_H we used the values of $Q_{\underline{k}}$ from the 15-OPW calculation but used Equation 5.5.18 with the curvature $\frac{1}{\rho} = \frac{1}{k_F}$ (free electron value). The result is tabulated in the last column of Table 5.5.2 and plotted as -·- in Figure 5.5.2. At once we see that the effect of the curvatures at the Bragg planes is to make R_H less negative. For example, at high temperatures (300°K), the curvature increases R_H from - 4.72 to - 3.76. The dip at the low temperature is typical of the behaviour of R_H, especially for a pure metal. In the alkali metals, a similar behaviour was found by Alderson and Farrell (1969) and explained by Hayman (1973), using a calculation similar to this one. The large dip of R_H at low temperatures can be looked upon as a reflection of the effects of the large anisotropies which exist in $\tau(\underline{k})$ at low temperatures. In the case of the alkali metals, it is a measure of the ratio of $\langle\tau\rangle^2$ and $\langle\tau^2\rangle$. Referring to Section 5.3, one will be convinced that the low temperature $\tau_{\underline{k}}$ have much more anisotropy than the high temperature $\tau_{\underline{k}}$. Moreover, that the curves hardly differ at low temperatures, indicates the FS curvature effects are masked by the phonon scattering time anisotropies. At high temperatures where the scattering times are more isotropic then we see that the curvature brings up the value of R_H.

A quick calculation of R_H using Equation 5.5.20 letting $\tau_{\underline{k}}$ = constant shows the importance of the effect of the curvature of the FS. We obtained the value of $R_H = -2.38$. This implies that the positive curvatures (which give a negative value of R_H) dominate over the negative curvatures (as found at the Bragg planes on the hole surface). Moreover, since the value of R_H is - 3.76 (- 3.51 experimentally), it means that the difference in R_H (- 1.38) is a measure of the anisotropies of the scattering times $\tau(\underline{k})$ at 300K which is not negligible.

(d) Effect of isotropic impurity scattering

The addition of impurities can be treated in a very simple manner. In Equation 5.5.6, if we assume that there are two types of collisions, phonons and impurities, then,

$$\left.\frac{\partial f_{\underline{k}}^{\circ}}{\partial t}\right|_{scat.} = -\frac{f_{\underline{k}}-f_{\underline{k}}^{\circ}}{\tau_{\underline{k}}^{P}} - \frac{f_{\underline{k}}-f_{\underline{k}}^{\circ}}{\tau_{\underline{k}}^{R}} \qquad 5.5.22$$

where $\tau_{\underline{k}}^{P}$, $\tau_{\underline{k}}^{R}$ are the phonon and impurity scattering relaxation times for state $\underline{k}$. This will replace the R.H.S. of Equation 5.5.6. It is evident that from the structure of Equation 5.5.22, we can take into account the effect of impurity scattering by defining an overall scattering time $\tau_{\underline{k}}$ through,

$$\frac{1}{\tau_{\underline{k}}} = \frac{1}{\tau_{\underline{k}}^{P}} + \frac{1}{\tau_{\underline{k}}^{R}} \qquad 5.5.23$$

Furthermore, if $\tau_{\underline{k}}^{R}$ can be assumed to be isotropic over the FS, then the relation between the residual resistivity ρ_R and $\tau_{\underline{k}}$ is simply given by ($\rho_{\underline{k}}^{P} = 0$ at $T = 0$),

$$\rho_R = \sigma_R^{-1} = \frac{e^2}{12\pi^3\hbar}\int_{F.S.}\frac{dS_{\underline{k}}}{v_{\underline{k}}}\tau_{\underline{k}}v_{\underline{k}}^2 \qquad 5.5.24$$

Hence, τ^R can easily be determined once ρ_R is known.

If we include various impurities into the calculation of R_H, assuming Equation 5.5.24 (isotropic $\tau_{\underline{k}}^R$), then we find that while the high temperature part of R_H is not essentially changed, a small concentration of impurities will make the low temperature part of R_H less negative. In Figure 5.5.2, we show the effect of including two concentrations of impurities equivalent to ρ_R = .0007 μΩ-cm and ρ_R = 0.015 μΩ-cm. It can be seen that the huge minimum at 20°K in the pure sample is reduced drastically by the addition of a small concentration of impurities. For ρ_R = .0007 μΩ-cm, it is reduced to - 8.0, and is reduced further to - 4.0 by an impurity concentration equivalent to ρ_R = 0.015 μΩ-cm. The temperature at which the minimum occurs also shifts to higher temperatures: ~ 25°K for ρ_R = 0.0007 μΩ-cm and ~ 40°K for ρ_R = 0.015 μΩ-cm. This shift in temperature can be easily explained by noticing that for the two impure samples τ_0^R = 4.24 x 10^{-11} sec. and 1.97 x 10^{-12} sec. The average phonon scattering time for pure Aluminium having a comparable value of 10^{-11} sec. occurs at about 15° - 20°K and 10^{-12} sec. at 30° - 35°K. The scattering mechanism is dominated by impurities at low temperatures and the broad hump indicates the competition between the phonon scattering and the impurity scattering. As the impurity scattering is isotropically treated here, the more isotropic the overall $\tau_{\underline{k}}$ is, the smaller the minimum. This can be seen by comparing the curves in Figure 5.5.2.

Fig. 5.5.2 Calculated R_H as a function of temperature with isotropic impurity scattering

(a) —— pure Aluminium $\rho_R = 0$

.... $\rho_R = .0007$ μΩ-cm

--- $\rho_R = .015$ μΩ-cm

-·-·-· pure Aluminium, $\rho_R = 0$, letting $\left(\frac{T}{\rho}\right) = \frac{1}{k_T}$

ISOTROPIC IMPURITY SCATTERING

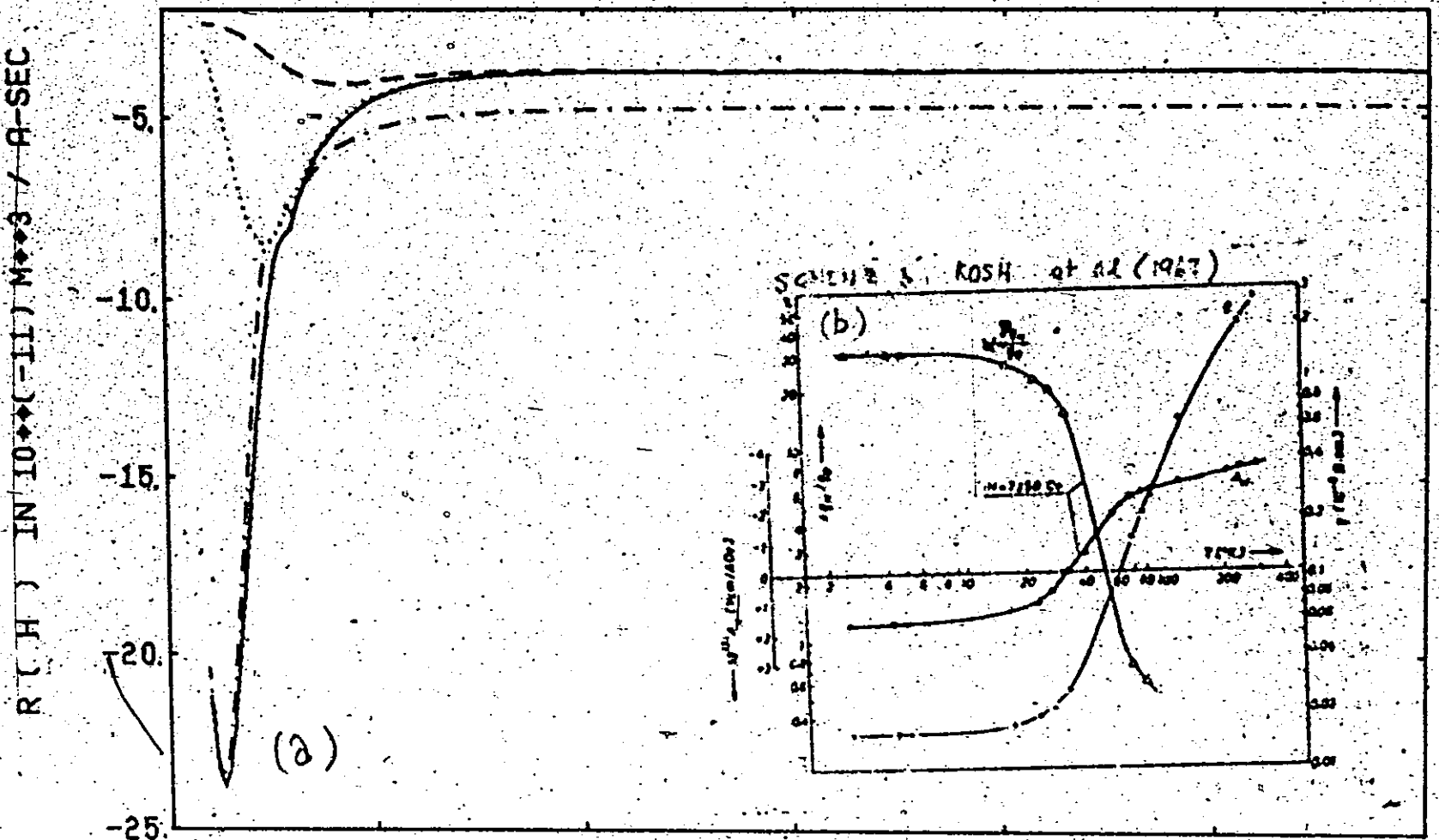

Table 5.5.2

R_H Low Field Hall Coefficient of Aluminium as a Function of Temperature (10^{-11} M^3/A-sec)

T	(a) $\tau^R=0$ ideally pure	(b) $\tau^R=4.24\times10^{-11}$ sec $\rho_o = .0007\,\mu\Omega$-cm	(c) $\tau^R=1.97\times10^{-12}$ $\rho_o = .015\,\mu\Omega$-cm	(d) $\tau^R=0$ pure, $(\frac{1}{\rho}) = \frac{1}{k_F^o}$
10	- 21.22	- 3.16	- 2.39	- 2.04
15	- 22.73	- 5.29	- 2.50	- 2.22
20	- 15.94	- 7.65	- 2.78	- 1.42
30	- 8.19	- 7.34	- 3.63	- 7.72
40	- 5.50	- 5.37	- 4.04	- 5.94
50	- 4.51	- 4.47	- 3.98	- 5.31
60	- 4.09	- 4.08	- 3.86	- 5.04
80	- 3.82	- 3.82	- 3.73	- 4.84
100	- 3.75	- 3.75	- 3.71	- 4.77
150	- 3.75	- 3.74	- 3.72	- 4.73
200	- 3.75	- 3.75	- 3.73	- 4.72
300	- 3.76	- 3.76	- 3.75	- 4.72

(e) Effect of anisotropic impurity scattering times on R_H

Experimental data on the Hall coefficient in the low field limit can best be found in Schenz and Kosh et al (1967). Other references can be obtained from Hurd (1972). The experimental data of Schenz and Kosh et al shows that the behaviour of R_H as a function of temperature is radically different from the plots obtained in Figure 5.5.2. At high temperatures R_H is negative and about - 3.5 but as the temperature is decreased, R_H increases and becomes positive crossing the axis at about

30°K. We have reproduced the graph of Schenz and Koch et al in Figure 5.5.2. Note that R_H is labelled as A_H and the scale for positive R_H is directed downwards. We note that the sample being used had a residual resistivity ρ_R of about .015 $\mu\Omega$-cm, which is the second impure sample used in the previous Section. But R_H in our model calculation always remains negative at all temperatures. The discrepancy does not lie in $\tau^P(\underline{k})$, the phonon-scattering times. Thus, perhaps then the assumption that $\tau^R(\underline{k})$ is isotropic, might be an oversimplification. We next investigate the possible anisotropies in $\tau^R(\underline{k})$ from a strictly phenomenological point of view.

In the study of the transport properties of dilute Cu and Ag alloys, Dugdale and Firth (1969a,b) used a so-called two band model. The crudeness of their model lies in the fact they did not have very good electron-phonon scattering times over the FS, together with the fact that a lot of basic quantities like $(\frac{1}{\rho})$, $V_{\underline{k}}$ and $dS_{\underline{k}}$ were not computed with great accuracy. These inadequacies make their work less useful. They have only two regions to parametrize, namely, the neck and belly regions of the FS. Here we are faced with two bands. In order not to leave out any reasonable physical possibilities in our consideration, we choose three important but plausible cases, utilizing only two scattering time parameters. But since ρ_R is determined by impurities scattering alone at very low temperatures, these two parameters reduced to a single parameter. The three cases are (suppressing the index R on the scattering times):

(i) $p = \frac{\tau_h}{\tau_e}$ where τ_h, τ_e are the average impurity scattering times

for the hole and electron surfaces. This model then corresponds to a similar one employed by Datars and Douglas (1973b) except that they have not separated out the phonon and impurity scattering times.

(ii) $q = \frac{\tau_B}{\tau_{HB}}$ where the use of τ_B and τ_{HB} assumes that scattering on the FS is different near the Bragg planes compared with far away from the Bragg planes.

(iii) $s = \frac{\tau_B}{\tau_{HB}}$ where τ_B represents the average scattering time of the FS regions near the Bragg plane but on the hole surface only, and τ_{HB} represents the rest of the FS. The physical argument for this model is that we know that the symmetries of the wavefunctions varies with relation to the $\underline{G}_n$ reciprocal lattice vectors. Moreover, they are different in different zones. As seen in the calculation of $\lambda_{\underline{k}}$ and $\delta_g^{(\rho)}(\underline{k})$, the same physical quantities can vary by an appreciable amount when crossing the Bragg plane into another zone. This is believed to be caused by the different characters in the wavefunctions.

We carried out the calculations for the three models, taking ρ_R to be .015 μΩ-cm. Figure 5.5.3 shows the results for p = 2, 1.5, 1.0 (isotropic), and 0.8. It is obvious that all the curves are negative in sign at low T and for larger values of p, R_H is more positive. Within this range of p we do not find that R_H becomes positive. Figure 5.5.4 shows the result for q = 3, 2.2, 2.0 and 0.8. We see that now for q larger than a value of 2.0, R_H can be positive. The crossing of the

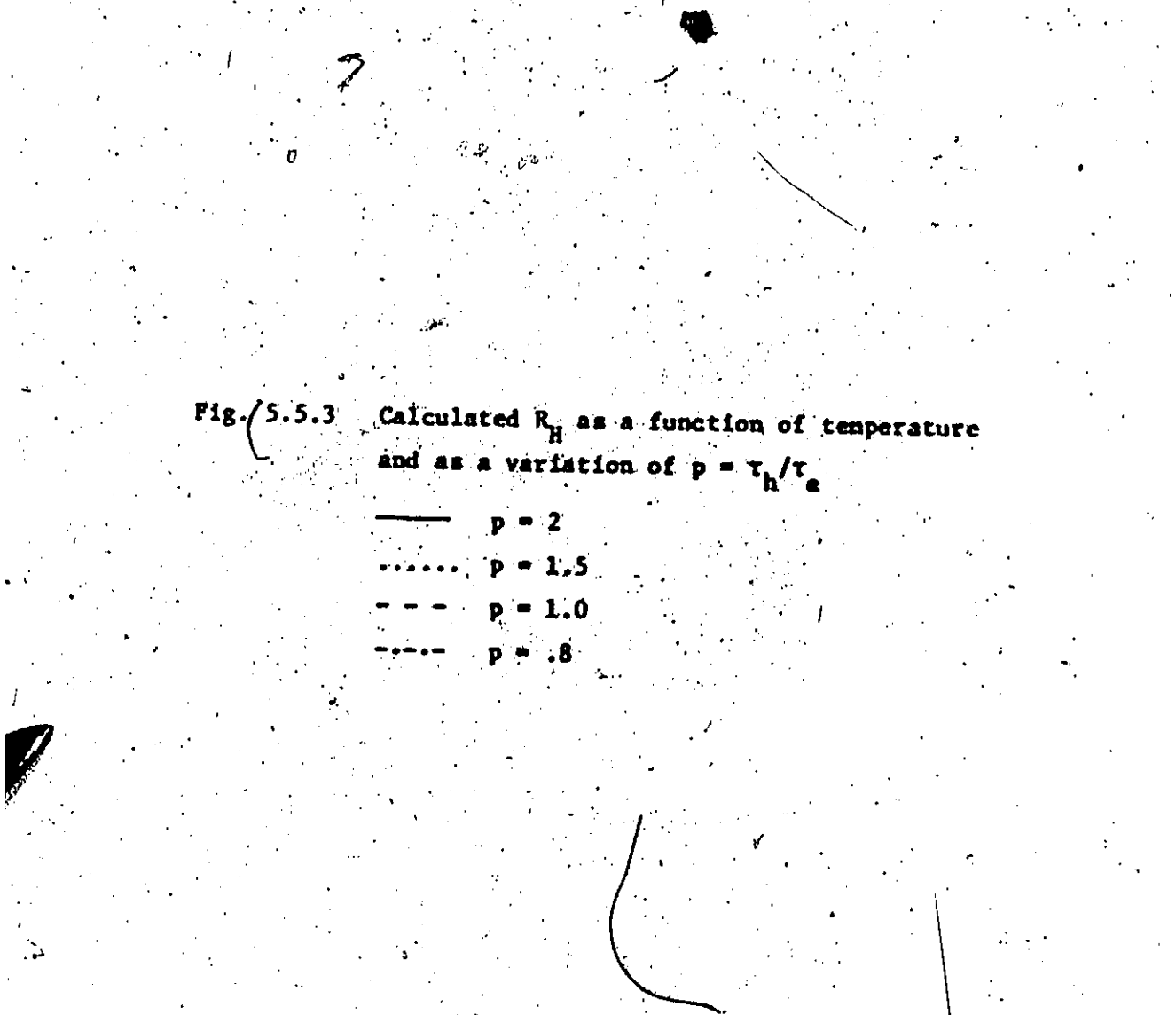

Fig. 5.5.3 Calculated R_H as a function of temperature and as a variation of $p = \tau_h/\tau_e$

——— p = 2
..... p = 1.5
- - - p = 1.0
-.-.- p = .8

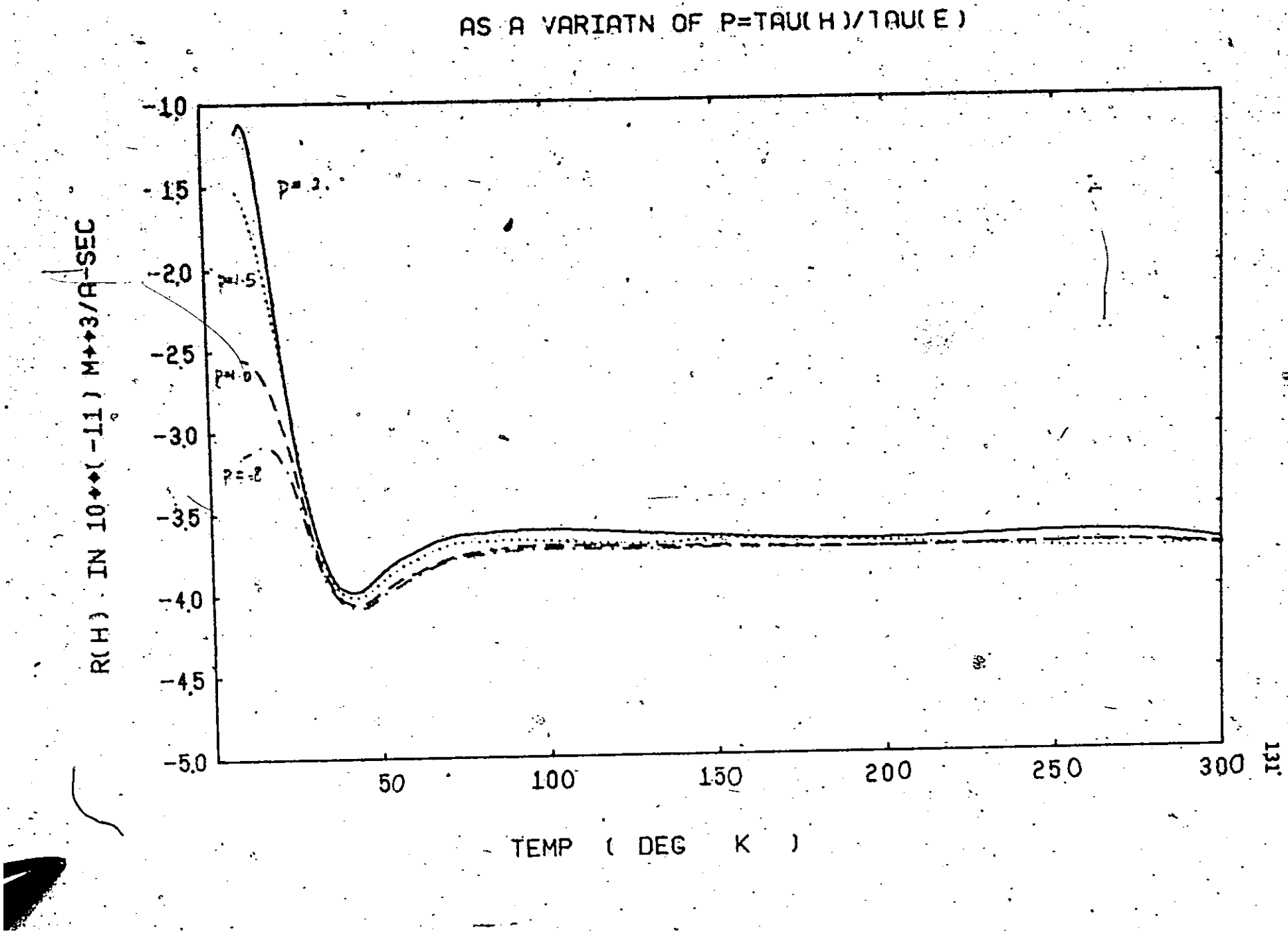
AS A VARIATN OF P=TAU(H)/TAU(E)
R(H) IN 10**(-11) M**3/A-SEC
-1.0
-1.5
-2.0
-2.5
-3.0
-3.5
-4.0
-4.5
-5.0
P= 3.
P=1.5
P= 0
P=-2
50
100
150
200
250
300
TEMP (DEG K)

Fig. 5.5.4 Calculated R_H as a function of temperature and as a variation of $q = \tau_B/\tau_{NB}$

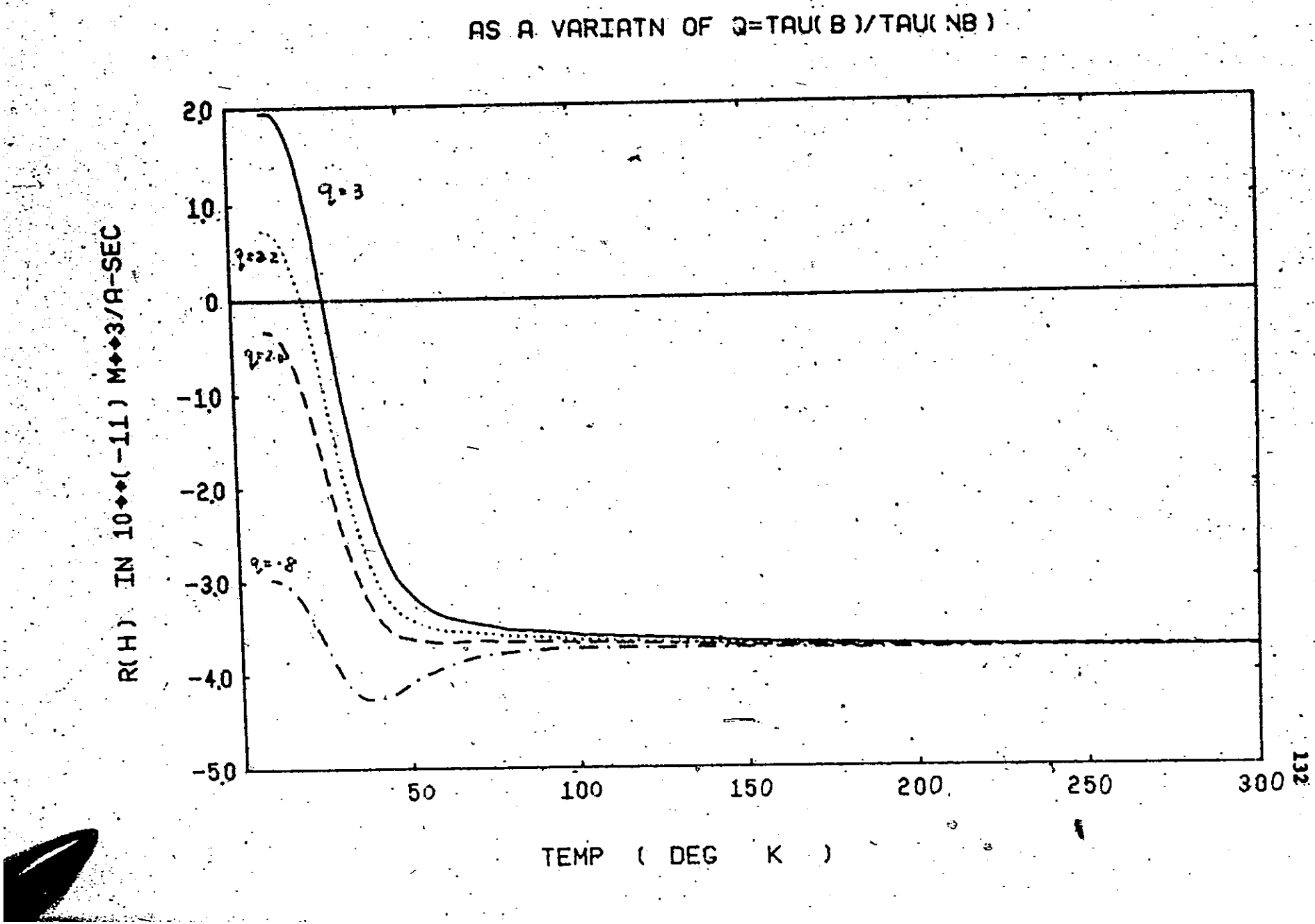
AS A VARIATN OF Q=TAU(B)/TAU(NB)
R(H) IN 10**(-11) M**3/A-SEC
TEMP (DEG K)
q=3
q=2.2
q=2.5
q=.8
2.0
1.0
0
-1.0
-2.0
-3.0
-4.0
-5.0
50
100
150
200
250
300

axis occurs at about ~ 25°K for q = 2.2 and at a higher T for q=3.0. This indicates that perhaps if the electrons at the Bragg planes are scattered less, then the R_H may be positive at low T. We note that for q = 3, R_H is + 2.0, comparable with the experimental value of 1.8. A ratio of less than unity will disagree with experiment. Figure 5.5.5 shows R_H as a variation of s = 3, 2.2, 2, 1.5 and 0.8. Again, s less than unity will disagree with experiment while s greater than unity (for example s = 1.5) will give positive values at low T. For the same ratio (s = q =3) this model seems to give much larger values of R_H. This means in order to give results comparable to experiment one needs s = 2. This suggests perhaps, then, that the scattering of hole surface electrons off impurities at the Bragg planes are much reduced compared with the rest of the FS, probably by a factor of two, if our interpretation of the Hall coefficient is valid.

Fig. 5.5.5 Calculated R_H as a function of temperature and as a variation of $s = \tau'_B/\tau'_{NB}$

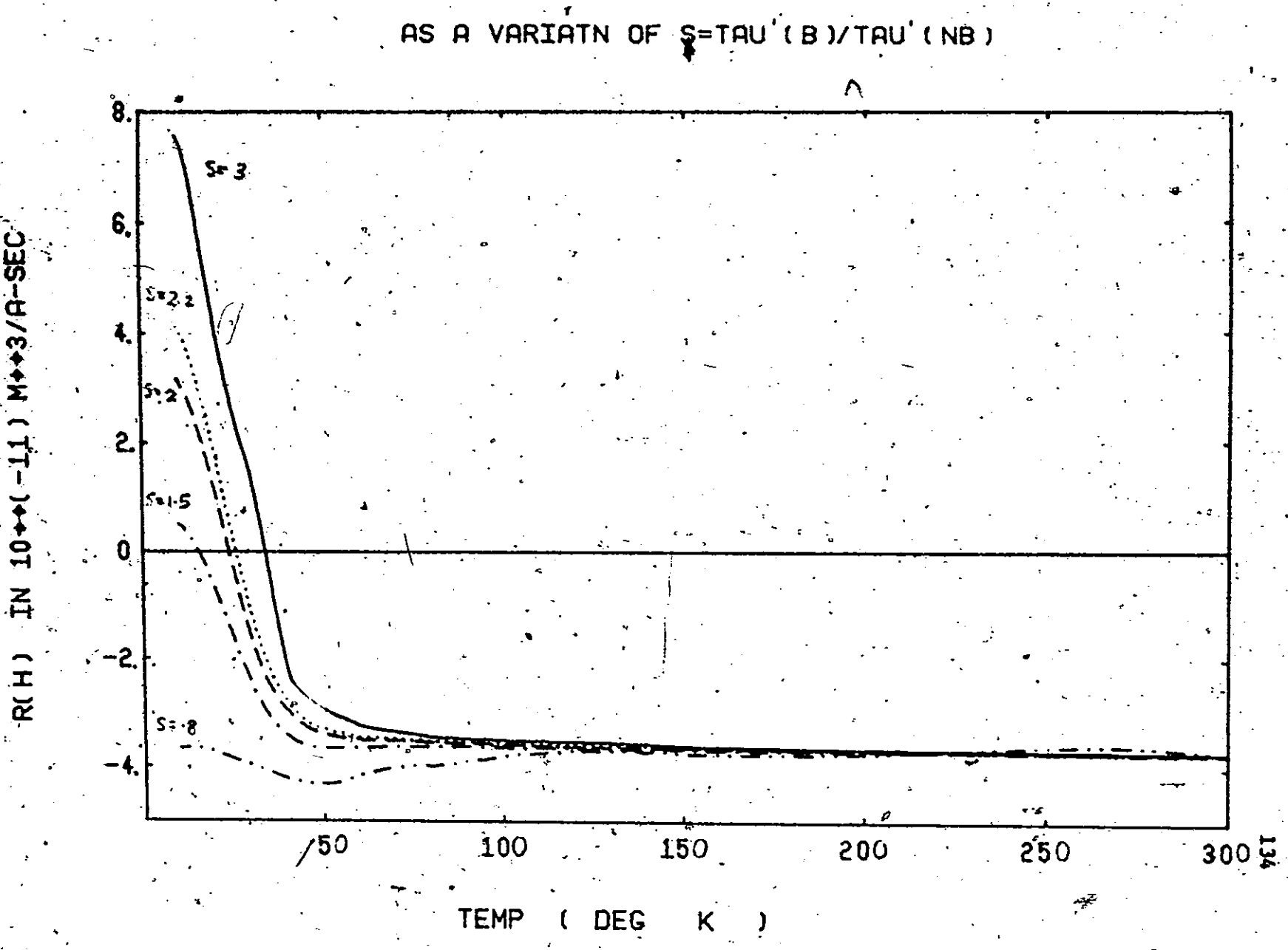
AS A VARIATN OF S=TAU'(B)/TAU'(NB)
R(H) IN 10**(-11) M**3/A-SEC
8.
6.
4.
2.
0
-2.
-4.
S=3
S=2.2
S=2
S=1.5
S=.8
50
100
150
200
250
300
TEMP (DEG K)

5.6 A Study of the Deviation from Matthiesson's Rule in Dilute Al-alloys due to the Anisotropies in the Relaxation Times

(a) Introduction

The total resistivity of a dilute alloy may be written as

$$\rho^{a}(T) = \rho^{ph}(T) + \rho_R + \Delta(T,c) \qquad 5.6.1$$

where $\rho^{ph}(T)$ is the phonon-limited ideal resistivity, ρ_R the temperature independent residual resistivity and $\Delta(T,c)$ is defined as the Deviation from Matthiesson's Rule (DMR).

There has been a great deal of interest in the study of deviations from Matthiesson's Rule. For a detailed account of the experiments and their theoretical interpretations, one can refer to the review article by Rasd (1972), and Kao's thesis (1973). The most recent experiments done on Al-alloys are those of Seth and Woods (1970), Carter (1971), and Panova et al (1969). Seth and Woods obtained results for Al-Mg with concentration c = 0.13, 0.61 and 1.75% and Al-Ag with c = 0.06 and 0.18% while Carter obtained results for Al-Mg with c = .03, .1, .5 and 1.5%, Al-Cu with c = 0.09, .52 and 1.03%, Al-Zn with c = .1 and 2.1% and Al-Ga with c = .035, .108, .198 and .664%. Panova et al obtained results for Al-Ag and Al-Cu which are similar to those obtained by Seth and Woods.

We note that Seth and Woods did experiments on Al alloys doped with small concentrations of impurities of the order of 1%. It is known from Mössbauer experiments (Brynkhanov et al, 1964) that the phonon spectrum of the host material is not substantially changed and from the de Haas van Alphen measurements of Shepherd and Gordon (1968) that the

electronic structure of the metal is not greatly altered.

Under these circumstances, one can expect that contributions to $\Delta(T,c)$ that arise from a deformed phonon spectrum as calculated by Lagun and Zhernov (1966, 1971) would be negligible. However, three other mechanisms could still give substantial contributions to (DMR): (i) Inelastic scattering of the electrons off the vibrating impurity atom, (ii) interference between the scattering by the vibrating impurities and the host-ions, (iii) anisotropies of the impurities scattering times over the FS.

We are going to restrict ourselves to non-magnetic impurities. Then, at low temperatures, we expect that the contributions due to (i) and (ii) should be small compared to (iii) (Fenton, 1973).

In this work, we shall confine ourselves to a study of the (DMR) due to (iii) — the anisotropies in scattering times which are believed to be the dominant process, especially at low temperatures. Sondheimer and Wilson (1947) made the first attempt to study (DMR) assuming two parabolic bands. By invoking the variational principle, Kohler (1949) investigated the nature of $\Delta(T,c)$ and found that the condition for $\Delta(T,c) = 0$ is equivalent to the statement that the trial functions $\phi^0_{\underline{k}}$, $\phi^R_{\underline{k}}$, for the phonon and residual resitivity case are identical, that is $\phi^0_{\underline{k}} = \phi^R_{\underline{k}}$. In terms of the scattering time solution generalized by McDonald (1956), this means that the anisotropies in $\tau^{ph}_{\underline{k}}$ and $\tau^R_{\underline{k}}$ are identical.

To see why this is so, we can start by writing down the conductivity $\sigma^a(T)$ for the alloy, described by the scattering time $\tau^a(\underline{k})$,

$$\left[\rho^{a}(T)\right]^{-1} \equiv \sigma^{a}(T) = \frac{e^2}{12\pi^3\hbar}\int_{F.S.} \tau^{a}_{\underline{k}}\, v_{\underline{k}}^{2}\, \frac{dS_{\underline{k}}}{v_{\underline{k}}} \qquad 5.6.2$$

and noting that $\tau^{a}_{\underline{k}}$ is obtained from $\tau^{ph}_{\underline{k}}$ and $\tau^{R}_{\underline{k}}$ through Equation 5.5.23,

$$\left[\tau^{a}_{\underline{k}}\right]^{-1} = \left[\tau^{ph}_{\underline{k}}\right]^{-1} + \left[\tau^{R}_{\underline{k}}\right]^{-1} \qquad 5.6.3$$

solving for $\tau^{a}(k)$,

$$\tau^{a}_{\underline{k}} = \tau^{ph}_{\underline{k}}\,\tau^{R}_{\underline{k}} \Big/ \left(\tau^{ph}_{\underline{k}} + \tau^{R}_{\underline{k}}\right) \qquad 5.6.4$$

The nonlinearity of $\rho^{a}(T)$ on impurity scattering as expressed in Equation 5.6.1 arises from Equation 5.6.4. If $\tau^{ph}_{\underline{k}}$ and $\tau^{R}_{\underline{k}}$ have the same anisotropies, that is assuming $\tau^{R} = \alpha\,\tau^{ph}$ hence $\rho^{ph} = \alpha\,\rho^{R}$ where α is some constant, then Equation 5.6.2 separates out into two terms,

$$\sigma^{a}(T) = \frac{\alpha}{1+\alpha}\,\sigma^{ph} = \frac{\alpha}{1+\alpha}\,\frac{1}{\rho^{ph}} \qquad 5.6.5$$

therefore, $$\rho^{a}(T) = \rho^{ph}(T) + \rho^{ph}/\alpha = \rho^{ph} + \rho^{R} \qquad 5.6.6$$

This implies $\Delta(T,c) = 0$ which is the Kohler's result.

For low concentration alloys, another interesting result is obtained for the behaviour of $\Delta(T,c)$ at high temperature in which the scattering due to phonons is stronger than that due to impurities, i.e. $\tau^{ph}_{\underline{k}} \ll \tau^{R}_{\underline{k}}$. Again we can write for the conductivity of the alloy,

$$\sigma^{a}(T) = \frac{e^2}{12\pi^3\hbar}\int_{F.S.} dS_{\underline{k}}\, v_{\underline{k}}\, \tau^{ph}_{\underline{k}} \left(1 + \frac{\tau^{ph}_{\underline{k}}}{\tau^{R}_{\underline{k}}}\right)^{-1}$$

$$\simeq \frac{e^2}{12\pi^3\hbar}\int_{F.S.} dS_{\underline{k}}\, v_{\underline{k}}\, \tau^{ph}_{\underline{k}} \left(1 - \frac{\tau^{ph}_{\underline{k}}}{\tau^{R}_{\underline{k}}}\right) \qquad 5.6.7$$

Rewriting in terms

$$\Delta/\rho^{R} = \left(\rho^{a}(T) - \rho^{ph} - \rho^{R}\right)/\rho^{R} \simeq \langle\tau^{R}\rangle\left\langle\frac{1}{\tau^{R}}\right\rangle - 1 \qquad \ldots\ldots 5.6.8$$

where $$\langle \alpha \rangle = \int_{F.S.} dS_{\underline{k}} \, v_{\underline{k}} \, \alpha \Big/ \int_{F.S.} dS_{\underline{k}} \, v_{\underline{k}} \qquad 5.6.9$$

The result in Equation 5.6.8 is essentially the same as the one derived by McDonald (1956). It states that the ratio Δ/ρ_R will be independent of concentration and temperature at sufficiently high temperatures. Moreover, it gives a measure of the anisotropies of impurity scattering i.e. of $\langle \tau^R \rangle \langle \frac{1}{\tau^R} \rangle$. As we can see from the definition in Equation 5.6.9, $\langle \tau^R \rangle$ is dominated by the large relaxation times over the FS while $\langle \frac{1}{\tau^R} \rangle$ is dominated by the very small relaxation times. If there are no anisotropies then the product $\langle \tau^R \rangle \langle \frac{1}{\tau^R} \rangle$ is unity and Equation 5.6.8 states that Δ is zero.

A small value of Δ then reflects that there is little anisotropy of τ^R over the FS.

(b) Calculations and discussions

The Al-alloys that we studied are mainly those taken from Seth and Woods (1970) (SW). These are alloys containing Mg and Ag as impurities. The residual resistivities and the corresponding scattering times assuming isotropy for these samples are listed in Table 5.6.1.,

Table 5.6.1

	ρ^R ($\mu\Omega$-cm)	$\langle \tau^R \rangle$ (secs)
(a) Al - .13% Mg	.0487	6.09×10^{-13}
(b) Al - .61% Mg	.2355	1.26×10^{-13}
(c) Al -1.75% Mg	.6815	4.35×10^{-14}
(d) Al - .06% Ag	.0707	4.19×10^{-13}
(e) Al - .18% Ag	.0195	1.52×10^{-13}

We first calculate the (DMR) by using the isotropic scattering times $\langle \tau^R \rangle$ computed in Table 5.6.1. The results for the Al-Mg alloys are plotted in Figure 5.6.1 for the temperature range (0-300°K). In Figure 5.6.2, we reproduce the experimental curves of (SW) on Al-Ag and Al-Mg alloys. A quick comparison shows that the isotropic calculations are unsatisfactory. First of all, the magnitudes of $\Delta(T,c)$ are too small, for example, the 0.13 at % Mg curve is out by a factor of 2 while the 1.75 at % calculation is out by a factor of 10. Referring to Equation 5.6.8, we understand that this is to be expected. Moreover, the peaks are at lower temperatures than the experimental curves. This latter behaviour is observed in work done by Kus (1973) on dilute alloys using isotropic impurity scattering.

Next we consider model calculations which include anisotropies in τ^R. Based on the calculations done on the Hall coefficient, we investigate the effects on $\Delta(T,c)$ introduced in these calculations by the three kinds of anisotropies.

In the first model, we assign two average scattering times τ_h and τ_e to represent the impurity scattering over the hole and the electron surface. By defining as in the previous Section 5.5 $p = \frac{\tau_h}{\tau_e}$, and demanding that at T=0 we have ρ_R for the residual resistivity, we have a one parameter model. We computed the $\Delta(T,c)$ for 0.13 at % Mg and 1.75 at % Mg samples varying p between 2 and .8. The results are presented in Figure 5.6.3 (a) for .13 at % Mg and Figure 5.6.3 (b) for 1.75 at % Mg. The peaks on the .13 at % Mg curve are small for all the ratios of p, typically less than 0.005 μΩ-cm, while experiment shows a value of .01 μΩ-cm. A smaller value of p increases the peak value but

Fig. 5.6.1 Calculated for Al-Mg alloys $\Delta(T,c)$ as a function of temperature

——— Al - .13% Mg

..... Al - .61% Mg

- - - Al - 1.75% Mg

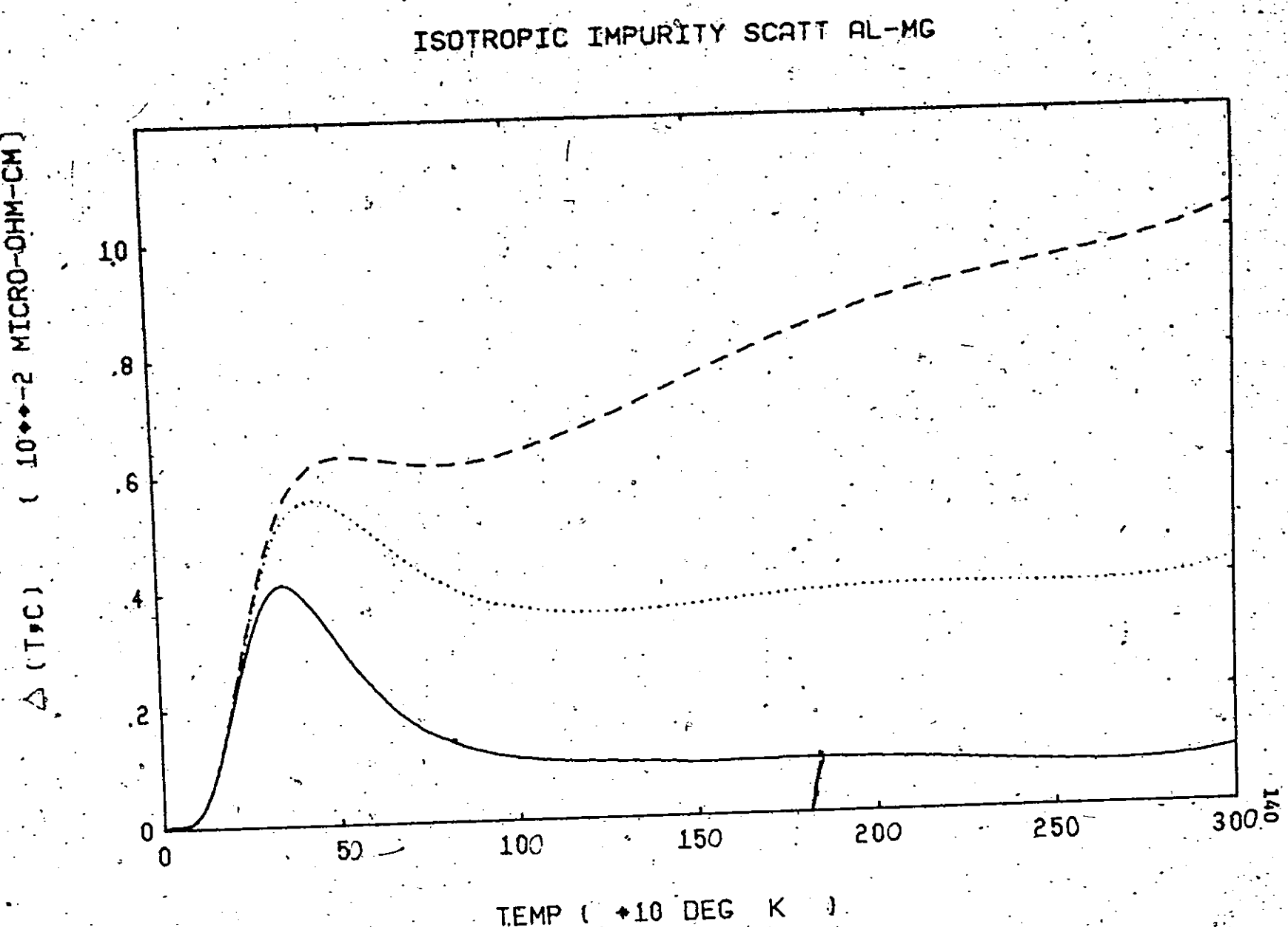
ISOTROPIC IMPURITY SCATT AL-MG
Δ (T•C) (10••-2 MICRO-OHM-CM)
1.0
.8
.6
.4
.2
0
0
50
100
150
200
250
300
140
TEMP (•10 DEG K)

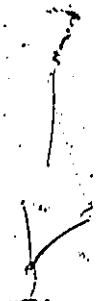

Fig. 5.6.2 Experimental $\Delta(T,c)$ for Al-Ag alloys and Al-Mg alloys as a function of temperature (Seth and Woods 1970)

(a) Al-Ag alloys

(b) Al-Mg alloys

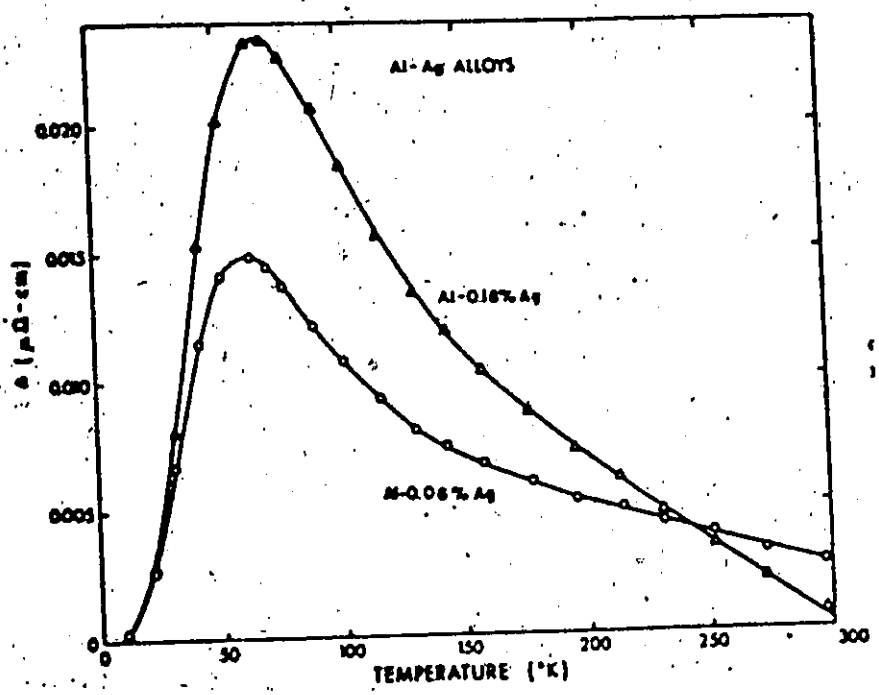
Al-Ag ALLOYS
Al-0.16% Ag
Al-0.06% Ag
0.020
0.015
0.010
0.005
0
50
100
150
200
250
300
TEMPERATURE (°K)

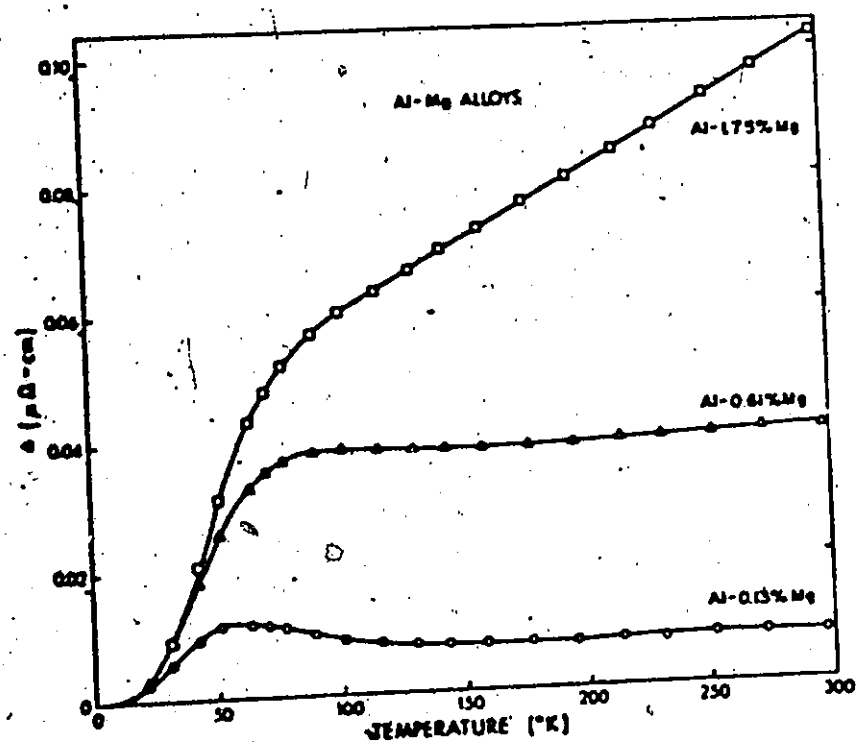
Al-Mg ALLOYS
Al-1.75% Mg
Al-0.61% Mg
Al-0.13% Mg
0.10
0.08
0.06
0.04
0.02
0
50
100
150
200
250
300
TEMPERATURE (°K)

Fig. 5.6.3 Calculated $\Delta(T,c)$ for Al-Mg alloys as a function of temperature

(a) Al - .13 Mg as a variation of $p = \tau_h/\tau_e$

——— $p = 2$

····· $p = 1.5$

——— $p = 1.0$

-·-·- $p = .8$

(b) Al - 1.73 Mg as a variation of $p = \tau_h/\tau_e$

——— $p = 2$

····· $p = 1.5$

——— $p = 1.0$

-·-·- $p = .8$

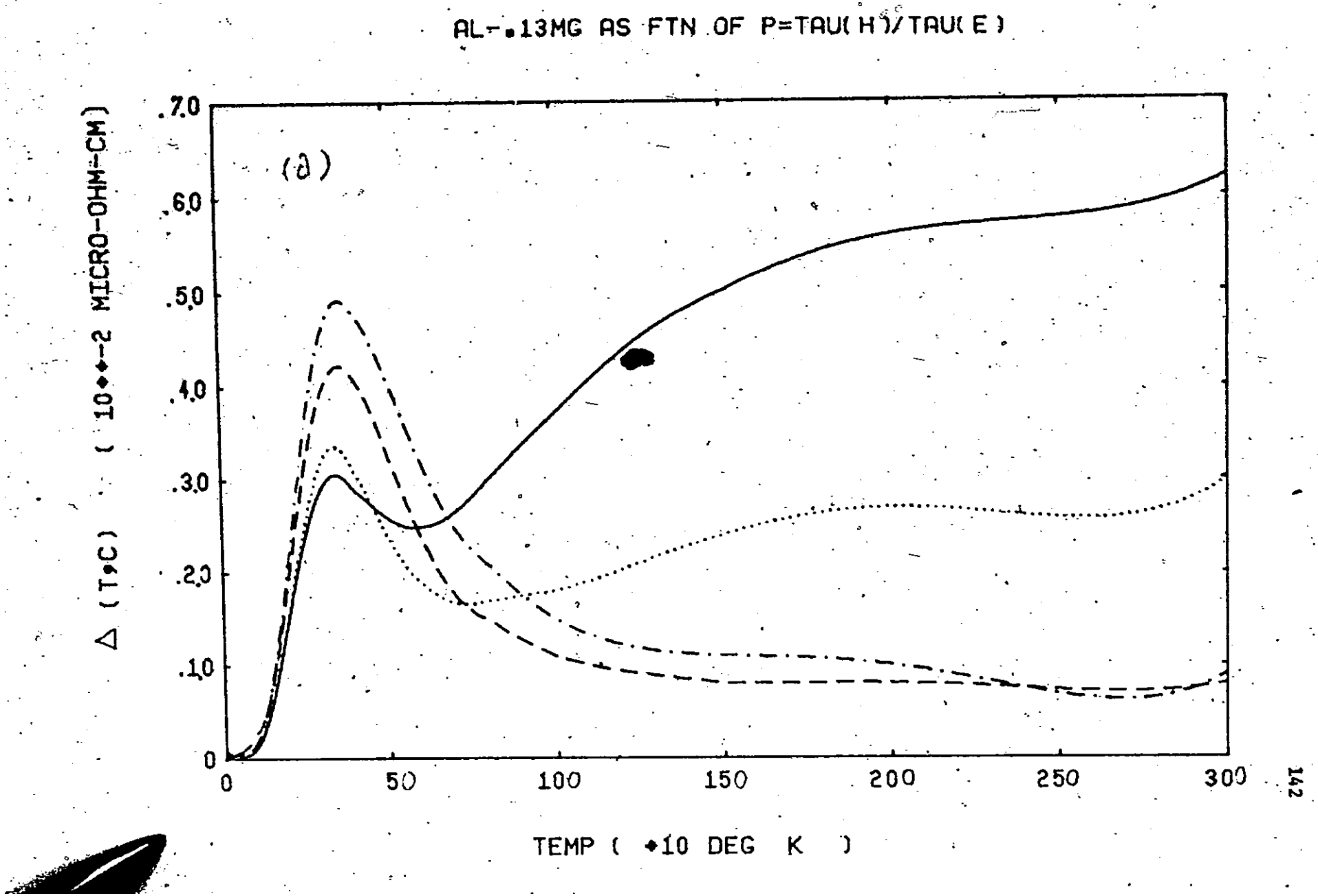
AL-.13MG AS FTN OF P=TAU(H)/TAU(E)
(a)
Δ (T•C) (10••-2 MICRO-OHM-CM)
.7.0
.6.0
.5.0
.4.0
.3.0
.2.0
.1.0
0
0
50
100
150
200
250
300
TEMP (•10 DEG K)

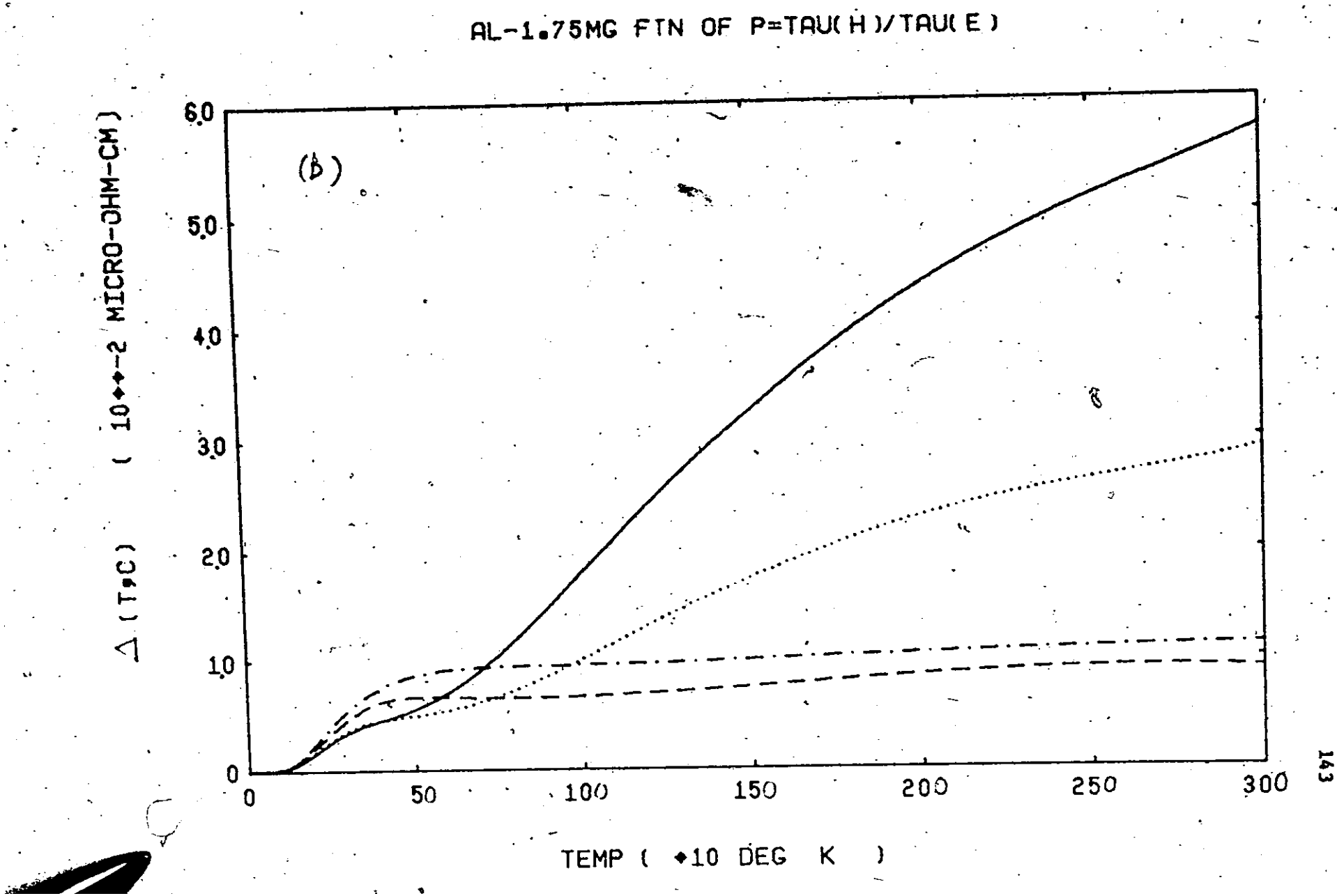
AL-1.75MG FTN OF P=TAU(H)/TAU(E)
(b)
Δ(T,C) (10**-2 MICRO-OHM-CM)
6.0
5.0
4.0
3.0
2.0
1.0
0
0
50
100
150
200
250
300
TEMP (*10 DEG K)

the curve decreases rapidly at high temperatures while experiment shows a saturation at about 0.008 μΩ-cm. For the 1.75 at % Mg sample, experimentally the Δ(T,c) rises quite steeply at low temperaturesand turns at about 80°K and becomes linear at high temperatures. For the computed curves, if p is less than unity Δ(T,c) resembles the 0.13 at % Mg experimental curve while for p = 1.5 it rises very rapidly to a value of .03 μΩ-cm at 300°K. With p = 2 the curve rises to a value of .055 μΩ-cm. The overall agreement is, however, poor, mainly because of the discrepancies at low temperatures (less than 150°K).

Next, we consider the model in which we separate the FS into two regions, near and far away from the Bragg planes. Defining the corresponding average scattering times by τ_B and τ_{NB} we made calculations for the 0.61 at % Mg sample for $q = \frac{\tau_B}{\tau_{NB}}$ ranging between 2 and .8. The results are plotted in Figure 5.6.4. The results are encouraging. For q = .8 and .95 the computed values are too small in magnitude (0.05×10^{-2} μΩ-cm as compared to 3.5×10^{-2} μΩ-cm experimentally), though qualitatively, they resemble the experimental data.. As q is increased, the computed curve rises rapidly and levels off at 0.013 μΩ-cm at q = 1.5 and .30 μΩ-cm at q = 2. The temperature at which Δ(T,c) levels off increases with increasing q. For q = 2, the temperature is approximately 80°K in agreement with experiment. The saturated value of Δ(T,c) is, however, slightly lower than experiment.

Lastly, we consider the model determined by the parameter $s = \tau'(B)/\tau'(NB)$, where the prime on $\tau'(B)$ means the Bragg regions are those regions on the hole surface only, while $\tau'(NB)$ denotes the rest of the FS. The computed results are shown for the .61 at % Mg sample in

Fig. 5.6.4 Calculated $\Delta(T,c)$ for Al - .61 Mg as a function of temperature

——— q = 2
····· q = 1.5
——— q = .95
-·-·- q = .8

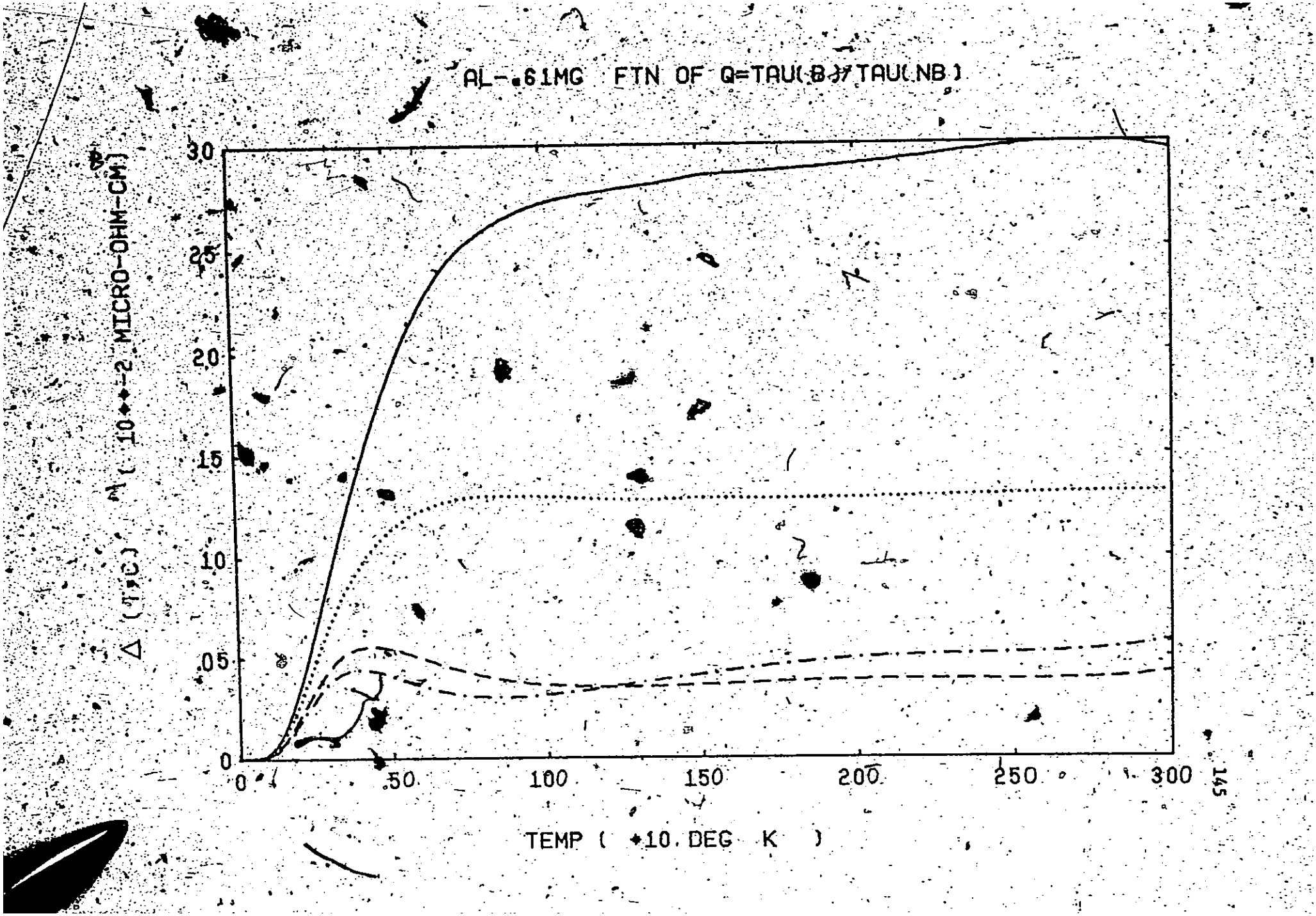
AL-.61MG FTN OF Q=TAU(B)/TAU(NB)
Δ (ρ,C)
(10**-2 MICRO-OHM-CM)
30
25
20
15
10
.05
0
0
50
100
150
200
250
300
TEMP (*10. DEG K)

Figure 5.6.5. The results are similar to those in the previous model, except that now the value $\Delta(T,c)$ is slightly larger in magnitude for the same ratio of s and q. As a matter of fact, comparing with Figure 5.6.2 one can see there is almost perfect agreement between the computed curve and experiment.

In Figure 5.6.6 (a) we present the computed results of $\Delta(T,c)$ for the Al-Mg alloys, and in Figure 5.6.6 (b) the Al-Ag alloys of (SW). In each diagram, there are a pair of curves corresponding to each sample, the upper one is for $s = 2$, the lower one is $q = 2$. We can see that except for small differences, the two models give essentially the same results. Comparing Figure 5.6.6 (a) to experiment, we see that we obtain almost perfect agreement. In particular, the temperatures at the maxima of the curves are about 50°K and 80°K for the .13 at % Mg and .61 at % Mg samples while for the 1.75 at % Mg, the temperature at which $\Delta(T,c)$ begins to saturate ($\sim$ 150°K) is higher than experiment.

Comparing the Al-Ag results with experiment shows that the .16 at % Ag alloy rises to about .013 μΩ-cm at about 60°K, as in the experiment. While experiment shows a decline after this temperature, our calculations show a gentle leveling off at about .011 μΩ-cm. For the .16 at % Ag alloy, $\Delta(T,c)$ again rises to about .025 μΩ-cm at T $\sim$ 80°K and saturates at high temperature while the experimental results show a rapid decrease after reaching the peak at about 80°K. The agreement is good below say 80°K for 0.06 at % Ag alloy and 100°K for the .16 at % Ag alloy.

Lastly, we compute the ratio Δ/ρ_R for the Al-Mg alloys in Carter's thesis and present the results in Figure 5.6.7. Again the agreement at

Fig. 5.6.5 Calculated $\Delta(T,c)$ of Al - .61 Mg alloy as a function of temperature

——— s = 2

····· s = 1.5

– – – s = .95

–·–·– s = .8

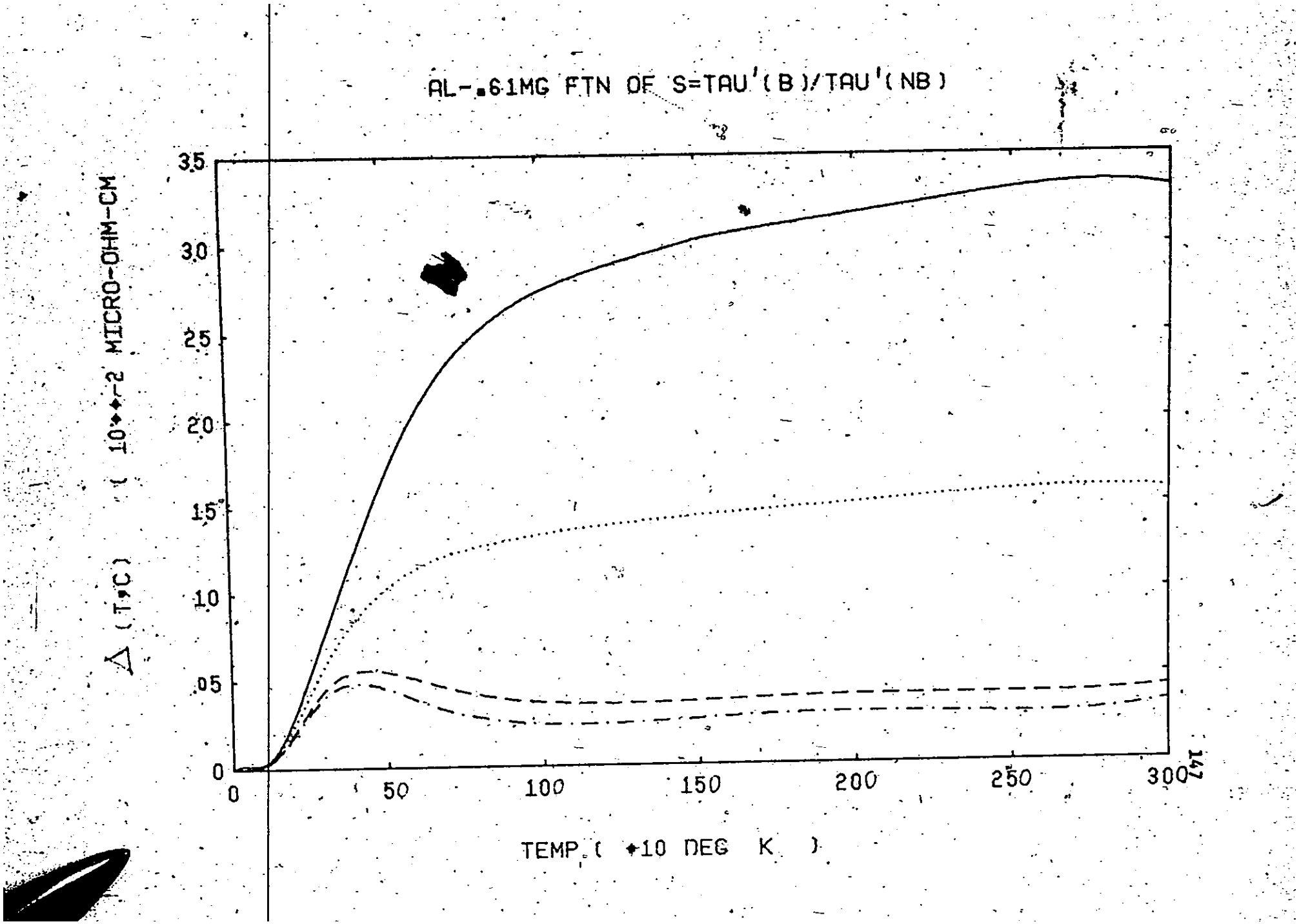
AL-.61MG FTN OF S=TAU'(B)/TAU'(NB)
Δ(T,C) (10**-2 MICRO-OHM-CM
3.5
3.0
2.5
2.0
1.5
1.0
.05
0
0
50
100
150
200
250
300
TEMP (*10 DEG K)

Fig. 5.6.6 Calculated $\Delta(T,c)$ for Al-Mg alloys and Al-Ag as a function of temperature for $q = s = 2$

(a) Al-Mg alloys, upper curve corresponds to $s = 2$ and lower curve, $q = 2$

(b) Al-Ag alloys, upper curve corresponds to $s = 2$ and lower curve, $q = 2$

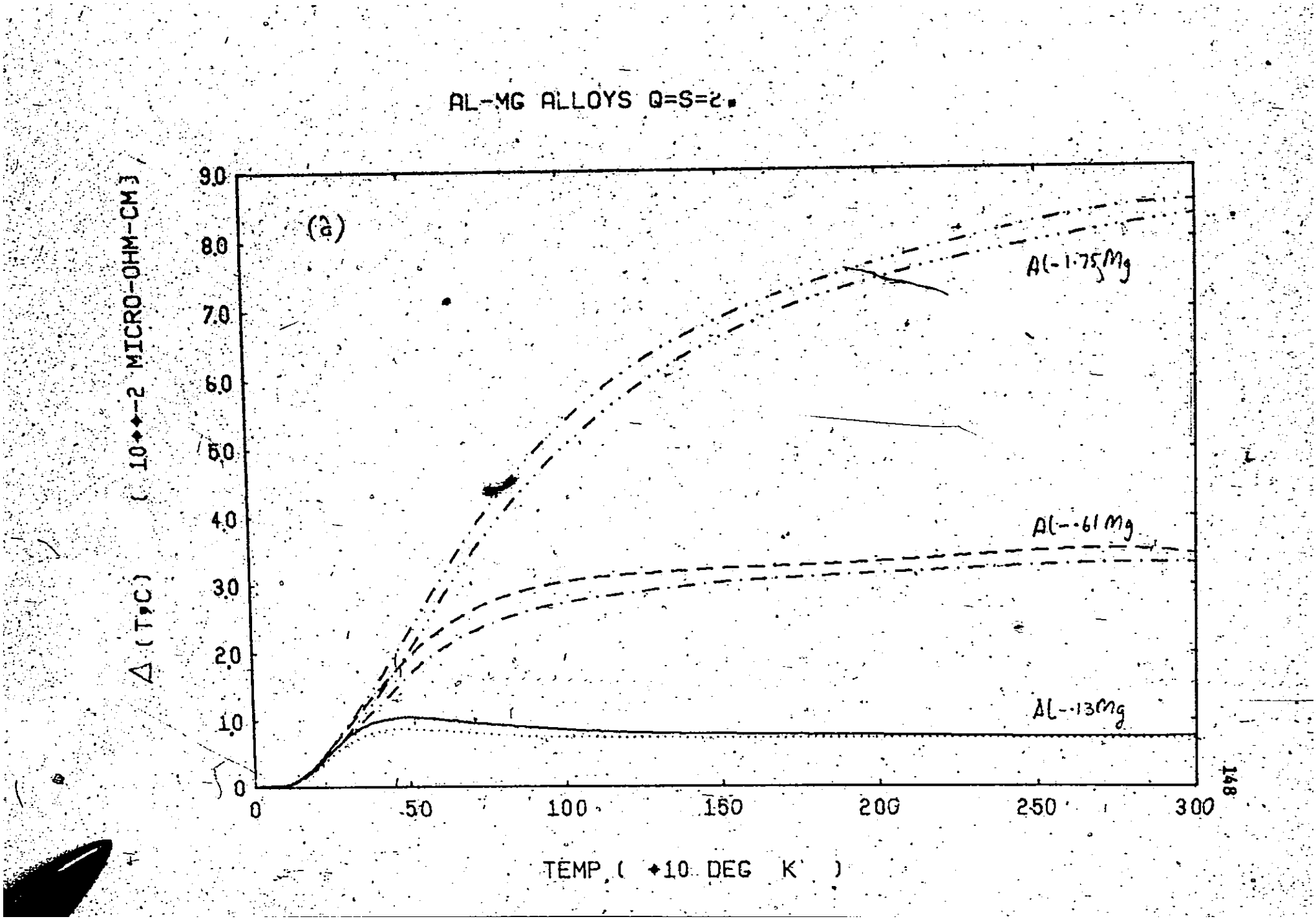
AL-MG ALLOYS Q=S=2.
(a)
Δ (T,C) (10**-2 MICRO-OHM-CM)
9.0
8.0
7.0
6.0
5.0
4.0
3.0
2.0
1.0
0
0
50
100
150
200
250
300
TEMP (*10 DEG K)
AL-1.75Mg
AL-.61Mg
AL-.13Mg
148

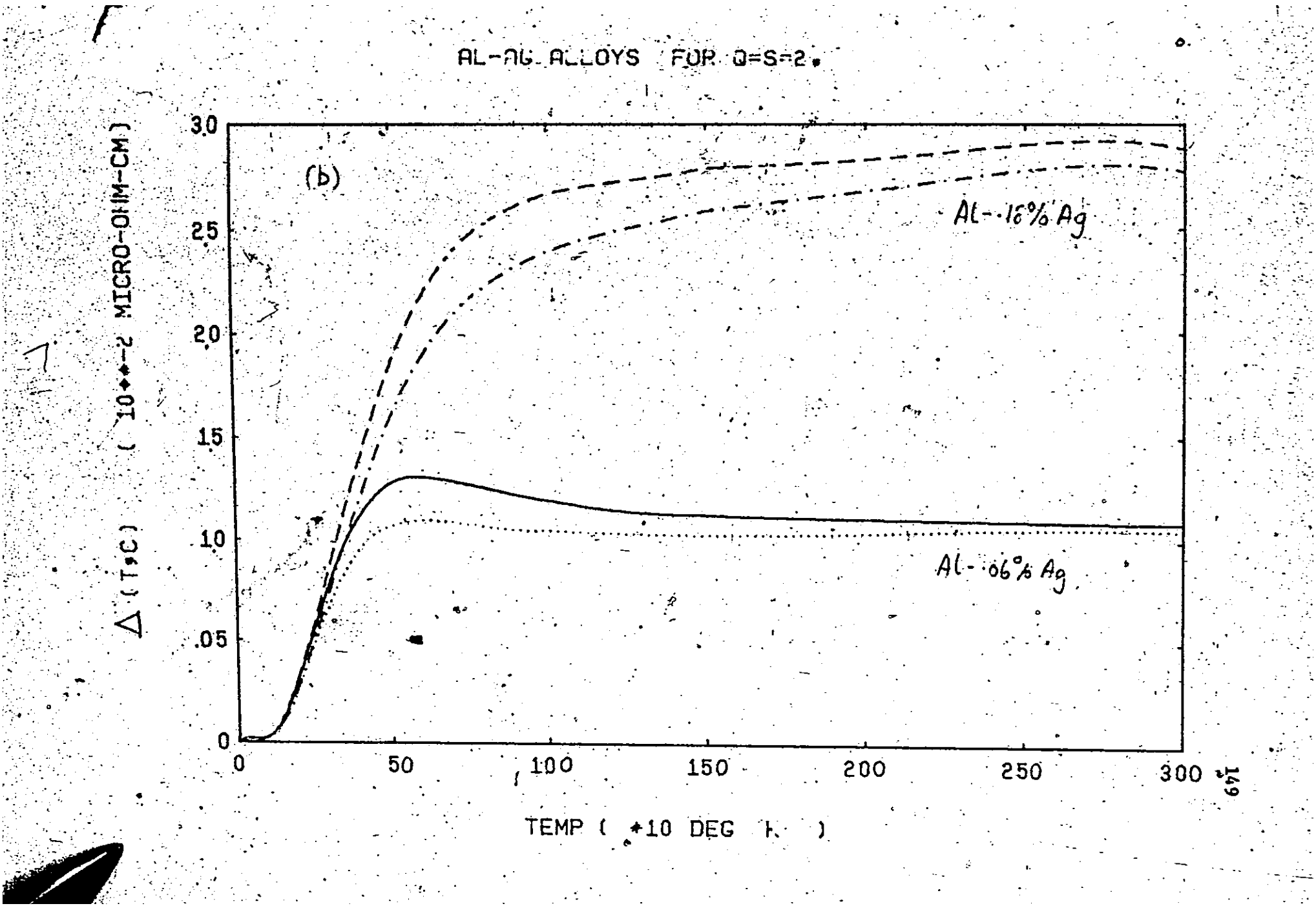
AL-AG ALLOYS FOR Q=S=2.
(b)
Al-.16% Ag
Al-.06% Ag
Δ (T,C) (10**-2 MICRO-OHM-CM)
TEMP (*10 DEG K)
0
.05
10
15
20
25
30
0
50
100
150
200
250
300

Fig. 5.6.7 Calculated ratio Δ/ρ_R for dilute alloys of Al as a function of temperature

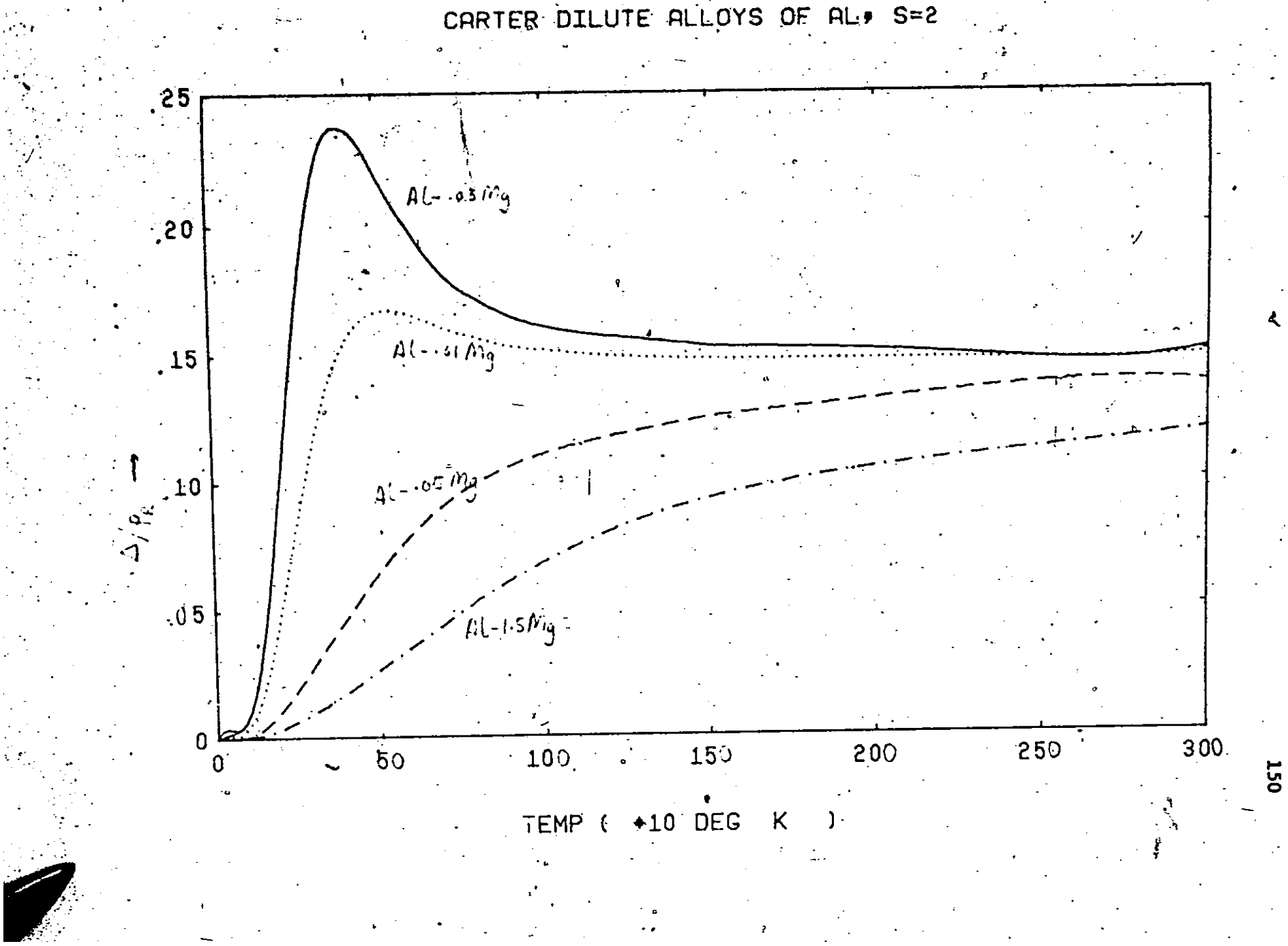
CARTER DILUTE ALLOYS OF AL, S=2
.25
.20
.15
.10
.05
0
Δ/ρ
Al-.03 Mg
Al-.01 Mg
Al-.05 Mg
Al-1.5 Mg
0
50
100
150
200
250
300
TEMP (*10 DEG K)

Fig. 5.6.8 Ratio Δ/ρ_R for dilute alloys of Aluminium as a function of temperature (from Carter's thesis, 1971)

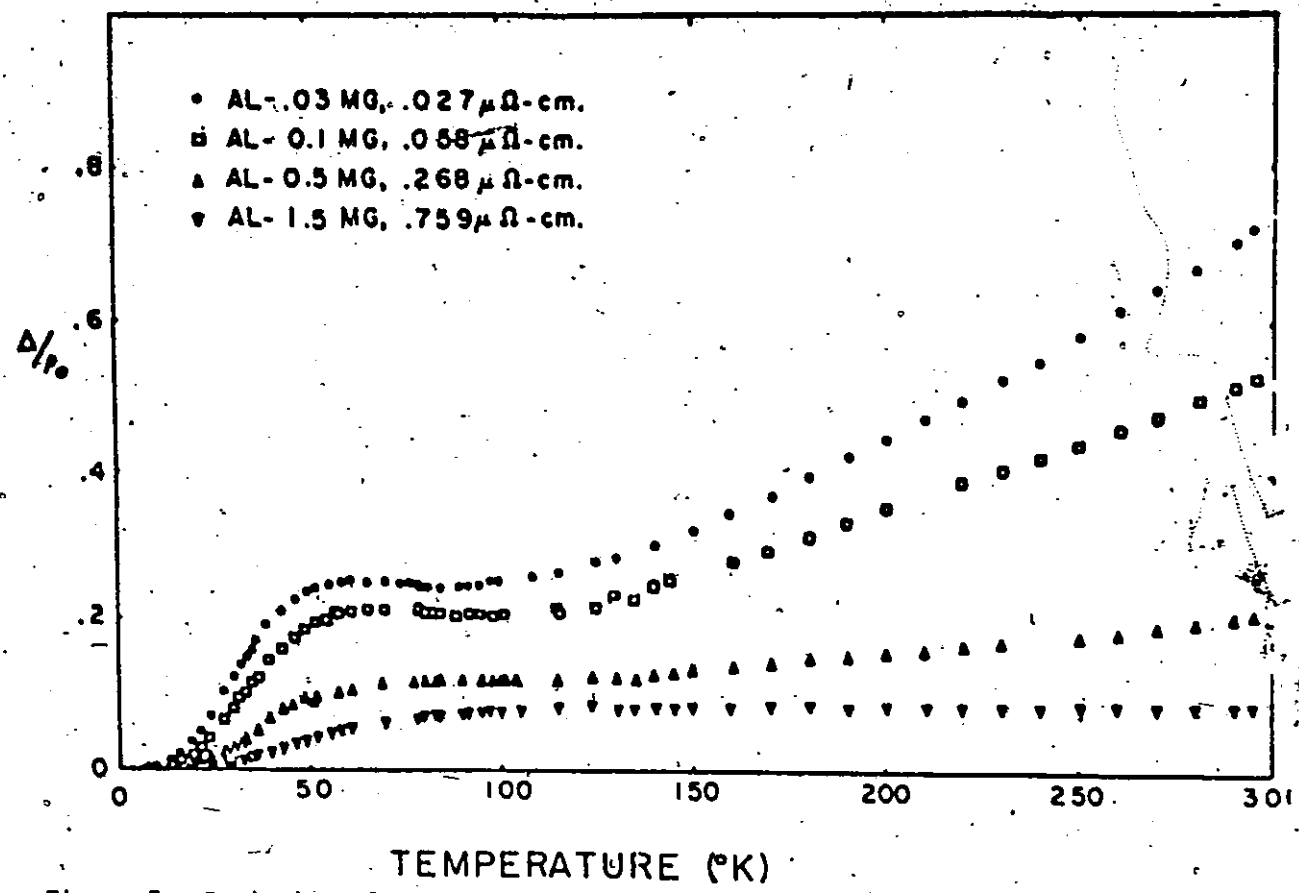

Figure 7.--Deviations from Matthiessen's Rule in Al-Mg alloys.

low temperatures is obvious whereas at high temperatures, Carter included effects due to thermal expansion in his data. A direct comparison is difficult. It is worthwhile to note that for the low concentrations, our calculation shows Δ/ρ_R approaches a value of 0.15. This means, then, using Equation 5.6.8, that a crude estimate of $\langle\tau_R\rangle\langle\frac{1}{\tau_R}\rangle$ is 1.15.

Dugdale and Basinski (1967) and Scheverer et al (1969) suggested that one should include the effects due to thermal expansion of the crystal. A careful treatment of this at high temperature is important, but unfortunately, it is beyond the scope of this thesis. For quantitative comparison with experiment, we should confine ourselves to low temperatures and low concentrations. But on the whole, considerations of the anisotropies in impurity scattering do give a consistent picture of (DMR) in dilute Al alloys.

Table 5.6.2

$\Delta(T,c)$ in $\mu\Omega$-cm

First Column q=2 Second Column s=2

T °K	(a) ρ_R=.0487 Al - .13 % Mg		(b) ρ_R=.2355 Al - .61 % Mg		(c) ρ_R=.6815 Al - 1.75 Mg		(d) ρ_R=.0707 Al - .06 % Ag		(e) ρ_R= 195 Al - .18 % Ag	
10	.0031	.00026	.00031	.00026	.0031	.00026	.0031	.00026	.00031	.00826
15	.0013	.0011	.0014	.0011	.0014	.0011	.0013	.0011	.0014	.0011
20	.0032	.0027	.0034	.0029	.0034	.0029	.0033	.0028	.0034	.0029
25	.0054	.0047	.0060	.0052	.0061	.0053	.0056	.0049	.0059	.0051
30	.0075	.0064	.0088	.0076	.0091	.0078	.0079	.0068	.0087	.0075
40	.0099	.0084	.0144	.012	.0156	.0136	.0112	.0096	.0140	.0121
50	.0105	.0087	.0194	.0168	.0228	.020	.0128	.0107	.0185	.0160
60	.0102	.0085	.0233	.0204	.0302	.0272	.0131	.0110	.0218	.0189
80	.00932	.0078	.0282	.0250	.0435	.040	.0126	.0107	.0253	.0223
100	.00867	.0075	.0304	.0274	.0536	.050	.0120	.0105	.0267	.0240
150	.00799	.0073	.0325	.0304	.0687	.0660	.0113	.0103	.0279	.0259
200	.00777	.0073	.0334	.0317	.0767	.0744	.0111	.0104	.0283	.0268
300	.00763	.0730	.0343	.0330	.0851	.0832	.0109	.0105	.0888	.0277

CHAPTER VI

THERMOPOWER IN ALUMINIUM

6.1 The Phonon-drag and Thermopower

In this Section, we discuss and compute the thermopower of Aluminium in the low temperature regime. An elementary theory of the thermopower can be found in Rosenberg (1963). Consider a current flowing through a metal rod, the ends of which are maintained respectively at temperatures T_1 and T_2 ($T_1<T_2$). Due to the temperature gradient, the electronic distributions at the two ends are different, thus an electron must be given energy in travelling from T_1 to T_2. They absorb energy from phonons giving rise to the Thomson effect. It can be shown that the thermopower S is given by

$$S = \int_0^T \frac{C_e(T')}{neT'} dT' \qquad 6.1.1$$

where $C_e(T) = \pi^2 k_B^2 nT/2E_f$ is the electronic specific heat, n = electron density, e is the electronic charge. From Equation 6.1.1, S will be of the order of a few tenths of $\mu V/k^0$, which agrees with experiment in order of magnitude. However, experiments have shown that even in the case of the alkalis (MacDonald et al, 1958, Collins and Ziman, 1961) the signs of the thermopower can vary drastically. In Lithium it is positive at all temperatures, Rb has a positive peak and then decreases and becomes negative, whereas Na and K are negative at all temperatures. It is clearly of interest to be able to account for even the qualitative behaviour of the thermopower.

It has become customary to explain these large variations in thermopower in terms of the effect of phonon-drag. The basis of this mechanism, which dates to Gurevich (1945,1946), can be understood when one considers a system where both electrical and thermal gradients are present. This has been treated in detail by Ziman (1960). Fundamentally, phonon-drag arises from the fact that in treating the problem, one must take into account not only that the electron distribution is not in equilibrium, but that the phonon system also deviates from equilibrium. The variational principle then involves two transport equations, one for the electrons like Equation 5.1.3, and another for the phonons. Thus, there are two coupled transport equations. Assuming that the phonon distribution has deviation ϕ_q which is non-zero and which is given by

$$\phi_{\underline{q}} \propto \underline{q} \cdot \underline{u} \qquad 6.1.2$$

where $\underline{u}$ is the directional unit vector of the field, Ziman obtained the following equations for the effects of the phonon-drag on the electrical resistivity and the thermopower:

$$\rho(T) = \rho_i(T)\left(1 - \frac{P_{IL}^2}{P_{II} P_{LL}}\right) \qquad 6.1.3$$

$$\delta(T) = \frac{k_B \, C_L(T)}{e\eta \, 3N k_B}\left(-\frac{P_{IL}}{P_{LL}}\right) \qquad 6.1.4$$

where $\rho_i(T)$ is the resistivity of the metal without the effect of phonon-drag and is given by Equation 5.2.8. $C_L(T)$ is the lattice specific heat at temperature T. P_{II} is related to the function $\alpha_{tr}^2 F(\omega)$, by

$$P_{II}(T) = \beta \int_0^\infty \frac{\hbar\omega \, \alpha_{tr}^2 F(\omega)}{(e^{\beta\omega}-1)(1-e^{-\beta\omega})} \, d\omega = \beta \int_0^\infty R(\omega) \alpha_{tr}^2 F(\omega) \, d\omega \qquad \ldots\ldots 6.1.5$$

$$\alpha^2_{tr}F(\omega) = \int_{F.S.} \frac{dS_k}{v_k} \alpha^2_{tr} F(\underline{k},\omega) \qquad 6.1.6$$

where $\alpha^2_{tr}F(\underline{k},\omega)$ is defined in Equation 3.1.2. The functions P_{IL} and P_{LL} are generalized by analogy to the nearly free electron case of Ziman (1960) and they are given by, in terms of $\alpha^2_{IL}F(\underline{k},\omega)$ and $\alpha^2_{LL}F(\underline{k},\omega)$ (Equations 3.1.3, 3.1.4)

$$P_{IL}(T) = \beta \int_0^\infty R(\omega)\, \alpha^2_{IL} F(\omega)\, d\omega \qquad 6.1.7$$

and

$$\alpha^2_{IL}F(\omega) = \int_{F.S.} \frac{dS_k}{v_k} \alpha^2_{IL} F(\underline{k},\omega) \qquad 6.1.8$$

$$P_{LL}(T) = \beta \int_0^\infty R(\omega)\, \alpha^2_{LL} F(\omega) d\omega \qquad 6.1.9$$

and

$$\alpha^2_{LL}F(\omega) = \int_{F.S.} \frac{dS_k}{v_k} \alpha^2_{LL} F(\underline{k},\omega) \qquad 6.1.10$$

The functions P_{II}, P_{IL} and P_{LL} have been related to the weighted frequency distributions defined in Section 3.1 by Hayman and Carbotte (1973).

While some rough estimates of the quantities that enter into the theory have been attempted (Collins and Ziman 1961), these authors have not performed any quantitative and realistic calculations of the effects of phonon-drag. Recent work of Kaveh and Wiser (1972a, 1972b) has attempted to calculate the effect of phonon-drag on the resistivity in Potassium at low temperatures. Some theoretical considerations on the phonon-drag problem in the framework of electron-phonon scattering times can be found in Bailyn's paper (Bailyn 1967). However, one needs details about phonon relaxation times, the calculation of which is beyond the scope of this thesis. Hayman and Carbotte (1973) calculated the effect

for the case of the alkali metals by using the equations due to Collins and Ziman (6.1.4-6.1.10) in the free electron approximation. They succeeded in explaining qualitatively the sign dependence of the thermopower as a function of temperature. In the same spirit, we apply Equations 6.1.4-6.1.10 to the study of the thermopower in Aluminium, including the details of the FS.

6.2 Results and Discussions

First, we calculate the frequency distribution functions $\alpha^2_{tr}F(\omega)$, $\alpha^2_{IL}F(\omega)$ and $\alpha^2_{LL}F(\omega)$ and compare them with the results obtained in the free electron (S-OPW) approximation using the simplified formulae in Rayman and Carbotte (1973). These are presented in Figure 6.2.1 (a)(b) for $\alpha^2_{tr}F(\omega)$, $\alpha^2_{IL}F(\omega)$ in Figure 6.2.2 (a)(b), and $\alpha^2_{LL}F(\omega)$ in Figure 6.2.3 (a) (b).

As a general remark, when we compare the 15-OPW and the S-OPW calculations, we find that the peaks in the corresponding functions occur at the same frequencies and qualitatively very similar.

Figure 6.2.1 (a)(b) show the $\alpha^2_{tr}F(\omega)$. The multi-OPW curve has a much higher peak at high frequency of about 0.47 whereas in the S-OPW it is only .35. In the plateau region between 0.4 ω_c and 0.6 ω_c, the 15-OPW is lower than the S-OPW. More important is the region below 0.4 ω_c where the 15-OPW calculation shows a rapid decrease to zero as $\omega \to 0$ whereas in the S-OPW calculation the decrease is very slow. The effect of this on the resistivity has been discussed in Section 5.3.

Figure 6.2.2 (a)(b) shows the $\alpha^2_{IL}F(\omega)$ functions. As we see in Equation 6.1.4, the thermopower depends on the function P_{IL} more than P_{LL}. Since P_{LL} is always positive as can be seen from Equation 3.1.4. a change in sign in P_{IL} will cause the thermopower to change sign. In this function, we see that the Fermi Surface and the 15-OPW treatment of the electron-ion matrix element plays a more important role. The S-OPW $\alpha^2_{IL}F(\omega)$ function has small positive values at low frequencies and

Fig. 6.2.1 The functions $\alpha^2_{tr}F(\omega)$ as functions of ω.

(a) 15-OPW approximation

(b) 5-OPW approximation

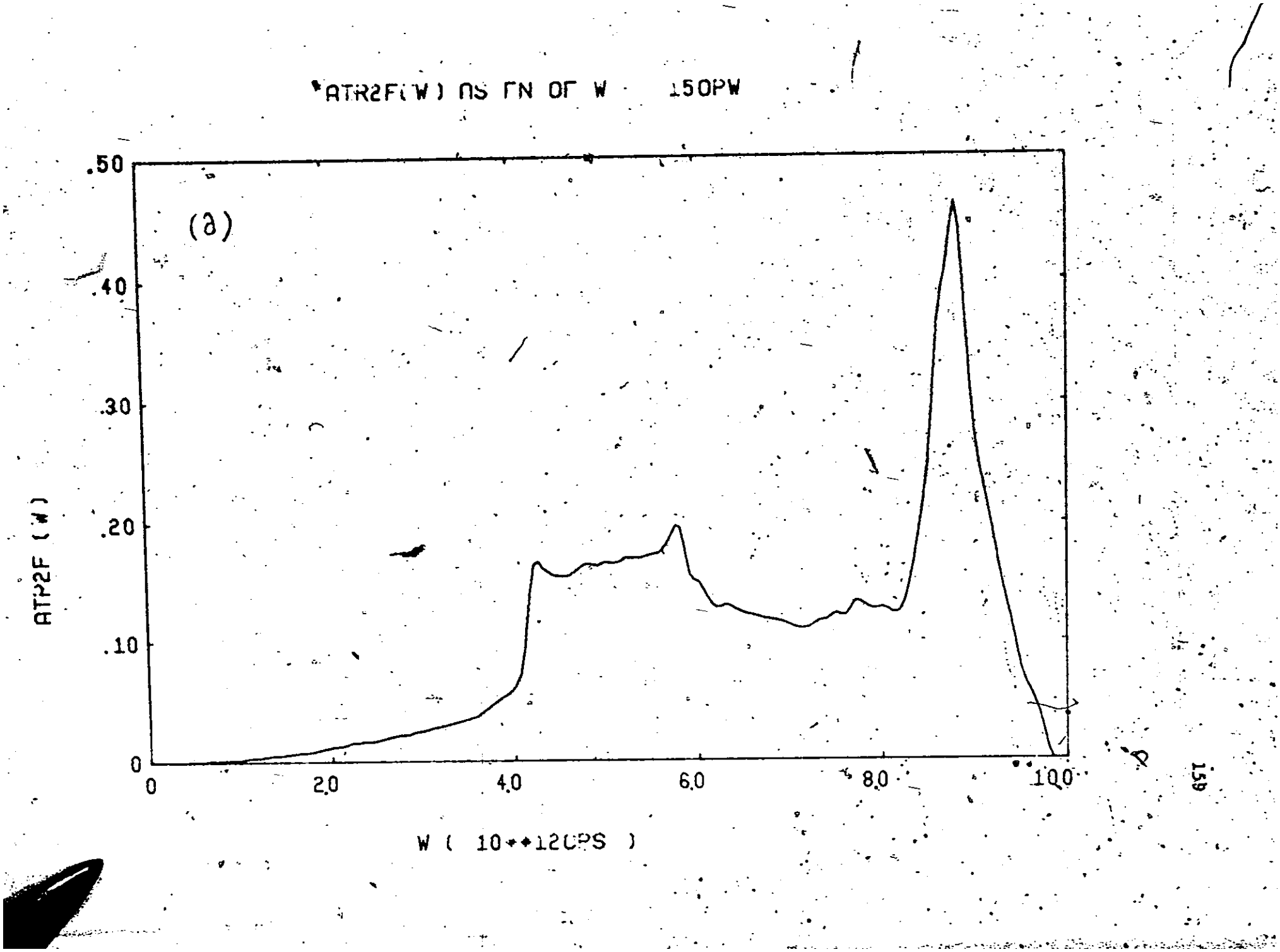
(a)
.50
.40
.30
.20
.10
0
0
2.0
4.0
6.0
8.0
10.0
W (10**12CPS)

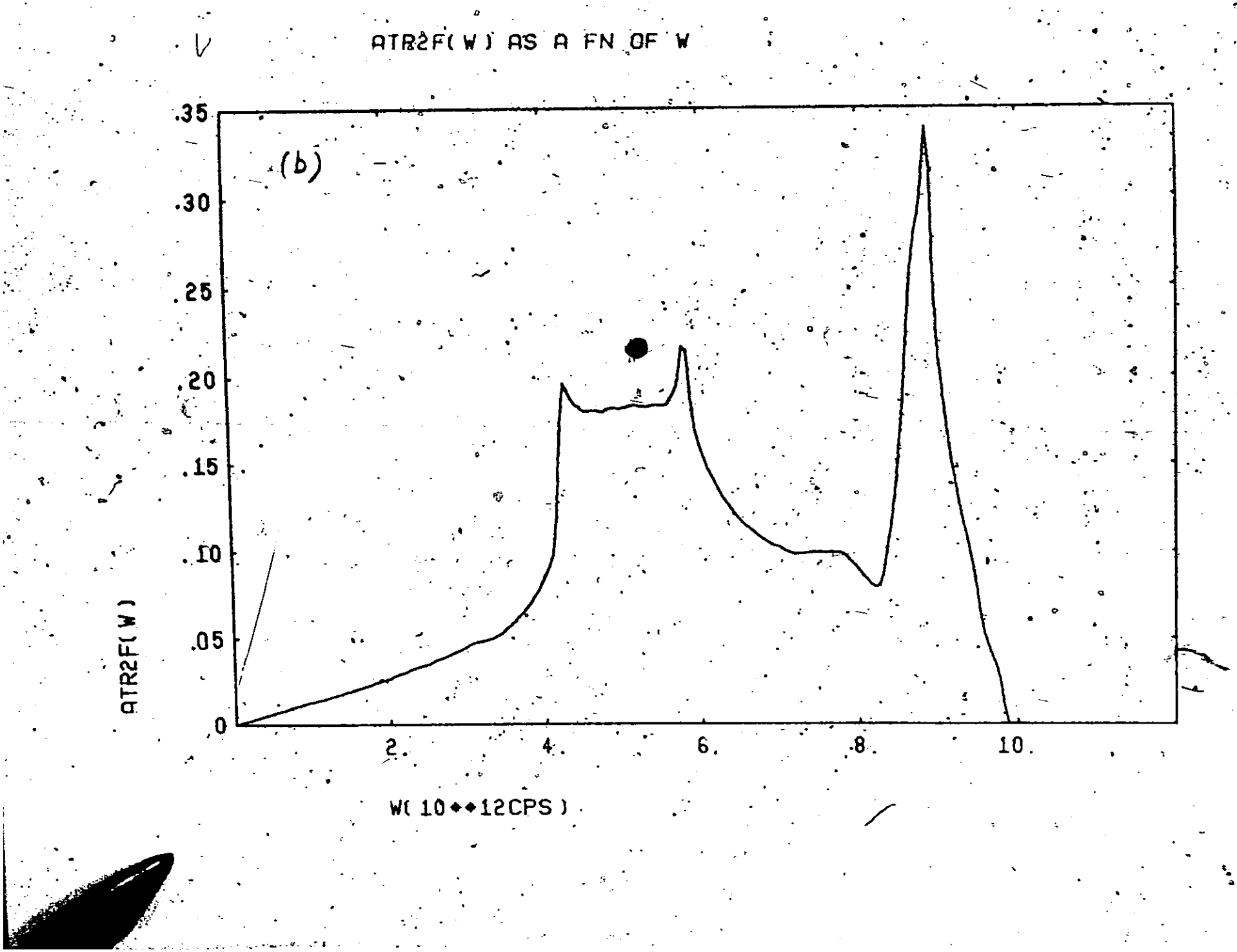
ATR2F(W) AS A FN OF W
(b)
.35
.30
.25
.20
.15
.10
.05
0
ATR2F(W)
2.
4.
6.
8.
10.
W(10**12CPS)

Fig. 6.2.2 The functions $\alpha^2_{IL}F(\omega)$ as functions of ω.

(a) 15-OPW approximation

(b) S-OPW approximation

(a)
.12
.10
.08
.06
.04
.02
0
0
20
40
60
80
100
W (10**12CPS)

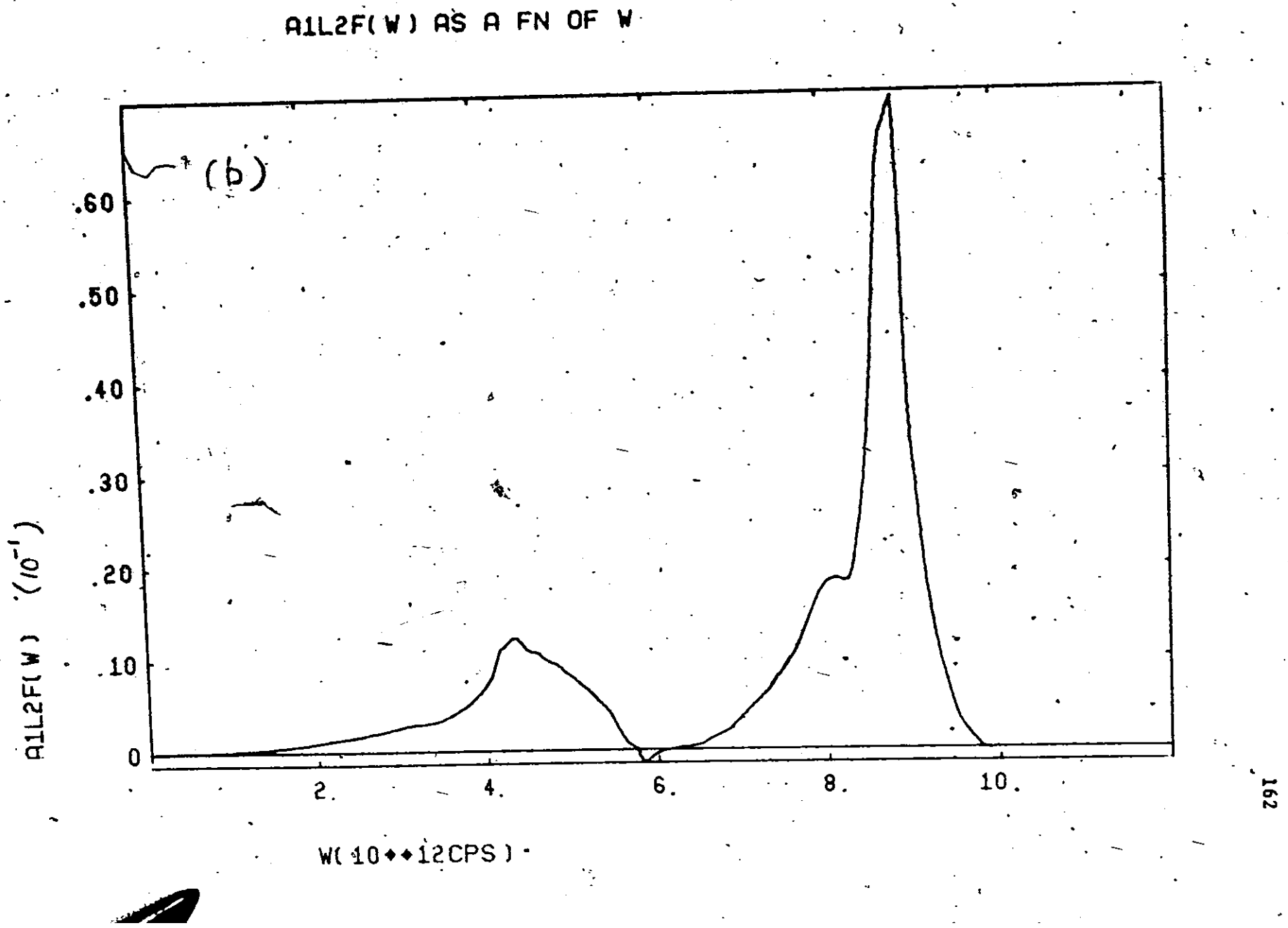
A1L2F(W) AS A FN OF W
(b)
.60
.50
.40
.30
.20
.10
0
A1L2F(W) '(10⁻¹)
2.
4.
6.
8.
10.
W(10**12CPS)

6.2.3 The functions of $\alpha^2_{LL}F(\omega)$ as function of ω.

(a) 15-OPW approximation

(b) 5-OPW approximation

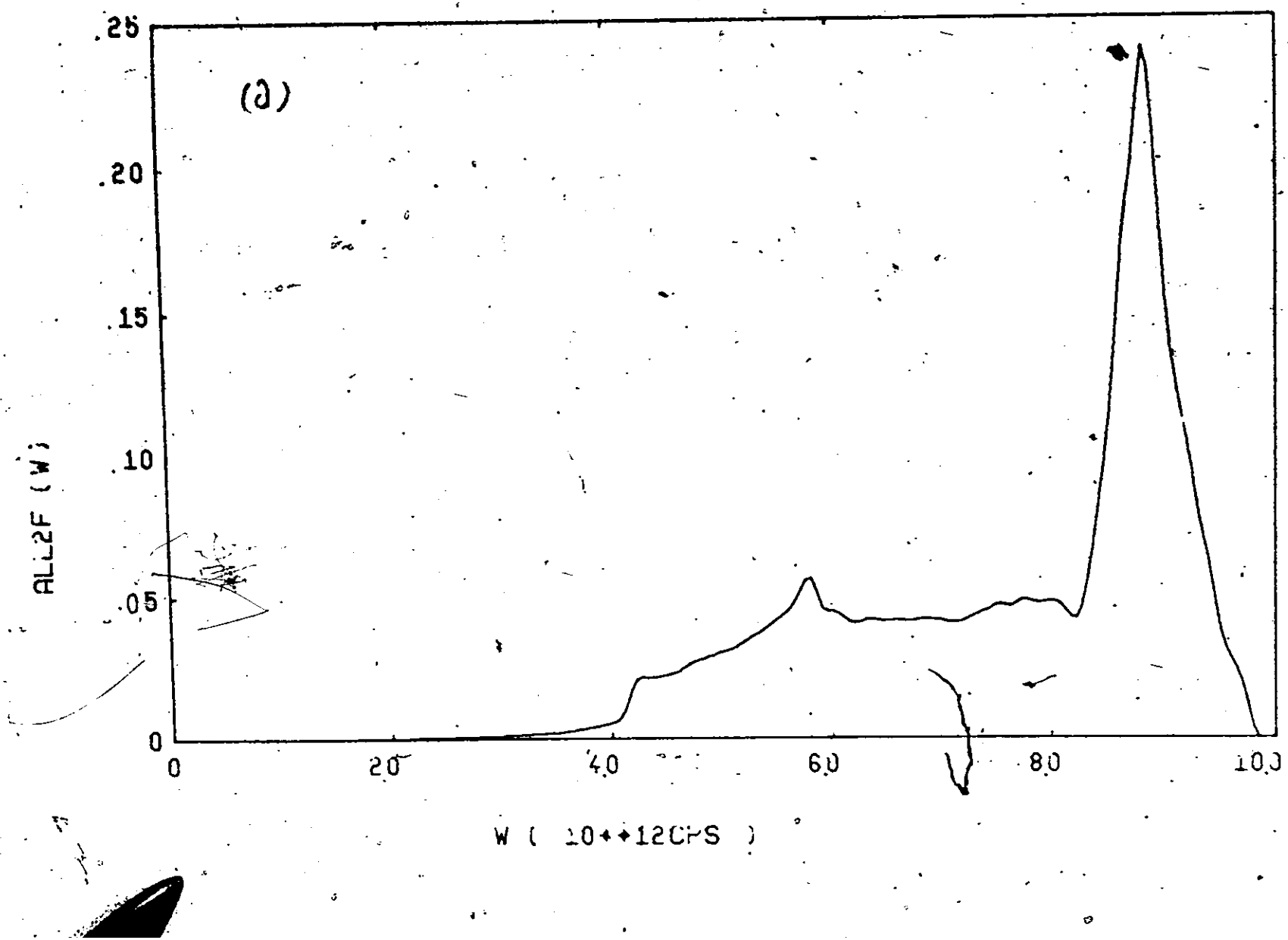
ALL2F(W) AS FN OF W - 150FW
(d)
.25
.20
.15
.10
.05
0
ALL2F (W)
0
2.0
4.0
6.0
8.0
10.0
W (10**12CPS)

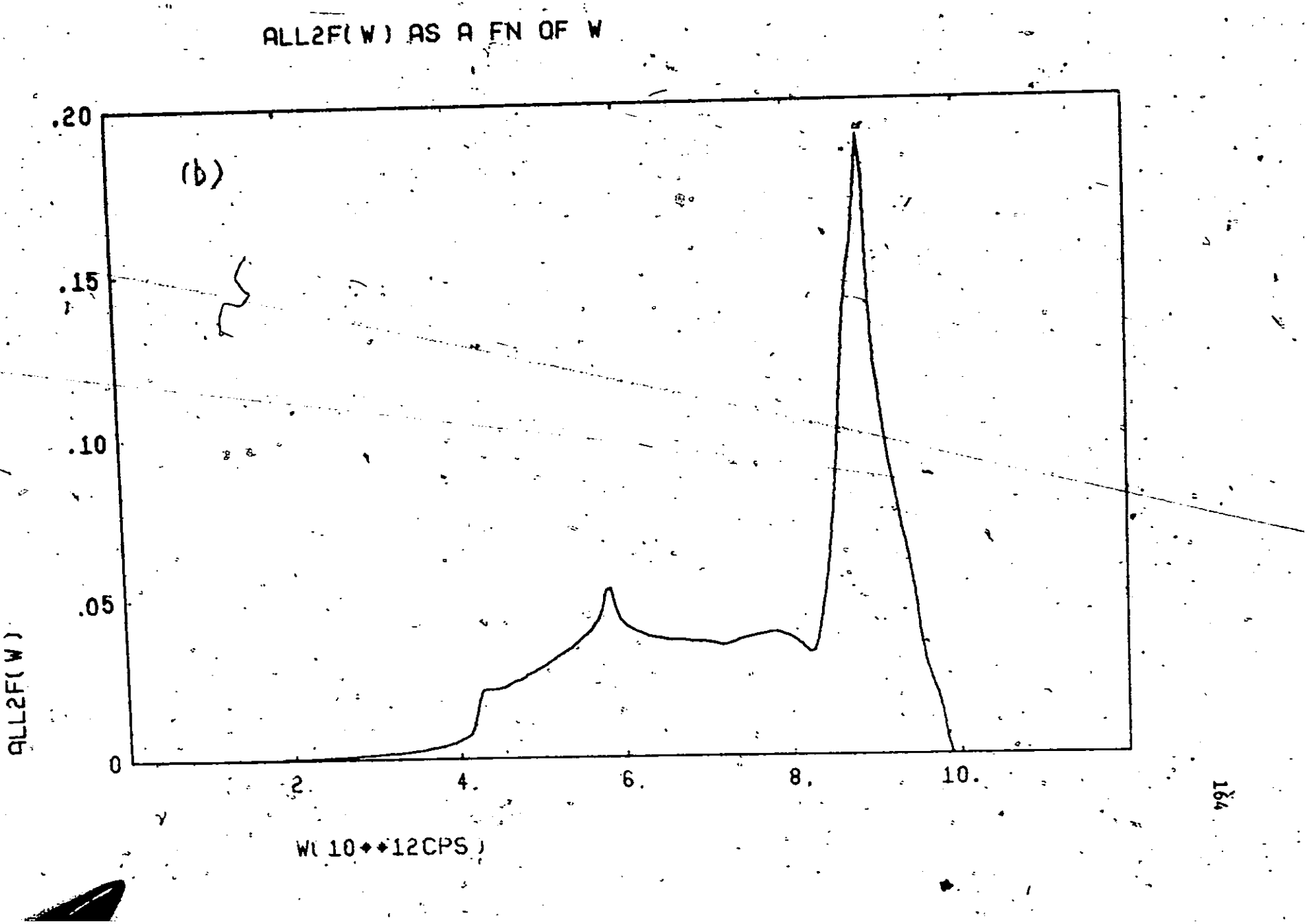
ALL2F(W) AS A FN OF W
(b)
.20
.15
.10
.05
0
2.
4.
6.
8.
10.
ALL2F(W)
W(10**12CPS)

increases to a maximum of 0.011 and then falls to a negative value of - 0.0001 near 0.6 ω_c. From then it increases to a maximum peak value of 0.06 and decreases to zero at $\omega = \omega_c$. The 15-OPW calculation, however, starts at negative values (too small to be seen on a graph), then achieves a positive maximum of .009 and decreases gradually to zero and between ω = .35 ω_c to ω = .70 ω_c it is negative with a minimum value of - .007. From then on it behaves like the S-OPW calculation except the peak value is at 0.109.

The $\alpha^2_{LL}F(\omega)$ functions are very similar except that the 15-OPW calculation has a higher peak at the high frequency end.

To calculate S(T), we need the specific heat $C_L(T)$ and instead of obtaining it from experiments, we calculate it through the expression (Ziman 1960),

$$C_L(T) = N k_B \int_0^\infty \frac{(\hbar\omega\beta)^2 e^{\hbar\omega\beta}}{(e^{\hbar\omega\beta}-1)^2} F(\omega)\, d\omega \qquad 6.2.1$$

where $F(\omega)$ is the phonon density of states. The results for S(T) are presented in Table 6.2.1 where the S-OPW calculation is compared with the 15-OPW calculation. These results are plotted in Figure 6.2.4 together with the experimental values obtained from Gripshover et al (1967). Both calculations are found to agree with experiment qualitatively in sign. However, the S-OPW calculation gives values that differ by an order of magnitude compared to the experimental data. The 15-OPW calculation shows remarkable agreement up to a temperature of 80°K.

The physics for explaining the behaviour of the phonon-drag is contained in the fact that the $\alpha^2_{IL}F(\omega)$ can achieve +ve or -ve values. Since in Equation 6.1.7 the integral over

$\alpha^2_{IL}F(\omega)\times R(\omega)$ gives $P_{IL}(T)$. and $R(\omega)$ samples the low frequencies regions of $\alpha^2_{IL}F(\omega)$ at low temperatures, a positive region of $\alpha^2_{IL}F(\omega)$ will contribute a negative amount to the thermopower (see Equation 6.1.4). For example, the S-OPW $\alpha^2_{IL}F(\omega)$ has large positive low frequency components, hence the thermopower is quite large and negative in sign. In the more proper 15-OPW treatment the low frequency components are small; moreover, there is a substantial negative region between .55 ω_c and .70 ω_c. This cuts down the positive contribution to S(T). The origin of these negative regions comes from Umklapp scattering and it was believed by Ziman (1960) and Bailyn (1958) responsible for the positive thermopowers. Through their careful analysis Hayman and Carbotte (1973) actually showed that in Lithium this is, indeed, the case.

Table 6.2.1

Thermopower of Aluminium

T °K	- Sg(T) (μV/°K) S-OPW cal.	- Sg(T) (μV/°K) 15-OPW cal.
10	.23	.08
15	.97	.32
20	1.49	.61
25	2.02	.86
30	3.41	1.08
40	5.41	1.52
50	7.32	1.94
60	9.14	2.37
80	12.45	3.25
100	15.25	4.08

Fig. 6.2.4 The thermopower of Aluminium as a function of temperature

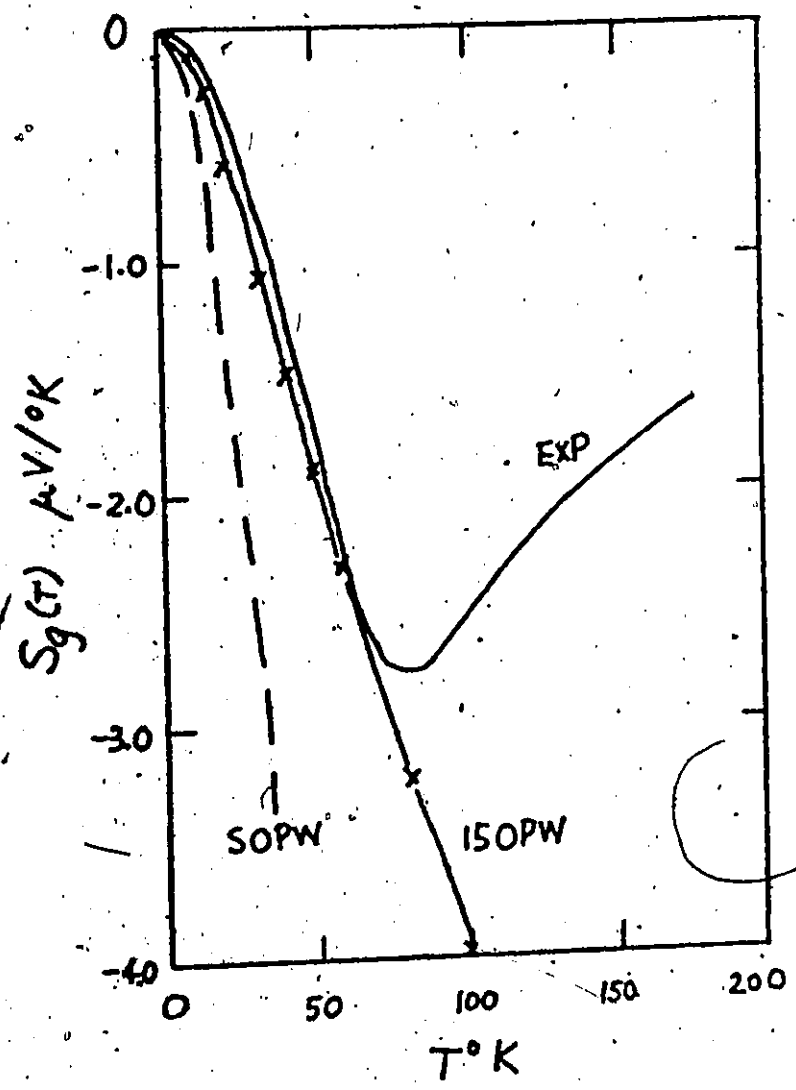
0
-1.0
-2.0
-3.0
-4.0
$S_g(T)$ μV/°K
EXP
50PW
150PW
0
50
100
150
200
T° K

Table 6.2.2

Ratio of Ideal Resistivity to the Value Without Phonon-Drag Corrections in S-OPW Approximation and 15-OPW Approximation

T °K	$\rho(T)/\rho_i(T)$ S-OPW	$\rho(T)/\rho_i(T)$ 15-OPW
10	.98959	.93958
20	.97244	.86411
30	.97139	.93132
40	.97600	.96439
50	.97948	.97714
60	.98144	.98214
80	.98281	.98511
100	.98288	.98401
150	.98221	.98463
200	.98172	.98411
300	.98125	.98343

In completing this Section, it is interesting to calculate in the above approximation the effect of phonon-drag on the electrical resistivity of Al. We compute Equation 6.1.3 the ratio $\rho(T)/\rho_i(T)$ and present it in Table 6.2.2. The effect due to phonon-drag is seen to be small at high temperatures and for the 15-OPW calculation has a minimum at about 20°K. This was also found by Hayman and Carbotte (1973) in their study of the alkali metals.

CHAPTER VII

CONCLUSION

The main purpose of this thesis is to show (through computation methods) that a fuller treatment of the electron-ion interactions in metals (a 15-OPW) can bring out more interesting results than the conventional 3-OPW calculations in a polyvalent metal such as Aluminium. The results are both interesting and encouraging. We use the Ashcroft fitting parameters to reproduce the 4-OPW Fermi Surface of Aluminium and the Heine-Abarenkov pseudopotential for calculating both the wavefunctions of the electrons and the electron-ion interaction, thus utilizing the best information available on the band structure of the electronic states in Aluminium. Together with the Born-von Kármán fitting to the phonons, all the subsequent calculations could then be done without any adjustable parameters. They all seem to agree quite satisfactorily with experiment.

First of all, we computed the directional weighted frequency distributions $\alpha^2F(\underline{k},\omega)$, $\alpha^2_{tr}F(\underline{k},\omega)$, $\alpha^2_{LL}F(\underline{k},\omega)$ and $\alpha^2_{LL}F(\underline{k},\omega)$. These functions agree with the 3-OPW calculations when $\underline{k}$ is far away from Bragg planes. When $\underline{k}$ is near to a Bragg plane, the usual catastrophic scattering (of the electron scattering into itself) singularity is completely removed in the 15-OPW calculation. It is shown that the matrix element $\alpha^2(\underline{q},\omega)$ which represents the electron-ion interaction actually goes towards zero as $|\underline{q}| \to 0$. ($\underline{q}$ is the wave vector reduced to the FBZ). There has been some surmize that $\alpha^2(\underline{q},\omega)$ goes like a constant as $\underline{q} \to 0$, however, this calculation shows otherwise. It actually goes

towards zero for all directions of $\underline{q}$.

The fact that the low frequency parts of the $\alpha^2F(\underline{k},\omega)$ functions are singular in the S-OPW approximation lead Cohen to a correcting procedure which consists of demanding it to go to zero linearly at small $\underline{k}$. Our calculations shows that the approximate treatment is qualitatively correct. More severe discrepancies lie in the calculation of the other quantities over the FS such as λ, $\bar{\lambda}$, Δ and the anisotropy parameters $\langle a^2 \rangle$, $\langle ab \rangle$, $\langle \bar{ab} \rangle$, etc. With the proper inclusions of the Bragg planes and the correct wavefunctions of the electrons, we found large discontinuities as we crossed the Bragg planes from one zone into the next. These discontinuities are usually absent in the S-OPW approximation and often lead to entirely different anisotropies.

With the inclusion of a more realistic FS, we did a different average over the FS by including the proper surface areas $dS_{\underline{k}}$ and the velocities $V_{\underline{k}}$ on the FS in different directions. As a result some regions show a higher density of states than the rest. Moreover, some are forbidden regions where there is simply no density of states. All these features are very important when one deals with physical quantities that are dependent, not just on the average, but also on the anisotropies of these features over the FS.

In the calculation of the superconducting properties of Aluminium the 15-OPW shows larger anisotropies due to phonons and band structure effects than the S-OPW calculations and are in fair agreement with experiment.

In calculating the transport properties, the electrical

resistivities agree very well with experiment. Its better agreement lies in the proper treatment of the low frequency part of $\alpha^2_{tr}F(\underline{k},\omega)$. Again, the scattering time approach is seen to do a better job than the variational solution. The reason is that the scattering time approach can incorporate the complicated features of the anisotropies in the scattering times (contained in $\phi_{\underline{k}}$). In the case of thermo-resistivities the computations are not in as good agreement with experiment. This is probably due to the inadequacy of the first order trial wavefunction used in $\phi_{\underline{k}}$, a conclusion both reached by Hayman and Carbotte (1972) in their study of the alkali metals and Tomlinson (1973), in his study of Zinc.

The study of the Hall coefficient in the low field limit generated some interesting results. Datars and Douglas applied the Chambers method of performing line integrals over the true Fermi Surface to study the field dependence. They found that a variation of $\frac{\tau_e}{\tau_h}$ will give a good fit to experimental data. In our study, we go beyond this by including both the Fermi Surface effects and the variation of the scattering times. As we know that the phonon scattering times are reliable from our study of electrical resistivities, we could direct our attention solely to the anisotropies of the impurity scattering times. By applying a model similar to Dugdale and Firth in their study of the Hall coefficient in dilute alloys of Cu and Ag, we were able to reproduce very well the experimental results in Al by lessening the scattering probability for impurity scattering of electrons at the Bragg planes by roughly a factor of 2. Otherwise, we are unable to reproduce the change of sign of the

Hall coefficient at about 30°K as a function of temperature.

The study of (DMR) was also done on the dilute alloys of Al, mainly the Al-Mg and Al-Ag alloys. Again, with the same assumption as in the study of the Hall coefficient about impurity scattering, we are able to produce Seth and Wood's experimental data with quite good agreement, especially at low temperatures (typically less than 100°K). A study by Tomlinson and the author (not included in this thesis) was carried out to try to understand the mechanism of impurity scattering in Al-Mg alloys. Preliminary results, indeed, showed the above phenomenological assumption is correct for the impurity scattering for electrons at the Bragg planes are smaller typically by a factor of about 2.

Lastly, we extended Ziman's formulae for the phonon-drag contribution to the thermopower of Aluminium, and are gratified to see that it gives reasonable qualitative and semi-quantitative results without further modifications at low temperatures.

Computations done in this thesis are quite time-consuming even with speedy electronic computers. When this work is done on the CDC 6400 computer at McMaster University, each directional calculation of the weighted distribution functions consumes about 1200 sec. So we have to limit ourselves to about 62 points distributed over the $(\frac{1}{48})$ of the BZ. Due to the fact that one has to interpolate every function over the $(\frac{1}{48})$ zone, the need for high accuracy is clear. Fortunately, we believe that the 62 points are quite evenly distributed so that we could simplify the interpolation by a linear one. Some very find details of the anisotropies are bound to be sacrificed although the results are still very

appealing. Improvements will lie in a better interpolation scheme.

The results of this work are, then, very encouraging and may be readily applied to metals such as Lead and maybe Copper, Silver and Gold.

REFERENCES

Alderson, J.E., and Farrell, T., 1969, Phys. Rev. 185, 876.

Allen, P.B., and Cohen, M.L., 1969, Phys. Rev. 187, 525.

Allen, P.B., and Cohen, M.L., 1970, Phys. Rev. B1, 1329.

Animalu, A.O.E., and Heine, V., 1965, Phil. Mag. 12, 1249.

Ashcroft, N.W., and Cuild, L.J., 1965, Phys. Letters 14, 23.

Ashcroft, N.W., and Wilkins, J.W., 1965, Phys. Letters 14, 285.

Ashcroft, N.W., 1963a, Phil. Mag. 8, 2055.

Ashcroft, N.W., 1963b, Phys. Letters 4, 202.

Ashcroft, N.W., 1968, J. Physics C1, 232.

Bailyn, M., 1960, Phys. Rev. 120, 381.

Bailyn, M., 1967, Phys. Rev. 157, 480.

Balsley, J.F., 1969, Ph.D. Thesis (unpublished).

Bardeen, J., 1937, Phys. Rev. 52, 688.

Bhatia, A.B., and Gupta, O.P., 1969, Phys. Letters A29, 358.

Bass, J., 1972, Adv. Phys. 21, 431.

Bassani, F., and Celli, V., 1961, Phys. Chem. Solids 20, 64.

Bennett, A.J., 1965, Phys. Rev. 140, A1902.

Bloch, F., 1928, Z. Physik. 52, 555.

Born, M., and Oppenheimer, J.R., 1927, Ann. Physik. 4, 84, 457.

Bryukhanov, V.A., Dalyagin, N.N., and Kagan, Y., 1964, Soviet Phys. JETP 19, 563.

Carbotte, J.P., and Dynes, R.C., 1967a, Phys. Letters 25A, 685.

Carbotte, J.P., and Dynes, R.C., 1967b, Phys. Letters 25A, 532.

Carbotte, J.P., and Dynes, R.C., 1968, Phys. Rev. 172, 476.

Carter, R.L., 1971, Ph.D. Thesis, Michigan State University, (unpublished).

Chambers, R.G., 1956, Proc. Roy. Soc. (London), A238, 344.

Chambers, R.G., 1960, "Magnetoresistance" in The Fermi Surface, W.A. Harrison and M.B. Webb (eds.), John Wiley & Sons, New York.

Cheeke, J.D.N., and Ducla-Soares, E., 1968, Phys. Letters 27A, 264.

Cohen, M.H., and Heine, V., 1961, J. Phys. Chem. Solids 20, 64.

Cohen, M.L., and Heine, V., 1970, Solid State Physics 24, Academic Press, New York and London.

Collins, J.G., and Ziman, J.M., 1961, Proc. Roy. Soc. A264, 60.

Cook, J.G., 1973, (private communication).

Cooper, J.R., and Raimes, S., 1959, Phil. Mag. 4, 145.

Deutsch, T., Paul, W., and Brooks, H., 1961, Phys. Rev. 124, 753.

Douglas, R.J., and Datars, W.R., 1973a, Solid State Comm. 13, 839.

Douglas, R.J., and Datars, W.R., 1973b, Cdn. J. of Phys. 51, 1770.

Dugdale, J.S., and Bailyn, M., 1967, Phys. Rev. 157, 485.

Dugdale, J.S., and Firth, L., 1969a, Physik Kandersierten Materie 9, 54.

Dugdale, J.S., and Firth, L., 1969b, J. Physics C2, 1272.

Dugdale, J.S., and Basinski, Z.S., 1967, Phys. Rev. 157, 552.

Ekin, J.W., and Bringer, A., 1973, Phys. Rev. B8, 3610.

Fenton, E.W., 1973, J. Physics F3, 10, L190.

Fukai, Y., 1969, Phys. Rev. 186, 697.

Gayley, R.I., Jr., Lynton, E.A., and Serin, B., 1962, Phys. Rev. 126, 43.

Gilat, G., and Nicklow, R.M., 1966, Phys. Rev. 143, 487.

Gilat, G., Rizzi, G., and Cubiotti, G., 1969, Phys. Rev. 185, 971.

Greene, N.P., and Kohn, W., 1965, Phys. Rev. 137, A513.

Gripshover, R.J., Van Zytveld, J.B., and Bass, J., 1967, Phys. Rev. 163, 598.

Grunnersen, E.M., 1957, Phil. Trans. A, 249, 299.

Gurevich, L., 1945, J. Physics USSR 9, 477:269.

Gurevich, L., 1946, J. Physics USSR 10, 67:269.

Hall, E.H., 1879, Am. J. Math. 2, 287.

Harrison, W.A., 1960, Phys. Rev. 118, 1182.

Harrison, W.A., 1966, Pseudopotential in the Theory of Metals, New York.

Hayman, B., and Carbotte, J.P., 1972, J. Phys. F. 2, 915.

Hayman, B., and Carbotte, J.P., 1973, Cdn. J. of Phys. 51, 1109.

Hayman, B., 1974, Ph.D. Thesis, McMaster University, Hamilton, Ontario, (unpublished).

Heine, V., and Abarenkov, I., 1964, Phil. Mag. 9, 451.

Herring, C., 1940, Phys. Rev. 57, 1109.

Hughes, A.J., Jones, D., and Lettington, A.H., 1969, J. Phys. C. 2, 102.

Hurd, M.C., 1972, The Hall Effects in Metals and Alloys, Plenum Press, New York and London.

Janak, J.F., 1968, Phys. Letters 27A, 105.

Kagan, K., and Zhernov, A.P., 1966, Soviet Phys. JETP 23, 737.

Kagan, K., and Zhernov, A.P., 1971, Soviet Phys. JETP 33, 990.

Kaveh, M., and Wiser, N., 1972a, Phys. Rev. 29, 1374.

Kaveh, M., and Wiser, N., 1972b, Phys. Rev. B6, 3648.

Kittel, C., 1967, Introduction to Solid State Physics, 3rd edition, John Wiley and Sons, New York, London and Sydney.

Kohler, M., 1949, Z. Physik 126, 495.

Koshino, S., 1960, Progr. Theoret. Phys. (Kyoto) 24, 1049.

Kus, F., 1973, Ph.D. Thesis, McMaster University, Hamilton, Ontario, (unpublished).

Laubitz, M.J., and Cook, J.G., 1973, Phys. Rev. B6, 2867.

Laubitz, M.J., and Cook, J.G., 1972, Phys. Rev. B6, 2082.

Leavens, C.R., 1971, Ph.D. Thesis, McMaster University, Hamilton, Ontario, (unpublished).

Leavens, C.R., and Carbotte, J.P., 1972, Annals Physics 70, 338.

Lynton, E.A., Serin, B., and Zucker, M., 1957, J. Phys. Chem. Solids 3, 165.

MacDonald, D.K.C., 1956, Hanbuchder Physik Vol. XIV, edited by S. Flugge, (Springer, Berlin).

MacDonald, D.K.C., Pearson, W.B., and Templeton, I.M., 1958, Proc. Roy. Soc. A248, 107.

Nowak, D., 1972, Phys. Rev. B6, 3691.

Panova, G.K., Zhernov, A.P., and Kutaitsev, V.I., 1969, Sov. Phys. JETP 19, 563.

Pecheur, P., and Toussaint, G., 1973, Phys. Rev. B7, 1223.

Phillips, J.C., and Kleinman, L., 1959, Phys. Rev. 116, 287.

Polovov, V.M., and Sumin, V.I., 1964, Phys. Met. Metal. 17, 24.

Pytte, E., 1967, J. Phys. Chem. Solids 28, 93.

Rice, T.M., 1968, Phys. Rev. 175, 858.

Rice, T.M., and Sham, L.J., 1970, Phys. Rev. B1, 4546.

Robinson, J.E., 1967, Phys. Rev. 161, 3, 533.

Robinson, J.E., and Dow, J.D., 1968, Phys. Rev. 171, 815.

Rooke, G.A., 1968, J. Phys. C. 1, 776.

Rosenberg, H.M., 1963, Low Temperature Physics, Oxford, Clarendon Press.

Schenz, R., Koch, K.H., and Lihl, F., 1967, Z. Naturforsch 22a, 1473.

Schlüter, M., Böning, K., Pfändner, K., and Rosher, P., 1973, Solid State Comm. 13, 1935.

Schrieffer, J.R., 1964, Theory of Superconductivity, W.A. Benjamin, Inc., New York.

Schwerer, F.C., Conroy, J.W., and Arajas, S., 1969, J. Phys. Chem. Solids 30, 1513.

Seth, R.S., and Woods, S.B., 1970, Phys. Rev. B2, 2961.

Sham, L.J., 1961, Proc. Phys. Soc. (London) 78, 895.

Sham, L.J., and Ziman, J.M., 1963, Solid State Physics 15, 221.

Shepherd, J.P.G., and Gordon, W.L., 1968, Phys. Rev. 169, 541.

Sondheimer, E.H., and Wilson, A.H., 1947, Proc. Roy. Soc. A190, 435.

Swihart, J.C., Scalapino, D.J., and Wada, Y., 1965a, 1965b, Phys. Rev. 14, 106.

Taylor, P.L., 1964, Phys. Rev. 135, A1333.

Tomlinson, P.C., 1973, Ph.D. Thesis, (unpublished).

Tomlinson, P.C., and Swihart, J.C., 1972, Proc. of the Thirteenth Int. Conf. on Low Temperature Physics, Boulder.

Trofimenkoff, P.N., Carbotte, J.P., and Dynes, R.C., 1968, Phys. Letters 27A, 394.

Trofimenkoff, P.N., and Eiken, J.W., 1971, Phys. Rev. B4, 2392.

Truant, P., 1972, Ph.D. Thesis, McMaster University, Hamilton, Ontario, (unpublished).

Tsuji, M., 1958, J. Phys. Soc. (Japan) 13, 979.

Ziman, J.M., 1960, Electrons and Phonons, Oxford University Press, London and New York.

Ziman, J.M., 1961a, Adv. Phy. 10, 1.

Ziman, J.M., 1961b, Phys. Rev. 121, 1320.